ISSN 1580-2949
UDK 669+666+678+53 MTAEC9, 46(4)317–427(2012)

MATER. TEHNOL.	LETNIK VOLUME 46	ŠTEV. NO. 4	STR. P. 317–427	LJUBLJANA SLOVENIJA	JULY–AUG. 2012

VSEBINA – CONTENTS

Predgovor urednika

Opažamo, da revija *Materiali in tehnologije* postaja cenjena v različnih strokovnih krogih, saj omogoča vpogled v dogajanje na področju kovinskih, polimernih in anorganskih materialov ter tehnologij s teh področij. Povečuje se število slovenskih avtorjev, povečuje pa se tudi interes avtorjev iz tujine. To je dokaz, da gre razvoj revije v pravo smer, vključenost v sistem SCI pa reviji še povečuje dodano vrednost. Revija je pomembna tudi iz nacionalnega stališča. Večina znanstvenih in strokovnih člankov je v angleškem jeziku, v slovenski jezik pa so prevedeni naslov, povzetek, ključne besede, naslovi tabel in napisi pod slikami. To prispeva k širjenju slovenske strokovne terminologije, kar je pomembno za bogatenje in nadaljnji razvoj slovenskega tehniškega jezika.

Podobno kot pri drugih revijah, se tudi v reviji *Materiali in tehnologije* pojavljajo tematske številke. Ena takih je bila tudi prva številka v letu 2012, ki je povzročila v določenem krogu bralcev nekoliko nepričakovan odziv. Podrobnejša analiza je pokazala, da je bila ta številka verjetno izrabljena tudi za povečanje samopromocije skupine raziskovalcev, kar je lahko sporno s stališča etike objavljanja člankov.

Sedanji sistem ocenjevanja raziskovalcev zelo upošteva citiranost kot temeljno merilo kakovosti raziskovalnega dela in posledično tudi financiranja projektov, premalo pa upošteva pomembnost dosežkov za okolje, ki delo financira. Uravnoteženo upoštevanje obeh meril bi morala biti, poleg izvirnosti ciljev raziskovanja, zelo pomembna komponenta ocenjevanja raziskovalnih projektov, ki so predloženi v financiranje iz javnih sredstev, in kakovosti raziskovalnih skupin. Prevelika teža števila objav in citatov spodbuja pisce rokopisov k pridobivanju čim več citatov, pri čemer ni dovolj upoštevana etika objavljanja. Večina avtorjev uporablja citiranje in samocitiranje v razumnih mejah. Mogoče pa so tudi zlorabe, ki jih uredništvo revije *MiT* ne more odkrivati, jih pa lahko odkrijejo dobri poznavalci tematike, predstavljene v članku, in še posebej recenzenti. Prav bi bilo, da bi v takih primerih na odmike opozorili uredništvo *MiT*, da bi lahko ukrepalo, ko bodo isti avtorji predložili v objavo nove rokopise.

Kot odgovorni urednik revije menim, da je neetično do avtorjev kakršno koli številčno omejevanje avtocitatov in citatov, zato pa naj avtorji pokažejo primerno samokritičnost in naj avtocitate in citate uporabljajo v razumnem obsegu, kot se to dela pri drugih uglednih revijah. Pri tem pa morajo ustrezno vlogo odigrati tudi

Foreword of the Editor-in-Chief

The journal *Materials and Technology* is becoming increasingly appreciated in various professional circles because it offers an insight into the metals, polymers and inorganic materials and technologies used in these fields. The number of Slovenian authors is increasing, but we are also seeing an increase in the level of interest from authors in other countries. This is proof that the journal is developing in the right direction, and our involvement in the SCI system increases the journal's added value. The journal is also important from a national point of view. Most of the scientific articles are in English, while the title, abstract, keywords, table headings and figure captions are translated into Slovene. This contributes to the spread of Slovenian technical terminology, which is important for the enrichment and further development of Slovene.

As is the practice with other journals, the journal *Materials and Technology* publishes thematic issues. One of these was the first issue in 2012, which resulted in a reaction from a certain circle of readers. A detailed analysis showed that this thematic issue was used by a group of scientists for the purposes of self-promotion, which may have been wrong from the point of view of ethics in publishing. The current evaluation system encourages researchers' citations, but the approach of different authors may vary. Most authors use citations within reasonable limits, but there are also exceptions.

The existing system for evaluating researchers takes into account citations as a fundamental measure of the quality of research work and, consequently, the funding of projects, but too little emphasis is given to the importance of the outcome for the environment that funded the work. A balanced consideration of the two criteria should be, in addition to the originality of the research goals, a very important component in the evaluation of research projects submitted for financing from public funds and for the evaluation of the quality of research groups. Too much weight given to the total number of citations encourages writers of manuscripts to obtain as many references as possible and not to take sufficient account of publishing ethics. Most authors use self-citations and citations within reasonable limits. However, there are also abuses that cannot be detected by the Editorial Board of the *MIT*, although they can be detected by people familiar with the subject of the article, and especially by referees. In such cases the problem would be pointed out to the Editorial Board, to act upon it when the same authors present new manuscripts for publication.

recenzenti, ki naj bodo v prihodnje pri pregledu in oceni rokopisov bolj pozorni tudi na ta vidik.

Nadaljnja rast kvalitete revije mora biti cilj nam vsem, ki smo s to revijo povezani že vrsto let, tudi članov uredniškega odbora in sveta.

Glavni in odgovorni urednik
doc. dr. Matjaž Torkar

As the responsible Editor-in-Chief I consider it unethical to impose a numerical limitation on authors' citations. Instead, authors should show more self-restraint and use citations within reasonable limits, as is customary with other reputable journals. The role of the referee, who should pay more attention to this aspect during the reviewing and evaluation of manuscripts, is also vitally important.

A steady growth in the quality of the journal should be the goal for all of us who have been connected with this journal for many years.

Editor-in-Chief
A/Prof. Dr. Matjaž Torkar

UDK 669.131.6:536.421.4
Original scientific article/Izvirni znanstveni članek

ISSN 1580-2949
MTAEC9, 46(4)321(2012)

NUMERICAL AND EXPERIMENTAL INVESTIGATION OF THE TEMPERATURE FIELD OF A SOLIDIFYING MASSIVE DUCTILE-CAST-IRON ROLLER

NUMERIČNE IN EKSPERIMENTALNE RAZISKAVE TEMPERATURNEGA POLJA PRI STRJEVANJU LITEGA VALJA IZ SIVE LITINE S KROGLASTIM GRAFITOM

František Kavička[1], Karel Stránský[1], Jana Dobrovská[2], Bohumil Sekanina[1], Josef Štětina[1], Vasilij Gontarev[3]

[1]Brno University of Technology, Technicka 2, 616 69 Brno, Czech Republic
[2]VSB TU Ostrava, 17. listopadu 15/2172, 708 33 Ostrava, Czech Republic
[3]University of Ljubljana, Aškerčeva 12, 1000 Ljubljana, Slovenia
kavicka@fme.vutbr.cz

Prejem rokopisa – received: 2011-10-17; sprejem za objavo – accepted for publication: 2012-02-24

The quality of the working rollers used for rolling rails of different profiles is determined by the chemical and structural composition of the material of the rollers and the production technology The requirements for the quality cannot be ensured without a perfect knowledge of the course of the solidification, the cooling and the heat treatment of the cast rollers as well as the kinetics of the temperature field of the casting and the mould. The solidification and cooling of the ductile-cast-iron roller in metal and non-metal moulds is a very complicated problem of heat and mass transfer with the phase and structural changes described by the Fourier equation. An original application of ANSYS simulated the forming of the temperature field of the entire system, comprising the casting, the mold and the ambient. The simulation of the release of the latent heats of the phase or structural changes is carried out by introducing the thermodynamic enthalpy function. In the experimental investigation of the temperature field, an original methodology for the measurement of the distribution of temperatures and heat flows in the roller-mould system had been developed and verified in operation. In the design of the original procedure, there were a number of problems connected with the large size of the roller and the mould, the uneven dimensional changes of the solidifying roller and the mould, the installation and the insulation of the thermocouples, the wiring of the thermocouple system, etc. The findings regarding the kinetics of the temperature field of the roller and the mould, obtained from experimental research, were used to determine the boundary conditions and for the verification of the numerical simulation program. The calculation of the temperature field focused on an analysis of the effect of the mould separator on the course of the solidification of the roller. The results of the mathematical modelling indicate that the distribution of the temperatures and the solidification in the vertical direction is significantly uneven – and this has an effect on the internal quality of the casting.

Keywords: spheroidized graphite cast iron (SGI), massive roller, solidification, temperature field, numerical model

Kakovost delovnih valjev za valjanje železniških tirnic različnih profilov je določena s kemijsko sestavo, mikrostrukturo in s proizvodno tehnologijo. Zahteve za kakovost ni mogoče zagotoviti brez popolnega poznanja poteka strjevanja, ohlajevanja in toplotne obdelave ulitih valjev ter kinetike temperaturnega polja ulitka in forme. Strjevanje in ohlajevanje ulitega valja, ki je ulit iz sive litine s kroglastim grafitom v kovinsko in nekovinsko formo, je zelo zapleten problem z vidika prenosa toplote in mase s faznimi in strukturnimi spremembami, ki jih opisuje Fourierjeva enačba. Z uporabo programskega paketa ANSYS-a je bilo simulirano temperaturno polje celotnega sistema, ki obsega ulivanje, formo in okolje. Simulacija prenosa latentne toplote faznih in strukturnih sprememb se izpelje z uporabo termodinamične funkcije entalpije. Pri eksperimentalni raziskavi temperaturnega polja je bila razvita izvirna metodologija za merjenje temperaturnega polja in toplotnega toka v sistemu valj – forma. V konstrukciji izvirnega postopka so številni problemi vezani z velikostjo valjev in forme, neenako dilatacijo pri strjevanju valja in forme, namestitvi in izolaciji termočlenov, napeljavi sistema termočlenov itd. Ugotovitve glede na kinetiko temperaturnega polja valja in forme, dobljene z eksperimentalnimi raziskavami, so bile uporabljene za določitev mejnih pogojev ter za potrditev numeričnega programa simulacije. Izračun temperaturnega polja je bil osredinjen na analizo učinka separatorja forme na potek strjevanja valja. Rezultati matematičnega modeliranja kažejo, da je porazdelitev temperatur in strjevanja v navpični smeri neenaka, kar vpliva na notranjo kakovost ulitka.

Ključne besede: siva litina s kroglastim grafitom, masivni valj, strjevanje, temperaturno polje, numerični model

1 INTRODUCTION

The solidification and cooling of these rollers – partly inside a sand mould and partly inside an iron mould – is a very complicated problem of heat and mass transfer with both phase and structural changes. An original application of ANSYS simulated the forming of the temperature field of the entire system. The introduced 3D model of the temperature field is based on the numerical finite-element method. Experimental research and temperature measurements must be conducted simultaneously with the numerical calculation in order to make the model more accurate and to verify it[1–3].

2 THE ASSIGNMENT AND PREPARATION OF THE INVESTIGATION

The assignment focused on investigating the transient 3D temperature field of a system comprising the casting, the mould and the ambient using a numerical model. The

dimensions of the cylindrical casting and of the iron mould are given in **Figure 1**, while the diameter of the actual roller is 1180 mm with a height of 2100 mm.

This figure illustrates the entire set-up, comprising two parts of the sand mould for the upper and lower spindle ends and the iron mould. The working surface of the iron mould is covered with a separating layer – hereafter referred to as the "separator" (which is a special lubricant applied in various thicknesses to the inside walls of the iron mould and kiln-hardened at 180 °C prior to casting). The initial temperature of the mould was 20 °C, while the pouring temperature of the melt was 1336 °C. The casting was performed from underneath with a tangential in-flow. The total time of the casting of the spheroidal graphite cast iron (SGI) was 175 s.

2.1 Numerical model of the temperature field of the roller

The mathematical model for the simulation of the temperature field of the roller-mould system was created by ANSYS. The simulation of the release of the latent heats of the phase or structural changes is carried out by introducing the thermodynamic enthalpy function[4,5]. The program also considers the non-linearity of the task, i.e.:

- The dependence of the thermo-physical properties of all the materials entering the system
- The dependence of the heat-transfer coefficients (on all the boundaries of the system) on the temperature of the surface of the casting and mould.

A series of experimental temperature measurements was conducted for the verification of the model and the closer determination of the boundary conditions of the numerical solution of the temperature field. The results from the experimental measurements were used for the verification of the model and the correction of the boundary conditions for the numerical solution of the temperature field. The calculation of the temperature field dealt mainly with the effect of the separator between the casting and the iron mould on the solidification of the roller.

2.2. The results of the simulation of the temperature field with respect to the separator thickness[1]

The thicknesses of the separator – for individual simulations of the solidification and cooling of the roller – were (0, 5, 10 and 15) mm. The point where the melt solidifies last is the centre – 2100 mm from the base of the iron mould. The centre of the body of the roller is on the axis at a distance of 1050 mm from the same base. **Table 1** contains the solidification times of the roller, which are calculated from the simulation.

Table 1: Solidification times for various separator thicknesses
Tabela 1: Čas strjevanja pri različnih debelinah separatorja

Separator thickness	Solidification time			
	Centre of roller		Entire roller	
(mm)	*t*/h	*t*/s	*t*/h	*t*/s
15	8 187	29 473	8 783	31 618
10	7 845	28 242	8 124	29 246
5	7 030	25 310	7 531	27 111
0	6 510	23 437	6 554	23 593

Figures 2 and **3** illustrate the temperature field along the longitudinal axis of the system without the separator and with a 15 mm separator after 7.845 h, i.e., at the time when the centre of the roller solidifies with a separator that has a mean thickness of 10 mm (**Table 1**).

It is possible to observe an enlargement of the above-mentioned red area along the vertical axis with an increasing thickness of the separator. **Figure 4** shows the dependence of the total solidification time of the centre of the roller and the entire roller on the separator

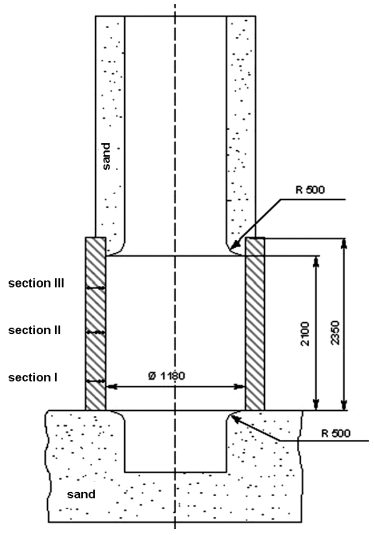

Figure 1: The set-up of a vertically cast
Slika 1: Sistem vertikalnega ulivanja

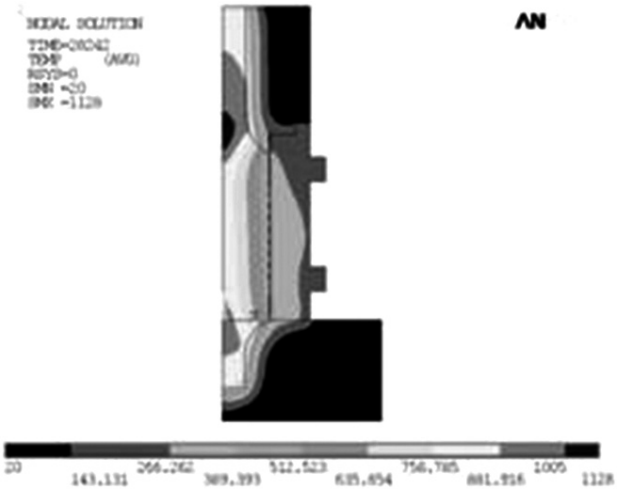

Figure 2: The temperature field along the longitudinal section (without the separator)
Slika 2: Temperaturno polje po vzdolžnem prerezu (brez separatorja)

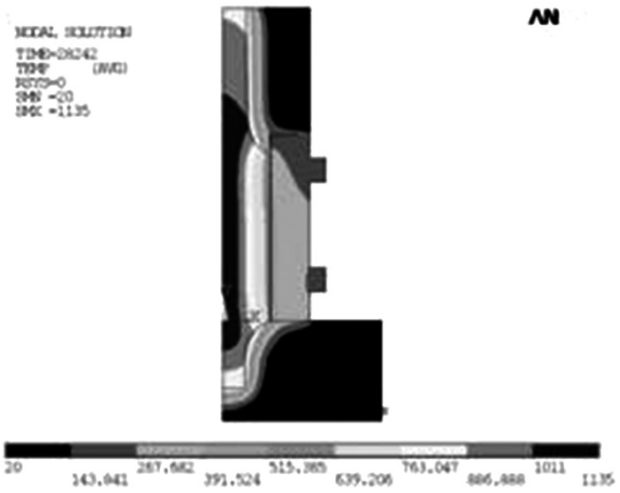

Figure 3: The temperature field along the longitudinal section (with a 15 mm separator)
Slika 3: Temperaturno polje po vzdolžnem prerezu (s separatorjem 15 mm)

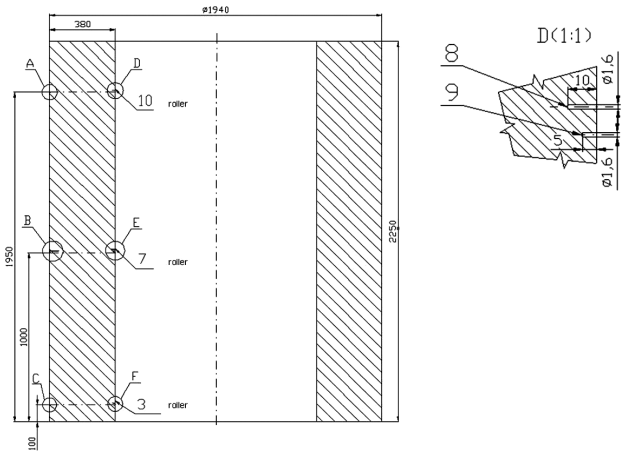

Figure 5: Layout of measurement points
Slika 5: Položaj merilnih točk

thickness. The relationship between the separator thickness and the solidification time can be described in great detail using the linear function – as the reliability coefficient values in **Figure 4** indicate for both straight lines. The separator has proven to be a good insulator. The solidification time of the roller inside the mould with a 15 mm separator increases by up to 26 % compared to that without the separator.

3 EXPERIMENTAL MEASUREMENT OF THE TEMPERATURES INSIDE THE PERMANENT MOULD AND ON THE SURFACE OF THE ROLLER

The distribution of the temperatures along the height of the iron mould and roller (**Figure 5**) was measured in three horizontal planes, 100 mm (section I), 1000 mm (sect. II) and 1950 mm (section III), from the bottom edge of the iron mould (**Figure 1**).

The inner surface of the permanent mould, i.e., point 9), was selected for the comparison of the temperatures from the numerical simulation with the experimentally obtained temperatures from inside the iron mould.

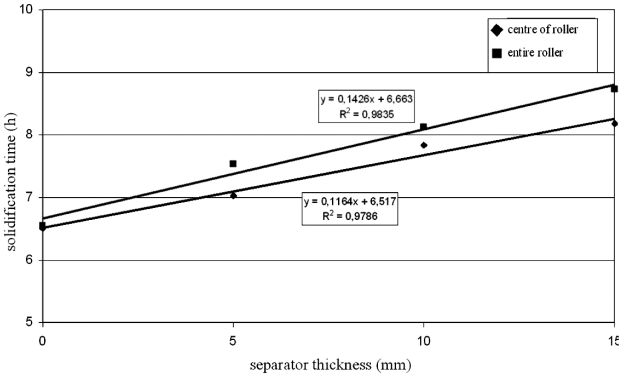

Figure 4: The influence of the separator thickness on the total solidification time
Slika 4: Vpliv debeline separatorja na celotni čas strjevanja

Figure 6 confirms the very close similarity between the calculated and measured temperatures of the permanent mould. It appears that the absolute values and the histories of the experimental and calculated temperatures in the points of the cylindrical casting and iron mould, which had been selected for comparison, are very similar. The determined relationship between the solidification time (of the entire casting or its geometrical centre) and the thickness of the separator applies. The simulation of the temperature field of the roller and the mould (using ANSYS) can therefore be considered to be successful.

The results of the mathematical model indicate that the distribution of the temperatures and the course of the solidification in the vertical direction is relatively uneven, which affects the internal quality of the casting. While the body of the roller is solidified along the entire height, the temperatures are still high in the lower spindle and could be the cause of the shrinkage porosity at the point where the spindle enters the roller. That is why the lower spindle should solidify in a mould with a higher heat accumulation, i.e., in a mould made of CT-CrMg or in an iron mould. A sooner topping-up of

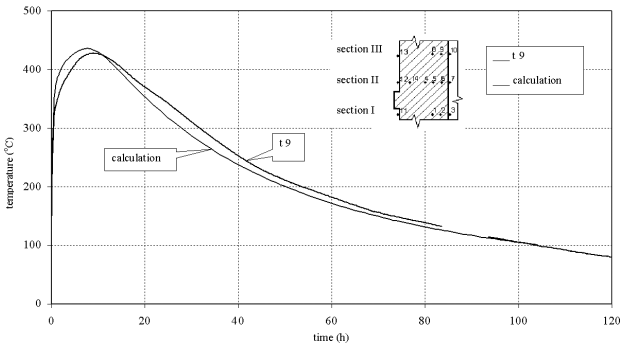

Figure 6: Calculated versus measured temperatures (point 9)
Slika 6: Izračunane temperature v primerjavi z izmerjenimi (točka 9)

the upper spindle should ensure replenishing of the mould with melt into the body of the roller in order to achieve increased quality.

Acknowledgements

This analysis was conducted using a program devised within the framework of the GACR projects No. 106/08/0606, 106/09/0940, 106/09/0969 and P107/11/1566.

4 REFERENCES

[1] J. Molinek, et al., Optimization of technological parameters of the gravity-cast rolls for rolling rails. In: Final research report of the project GACR 106/04/1334, Ostrava, Czech Republic, January 2007

[2] J. Dobrovska et al., Two numerical models for optimization of the foundry technology of the ceramics EUCOR. In: Proceedings and CO ROM of the 2004 ASME Heat Transfer Fluids Egineering Summer Conference, Charlotte, North Carolina, USA, 2004, 30–36

[3] F. Kavicka et al., A numerical model of the crystallization of pure aluminium, in Fluid Structure Interaction and Moving Boundary Problems, WITpress Southampton, Great Britain, 2005, 619–629

[4] F. Kavicka et al., Numerical optimization of the method of cooling of a massive casting of ductile cast-iron. In: Book of Abstracts and CD ROM of the 13th International Heat Transfer Conference, Sydney, Australia, August 2006, 27

[5] F. Kavicka et al., The optimization of a concasting technology by two numerical models, Journal of Materials Processing Technology, 185 (**2007**), 152–159

UDK 621.74.047:66.011
Original scientific article/Izvirni znanstveni članek

ISSN 1580-2949
MTAEC9, 46(4)325(2012)

A FUZZY-BASED OPTIMAL CONTROL ALGORITHM FOR A CONTINUOUS CASTING PROCESS

ALGORITEM, KI TEMELJI NA MEHKI LOGIKI, ZA OPTIMALNI NADZOR KONTINUIRNEGA PROCESA ULIVANJA

Tomas Mauder, Cenek Sandera, Josef Stetina

Brno University of Technology, Faculty Mechanical Engineering, Technicka 2, Brno, Czech Republic
ymaude00@stud.fme.vutbr.cz

Prejem rokopisa – received: 2011-10-19; sprejem za objavo – accepted for publication: 2012-02-24

Nowadays, continuous casting is used for processing almost one hundred percent of liquid steel into an intermediate shape. Steel with a poor structure and many defects is not acceptable to final customers, and therefore the producers must put strong emphases on its quality. Many serious steel defects can be eliminated by a preceding computer simulation, optimization and a proper control of the casting process. This paper describes an algorithm that optimizes the control parameters to ensure both a high production rate and a high quality of the products. These controlled parameters are the casting speed and all the cooling rates in the secondary cooling zone. The main principle of the algorithm is to get the surface and core temperatures to the prescribed values corresponding to the required ductility of steel. The whole optimization procedure consists of two separate parts, i.e., the numerical simulation of the process and the decision-making part based on fuzzy logic for modifying the control parameters. By incorporating the fuzzy logic into the optimization process, the algorithm has a very robust behaviour and an easy adaptation for different grades of steel. This algorithm runs in an off-line version and can be used as a preparation tool for a real casting process where the proper setting of the casting parameters is crucial for achieving high-quality products at an economical price.

Keywords: fuzzy optimization, heuristic optimization, temperature field, continuous casting

Postopek kontinuirnega ulivanja za pridobivanje vmesne oblike se danes uporablja pri obdelavi skoraj stoodstotnega deleža tekočega jekla. Jeklo s slabo strukturo in številnimi napakami ni sprejemljivo za končne kupce, zato morajo proizvajalci veliko pozornosti posvetiti kakovosti jekla. S predhodnimi računalniškimi simulacijami, z optimizacijo in ustreznim nadzorom procesa ulivanja se lahko odpravijo mnoge resne napake jekla. V tem prispevku je opisan algoritem za optimizacijo parametrov nadzora, ki zagotavlja visoko stopnjo proizvodnje ter visoko kakovost izdelkov. Med omenjene parametre nadzora spadata hitrost ulivanja in hitrost ohlajevanja v sekundarni coni ohlajanja. Glavno načelo algoritma je, da površina in temperatura sredice dosežeta določene vrednosti, ki ustrezajo zahtevani razteznosti jekla. Celoten postopek optimizacije obsega dva med seboj ločena dela – numerično simulacijo postopka in pa del, namenjen odločanju, ki temelji na mehki logiki za spreminjanje parametrov nadzora. Z integracijo mehke logike v postopek optimizacije algoritem doseže zelo robustno vedenje in enostavno prilagoditev različnim vrstam jekla. Ta algoritem deluje v različici »off-line« in se lahko uporablja kot pripravljalno orodje za dejanski proces ulivanja, kjer je ustrezna nastavitev parametrov ulivanja ključnega pomena za proizvodnjo visokokakovostnih izdelkov po ekonomični ceni.

Ključne besede: mehka optimizacija, hevristična optimizacija, temperaturno polje, kontinuirno ulivanje

1 INTRODUCTION

Nowadays, continuous casting represents the main method worldwide for forming molten steel into semi-finished products, such as slabs, blooms, and billets. The quality of final products plays one of the most significant roles for customers, and thus to satisfy their demands and maintain the highest possible productivity is a key goal for each steelmaker.

Quality control is a prerequisite for continuous casting and cannot be achieved without a proper knowledge of the main physical influences of the casting process, i.e., the solidification, the micro and macro segregation, the crack formation, etc. During the processing of the steel in the continuous caster, there can arise many problems with its final quality. The solid shell is permanently subjected to thermal and mechanical stresses and this can result in cracks or the breakout of liquid steel through the solid shell. The sources of the mechanical stresses are the friction in the mould, ferrostatic forces, a poor adjustment of the casting speed, roll gaps, bending and straightening of strand, etc. The cracks caused by bending and straightening are influenced by the ductility of steel, and it is well documented that the ductility of steel is reduced over specific temperature ranges depending on the chemical composition[1].

Conducting industrial trials is very expensive, time-consuming and in some cases even impossible, which makes a computer simulation the only sustainable option. There exist various ways of computer or mathematical optimization and each of them has its advantages and drawbacks. Therefore, to ensure the correctness of the algorithm, it is necessary to validate the simulation output using real, measured data.

Previous researches concerned with the optimal control of a continuous casting process were generally based on simplified 1D or 2D temperature-field models[1] and were optimized by mathematical programming or heuristic methods, e.g., genetic algorithms[2], the firefly

algorithm[3] or by neural networks. Many of these models are based on simplified assumptions, and therefore they describe the casting process very roughly and not satisfactory. We developed our original numerical model for the temperature field of the real caster and its results were validated by temperature measurements acquired by pyrometers. This more precise model simulates the process controlled by several numerical parameters and the goal is to find their values such that the resultant temperature field is optimal. This algorithm is inspired by our previous research[3] and it is enhanced by a fuzzy logic inference mechanism, which makes its behaviour more robust and its setting easier to adjust.

2 PROBLEM DESCRIPTION AND AN OUTLINE OF THE ALGORITHM

The natural inclination of all steelmakers is to cast as fast as possible but with a preservation of the required material quality. Thus, the problem of optimal casting control can be formulated as follows.

The properties of the final material are highly dependent on its temperature courses emerging during the casting process. Therefore, we need to adjust the parameters of a caster in such a way that the final temperature field is optimal. We can control the process by the regulation of the casting speed and by all the cooling rates in the secondary cooling zone.

Before the optimization starts, it is necessary to define the temperature field, which leads to the optimal material and mechanical properties. These optimal temperature courses are defined by experts (casting operators, material scientists, etc.) and they differ with the chemical composition of the steel.

To deal with the high variability of the described problem, the heat and mass phenomenon must also be taken into account, and therefore the employed numerical model has to cover all the phase and structural changes. The search for the optimal cooling rates and the highest possible casting speed is left to the following fuzzy-logic heuristic algorithm.

To describe the optimal temperature field, the experts define a set of points along the caster and prescribe their optimal temperature ranges. Then the algorithm randomly generates the values for all the input parameters and simulates the final temperature field. After comparing the computed temperatures with the prescribed ones, the algorithm decides which nozzles need to be adjusted and how to change the casting speed. Particular decisions for changing the values are taken by the fuzzy inference logic. These steps are iteratively repeated until the required temperatures are successfully reached.

3 MATHEMATICAL MODEL OF THE TEMPERATURE FIELD

The developed numerical model of the 2D temperature field computes the formation of the solidification and the temperature distribution of the cast strand. This temperature field is modelled by the Fourier-Kirchhoff equation[1–3], where the velocity component v_y(m/s) is considered only in the direction of casting:

$$\frac{\partial H}{\partial \tau} = k_{\text{eff}}(T)\Delta(T) + v_y \frac{\partial H}{\partial y} \tag{1}$$

Equation (1) describes a transient heat transfer, where k_{eff}/(W/m K) is the effective thermal conductivity, T/K is the temperature, H/(J/m^3) is the volume enthalpy, τ/s is the time and x and y are spatial coordinates. The phase and structural changes are included in the model by the latent-heat accumulation method, where the enthalpy is used as the primary variable and the temperature is calculated from a defined enthalpy-temperature relationship[3]:

$$H = \int_0^T \left(\rho(\xi)c(\xi) - \rho(\xi)\Delta H \frac{\partial f_s}{\partial T} \right) \mathrm{d}\xi \tag{2}$$

where ΔH/(J/kg) is the latent heat, ρ/(kg/m^3) is the density, c/(J/kg K) is the specific heat capacity and f_s is the solid fraction.

In order to have a well-posed problem, the initial and boundary conditions must be stated. The boundary conditions include the heat fluxes in the mould and under the rollers, the forced convection under the nozzles and the free convection and radiation in the tertiary cooling zone. Equation (1) is discretized by the finite-difference method[3,4] using an explicit formula for the time derivative. The mesh for the finite-difference scheme is non-equidistant and its nodes are adapted to the real rollers and nozzle positions. Our numerical model allows us to apply various enthalpy-temperature functions and thermal conductivity-temperature curves, and thus the temperature field can be calculated for various steels just by redefining the chemical composition.

Thermo-physical parameters such as the thermal conductivity, the density, the specific heat capacity and the enthalpy and their temperature dependence are computed from a specific chemical composition of steel by using the solidification analysis package IDS.

The numerical model is designed and verified for the radial slab caster operating in EVRAZ VÍTKOVICE STEEL, a. s. The caster contains 12 coolant circuits and the cross-section of the investigated slab is 1550 mm × 250 mm.

4 DESCRIPTION OF THE ALGORITHM

The algorithm searches for the optimal values of the control parameters (cooling rates and the casting speed). The inputs to the algorithm are the required temperature

ranges in the points along the caster and the maximum metallurgical length. For each cooling circuit, the maximum cooling rate is defined. The initial value of each control parameter is randomly chosen from the permitted range and the model is consequently evaluated by the numerical simulation. From the computed result, the algorithm extracts temperatures in the controlled points and by a comparison with the prescribed values determines their deviations (errors). Also, the metallurgical length (the length from the meniscus to the point where the steel is fully solidified) is computed. Using all this information the algorithm infers the modifications for all the controlled input parameters.

The temperature courses at the controlled points are dominantly influenced by the two preceding coolant circuits. The closer circuit has a greater influence. Therefore, each coolant circuit defines a numerical value for each controlled point that describes how much it impacts on the temperature in the controlled point. These values are expertly estimated (in the range from 0 to 10) and they are strongly related to the distance from the controlled points.

In the presented model there are two fuzzy inference mechanisms – one for the modification of the cooling rates and one for the control of the casting speed.

The inference rules for the cooling rates have the following form: "IF error IS *adj1* AND impact IS *adj2* THEN modification IS *adj3*". For each controlled point the *adj1* describes the temperature error, the *adj2* is the cooling impact of the given circuit and the *adj3* is the modification inferred for the cooling rate. **Table 1** shows all the rules in the matrix form.

Table 1: The dependences of adj3 on adj1 and adj2. The abbreviations stand for Very Small, Small, Medium, Big and their fuzzy sets are equidistantly distributed along the corresponding universes.

Tabela 1: Odvisnost označevalca 3 od označevalca 1 in označevalca 2. Okrajšave pomenijo VS – zelo majhen, S – majhen, M – srednji, B – velik, njihove mehke nastavitve pa so v enakih razdaljah razporejene po ustreznih splošnih parametrih.

adj2 / adj1	VS	S	M	B
S	VS	VS	S	S
M	VS	VS	S	M
B	VS	S	M	B

Sometimes, one circuit can get several different modifications and if it happens the algorithm takes the one with the highest absolute value. The defuzzification method is the standard centre-of-gravity function. If the maximum absolute value of all the temperature errors does not exceed a particular limit, the algorithm consequently computes the modification for the casting speed. The reason for introducing the limit is that if the maximum error is too big (i.e., the solution is far from the optimum), we have no information about whether the speed is high or not and at first it is better to stabilize the process and then to infer the speed modification.

The rules for the modification of the casting speed (**Table 2**) are in the form: "IF maximum_error IS *adj4* AND metalurgical_length IS t*adj5* THEN modification IS *adj6*". The *adj4* describes the maximum error over all the controlled points, the *adj5* is the metallurgical length and the *adj6* is the inferred modification of the casting speed.

For a detailed explanation of the fuzzy logic and the fuzzy inference, see[5].

The values of the impacts for each cooling circuit to the controlled point are chosen to be 8 for the closest preceding circuit and 2 for the circuit placed before (except the last controlled point, where the distance to the second closest circuit is much longer, and therefore the values are 9 and 1).

Table 2: The dependences of adj6 on adj4 and adj5. The abbreviations stand for Very Small, Small, OK, Big, Very Big and More, Little More, Little Less, Less, Nothing and their fuzzy sets are equidistantly distributed along the corresponding universes.

Tabela 2: Odvisnost označevalca 6 od označevalca 4 in označevalca 5. Okrajšave pomenijo VS – zelo majhen, S – majhen, OK, B – velik, VB – zelo velik in MO – več, LM – malo več, LL – malo manj, L – manj, N – nič, njihove mehke nastavitve pa so v enakih razdaljah razporejene po ustreznih splošnih parametrih.

adj4 / adj5	VS	S	OK	B	VB
S	MO	LM	LM	LL	L
M	LM	N	N	N	LL

5 RESULTS OF EXPERIMENT

The examined grades of steel are the low-carbon steel S355J0H and the high-carbon steel X210CrW12. The expertly defined temperature ranges in the controlled points are depicted in **Figure 1** and **Figure 2** (the grey rectangles). The crucial reason for defining these temperature ranges in this way is that approximately the first half of caster is curved and therefore to decrease the mechanical stresses it is better to keep the temperature

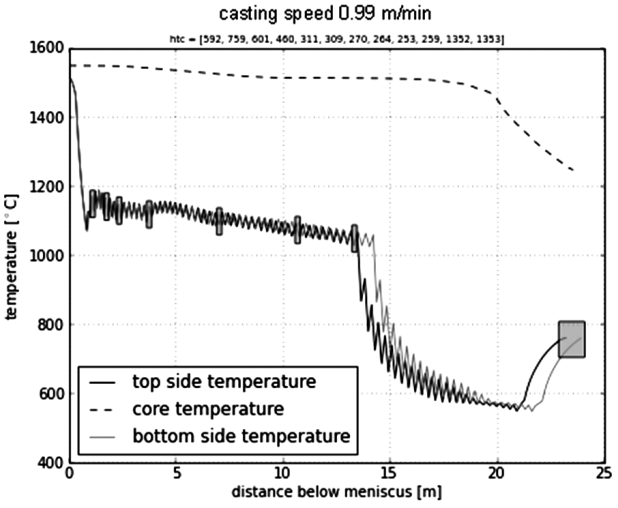

Figure 1: Final temperature distributions (S355J0H)
Slika 1: Končne razporeditve temperature (S355J0H)

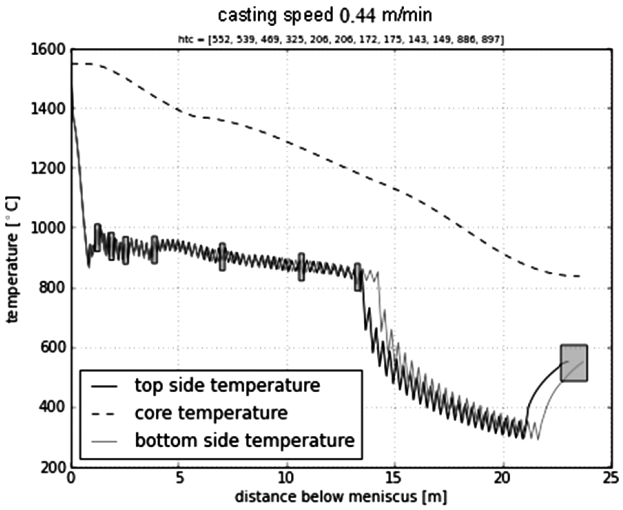

Figure 2: Final Temperature distributions (X210CrW12)
Slika 2: Končne razporeditve temperature (X210CrW12)

above a certain level (for S355J0H, 1000 °C, and for X210CrW12, 800 °C). The value of the maximum metallurgical length is 20 m (from the practice) and the casting temperature is 1550 °C. Reaching the temperature courses on surface ensures that the mechanical and material qualities of the final material will satisfy the demands. The optimal values computed by this algorithm (casting speed and heat-transfer coefficients) are shown in **Figure 1** and **Figure 2**.

Usually, the most important indicator characterizing the efficiency of iterative optimization algorithms is the number of evaluations of the model. The computation of the numerical model is very time-consuming, and therefore each repetition can significantly prolong the computations. Our algorithm is able to find the optimal input parameters in 50 evaluations, on average. The tests ran several times for different grades of steel and the number of evaluations never exceeded 65. The computation time takes a few hours.

6 CONCLUSION

The problem of the optimization of a continuous casting process can be efficiently solved by the described algorithm. The algorithm based on heuristics and incorporating the fuzzy logic behaves in a very robust way and it is easily adaptable to any grade of steel and caster geometry. The number of evaluations of the included numerical model is low, and thereby the algorithm proves its high efficiency. Further research will be focused on extending the numerical model to 3D and a generalization of the used optimization constraints.

Acknowledgement

The authors gratefully acknowledge the financial support from the projects GA106/08/0606, GA106/09/0940 and GACR P107/11/1566, funded by the Czech Science Foundation, project ED0002/01/01 – NETME Centre and Specific research BD 13101001.

7 REFERENCES

[1] J. P. Birat, et al.: The Making, Shaping and Treating of Steel: Casting Volume: 11th Edition. Alan W. Cramb, Pittsburgh, PA, USA: The AISE Steel Foundation, 2003, 1000 s

[2] C. A. Santos, J. A. Spim, A. Garcia, Mathematical modeling and optimization strategies (genetic algorithm and knowledge base) applied to the continuous casting of steel, Engineering Applications of Artificial Intelligence, 16 (**2003**), 511–527

[3] D. M. Stefanescu, Science and Engineering of Casting Solidification, Second Edition, New York, Springer Science, 2009, 402

[4] T. Mauder, C. Sandera, J. Stetina, M. Seda, Optimization of Quality of Continuously Cast Steel Slabs by Using Firefly Algorithm, Mater. Tehnol., 45 (**2011**) 4, 347–350

[5] H. T. Nguyen, E. A.Walker, A First Course in Fuzzy Logic, CRC Press, 1999, 392

UDK 669.71'74'725:621.74.046
Original scientific article/Izvirni znanstveni članek

ISSN 1580-2949
MTAEC9, 46(4)329(2012)

THERMAL STABILITY OF Al-Mn-Be MELT-SPUN RIBBONS

TEMPERATURNA OBSTOJNOST HITRO STRJENIH TRAKOV Al-Mn-Be

Gorazd Lojen, Tonica Bončina, Franc Zupanič

University of Maribor, Faculty of Mechanical Engineering, Smetanova 17, Si-2000 Maribor, Slovenia
gorazd.lojen@uni-mb.si

Prejem rokopisa – received: 2011-10-19; sprejem za objavo – accepted for publication: 2012-03-01

As with other kinds of finely dispersed, small particles, icosahedral quasicrystals (IQCs) also have a distinct strengthening effect, which can be utilised to enhance the mechanical properties of aluminium alloys. In Al–Mn–Be alloys, IQCs already form at moderate cooling rates, which can be utilised when using some conventional casting processes, like mould or injection casting. In this case, however, crystalline intermetallic phases are also present and the mechanical properties are inferior to those of two-phase α_{Al}-IQC alloys. Two-phase microstructures are feasible using rapid solidification techniques, e.g., melt spinning. Further processing often involves technologies (consolidation, extrusion etc.), which include the influence of heat. The alloy must not be overheated in order to preserve the strengthening effect of the metastable IQC-particles.
In this investigation the Al-Mn-Be alloy was melt-spun using a free-jet melt spinner. Subsequently, the thermal stability of the IQCs was explored by annealing the ribbons for 24 h at different temperatures. The samples were examined in the as-cast and heat-treated conditions using a dual-beam, scanning electron microscope (SEM-FIB), X-ray diffraction (XRD) and differential scanning calorimetry (DSC). It was discovered that in the as-cast condition, the ribbons had a two-phase microstructure, consisting of an α_{Al} matrix and finely dispersed IQCs. During annealing at temperatures up to 400 °C, the IQCs did not decompose and the phase composition remained unchanged. Annealing at 500 °C and at higher temperatures caused a decomposition of the IQCs, and only the crystalline intermetallic phases Al_6Mn and Be_4AlMn could be found in the α_{Al} matrix.

Keywords: quasicrystal, Al-Mn-Be alloy, thermal stability

Ikozaedrični kvazikristali (IQC) imajo kakor druge vrste fino razpršenih drobnih delcev utrjevalni učinek, ki ga lahko izkoristimo za povečanje trdnosti aluminijevih zlitin. V zlitinah Al-Mn-Be kvazikristali nastajajo že pri zmernih ohlajevalnih hitrostih, kakršne dosežemo pri postopkih litja, kot sta npr. kokilno litje in tlačno litje. Toda mikrostruktura, ki nastane pri teh postopkih litja, vsebuje tudi kristalne intermetalne faze in trdnostne lastnosti so slabše kot pri zlitinah z dvofazno mikrostrukturo (α_{Al}-IQC). Dvofazno mikrostrukturo pa lahko dosežemo le z velikimi ohlajevalnimi hitrostmi, tj. s postopki hitrega strjevanja. Nadaljnja predelava hitro strjenih materialov pogosto poteka s postopki (kompaktiranje, iztiskovanje itd.), ki zahtevajo segrevanje. Pri tem materiala ne smemo pregreti, če želimo ohraniti utrjevalni učinek kvazikristalov.
V okviru te raziskave so bili uliti hitro strjeni trakovi Al-Mn-Be s postopkom prostega litja na vrteče se kolo (angl.: melt spinning). Temperaturno obstojnost trakov hitro strjene zlitine smo ugotavljali z žarjenjem 24 h pri različnih temperaturah. Mikrostrukture trakov smo analizirali v litem stanju in po toplotni obdelavi z vrstičnim elektronskim mikroskopom z elektronskim in ionskim curkom (SEM-FIB), rentgensko difrakcijo (XRD) in z diferenčno dinamično kalorimetrijo (DSC). Trakovi so imeli v litem stanju dvofazno mikrostrukturo, sestavljeno iz matice α_{Al} in fino dispergiranih kvazikristalov. Žarjenje pri temperaturah do 400 °C ni povzročilo razpada kvazikristalov in fazna sestava je ostala nespremenjena. Po žarjenju pri 500 °C ali višjih temperaturah pa je bila mikrostruktura sestavljena iz matice α_{Al} in kristalnih intermetalnih faz Al_6Mn ter Be_4AlMn.

Ključne besede: kvazikristal, zlitina Al-Mn-Be, temperaturna obstojnost

1 INTRODUCTION

The existence of icosahedral quasicrystals (IQCs or i-phase) was discovered by Schechtman et al. in melt-spun Al-Mn alloys[1]. Later, the possibility of IQC formation was proven for dozens of others alloys[2,3].

Some elements, beryllium being one of them, strongly increase the quasicrystalline-forming ability in Al–Mn alloys[4–6]. IQCs had already been observed in different conventionally cast ternary and quaternary alloys based on the Al-Mn system, and also in several Al-Mn-Be alloys. In conventionally cast alloys, however, other crystalline phases are also present[4–8] in addition to the IQCs.

One of the most promising potential applications for quasicrystals is their utilisation as a strengthening phase in lightweight aluminium alloys. As early as 1992 Inoue[9] reported on Al–Mn–Ce melt-spun ribbons achieving tensile strengths above 1 GPa. Recently, a hardness of over 290 HV was reported[10] for Al-Mn-Be melt-spun ribbons, which, based on the well-known empirical relationship between hardness and tensile strength, also allows us to expect tensile strengths in the range of 1 GPa. However, extraordinarily high strengths were only reported for alloys having two-phase (α_{Al} + IQCs) microstructures, consisting of a fine dispersion of quasicrystalline particles in an Al-rich solid solution matrix, as yet unattained by conventional casting.

Melt-spun ribbons are rarely directly applicable, because of their dimensions. Consequently, for the vast majority of applications the ribbons must be compacted into much larger pieces of material. The compacting processes mostly involve heating, so rapidly solidified materials must exhibit sufficient thermal stability in order to preserve their advantages.

Unfortunately, IQCs in Al–Mn-based alloys have been discovered to be metastable. The thermal stability of the IQCs in a rapidly solidified binary Al-5 wt.% Mn alloy was reported to be below 1 hour of isothermal annealing at 500 °C [11], and by means of DSC analysis with a high heating rate of 40 K min^{-1}, the onset temperature of thermal decomposition was estimated to be 472 °C for the mole fraction Al-14 % Mn alloy[8]. The thermal stabilities of the conventionally cast ternary alloys Al-2.5Mn-7.5Be (in mole fractons, *x*/%) and Al-5Be-1.5Mn (in mass fractions, *w*/%) were investigated by Song et al.[4] and Chang et al.[7], respectively. In both studies the ingots, initially consisting of ICQs and hexagonal approximants dispersed in an α_{Al} matrix, were annealed for 100 h at 540 °C. According to Song et al.[4] the annealing caused no phase transformations, and in addition the DSC did not reveal any transformations below 600 °C. In contrast, Chang et al.[7] reported that upon annealing the IQC-phase dissolved and only hexagonal approximants remained in the matrix. Although these results appear to be contradictory, the differences could possibly be attributed to different chemical compositions and different cooling rates during the solidification of the ingots and, in addition, because in both cases no shorter and no longer annealing times than 100 h were applied, the actual thermal stabilities did not necessarily need to be significantly different at all.

In any case, due to much lower cooling-rates, conventionally cast ingots as well as IQCs also contain crystalline intermetallics, and the microstructure is much coarser than in rapidly solidified alloys. As a result, the conventionally cast material is, already in an as-cast condition, much closer to the thermodynamic equilibrium than the rapidly solidified one, which in an as-cast condition exhibits an extremely fine, two-phase (α_{Al} + IQCs) microstructure. Therefore, the driving force for changes during annealing is higher in rapidly solidified materials and, consequently, a lower thermal stability can be expected. On the other hand, due to the stabilising effect of Be, the thermal stability of the IQC phase could be improved in rapidly solidified, ternary, Al-Mn-Be alloys.

The aim of this work was to evaluate the thermal stability of IQCs in a rapidly solidified, ternary, Al-Mn-Be alloy, which has yet to be determined.

2 EXPERIMENTAL

Although with beryllium the critical content of Mn to produce IQCs is reduced to no more than x = 2.5 % [4], a higher Mn content was chosen in order to achieve a higher volume fraction of quasicrystals. The nominal composition of the alloy was (in mole fractions x) 89 % Al, 6 % Mn and 5 % Be, **Table 1**. It was prepared from Al 99.99, and master alloys of Al–Mn and Al–Be containing (in mass fractions) 30 % Mn and 5.5 % Be, respectively. The precursors were vacuum induction melted and cast into 50-mm round bars. The bars were cut into appropriate lengths and melt-spun in a 30 M-type Melt Spinner, Marko Materials Inc, USA. The melt-spinning conditions were as follows: a BN-protected graphite crucible with a 1-mm orifice, a wheel speed of 25 m min^{-1}, a casting temperature of 900–950 °C.

Table 1: Nominal and analysed chemical compositions of the melt-spun ribbons (ICP-AES)
Tabela 1: Imenske in analizirane kemične sestave hitro strjenih trakov, ulitih s postopkom litja na vrteče se kolo (ICP-AES)

element	*x*(Al)/%	*x*(Mn)/%	*x*(Be)/%
nominal	89	6	5
analysed	88.6	5.6	5.8

x/% – mole fraction; *x*/% – molski delež

The chemical composition of the melt-spun ribbons was verified using ICP-AES (inductively coupled plasma-atomic emission spectroscopy), see **Table 1**.

The microstructures were investigated in the as-cast condition and after annealing under a protective atmosphere of Ar. The annealing temperatures were (200, 300, 400, 500 and 550) °C, where the annealing time was always 24 h, regardless of the temperature. Different techniques were applied for the metallographic characterisation. The scanning electron microscopy was performed using a dual-beam FEI Quanta 200-3D microscope (SEM-FIB). The X-ray diffraction was carried out at the XRD1 beam-line (Elettra, Sinchrotrone Trieste, Italy) using synchrotron X-rays with a wavelength of 0.1 nm in the transmission mode. The phase compositions were identified using Powder Diffraction File-2[12]. The DSC analyses were performed with a STA 449 Jupiter, from room temperature to 640°C, with heating and cooling rates of 10 °C min^{-1} in nitrogen.

3 RESULTS AND DISCUSSION

3.1 As-cast ribbons

The analysed composition is given in **Table 1**, along with the nominal composition. The actual composition only slightly deviated from the nominal one; therefore, the ribbons were evaluated as being appropriate for the intended purpose.

The microstructural analysis of the as-cast ribbons revealed a two-phase microstructure, consisting of fine IQCs dispersed throughout the α_{Al} matrix. **Figure 1** shows a backscattered-electron SEM image. The backscattered-electron imaging provided the best phase contrast. The α_{Al}-matrix appears dark. The coarser quasicrystals could be identified by their characteristic dendritic morphology and the finer ones, most of them being too small to be distinguishable in a SEM micrograph, by their shapes as pentagonal dodecahedrons[13]. Beside IQCs, no other phase could be found in the matrix of the as-cast ribbons when using scanning

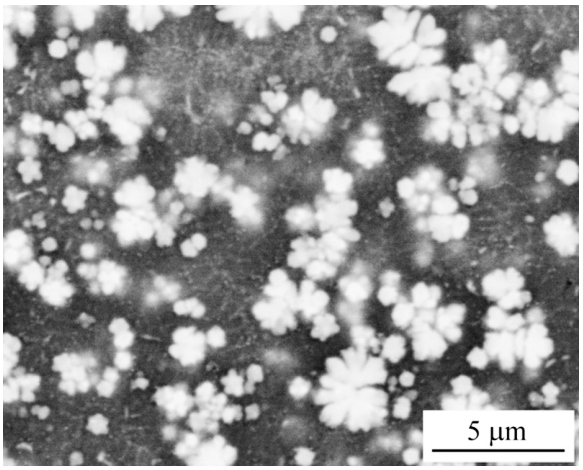

Figure 1: Microstructure of the as-cast ribbon, SEM-image. The coarser quasicrystals exhibit a characteristic dendritic morphology.
Slika 1: Mikrostruktura traku v litem stanju, SEM-slika. Grobi kvazikristali imajo značilno dendritno morfologijo.

electron microscopy. In addition, the XRD analysis (the lowest curve in **Figure 2**) only confirmed the presence of the IQC and the α_{Al}. Therefore, the as-cast ribbons were considered to have a two-phase α_{Al} + IQC microstructure.

Upon heating, **Figure 3**, the DSC analysis of as the as-cast ribbons showed a phase transformation that started at approximately 530 °C, reached its peak at approximately 570 °C and ended at approximately 600 °C. The thermal decomposition of the metastable ICQs started at 530 °C, as indicated by the absence of a reverse transformation upon cooling. As is quite common for DSC, the heating rate was relatively fast. Therefore, the influence of the transformation kinetics

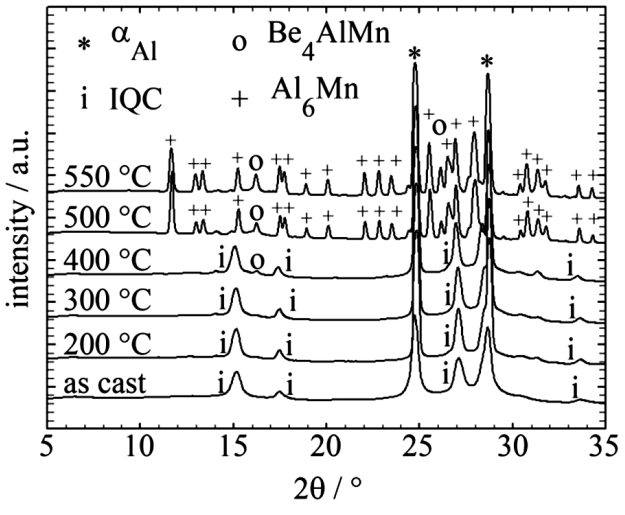

Figure 2: X-ray diffractograms. From bottom to top: as-cast ribbon, ribbons annealed for 24 h at 200 °C, 300 °C, 400 °C, 500 °C and 550 °C.
Slika 2: Rentgenski difraktogrami. Od spodaj navzgor: trak v litem stanju, trakovi, žarjeni 24 h pri 200 °C, 300 °C, 400 °C, 500 °C in 550 °C.

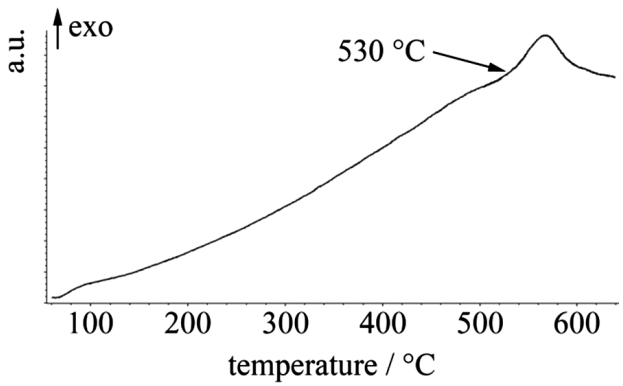

Figure 3: DSC curve of as-cast sample upon heating; heating rate 10 K min^{-1}
Slika 3: DSC-krivulja traku v litem stanju; hitrost segrevanja 10 K min^{-1}

was unavoidable and the determined transformation temperatures were shifted to higher values. The influence of the transformation kinetics reduced with the prolongation of the annealing time, so it was expected that during the 24-hours of isothermal annealing, decomposition would take place at a lower temperature. Therefore, only one of the temperatures for the 24 h annealing was selected above the DSC-estimated start of the decomposition, 550 °C, and one of the lower temperatures only slightly below, i.e., 500 °C.

3.2 Annealed ribbons

The X-ray diffractograms of the samples annealed at 200 °C, 300 °C, and 400 °C were very similar to the diffractograms of the as-cast sample, **Figure 2**. No distinguishable peaks for the crystalline intermetallic phases could be recognised and, only those peaks for IQCs and α_{Al} could be observed. The absence of peaks of the crystalline intermetallics indicates that at temperatures up to 400 °C over 24 h the decomposition did not start or at least did not advance enough to be detected by XRD. Also, in the SEM micrographs of those samples annealed at temperatures up to 400 °C, **Figure 4**, no distinct changes in the average size and morphology of the larger IQCs could be observed. Compared to the as-cast condition (**Figure 1**), the number of smaller particles slightly diminished, indicating that annealing at 400 °C caused a certain degree of Ostwald ripening.

In the XRD diffractograms of the samples annealed at 500 °C and 550 °C an absence of IQC peaks could be observed at first sight. In their place, distinct peaks for the intermetallic phases Be_4AlMn and Al_6Mn were present. The pronounced equality of both XRD diffractograms indicated that at 500 °C the decomposition of the IQCs had already been completed within the 24 h. The SEM micrograph of the sample annealed at 550 °C, **Figure 5a**, at first sight appeared similar to the micrographs of samples annealed at temperatures up to 400 °C. The average size of the large particles remained almost unchanged. However, their morphology changed

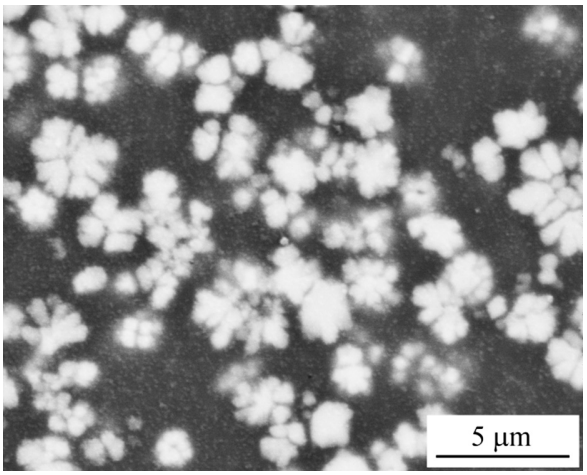

Figure 4: SEM micrograph of a sample after 24-h annealing at 400 °C: compared to the as-cast sample, no distinct changes can be observed.

Slika 4: SEM-slika vzorca po 24-urnem žarjenju pri 400 °C: v primerjavi z vzorcem v litem stanju ni opaziti večjih sprememb.

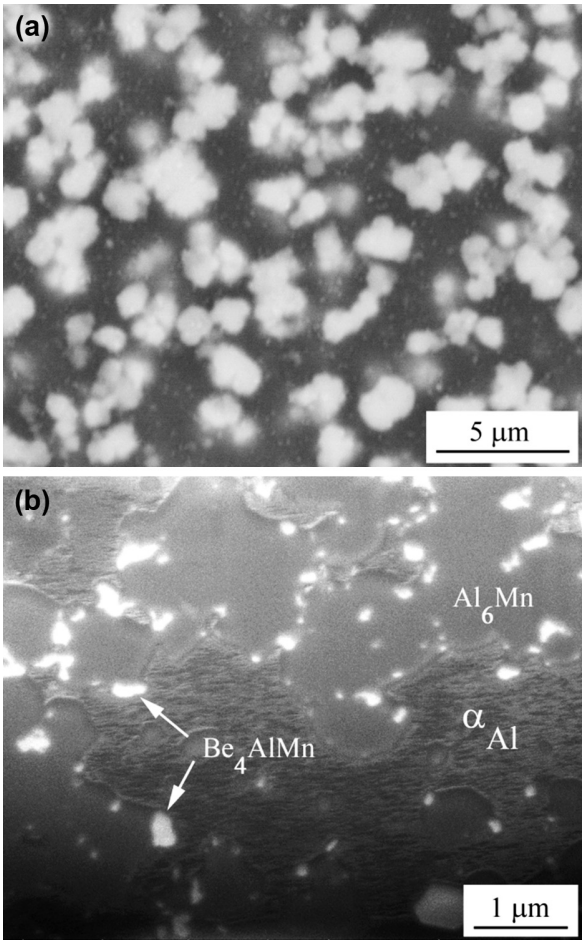

Figure 5: Ribbon annealed for 24 h at 550 °C: a) SEM back-scattered-electron image: Be_4AlMn and Al_6Mn can practically not be distinguished; b) FIB secondary-electron image of an in-situ prepared cross-section: all phases identified by XRD can be recognised

Slika 5: Trak, žarjen 24 h pri 550 °C: a) SEM-slika z odbitimi elektroni: Be_4AlMn in Al_6Mn praktično ni mogoče razlikovati; b) FIB-slika in situ pripravljenega prereza: prepoznavne so vse faze, odkrite z XRD

to a more compact shape. According to the XRD analysis, Be_4AlMn and Al_6Mn were present in the α_{Al} matrix. As can be seen from the micrographs in **Figures 4** and **5a**, through the thermal decomposition of the IQCs, neither the size nor the distribution of the dispersed particles changed significantly. Obviously, the sizes and the distribution of the crystalline intermetallic particles, grown through the thermal decomposition of the IQCs, were determined by the sizes and distribution of the IQCs. However, as reported by Bončina et al.[14], in the SEM backscattered-electron images the Be_4AlMn appears only slightly brighter than the Al_6Mn and, consequently, cannot be unerringly recognised. Therefore, cross-sections were cut by the focused ion beam in-situ in the dual-beam SEM-FIB microscope. In the FIB secondary-electron image in **Figure 5b**, both phases could be clearly distinguished. The Be_4AlMn appeared as very bright, almost white, and the surface of the Al_6Mn appeared as smoothly grey. Consistent with the peak heights in the XRD diagrams in **Figure 5b**, it can be observed that the volume fraction of Be_4AlMn was significantly lower than the fraction of Al_6Mn.

4 CONCLUSIONS

The metallographic investigations of the rapidly solidified (melt-spun) Al-Mn-Be alloy led to the following conclusions:

1. The microstructure of the as-cast melt-spun (in mole fractions) 89 % Al-6 % Mn-5 % Be ribbons consisted of IQCs dispersed in an α_{Al} matrix. No quasicrystal approximants or equilibrium intermetallics could be detected.
2. The thermal stability of the rapidly solidified 89 % Al-6 % Mn-5 % Be alloy lasted at least 24 h at temperatures up to 400 °C. After 24 h annealing at 400 °C, only insignificant coarsening of the IQCs was perceivable, whilst the phase composition was preserved.
3. Upon annealing at 500 °C the thermal decomposition of the IQCs into Al_6Mn and Be_4AlMn was completed after no later than 24 h. The sizes and dispersion of the newly formed Al_6Mn–Be_4AlMn clusters were very similar to the sizes and dispersion of the dendritic IQCs. As a result, due to the thermal decomposition of the IQCs, the mechanical properties may not drastically decrease.
4. The rapidly solidified 89 % Al-6 % Mn-5 % Be alloy can be processed using techniques that involve elevated temperatures.

Acknowledgments

The research leading to these results received funding from the European Community's Seventh Framework Programme (FP7/2007–2013) under grant agreement N' 226716. This work was also partly financed from the

research programme P2–0120, ARRS. The authors also wish to thank Mr. Rok Šulek, University of Maribor, Faculty of Mechanical Engineering, for preparing the alloy billets, Mr. Borivoj Šuštaršič PhD, Institute of Metals and Technology in Ljubljana, for melt spinning, and prof. Jože Medved PhD, University of Ljubljana, Faculty of Natural Sciences and Engineering, for the DSC analyses.

5 REFERENCES

[1] D. Shechtman, I. Blech, D. Gratias, J.W. Cahn, A Metallic Phase with Long-Ranged Orientation Order and No Translation Simetry, Phys. Rev. Lett., 53 (**1984**), 1951–1953

[2] C. Suryanarayana, H. Jones, Formation and characteristics of quasicrystalline phases: a review, Int. J. Rapid Solidif., 3 (**1987**), 253–93

[3] K. F. Kelton, Quasicrystals: structure and properties, Int. Mater. Rev., 38 (**1993**), 105–37

[4] G. S. Song, E. Fleury, S. H. Kim, W. T. Kim, D. H. Kim, Enhancement of the quasicrystal-forming ability in Al-based alloys by Be-addition, J. of Alloys and Compounds, 342 (**2002**), 251–255

[5] G. S. Song, E. Fleury, S. H. Kim, W. T. Kim, D. H. Kim, Formation and stability of quasicrystalline and hexagonal approximant phases in an Al–Mn–Be alloy, J. Mater. Res., 17 (**2002**), 1671–1677

[6] S. H. Kim, G. S. Song, E. Fleury, K. Chattopadhyay, W. T. Kim, D. H. Kim, Icosahedral quasicrystalline and hexagonal approximant phases in the Al–Mn–Be alloy system, Philosophical Magazine A, 82 (**2002**), 1495–1508

[7] H. J. Chang, E. Fleury, G. S. Song, W. T. Kim, D. H. Kim, Formation of quasicrystalline phases in Al-rich Al–Mn–Be alloys, J. Non-cryst. solids, 334 (**2004**), 12–16

[8] F. Schurack, J. Eckert, L. Schultz, Synthesis and mechanical properties of cast quasicrystal-reinforced Al-alloys, Acta mater., 49 (**2001**), 1351–1361

[9] A. Inoue, M. Watanabe, H. M. Kimura, F. Takahashi, A. Nagata, T. Masumoto, High mechanical strength of quasicrystalline phase surrounded by fcc-Al phase in rapidly solidified Al-Mn-Ce alloys, Materials transactions JIM, 33 (**1992**) 8, 723–729

[10] F. Zupanič, T. Bončina, B. Šuštaršič, I. Anžel, B. Markoli, Microstructure of Al-Mn-Be melt-spun ribbons, Mater. charact., 59 (**2008**) 9, 1245–1251

[11] K. Saksl, D. Vojtech, H. Franz, Quasicrystal–crystal structural transformation in Al–5 wt.% Mn alloy, J. Mater. Sci., 42 (**2007**), 7198–7201

[12] Powder Diffraction File-2, Release 2004. International Center for Diffraction Data, Newtown, USA, 2004

[13] F. Zupanič, B. Markoli, Morphologies of Icosahedral quasicrystals in Al-Mn-Me-(Cu) alloys, In: Puckermann B. E. (editor): Quasicrystals. Nova science publishers Inc., New York 2011, 195–217

[14] T. Bončina, B. Markoli, I. Anžel, F. Zupanič, Metallographic techniques for the characterization of quasicrystalline phases in aluminium alloys, Z. Kristallogr., 223 (**2008**), 747–750

UDK 669.017.3:536.65
Original scientific article/Izvirni znanstveni članek

ISSN 1580-2949
MTAEC9, 46(4)335(2012)

CHALLENGES IN THE COMPUTER MODELING OF PHASE CHANGE MATERIALS

IZZIVI V RAČUNALNIŠKEM MODELIRANJU MATERIALOV S FAZNO SPREMEMBO

Lubomir Klimes[1], Pavel Charvat[1], Milan Ostry[2]

[1]Brno University of Technology, Faculty of Mechanical Engineering, Technická 2896/2, 616 69 Brno, Czech Republic
[2]Brno University of Technology, Faculty of Civil Engineering, Veveří 331/95, 602 00 Brno, Czech Republic
yklime17@stud.fme.vutbr.cz

Prejem rokopisa – received: 2011-10-20; sprejem za objavo – accepted for publication: 2012-03-01

Phase-change materials (PCMs) are a well-established category of materials with many possible applications, ranging from the stabilization of temperature to heat or cold storage. The main principle of PCMs is the utilization of the latent heat of a phase change for energy storage. Though many pure chemical elements can be used as PCMs, a PCM very often consists of a number of substances. The main reason for creating a PCM as a mixture of various substances is to achieve a desirable melting temperature for a particular application. However, these mixed PCMs require accurate and reliable methods for determining their physical properties, since for numerical modeling the thermal properties of materials and their proper determination represent a significant issue that considerably affects the accuracy and credibility of numerical simulations and their outcomes. The thermal properties of PCMs are usually obtained by differential scanning calorimetry (DSC), based on temperature and heat measurements of the investigated and reference materials. There are several approaches to modeling materials with phase changes. In this paper, the focus is on the enthalpy approach and the effective heat capacity method. Both techniques, which utilize the results from a particular DSC measurement, allow a treatment with the latent heat, and as a result the desired heat or cold storage may be effectively simulated. The presented methods were implemented using the results from DSC measurements in order to simulate a solar air collector with a PCM. The obtained results are presented and discussed. The paper also concerns the problems associated with the uncertainty of material properties and their influence on numerical simulations.

Keywords: phase change material (PCM), enthalpy method, effective heat capacity method, solar air collector

Materiali s faznimi premenami (PCM) so uveljavljena kategorija materialov z mnogimi področji uporabe: od stabilizacije temperature do shranjevanja toplote ali hladu. Glavni princip PMS je uporaba latentne toplote pri fazni premeni za shranjevanje energije. Čeprav je mogoče uporabiti kot PCM mnoge čiste kemijske elemente, se pogosto uporablja mešanica različnih elementov. Glavni razlog za uporabo mešanice za PCM je zagotavljanje želene temperature tališča za določen namen. Vendar pa mešanica PCM-ov zahteva natančne in izvedljive metode za določanje fizikalnih lastnosti. Numerično modeliranje termičnih lastnosti materialov zahteva zanesljivo določene termične lastnosti, kar bistveno vpliva na natančnost in zanesljivost simulacij in njihovih rezultatov. Termične lastnosti PCM-materialov navadno določamo z DSC-metodo, ki temelji na merjenju temperature in toplote preiskovanega in referenčnega materiala. Obstaja več načinov, kako modelirati materiale s faznimi premenami. V tem članku je glavna pozornost posvečena entalpijskemu približku in metodi efektivne toplotne kapacitete. Obe tehniki, ki uporabljata rezultate DSC-meritev, omogočata uporabo latentne toplote, kar omogoča učinkovito simuliranje shranjevanja toplote ali hladu. Predstavljeni metodi sta bili uporabljeni z uporabo rezultatov iz DSC-meritev za simulacijo sončnega kolektorja s PCM-materiali. Predstavljeni so rezultati z diskusijo. Članek obravnava tudi problem nezanesljivosti podatkov o lastnostih materialov in njihov vpliv na numerično simulacijo.

Ključne besede: materiali s faznimi premenami (PCM), entalpijska metoda, metoda učinkovite toplotne kapacitete, sončni kolektor

1 INTRODUCTION

Due to the increasing consumption of energy, the demands for thermal comfort and the need to decrease temperature fluctuations and energy losses, new construction and thermal storage materials have been developed over the past 10 years. Phase change materials (PCMs) are substances that are used to absorb, store and release energy. This is accomplished by utilizing the latent heat of the phase change from the liquid to the solid state and vice versa, since the amount of energy included in a phase change is usually considerably larger than the sensible heat[1]. Nowadays, PCMs are being used in a wide range of applications in architecture and civil engineering, from heat or cold storage to temperature stabilization and balancing.

PCMs are usually composed of several substances rather than being a pure chemical element. The reason is that a particular application requires a specific range of phase change according to the operating conditions and a desired melting temperature can be achieved with a mixture of several components with a certain chemical composition.

The optimal layout, usage, integration, and design of PCMs in buildings, constructions and other equipment cannot be carried out without using numerical and computer simulations, optimization methods and experimental measurements. In order to obtain accurate and credible results, it is essential to properly determine all the physical properties of the used materials and to precisely describe the operating conditions[2]. For this purpose differential scanning calorimetry (DSC) is very often used.

There are several methods and approaches as to how the materials embracing phase change and related phenomena can be modeled. In this paper the attention is focused on the enthalpy approach and the effective heat capacity method that enable the simulation of the heat transfer in materials with phase changes. As the inputs and parameters (e.g., the physical properties of a material) of the simulation the results from a DSC measurement may be utilized.

2 DIFFERENTIAL SCANNING CALORIMETRY

Differential scanning calorimetry is a thermo-analytical method and is widely used to assess and construct phase diagrams and to determine the thermophysical properties of materials, e.g., the crystallization and melting temperatures, heat capacity and the enthalpy[3].

The principle of differential scanning calorimetry is a measurement of the difference in the amount of heat needed to raise the temperature of the sample and the reference materials. The aim is to keep the temperature of both the sample and the reference materials at the same level during the experiment, while the temperature increases linearly. In order to precisely determine the properties and parameters of a sample material, the thermophysical properties of the reference material have to be known. The particular outcome of a DSC measurement for a PCM is shown in **Figure 1**.

3 ENTHALPY METHOD

The numerical modeling of PCMs requires solving the heat transfer problem in order to obtain the transient temperature distribution for the examined material. The heat transfer is described by the heat equation that is a partial differential equation of the second order:

$$\frac{\partial T}{\partial t} - \alpha \Delta T = 0 \tag{1}$$

where T/K is the temperature, t/s is the time and α/(m^2 s^{-1}) is the thermal diffusivity of the material.

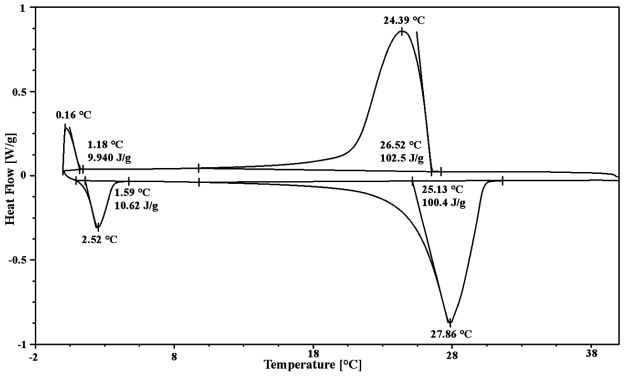

Figure 1: Results of a DSC measurement of a PCM
Slika 1: Rezultati meritev DSC s PCM

The enthalpy method[4,5] introduces the volume enthalpy H/(J m^{-3}), which includes the phase change phenomenon, to the equation since the enthalpy represents the sum of the sensible heat and the latent heat of the phase change. The function of the volume enthalpy is defined as follows:

$$H(T) = \int_0^T \left(\rho c - \rho L_\mathrm{f} \frac{\partial f_\mathrm{s}}{\partial T} \right) \mathrm{d}\theta \tag{2}$$

where ρ/(kg m^{-3}) is the density, c/(J kg^{-1} K^{-1}) is the specific heat, L_f/J is the latent heat of the phase transformation and f_s is the solid fraction. By substituting the enthalpy relation (2) into equation (1) we can obtain the reformulated equation describing the unsteady heat transfer in a material with phase changes:

$$\frac{\partial H}{\partial t} = \nabla(\lambda \nabla T) \tag{3}$$

where λ/(W m^{-1} K^{-1}) is the thermal conductivity. As can be seen, in equation (3) there are two unknown quantities – the enthalpy and the temperature. However, they are coupled together through the enthalpy-temperature (H-T) relationship that can be obtained from a DSC measurement. An example of the H-T relationship for a particular material with a phase change range from 25 °C to 27 °C is shown in **Figure 2**.

In order to solve equation (3) for a particular application the corresponding initial and boundary conditions have to be provided. To solve the system numerically, an appropriate numerical method is needed to assemble a system of discretized equations. For this purpose many numerical methods can be utilized, e.g., the finite-difference method, the finite-volume method, the finite-element method or the mesh-free methods[6]. For simplicity, let us assume the finite-difference method. Thus, the partial derivatives in equation (3) are replaced by their finite-difference approximations and the original system is reformulated into a system of linear algebraic equations:

$$H_{i,j,k}^{n+1} = H_{i,j,k}^{n} + f(T_{i,j,k}^{n}, T_{i\pm\Delta x, j\pm\Delta x, k\pm\Delta z}^{n}, \ldots) \tag{4}$$

However, due to the presence of unknown values of both the enthalpy and the temperature, the explicit scheme of the finite-difference method for the discretization in time has to be used. The temperature field is calculated in two successive steps: in the first step the enthalpy $H^{(n+1)}$ in time $t + 1$ is calculated from the known enthalpy and temperature values H^t, T^t in time t according to equation (4). After that the temperature $T^{(n+1)}$ in time $t + 1$ is calculated from the enthalpy $H^{(n+1)}$ according to the enthalpy-temperature relationship obtained, for instance, from a DSC measurement. Repeating the described procedure over all the time nodes leads to the targeted transient temperature field.

4 EFFECTIVE CAPACITY METHOD

The effective capacity method is based on the idea of incorporating the phase change phenomenon into the heat capacity calculations[4,5]. This physical property represents the amount of heat needed for the matter to increase its temperature.

It means that the effective heat capacity c_{eff}/(J kg^{-1} K^{-1}) has to include the latent heat of the phase change. Therefore, the function of the effective heat capacity increases and decreases sharply with an apparent peak when the material undergoes the phase change. An example of the effective heat capacity function corresponding to the enthalpy curve is shown in the same Figure (**Figure 2**).

In order to calculate congruous and trustworthy results it is crucial to properly determine the effective heat capacity. For this purpose differential scanning calorimetry is one of the tools and techniques available.

By introducing the effective heat capacity, equation (1) becomes:

$$\rho c_{\text{eff}} \frac{\partial T}{\partial t} = \nabla(\lambda \nabla T) \tag{5}$$

In equation (5) there is only one unknown variable, the temperature T, and therefore a wider class of discretization approaches can be used. One of the most significant features is that the implicit scheme can be utilized. Hence, using the temperatures T^n from the foregoing time step for the determination of the effective heat capacity in a successive time $n + 1$, the discretized equation for each node i, j, k can be written in the form:

$$f(T^{n+1}_{i,j,k}, T^{n+1}_{i\pm\Delta x, j\pm\Delta x, k\pm\Delta z}, \ldots) = T^{n}_{i,j,k} \tag{6}$$

The system of algebraic equations can be assembled by using equation (6) applied to all the nodes of the discretized domain and an appropriate numerical method has to be used to solve it.

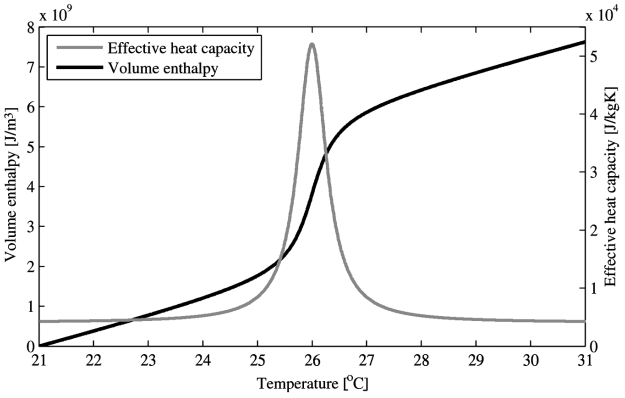

Figure 2: The enthalpy temperature relationship and the effective heat capacity function

Slika 2: Sprememba entalpije v odvisnosti od temperature in efektivne toplotne kapacitete

5 COMPARISON OF METHODS

The enthalpy method is based on the introduction of an additional quantity to the governing equation in order to include the phase change. From the computing point of view the volume enthalpy function introduces difficulties. Namely, (a) the desired quantity, i.e., the temperature, cannot be computed directly and the computation is split into two steps with an intermediate calculation, (b) the temperature search from a known enthalpy is demanding and requires a powerful search algorithm and (c) without additional techniques the explicit scheme, which is conditionally stable, must be used. The advantages of the enthalpy method are a better numerical stability when an explicit discretization scheme in time is used for both methods and its better accuracy in comparison with the effective heat capacity method[4,5].

The effective heat capacity method calculates the temperature field directly without intermediate steps and it allows the use of an implicit discretization scheme that is unconditionally stable[6]. However, without additional techniques an assumption is required that the effective heat capacity is calculated using the temperature from a previous step. In the case that the effective heat capacity is a function of an unknown time, this makes the system of equations considerably more difficult to solve, and therefore the possibility of using an arbitrary time step (owing to the implicit scheme) is strictly confined. Moreover, when a problem with a large number of nodes (a 3D case with a large and intricate geometry) the computational demands of solving the system of equations becomes more arduous and time consuming.

6 RESULTS AND DISCUSSION

Both discussed methods were implemented in order to simulate and analyze the solar air collector, which is a solar thermal device that is used for heating in buildings. An issue with solar thermal systems is the general need for thermal storage in order to balance the heat demands over a certain time period. Therefore, the utilization of

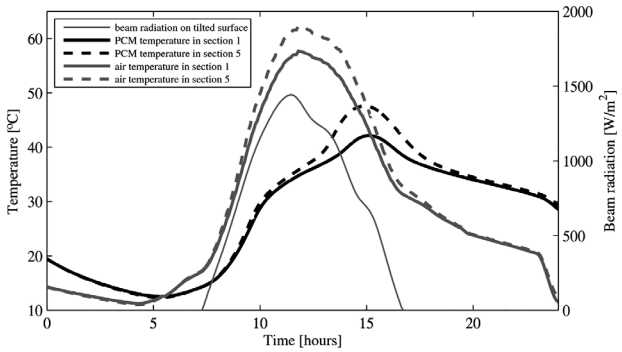

Figure 3: The results of the numerical simulation based on the effective heat capacity for the solar air collector

Slika 3: Rezultati numerične simulacije na osnovi efektivne kapacitete za sončni kolektor zraka

phase change materials and their feature of energy storage can overcome the mentioned problem.

The TRNSYS software, which is a simulation tool designed for the analysis of transient systems, was used for modeling the solar air collector. Owing to the phase change material, in the case of the enthalpy method, the numerical model of heat transfer in a PCM has been implemented in MATLAB and both software packages, TRNSYS and MATLAB, were coupled together. In the case of the effective heat capacity method the numerical model of the PCM was implemented in the form of a stand-alone module (a DLL library) for TRNSYS in the programming language C++.

Both the software implementations utilized a result obtained from a DSC measurement of the PCM with the phase change temperature ranging from 30 °C to 38 °C and the latent heat of the phase change being 70 kJ kg^{-1}.

The simulations performed with the described methods produced comparable results. **Figure 3** shows the outcomes of the simulation (meteorological data for 24 h in June, using the effective capacity method, the finite-difference discretization and the explicit scheme, the time step 2 seconds) for the so-called front-pass solar air collector that was split longitudinally into five separate sections. As seen in **Figure 3** the courses of the PCM temperatures show the phase change in the given temperature ranges, the absorption and the release of the latent heat.

However, even though the material properties are properly determined by the DSC there are still quantities under uncertainty that may considerably influence the result of the simulations. A typical example is the heat transfer coefficient (HTC), since it can randomly fluctuate according to various factors. The HTC belongs to the class of operating conditions that can significantly affect the behavior of the system through the initial and boundary conditions. In order to properly solve the systems with parameters under uncertainty, additional techniques and methods, e.g., stochastic modeling and stochastic optimization, must be considered.

Moreover, the presented methods and their implementations can be utilized in a wide range of applications, e.g., for steel solidification and optimal control in the steel industry[7].

7 CONCLUSION

The presented paper introduces two possible approaches to modeling materials undergoing phase changes. Both techniques assume some particular thermophysical properties obtained, e.g., from the differential scanning calorimetry method. The concepts of the enthalpy approach and the effective heat capacity are described and the advantages, drawbacks and the usage are discussed.

The implemented methods were successfully tested on the simulation of the solar air collector with a PCM absorber. The obtained results suggest that the described approaches of numerical modeling and their implementations are valuable tools for solving problems in optimizing the design, usage and the integration of materials with phase changes.

Acknowledgement

The presented research was supported by the project OC10051 of the Czech Ministry of Education and by the BUT project BD13102003 for young researchers. The main author, the holder of the Brno PhD Talent Financial Aid sponsored by Brno City Municipality, also gratefully acknowledges the financial support.

8 REFERENCES

[1] F. Kuznik, D. David, K. Johannes, J. J. Roux, A review on phase change materials integrated in building walls, Renewable and Sustainable Energy Reviews, 15 (**2011**), 379–391

[2] F. Kuznik, J. Virgone, J. J. Roux, Energetic efficiency of room wall containing PCM wallboard: A full-scale experimental investigation, Energy and Buildings, 40 (**2008**), 148–156

[3] G. H. Zhang, C. Y. Zhao, Thermal and rheological properties of microencapsulated phase change materials, Renewable Energy, 36 (**2011**), 2959–2966

[4] D. M. Stefanescu, Science and Engineering of Casting Solidification, 2nd ed., Springer, 2009

[5] M. Muhieddine, E. Canot, R. March, Various approaches for solving problems in heat conduction with phase change, International Journal On Finite Volumes, 6 (**2009**) 1

[6] Handbook of numerical heat transfer. Editors W. J. Minkowycz, E. M. Sparrow, J. Y. Murthy, 2nd ed., Wiley, 2006

[7] J. Stetina, F. Kavicka, The influence of the chemical composition of steel on the numerical simulation of a continuously cast slab, Mater. Tehnol., 45 (**2011**) 4, 363–367

UDK 621.762:669.715
Original scientific article/Izvirni znanstveni članek

ISSN 1580-2949
MTAEC9, 46(4)339(2012)

APPLICATION OF POWDER METALLURGY IN THE PROCESSING OF ALUMINIUM SCRAPS WITH HIGH-IRON CONTENTS

UPORABA POSTOPKOV PRAŠNE METALURGIJE ZA PREDELAVO ODPADKOV NA OSNOVI Al Z VISOKO VSEBNOSTJO Fe

Dalibor Vojtěch, Filip Průša

Department of Metals and Corrosion Engineering, Institute of Chemical Technology, Technická 5, 166 28 Prague 6, Czech Republic
dalibor.vojtech@vscht.cz

Prejem rokopisa – received: 2011-10-20; sprejem za objavo – accepted for publication: 2012-03-12

The Al-14Si-8Fe and Al-22Si-8Fe-1Cr (*w*/%) alloys were prepared via melt centrifugal atomization and compaction at a pressure of 6 GPa. The resulting alloys were porosity-free with good contacts between the particles. The structures were very fine and consisted of primary α(Al) dendrites, eutectic silicon and the β-Al_5FeSi phase. The Vickers hardness values of the Al-14Si-8Fe and Al-22Si-8Fe-1Cr alloys were (170 ± 10) HV5, (185 ± 16) HV5, respectively. Compressive strength values were 670 MPa and 720 MPa, respectively. Surprisingly, both alloys exhibited a very good plasticity due to the refined structure. The alloys were annealed at 300–400 °C for 100 h to reveal their thermal stability. When the thermal stability of the powder-metallurgy Al-14Si-8Fe and Al-22Si-8Fe-1Cr alloys was compared to that of the casting-piston Al-12Si-1Cu-1Mg-1Ni alloy, the former was found to be superior.

Keywords: aluminium, powder metallurgy, rapid solidification, iron

Zlitini Al-14Si-8Fe in Al-22Si-8Fe-1Cr (*w*/%) sta bili pripravljeni s centrifugalno atomizacijo in hladnim enoosnim stiskanjem s tlakom 6 GPa. Izdelane zlitine so bile brez por z dobrim stikom med delci. Zlitini sta imeli zelo fino mikrostrukturo, ki je vsebovala primarne α(Al)-dendrite, Si-evtektik in fazo β-Al_5FeSi. Trdota zlitine Al-14Si-8Fe je bila (170 ± 10) HV5 in (185 ± 16) HV5 zlitine Al-22Si-8Fe-1Cr. Tlačna trdnost zlitin je bila 670 MPa oziroma 720 MPa. Presenetljivo sta imeli obe zlitini tudi odlično plastičnost zaradi rafinirane strukture. Zlitini smo žarili 100 h pri 300–400 °C, da bi ugotovili njuno termično stabilnost. Ugotovili smo, da je termična stabilnost izdelanih P/M-zlitin Al-14Si-8Fe in Al-22Si-8Fe-1Cr superiorna v primerjavi z ventilsko litino Al-12Si-1Cu-1Mg-1Ni.

Ključne besede: aluminij, metalurgija prahov, hitro strjevanje, železo

1 INTRODUCTION

Aluminium alloys exhibit a relatively high strength-to-weight ratio and good corrosion resistance. This makes them attractive for automotive and aerospace industries. In the recycling of aluminium, various grades of the Al-containing scraps are processed. In addition to water, oils, plastics and other non-metallic contaminants, the main metallic impurity in the Al scraps is iron (Fe). The iron contents depend on the actual scrap grade that can exceed the mass fraction (*w*/%) 10 %. Unfortunately, iron very negatively influences the mechanical properties of Al alloys, because it forms hard and brittle intermetallic phases in the structure, as seen in **Figure 1**. Therefore, the iron contents in most of the commercial, wrought, Al-based alloys must be minimized to a few tenths of *w*/%. Only die-casting Al-Si alloys can contain approximately 1 % of Fe, but the negative effect of the intermetallic phases is balanced with the relatively high cooling rates and fine structures of the castings. In the processing of the Fe-containing Al scraps, the iron contents can be lowered, for example, by magnetic separation before melting or by melting at carefully controlled temperatures to prevent dissolution of Fe in the molten aluminium. These techniques increase the investment and processing costs. For this reason, the Fe-containing Al scraps are significantly cheaper than the Fe-free Al scraps. For example, the price of the scrap

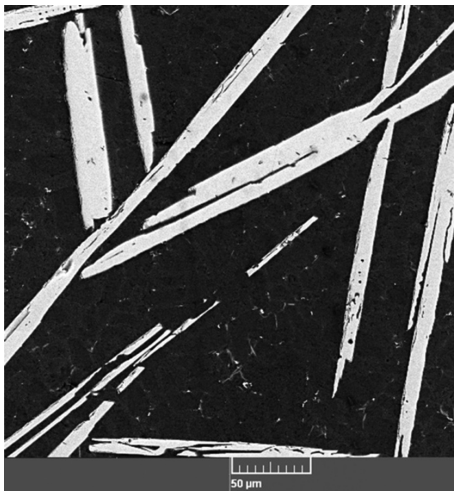

Figure 1: SEM micrograph of the as-cast Al-14Si-8Fe alloy containing large β-Al_5FeSi plates (light) deteriorating the mechanical properties

Slika 1: SEM mikroskopski posnetek litine na osnovi Al-14Si-8Fe, ki vsebuje velike β-Al_5FeSi (svetle) ploščice, vzrok za slabše mehanske lastnosti

containing up to 10 % of Fe is only one third of that of the Fe-free scrap.

In addition to the classic ingot and casting metallurgy of the Al-based alloys, these alloys can also be processed with powder metallurgy (P/M). It is shown in this study that the P/M is a method which enables the preparation of the qualitatively new Al-based alloys containing transition metals, such as Fe, in the concentrations far exceeding those in common casting and wrought alloys.[1] Therefore, aluminium scraps containing high amounts of iron can be processed with this technique. A rapid solidification of a melt, which generally occurs during the powder preparation, refines the structure, reduces the volume fraction of the intermetallic phases and forms new metastable crystalline, quasi-crystalline and amorphous phases.[1] All of these structural features are beneficial for achieving desirable combinations of strength and ductility. Powder compaction is generally performed by pressing and sintering or by hot extrusion.[2]

2 EXPERIMENT

The P/M alloys with the nominal chemical compositions (in mass fractions, *w*/%) of Al-14Si-8Fe and Al-22Si-8Fe-1Cr are studied in this work. The P/M alloys are compared with the commercial, Al-Si-based casting alloy with the nominal composition of Al-12Si-1Cu-1Mg-1Ni. This alloy is used for the pistons of combustion engines and is generally considered as thermally very stable. The P/M alloys were prepared by melting pure elements and master alloys in a vacuum induction furnace under an argon atmosphere. After a sufficient homogenization of the melt was achieved, the melt was poured into a cast-iron metal mould to prepare an ingot of 20 mm in diameter and 150 mm in length. Solidified powder was rapidly prepared with centrifugal atomization, which is schematically shown in **Figure 2**. The alloy ingot was remelted under argon and ejected onto a rapidly rotating graphite wheel (the rotation speed of 30 000 r/min) to produce flake-like particles (**Figure 3**). The dimensions of the powder particles ranged from 0.1 mm to 2 mm with a thickness of approximately 50 μm. The centrifugal atomization technique allows a production of large quantities of powders at low cost.

The powder was then placed into a tungsten-carbide mould and was compacted by uni-axial pressing at an ultra-high pressure of 6 GPa to prepare cylindrical samples of 15 mm in diameter and 5 mm in height. The pressing temperature and time were 450 °C and 1 h, respectively. The casting alloy was provided by an industrial supplier in the form of an ingot with a thickness of 20 mm and a length of 100 mm. The alloy was heat treated by the T6 regime consisting of solution annealing at 510 °C/5 h, water quenching and artificial aging at 230 °C/6 h.[3]

For all of the investigated materials, compressive mechanical properties were measured with an Instron 5882 machine at a deformation rate of 1 mm/min. Vickers hardness tests were performed at room temperature with a 5-kg load. To examine the thermal stability of the alloys, compressive tests were also performed after annealing the samples for 100 h at 300–400 °C, and the development of the Vickers hardness at room temperature was observed to follow the structural changes induced by the long annealing time. The structures of the alloys were investigated using light microscopy (LM), scanning electron microscopy (SEM, Tescan Vega 3) and energy dispersion spectrometry (EDS, Oxford Instruments Inca 350). The phase composition was determined with X-ray diffraction (XRD, X Pert Pro).

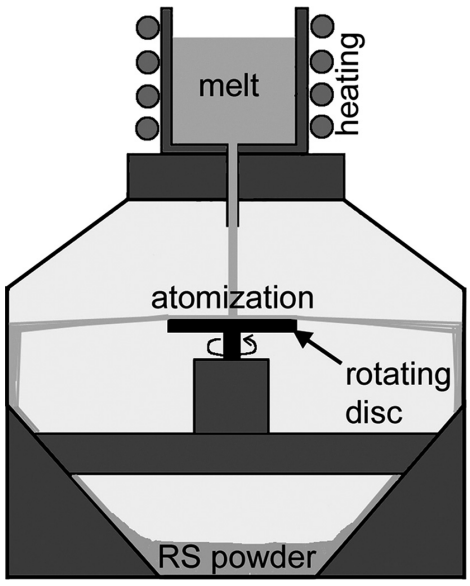

Figure 2: Schematic drawing of the centrifugal atomization used in this study to prepare the P/M alloys

Slika 2: Shematični prikaz centrifugalne atomizacije, ki je bila uporabljena v tej študiji za pripravo P/M zlitin

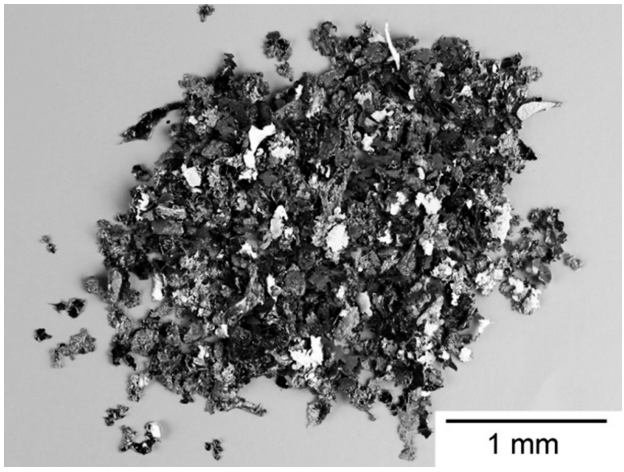

Figure 3: Flake-like powder particles prepared with the centrifugal atomization

Slika 3: Prašni delci v obliki ploščic, izdelani s centrifugalno atomizacijo

3 RESULTS AND DISCUSSION

The structures of the investigated alloys are shown in **Figure 4**. The P/M Al-14Si-8Fe alloy (**Figure 4a**) is dominated by the α(Al) (dark) and β-Al_5FeSi (light) phases. XRD (not shown) also proved the presence of a small volume fraction of eutectic silicon that is hardly seen in an SEM micrograph in the secondary-electron regime. The β-Al_5FeSi phase appears as very fine needles with an average thickness of 2 μm and the length of 8 μm. The P/M Al-22Si-8Fe-1Cr alloy is shown in **Figure 4b**. This alloy has the same phase composition as the previous one, i.e., it contains the β(Al) (dark), β-Al_5FeSi (light) and Si (not seen) phases. The EDS analysis reveals that chromium does not create any new phases. Instead, it is incorporated in the β-Al_5FeSi phase where it substitutes iron atoms. In addition, chromium significantly changes the morphology of the β-Al_5FeSi(Cr) phase from a needle-like to an almost spherical structure. The observed phase composition of the P/M alloys corresponds to the well known ternary equilibrium diagram of the Al-Si-Fe system[4] that is illustrated in **Figure 5**. The structure of the casting Al-12Si-1Cu-1Mg-1Ni (T6) alloy in **Figure 4c** consists of primary α(Al) dendrites (light), α(Al)+Si eutectic and intermetallic phases containing mainly Ni and Al. During the T6 heat treatment of the alloy, plate-like $Al_2CuMgNi$ precipitates were formed which are seen in the TEM micrograph in **Figure 4c**.

By comparing **Figures 1** and **4a**, one can see that the centrifugal atomization of the P/M alloys causes a significant structural refining. This refining is a direct consequence of the rapid solidification occurring during the centrifugal atomization of the melt. In this process (**Figure 2**), the melt stream falls onto a fast rotating wheel, where it is broken into small droplets by the centrifugal force. These droplets are ejected towards the cooled wall of the atomizer, where they rapidly solidify and obtain the typical flake-like shape. It will be shown later that the structural refining has a positive impact on the resulting mechanical properties. It is also important to note that the P/M alloys exhibit almost no porosity and have very good contacts between the particles. Apparently, sufficient diffusion bonding between the

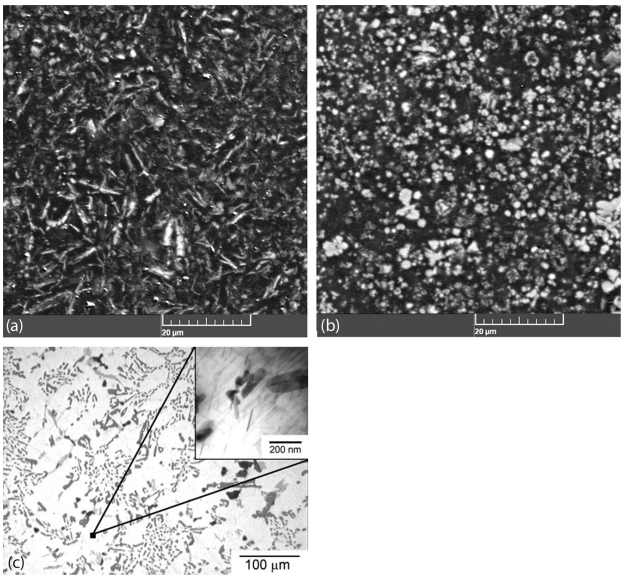

Figure 4: Microstructures of the investigated alloys: a) the PM Al-14Si-8Fe alloy (SEM), b) the PM Al-22Si-8Fe-1Cr alloy (SEM), c) the casting Al-12Si-1Cu-1Mg-1Ni (T6) alloy (LM, TEM)

Slika 4: Mikrostrukture preiskovanih zlitin: a) P/M Al-14Si-8Fe (SEM), b) P/M Al-22Si-8Fe-1Cr (SEM), c) litina Al-12Si-1Cu-1Mg-1Ni (T6) (LM, TEM)

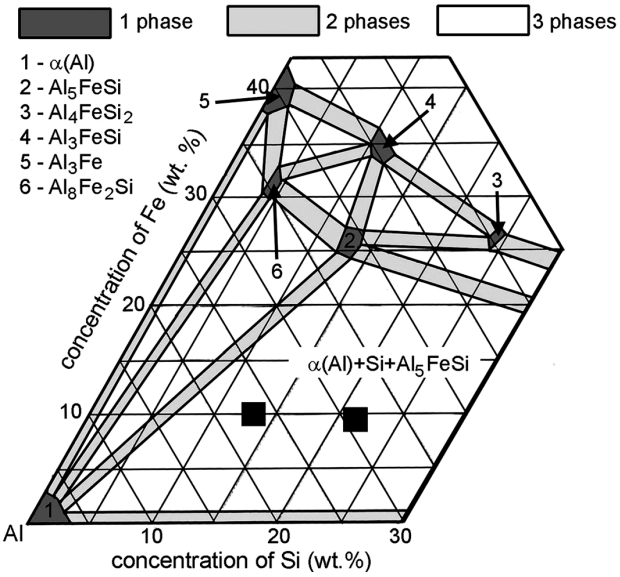

Figure 5: Aluminium corner of the Al-Si-Fe phase diagram[4] (the chemical compositions of the investigated P/M alloys are marked with black cubes)

Slika 5: Al kot v ternarnem faznem diagramu Al-Si-Fe (kemijske sestave preiskovanih litin so označene s črnimi kockami)[4]

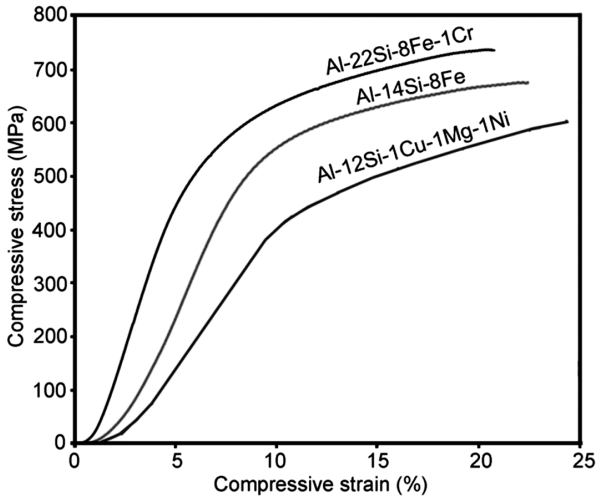

Figure 6: Compressive stress-strain diagrams of the investigated alloys

Slika 6: Diagram odvisnosti med deformacijo in tlačno trdnostjo preiskovanih zlitin

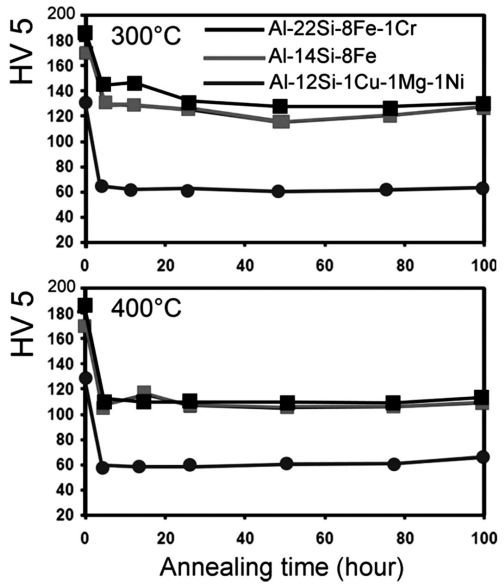

Figure 7: Room-temperature Vickers hardness as a function of the annealing time at 300 °C and 400 °C

Slika 7: Vickersova trdota, izmerjena pri sobni temperaturi v odvisnosti od časa žarjenja pri 300 °C in 400 °C

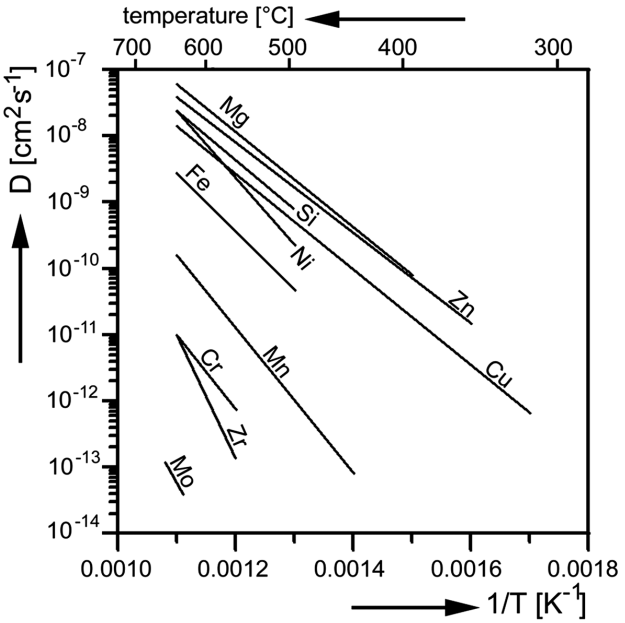

Figure 9: Arrhenius plots of diffusion coefficients D_s, of various metals in Al.[7] Transition metals like Fe have significantly lower diffusion coefficients than the commonly used alloying elements like Cu, Si or Mg.

Slika 9: Arrheniusov diagram difuzijskih koeficientov D_s različnih kovin v Al.[7] Prehodne kovine, kot je Fe, imajo manjše difuzijske koeficiente kot pogosti zlitinski elementi v Al-zlitinah (Cu, Si ali Mg).

particles was induced by the high pressure of 6 GPa used in this experiment. A similar finding was also reported by Cieslak et al.[5]

Figure 6 compares the compressive stress-strain diagrams of the investigated P/M and casting alloys. It is observed that the P/M Al-14Si-8Fe and Al-22Si-8Fe-1Cr alloys exhibit a significantly higher compressive strength (670 MPa and 720 MPa, respectively) than the Al-12Si-1Cu-1Mg-1Ni alloy (600 MPa). Moreover, the P/M alloys also exhibit a higher hardness than their casting counterparts. Vickers hardness values for the Al-14Si-8Fe, Al-22Si-8Fe-1Cr and Al-12Si-1Cu-1Mg-1Ni alloys are (170 ± 10) HV5, (185 ± 16) HV5 and (130 ± 8) HV5, respectively. Higher compressive strength and hardness of the P/M alloys are caused by their observed structural refining due to the rapid solidification (**Figure 4**). An additional contribution to both the hardness and compressive strength is the high volume fraction of the hard phases, namely β-Al_5FeSi, in the structure of the P/M alloys (**Figure 4**). In contrast, the casting alloy contains large α(Al) grains, whose contribution to the Hall-Petch strengthening is negligible (**Figure 4c**). The most pronounced strengthening mechanism operating in this alloy is the precipitation strengthening caused by the semi-coherent $Al_2CuMgNi$ precipitates (**Figure 4c**). The compressive strengths of the P/M alloys investigated in this study (670 MPa and 720 MPa) are higher than the recently reported compressive strengths (→500 MPa) of similar alloys (Al-20Si-5Fe-2(Cu, Ni, Cr)) [6] compacted at 400 °C/1 h, but at a lower pressure of 300 MPa. This suggests that the ultra-high-pressure compaction at 6 GPa positively influences the resulting mechanical properties.

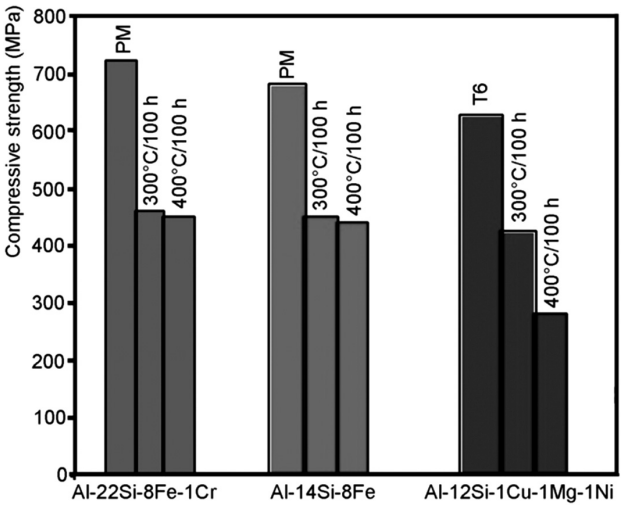

Figure 8: Compressive strength of the alloys as a function of annealing regime

Slika 8: Tlačna trdnost izdelanih zlitin v odvisnosti od režima žarjenja

Another important finding is that both P/M alloys exhibit a very good plasticity, despite the high iron content (**Figure 6**). The alloys with the same chemical composition prepared with the classic casting metallurgy would be extremely brittle due to the presence of the large β-Al_5FeSi plates (**Figure 1**), acting as primary stress concentrators during the compressive loading. The plasticity of the P/M alloys can be attributed to the preparation procedure, including the rapid solidification

of the melt. Due to this procedure, the β-Al_5FeSi particles became very fine, short or almost spherical (**Figures 4a** and **4b**). As the stress concentration is proportional to the dimensions of the needles, the refining caused by rapid solidification is able to reduce the local stresses and allow the plastic α(Al) phase to be deformed before the formation of fracture micro-cracks.

Figures 7 and **8** illustrate the thermal stability of the mechanical properties of the investigated alloys. They show the development of the room-temperature Vickers hardness and compressive strength of the alloys during the long-term annealing at 300 °C and 400 °C. Both the hardness and the compressive strength of the P/M alloys decrease during the annealing at 300–400 °C, but these decreases occur much more slowly than in the case of the casting Al-12Si-1Cu-1Mg-1Ni alloy. The P/M alloys retain a relatively high hardness and compressive strength of above 120 HV5 and 450 MPa, respectively, even after the 100 h annealing at 400 °C. One reason for a better thermal stability of the P/M alloys is a lower diffusivity of iron in solid aluminium in comparison with silicon, copper, magnesium and nickel (**Figure 9**).[7] The structural coarsening of the β-Al_5FeSi particles is therefore very slow in the P/M alloys. In contrast, the growth and transformations of precipitates in the casting alloy (**Figure 4c**) occurs fast and, therefore, this alloy softens rapidly during the annealing.

4 CONCLUSIONS

It is demonstrated in this work that the Al-based alloys with a high iron content of 8 % can be successfully prepared with the powder-metallurgy technology that consists of a combination of centrifugal atomization and high-pressure compaction. The resulting alloys have significantly refined structures that have a positive impact on strength, hardness and, particularly, plasticity. The alloys also exhibit excellent thermal stability in comparison with the casting Al-12Si-1Cu-1Mg-1Ni alloy commonly used for the production of the combustion-engine pistons. The classic casting processes cannot be used for the preparation of the high-iron alloys because iron would form large, needle-like β-Al_5FeSi particles, resulting in an extreme brittleness of the as-cast alloys.

Acknowledgements

The authors wish to thank the Czech Academy of Sciences (project no. KAN 300100801) for its financial support of this research.

5 REFERENCES

[1] D. Vojtěch, J. Verner, J. Šerák, F. Šimančík, M. Balog, J. Nagy, Mat. Sci. Eng., A458 (**2007**), 371

[2] L. Shaw, H. Luo, J. Villegas, D. Miracle, Scripta Mater., 50 (**2004**), 921

[3] S. Michna, Aluminium Materials and Technologies from A to Z., Adin, Presov 2007, 375

[4] L. F. Mondolfo, Aluminum Alloys: Structure and Properties, Butter Worths, London 1976, 535

[5] G. Cieslak, J. Latuch, Rev. Adv. Mater. Sci., 18 (**2008**), 425

[6] M. Rajabi, M. Vahidi, A. Simchi, P. Davami, Mater. Charact., 60 (**2009**), 1370

[7] Y. Du, Y. A. Chang, B. Huang, W. Gong, Z. Jin, H. Xu, Z. Yuan, Y. Liu, Y. He, F. Y. Xie, Mat. Sci. Eng., A363 (**2003**), 140

UDK 620.178.3:519.61/.64
Original scientific article/Izvirni znanstveni članek

ISSN 1580-2949
MTAEC9, 46(4)345(2012)

FATIGUE-LIFE BEHAVIOUR AND A LIFETIME ASSESSMENT OF A DOUBLE-LEAF SPRING USING FEM-BASED SOFTWARE

UTRUJANJE IN OCENA DOBE TRAJANJA DVOLISTNATIH VZMETI Z UPORABO MKE-ORODJA

Predrag Borković, Borivoj Šuštaršič, Milan Malešević, Borut Žužek, Bojan Podgornik, Vojteh Leskovšek

Institute of Metals and Technology, Lepi pot 11, SI-10000 Ljubljana, Slovenia
predrag.borkovic@imt.si

Prejem rokopisa – received: 2011-10-20; sprejem za objavo – accepted for publication: 2012-04-05

A lifetime assessment of any component by performing classical fatigue tests on real geometry is a very expensive and time-consuming task. For this reason, many efforts have been made to produce a computer software which will be able to replace this conventional fatigue testing. Although there is some dissimilarity between these two testing methods, we are free to use such a computer tool to shorten the testing time. The Finite Element Method (FEM) is one of the most frequently used methods for component designing, as well as for fatigue assessment. This assessment includes the stresses, the loads and the strength behavior of the material component. As the input values for the material properties, S/N curves were defined on the basis of the test results. The tensile and fatigue tests on the notched, as well as on the unnotched specimens under compression-tension loading were carried out in order to obtain the static and dynamic (S/N curves) properties of the investigated spring steel (51CrV4). Two groups of specimens were prepared: the longitudinal and perpendicular specimens relative to the rolling direction, both with two different heat-treatments (tempering temperatures).
The results of the performed investigation showed a clear difference between the fatigue strengths of the specimens with two outmost segregation orientations and two different tempering temperatures. In addition, other influences, such as the residual stresses due to shoot peening and machining, surface roughness and metallurgical variables, can affect the fatigue strength of a material. All these effects can be taken into account by using the FEM-based simulations.

Keywords: fatigue life, leaf spring, FEM simulation, spring steel

Ocenjevanje dobe trajanja komponent pri izvajanju klasičnega preizkusa utrujanja realne geometrije je zelo drag in dolgotrajen postopek. Zaradi tega je bil vložen velik napor, da bi pridobili računalniško podprto orodje, ki bi bilo sposobno zmanjšati število konvencionalnih preizkusov utrujanja. Čeprav realno lahko pričakujemo, da obstajajo nekatere razlike med rezultati preizkušanja na realnih preizkušancih in tistimi, dobljenimi z računalniško podprtim orodjem, je prednost slednjega nedvomna, saj močno skrajša čas do pridobitve dokaj uporabnih podatkov. Metode končnih elementov (MKE) so med najbolj uporabnimi za načrtovanje komponent tudi pri oceni vpliva utrujanja nanje za neko izbrano realno geometrijo. Ta ocena je sestavljena iz trdnostnih, obremenitvenih in napetostnih značilnosti materiala oz. komponent. Pri vzorcih iz izbranega materiala (vzmetno jeklo 51CrV4) smo določili njegovo trdoto ter statične (natezno trdnost) in dinamične (S/N-krivulje) lastnosti. Preizkusi utrujanja oz. določevanje S/N-krivulj je potekalo na zarezanih in nezarezanih vzorcih v natezno-tlačnem načinu obremenitve. Pripravljeni sta bili dve skupini vzorcev: v prečni in vzdolžni smeri glede na smer valjanja (smer izcejanja), obe skupini pa sta bili še dodatno različno toplotno obdelani (pri dveh različnih temperaturah popuščanja).
Rezultati preiskav kažejo jasno razliko med dinamično trajno trdnostjo vzorcev za izbrani orientaciji izcej in izbrani temperaturi popuščanja. Poleg tega moramo upoštevati, da tudi drugi vplivi (metalurgija izdelave jekla, zaostale napetosti zaradi peskanja in mehanske obdelave, hrapavost površine itd.) lahko vplivajo na dinamično trajno trdnost materiala. Vsi navedeni vplivi se lahko upoštevajo pri uporabi MKE-orodja.

Ključne besede: doba trajanja, listnate vzmeti, MKE-simulacije, vzmetno jeklo

1 INTRODUCTION

The basic function of a leaf spring is to store mechanical energy when it initially elastically deforms and to recoup this energy after being released. Since a leaf spring is subjected to dynamic loading it is possible for a failure to occur even at a stress level considerably lower than the tensile or the yield strengths determined by the quasi static loading. In addition, the fatigue strength of a leaf spring may be influenced by many factors such as: surface roughness, surface treatment, component size, residual stresses, corrosion, temperature, metallurgical structure, etc. In order to provide stability and safety to a vehicle, all these influences should to be taken into account in the manufacturing and designing processes of spring steel, as well as of spring semifinal products (plates or profiles). Unfortunately, all of these influencing factors often cannot be accurately taken into consideration without an exact experimental investigation.

Particular care has to be taken during a spring-manufacturing process (profiling, eye making, punching, etc) that, together with the final heat-treatment, has a crucial effect on the fatigue behavior of a spring. Among all the mentioned factors that influence the dynamic property of a spring, in this paper the influences of the intensities of the alloying elements, as well as of different tempering temperatures, on the fatigue behavior were examined.

2 EXPERIMENTAL WORK

The experimental work consisted of the compression-tension fatigue tests carried out on the notched and smooth (unnotched) specimens on a servo-hydraulic testing rig ±250 kN INSTRON 8802 at the frequency of 30 Hz. Some additional tests were also performed on a high-frequency pulsator (Rumul, Switzerland) that is known for providing a fast and reliable method of steel-quality assessment[1,2]. The tested spring steel 51CrV4 was produced with a modified deoxidation technology at the steel plant Štore Steel, Slovenia. The chemical composition of the selected spring steel is given in **Table 1**.

To determine the dynamic properties of the spring steel two groups of specimens were prepared and tested. As it is illustrated in **Figure 1**, one group of specimens is oriented along the rolling direction, while another group is perpendicular to the rolling direction.

Both the perpendicularly ($\lambda = 90°$) and longitudinally ($\lambda = 0°$) oriented specimens relative to the rolling direction are presented in **Figures 2** and **3**.

For the purpose of both static-tensile test and dynamic-loading test, all specimens are cut off from the base spring-steel material in the as-delivered condition (a flat profile with the dimensions of 90 mm × 28 mm). After cutting and machining, the specimens were heat-treated, quenched in nitrogen at 5 bar of overpressure and then tempered at two different temperatures. Both perpendicular and longitudinal specimens were divided into these two groups of tempering temperatures: 425 °C (HT1) and 475 °C (HT2).

At the end of the experiment, an FEM simulation of the dynamic loading (fatigue) of a double-leaf spring with a selected geometry was carried out with the use of the experimental testing results. Among the many accessible computer codes based on the stress or strain-life approaches[3–7] and on a cumulative-damage analysis[8] relating to the fatigue-life prediction of the double-leaf spring, ANSYS computer software was used. The presented FEM simulation was based on the high-cycle fatigue approach and the S/N curves for the investigated spring steel 51CrV4 obtained with the compression-tension tests of differently oriented specimens at both tempering temperatures. The used computer tool was first successfully tested by performing an FEM simulation on the smooth and notched cylindrical specimens during the mechanical testing.

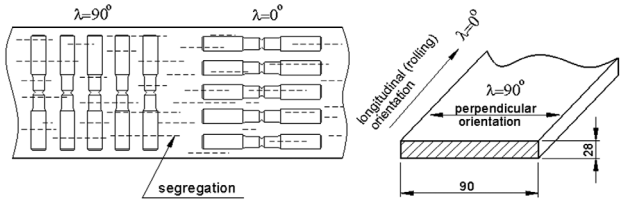

Figure 1: Orientation of the specimens with respect to the rolling direction
Slika 1: Orientacija preizkušancev glede na smer valjanja

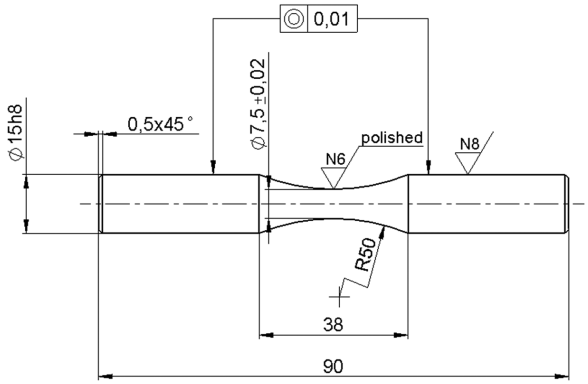

Figure 2: Standard smooth cylindrical specimen; *Kt* = 1 (calculated with ANSYS)
Slika 2: Standardni cilindrični preizkušanec brez zareze; *Kt* = 1 (izračunan v ANSYS-u)

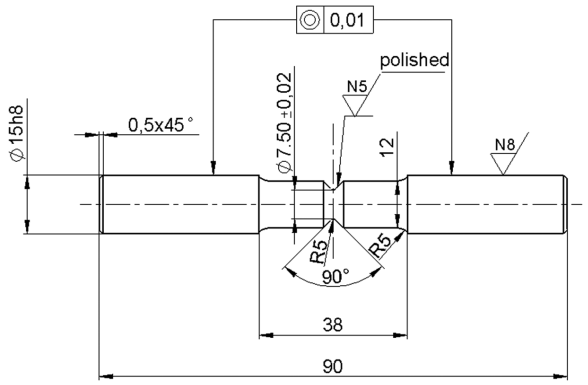

Figure 3: Standard notched cylindrical specimen; *Kt* = 2 (calculated with ANSYS)
Slika 3: Standardni cilindrični preizkušanec z zarezo; *Kt* = 2 (izračunan v ANSYS-u)

3 RESULTS AND DISCUSION

3.1 Static test

Before the compression-tension fatigue testing, the static-tensile tests were also carried out using a 500-kN Instron 1255 test rig with an extensometer. As illustrated in **Table 2** it is obvious that both tensile and yield strengths increase with a decrease in the tempering

Table 1: Chemical composition of the spring steel 51CrV4 in mass fraction (*w*/%)
Tabela 1: Kemijska sestava vzmetnega jekla 51CrV4 v masnih deležih (*w*/%)

Chemical element	C	Si	Mn	P	S	Cr	Mo	Ni	V
Composition	0.52	0.35	0.96	0.011	0.004	0.94	0.05	0.13	0.12

Table 2: Tensile-test results
Tabela 2: Rezultati nateznega preizkusa

Orientation	Tempering temperature	Yield strength (MPa)	Tensile strength (MPa)	Fracture elongation (%)	Fracture contraction (%)
Perpendicular (λ = 90°)	475 °C/1 h	1373	1448	7.04	24.6
	425 °C/1 h	1502	1591	5.16	15.8
Longitudinal (λ = 0°)	475 °C/1 h	1366	1442	10.6	41
	425 °C/1 h	1502	1606	9.9	42

temperature. The fracture elongation also varies with the changes in the tempering temperature. When the tempering temperature decreases the fracture elongation decreases as well. Ductility is larger in the longitudinal direction than in the perpendicular one.

3.2 Hardness measurement

A slight difference between the hardness measurements at 425 °C and at 475 °C of the tempering temperature was also found (**Table 3**). Before the heat treatment, the base material had the Rockwell hardness of about 30 HRC, whereas after the heat treatment the average hardness increased to about 45 HRC at 425 °C and to 43 HRC at the tempering temperature of 475°C. Nearly the same results were obtained for both the perpendicularly and parallelly oriented specimens.

Table 3: Hardness in dependence of the heat-treatment condition and the segregation orientation
Tabela 3: Trdota v odvisnosti od pogojev toplotne obdelave in orientacije izcej

Longitudinal (λ = 0°)		Perpendicular (λ = 90°)	
425 °C	475 °C	425 °C	475 °C
45.0 HRC	43.4 HRC	45.8 HRC	43.0 HRC

3.3 Dynamic test

The influences of the heat treatment and the segregation orientation under the compression-tension dynamic loading were investigated. These experiments were performed at the Institute of Metals and Technology (IMT), Ljubljana, Slovenia, using a compression-tension testing machine Instron 8802 of ±250 kN with the operating frequency of 30 Hz.

The S/N curves obtained with the compression-tension fatigue tests on the notched, as well as on the smooth specimens are presented in the diagrams in **Figures 4** and **5**, respectively. The specimens shown in **Figures 2** and **3** were mechanically polished (fine metallographic grinding; final paper 800) after the heat treatment in order to achieve the required surface roughness.

Figures 4 and **5** show that the fatigue strength of the specimens tempered at 425 °C is slightly higher than that of the specimens tempered at 475 °C. It is also clear that the fatigue strength of the longitudinally oriented specimens is significantly higher than the fatigue strength of the perpendicularly oriented specimens. We still need to finish the fatigue testing on the smooth, perpendicularly oriented specimens tempered at 475 °C to get more information about the influence of the notch on the fatigue strength. A tabular review of the fatigue-strength dependence on the segregation orientation and the heat-treatment conditions, for both notched and smooth specimens, is given in **Table 4**.

The 5.2 slope of the S/N curve for the perpendicularly oriented HT2 specimens is surprisingly lower than the 5.9 slope of the HT1-S/N curve. For more accurate findings, this fatigue test has to be repeated.

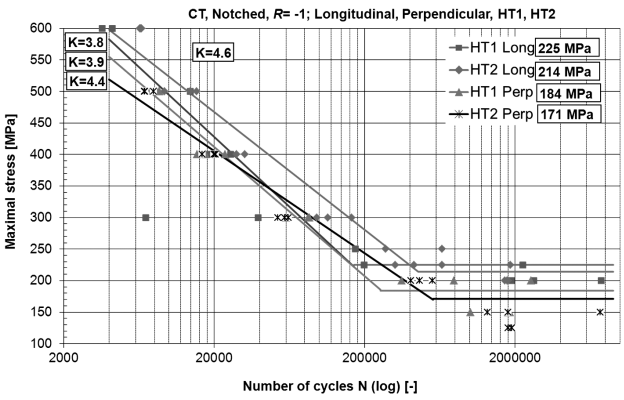

Figure 4: S/N curves for the notched specimens of both segregation orientations
Slika 4: S/N-krivulje zarezanih preizkušancev za obe orientaciji izcej

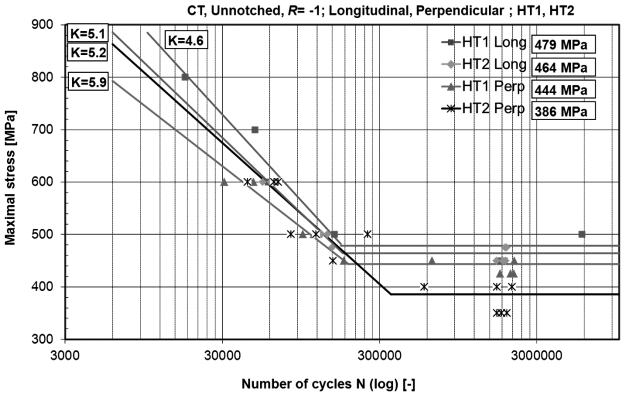

Figure 5: S/N curves for the smooth, longitudinally orientated specimens
Slika 5: S/N-krivulje nezarezanih preizkušancev za obe orientaciji izcej

Table 4: Fatigue limits of the tested specimens
Tabela 4: Trajna dinamična trdnost preizkušancev

Segregation orientation	Tempering temperature	Notched specimens	Smooth specimens
Perpendicular (λ = 90°)	HT1 (425 °C)	184 MPa	444 MPa
	HT2 (475 °C)	171 MPa	386 MPa
Longitudinal (λ = 0°)	HT1 (425 °C)	225 MPa	479 MPa
	HT2 (475 °C)	214 MPa	464 MPa

From the fatigue-limit values for the smooth and notched specimens it is evident that the fatigue limits of the notched specimens are nearly reduced by the theoretical stress-concentration factor (Kt = 2 for the notched specimens).

3.4 Double-leaf-spring simulation using FEM-based software

Fatigue simulations of the double-leaf spring with the selected geometry were performed using three standard loading conditions that the spring manufacturers normally use for the structural testing of leaf springs (**Figure 7**). The fatigue simulations were also based on the results of the above described mechanical testing. First, the simulations on the specimens were performed in order to evaluate the usability of ANSYS software for the double-leaf spring. All specimens were first generated in Solid Works 3D computer programme. After exporting, the specimen models were further prepared (meshed, constrained, loaded, etc) and finally simulated with ANSYS computer programme using the fatigue module. No remarkable difference was found in the number of cycles between the mechanically tested specimens and the computer-simulated specimens using ANSYS software with the corresponding S/N curves. Afterwards the fatigue simulations using the ANSYS computer tool were carried out on the double-leaf spring. One model of the double-leaf spring is presented in **Figure 6**.

The ANSYS material database was created using a new spring-steel material with the required static properties, forming six S/N curves obtained with the dynamical testing. The fatigue-life results for the double-leaf spring obtained with the ANSYS simulation are gathered in **Figure 7**. The results are based on the variation of different parameters, i.e., the segregation orientation, the heat treatment and the notch effect. The double-leaf-spring model was loaded in the case of a free displacement in one direction (z) and constrained in the other two directions (x and y), **Figure 6a**.

From the fatigue simulation it is clear that the longest fatigue life of the double-leaf spring was obtained by using the dynamic properties of the smooth, longitudinally oriented specimens, tempered at 425 °C. For the lowest loading condition it can be seen that all three S/N curves relating to the smooth specimens give a fatigue lifetime of more than 5 million cycles, which is already in the range of the fatigue limit. The S/N curves obtained with the fatigue testing of the notched specimens were corrected with the stress-concentration factor to avoid the influence of the notch.

The expected life of the double-leaf spring is above $1.5 \cdot 10^5$ cycles. It is evident that this expectation is fulfilled only at the lowest loading condition. Accordingly, the suspension system of a truck has to be designed in such a way that this dynamic loading condition is not exceeded. One can also notice that the highest prescribed testing conditions are already in the low-cycle fatigue region (the regime of loading very close to, or even above, the yield point of the selected spring steel; **Table 2**). From this point of view the selected structural testing condition seems problematic and inadequate.

4 CONCLUSION

The investigations have shown scattered results of the fatigue testing performed at a certain stress level. This dispersion of the results among the repeated specimens is

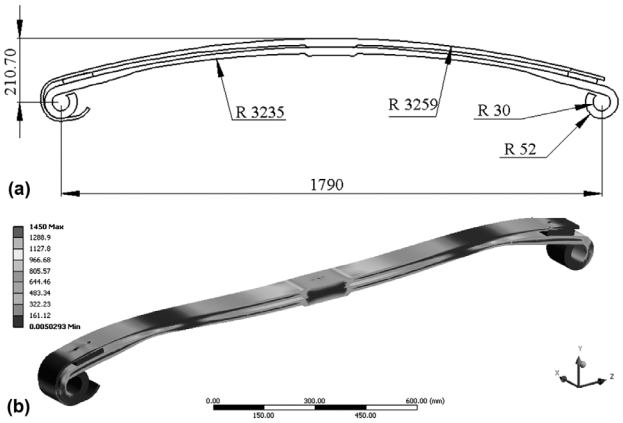

Figure 6: a) Basic dimensions of the double-leaf spring generated with Solid Works and b) an ANSYS fatigue simulation of the double-leaf spring
Slika 6: a) Osnovne dimenzije dvolistnate vzmeti, modelirane v Solid Worksu in b) ANSYS-simulacije utrujanja dvolistnate vzmeti

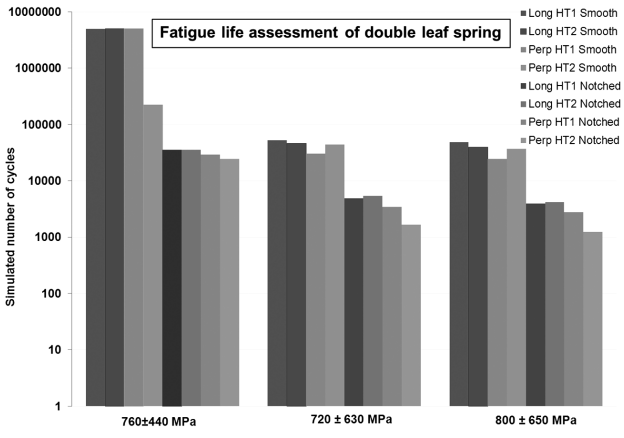

Figure 7: Simulated fatigue lifetime of the tested double-leaf spring
Slika 7: Simulacijska doba trajanja preizkušanih dvolistnatih vzmeti

mainly influenced by different nonmetallic inclusions[9] in the spring steel (MnS, CaS, Al_2O_3). Insufficient polishing quality after the heat treatment of the specimen surface can also lead to the number of cycles being lower than expected, causing a lower fatigue strength of the investigated steel. In general, in the case of the selected spring steel 51CrV4, the fatigue strength of the perpendicularly oriented specimens decreases by about 25 % more than the strength of the longitudinally oriented specimens, accompanied with the lower tensile and yield strengths. Considering different stress-concentration factors relating to the notched and smooth specimens, it is shown that the fatigue strength of the notched specimens is effectively lower, as indicated by the stress-concentration factor.

Generally speaking, when dealing with a fatigue-module simulation, one has to take into consideration not only the metallurgical and manufacturing effects, but also the other effects related to the used software, such as the type and the size of the mesh element (tetrahedral, hexahedral etc), the input file (IGES, STEP, SLDPRT etc), the boundary conditions and the constraint type.

5 REFERENCES

[1] B. Šuštaršič, B. Senčič, B. Arzenšek, P. Jodin, The notch effect on the fatigue strength of 51CrV4Mo spring steel, Mater. Tehnol., 41 (**2007**) 1, 29–34

[2] B. Šuštaršič, B. Senčič, V. Leskovšek, Fatigue strength of spring steels and life-time prediction of leaf springs, Assessment of reliability of materials and structures (RELMAS'2008), St. Petersburg, Russia, June 17–20, 2008; problems and solutions; international conference, Volume 1, St. Petersburg, Polytechnic Publishing House, 2008, 361–366

[3] S. Tavakkoli, F. Aslani et al., Analytical Prediction of Leaf Spring Bushing Loads Using MSC/NASTRAN and MDI/ADAMS, http://www.mscsoftware.com/support/library/conf/wuc96-/11b_asla.pdf

[4] M. S. Kumar, S. Vijayarangan, Static analysis and fatigue life prediction of steel and composite leaf spring for light passenger vehicles, Journal of Scientific and Industrial research, 66 (**2007**) 2, 128–134

[5] F. N. A. Refngah, S. Abdullah, A. Jalar, L. B. Chua, Fatigue life evaluation of two types of steel leaf springs, International Journal of Mechanical and Materials Engineering (IJMME), 4 (**2009**) 2, 136–140

[6] N. Philipson, Leaf spring modeling http://www.modelica.org/events/modelica2006/Proceedings/sessions/Session2d1.pdf

[7] G. S. S. Shankar, S. Vijayarangan, Mono Composite Leaf Spring for Light Weight Vehicle – Design, End Joint Analysis and Testing, Materials Science (Medžiagotyra), 12 (**2006**) 3, 220–225

[8] W. Eichlseder, Enhanced Fatigue Analysis – Incorporating Downstream Manufacturing Processes, Mater. Tehnol., 44 (**2010**) 4, 185–192

[9] M. Kovačič, S. Senčič, Critical inclusion size in spring steel and genetic programming, RMZ – Materials and Geoenvironment, (**2010**), 17–23

UDK 621.793:669.058.67:66.019
Original scientific article/Izvirni znanstveni članek

ISSN 1580-2949
MTAEC9, 46(4)351(2012)

CHARACTERIZATION OF DEFECTS IN PVD TiAlN HARD COATINGS

KARAKTERIZACIJA DEFEKTOV PVD TiAlN TRDIH PREVLEK

Peter Gselman[1,2], Tonica Bončina[2], Franc Zupanič[2], Peter Panjan[1], Darja Kek Merl[1], Miha Čekada[1]

[1]Jožef Stefan Institute, Jamova cesta 39, SI-1000 Ljubljana, Slovenia
[2]University of Maribor, Faculty of Mechanical Engineering, Smetanova 17, SI-2000 Maribor, Slovenia
peter.gselman@ijs.si

Prejem rokopisa – received: 2011-10-23; sprejem za objavo – accepted for publication: 2012-03-07

PVD hard coatings are continuously gaining their importance in different fields of applications. In industrial use, they are often exposed to corrosive environments. Hard coatings possess inherently good corrosion resistance, but the substrate-hard coating systems may suffer from a severe corrosion attack due to the defects (craters, pin holes) in the coatings. On the sites, where defects extend through the coating, pitting corrosion can take place. These sites are drawbacks in the applications of hard coating.
A PVD TiAlN hard coating was prepared on cold-work, tool-steel (AISI D2) substrates by sputtering using unbalanced magnetron sources. The growth defects incorporated into the coating were studied after the deposition and corrosion experiments. We used two methods: (1) scanning electron microscopy (SEM) for general overview of the coating topography and 2D-characterization of defects, and (2) scanning electron microscopy with a focused ion beam (SEM-FIB) for making serial cross-sections through the selected defects in order to provide images for a 3D-reconstruction of defects. In this work we tried to investigate the formation of a defect at a specific location and find out whether the selected defect causes pitting corrosion.

Keywords: PVD hard coating, defect, 3D-reconstruction, FIB, SEM

PVD trde prevleke pridobivajo pomen na različnih področjih uporabe. Pri različnih aplikacijah so pogosto izpostavljene korozijskemu okolju. Trde prevleke so kemijsko inertne in same po sebi korozijsko obstojne. Med njihovo pripravo pa nastane v njih veliko defektov (kraterji, "pinholi"). Nekateri od njih segajo do podlage. Na teh mestih pride do jamičaste korozije, kar pa je z vidika uporabe neželeno.
TiAlN-prevleko smo nanesli na podlago orodnega jekla D2 po postopku napršenja z neuravnoteženim magnetronskim izvirom. Defekte, ki so nastali med pripravo plasti, smo preučili po korozijskem preizkusu. Za analizo smo uporabili dve metodi. Vrstični elektronski mikroskop (SEM), s katerim smo pridobili splošni pregled prevleke, kot tudi 2D-karakterizacijo defektov. Kot drugo metodo smo uporabili fokusiran ionski curek, ki je integriran v klasični SEM, s katerim smo izvedli serijo rezov izbranih defektov za njihovo 3D-karakterizacijo. V delu smo poskušali na specifičnih mestih ugotoviti mehanizem nastanka defektov in ugotovljali, ali povzročajo jamičasto korozijo.

Ključne besede: trde PVD-prevleke, defekti, 3D-rekonstrukcija, FIB, SEM

1 INTRODUCTION

In hard coatings, macro- and microdefects typically appear during the deposition[1–5]. The most common macrodefects are: (a) large and shallow craters with diameters greater than 5 μm, (b) nodular defects (spherical droplets, conical features) with diameters in the range of 1–5 μm and (c) disk-like holes arising from droplet wrenching and pin holes[1,2]. The defects smaller than 1 μm can be regarded as microdefects. Their main representatives are: (I.) small micro-sized holes (so-called pin holes) extended through the entire thickness of a coating and (II.) small islands generated by the built-in particles with a diameter of slightly less than 1 μm. These surface imperfections in the coatings can cause local stresses, higher friction, sticking of the material, local loss of adhesion and pitting corrosion. All these facts are drawbacks in the application of hard coatings. Therefore, it is very important to reduce their concentration. However, the question is how to deposit denser and less defective coatings.

In this paper we tried to investigate the formation of a defect at a specific location and find out whether such a defect can cause pitting corrosion. For scientific and technological reasons, this topic remains very important also for further investigations and our main goal was to make a contribution to the researched area by using microstructural characterization and 3D-reconstruction of defects.

2 EXPERIMENTAL WORK

The industrial unbalanced sputtering system CC800/7 (CemeCon) was used for the deposition of the TiAlN hard coating. The sputtering system was equipped with four unbalanced magnetron sources that were positioned pairwise at the two sides of the vacuum chamber. A cold-work, high-chromium, high-carbon-type, tool-steel D2 (OCR12VM) was used as the substrate material. The substrates were polished to R_a = 9–15 nm, ultrasonically cleaned in detergents, rinsed in deionized water and dried in hot air. The final cleaning was performed by ion etching. The RF bias with the maximal power of 2000 W

was applied in CC800/7 for 85 min. During the deposition, the bias voltage and the substrate temperature were 125 V and 450 °C. The thicknesses of the coatings were around 4 μm and a 2-fold rotation was used during the sputtering.

The growth defects integrated into the hard coating were studied after the corrosion test. The corrosion experiment was performed in a 0.1 M chloride solution at pH = 6.8 using a PARSTAT 2263 device for electrochemical impedance spectroscopy. The immersion time was 24 h. The defect morphology and the distribution of defects were studied with field emission scanning electron microscopy (SIRION NC400, FEI).

The focused ion beam (SEM-FIB) installed in a conventional scanning electron microscope (QUANTA 200 3D, FEI) was used to prepare different cross-sections through the defect. The primary opening (required for further observations of cross-sections) with the dimensions of 20 μm × 10 μm × 10 μm was ion milled with a 20-nA beam current, while the acceleration voltage of ions was 30 kV. Then the cross-sectioning was executed with the medium-high beam current (5 nA). The next step was polishing, which was divided into two stages. First, there was rough polishing with a 3-nA beam current and an exposure time of around 3 min, while the second one was fine polishing with a 1-nA beam current for another 3 min. At the end of the polishing, the specimen was tilted and an image of the cross-section was taken using low ion-beam current (10 pA). After the image acquisition the next slice of sample, with the thickness of about 1 μm, was removed by ion milling. The image of the new cross-section was acquired again by ions. This method was repeated until the entire area of the defect was examined.

The SEM-FIB cross-section images were put together into a 3D-image of the defect with the Avizo Fire 6.3 software. First, the images were imported into the software, where the voxel size and the slice thickness were defined. Then the images were arranged and aligned in such a way that a pixel of any picture represents the same site of interest on all the images. After that the voxel was cropped to a volume which contained only the defect, the coating and the part of the substrate, where pitting corrosion took place. All the images were then labeled. During the next step, several algorithms (resampling, surface generation and smoothing) were used for the 3D-image processing. Finally, a 3D-reconstruction was performed utilizing the same software[6].

3 RESULTS AND DISCUSSION

A corrosion test of TiAlN on a D2 substrate, using electrochemical spectroscopy, was carried out in a chloride medium. After that a characterization of defects was performed.

As a very useful tool for cutting and examining internal structure of defects, we applied focused-ion-beam milling. We prepared cross-sections through the growth defects by ion-beam milling (**Figures 1** and **2**). After several cuts of different defects we found out that with a non-destructive top-view examination (SEM, LM) it is almost impossible to determine which defect can cause pitting corrosion, because we cannot observe if there is any direct diffusion path (pin holes, crevices, columnar grain boundaries) through the coating that enables a corrosion attack on the substrate[4,7].

To reveal the problem we analyzed two typical defects. **Figure 1** shows a crater that was formed in the TiAlN coating on the D2 tool steel, while **Figure 2** displays a spherical droplet on the same substrate. From these two images it is difficult to conclude that corrosion

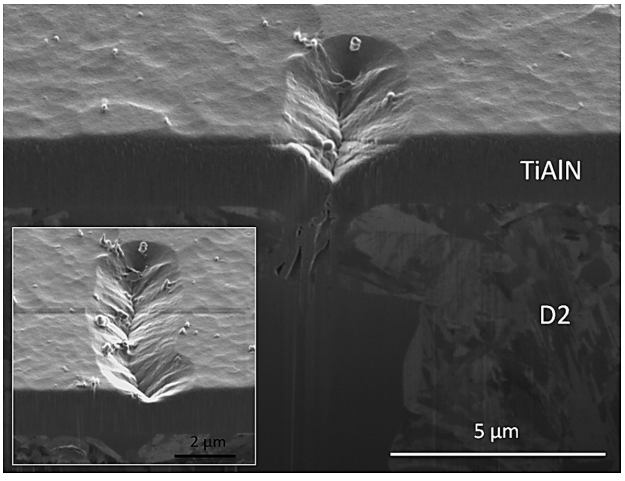

Figure 1: SEM image and FIB cross-sectional micrograph of the same growth defect (crater) on a sample TiAlN/D2 tool steel

Slika 1: SEM- in FIB-slika prereza defekta (kraterja) na vzorcu TiAlN/D2 orodnega jekla

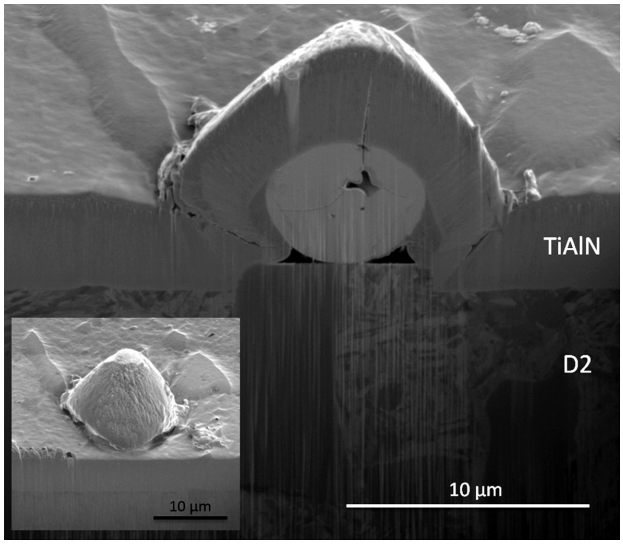

Figure 2: SEM-micrograph and an FIB cross-section image of a spherical droplet on a sample TiAlN/D2 tool steel

Slika 2: SEM- in FIB-slika prereza sferične kapljice na vzorcu TiAlN/D2 orodnega jekla

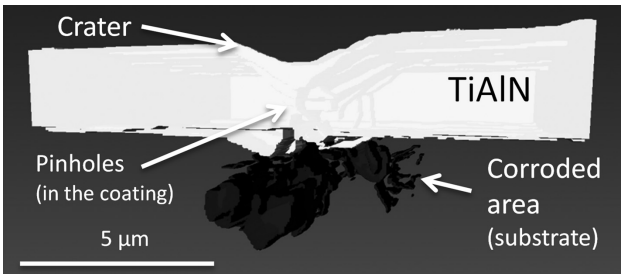

Figure 3: 3D reconstruction of a corrosion volume under a TiAlN coating on a site where a crater with pin holes was present
Slika 3: 3D-rekonstrukcija korodiranega območja pod TiAlN-prevleko na mestu, kjer se je nahajal krater s "pinholi"

took place, but when we continue with a series of slices, we can realize that the crater extends through the whole coating and originates in a small hole on the surface of the D2 tool steel (**Figure 1**). It is known that PVD processes have a poor ability to cover small pits or holes with a low aspect ratio (where depth is similar to their width) due to the shadowing effect.

Spherical droplets (**Figure 2**) are created as a result of arcing. The arc tendency during the deposition or etching cycles is increased with impurities on substrates, shields, fixtures, turntables and targets. Arcs are the origin of microdroplet formation. Some of these microdroplets can be incorporated into the coating during its growth or deposit on the surface of the substrate.

In our case a microdroplet was deposited on the surface of the substrate material during etching or at the beginning of the deposition cycle (**Figure 2**). This conclusion can be confirmed by the fact that the droplet is in contact with the uncoated surface and that the substrate surface under the droplet is untreated by ion etching due to the shadowing effect (the step on the surface).

Figure 2 shows that the region under the spherical droplet is not completely filled with coating due to the shadowing effect. Unexpectedly, the corrosion did not occur under it. After a detailed FIB analysis we recognized that pitting corrosion did not appear because there were no pin holes or porosities that could allow the solution to penetrate into the substrate. However, it is necessary to point out that corrosion was found under the other examined spherical droplets due to the existing pin holes.

The 3D image clearly shows that under the crater a pin hole extends through the entire thickness of the coating (**Figure 3**). It is known that corrosion takes place on the spots, where the solution can directly reach the substrate. Black pits on the image represent the corroded volume of the substrate. The calculated volume of the corroded area is surprisingly large (around 23 µm^3), while the volume of the crater is approximately two times smaller (12 µm^3). The corrosion products had a depth of 5 µm in the base material. On the spots where the corrosion has occurred, the substrate cannot provide

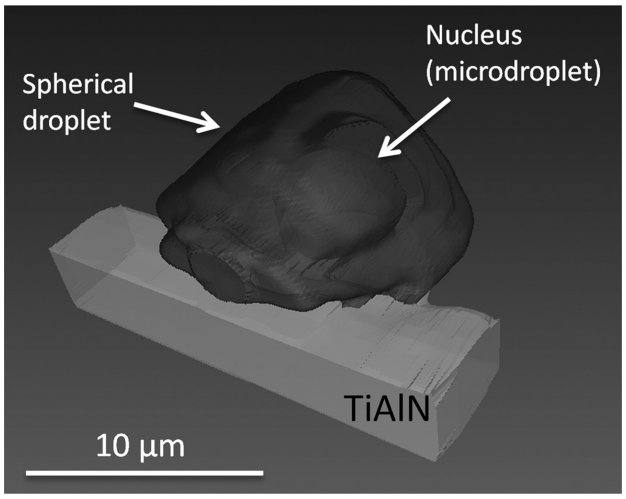

Figure 4: 3D-transparent image of a spherical droplet
Slika 4: 3D-transparentna slika sferične kapljice

sufficient support to the coating, so it can be damaged easily.

A 3D rendering of a spherical droplet without a nucleus (microdroplet) is shown in **Figure 4**.

4 CONCLUSION

Growth defects (large and shallow craters or cone structures due to the inclusion in the middle of a dense coating layer) do not always present a break point for the corrosion resistance. We found that small pits on the substrate surface and growth defects lead to the formation of pin holes. It is well known that pin holes cause pitting corrosion.

Selected pits were analyzed by FIB in combination with SEM. In this way we obtained an insight into the pitting-corrosion process.

We can conclude that 3D imaging and analyzing provide new insights in understanding the growth-defect formation as well as its influence on the corrosion processes, which will help us solve challenging problems regarding the extension of the coating/substrate-system life time.

Acknowledgement

This work was supported by the Slovenian Research Agency, ARRS (project L2-2100). Special thanks go to the company VSG for the free Avizo Fire 6.3 software.

5 REFERENCES

[1] P. Panjan, D. Kek-Merl, F. Zupanič, M. Čekada, M. Panjan, Surf. Coat. Technol., 202 (**2008**) 11, 143
[2] M. Čekada, P. Panjan, D. Kek-Merl, M. Panjan, G. Kapun, Vacuum, 82 (**2008**) 2, 252
[3] D. B. Lewis, S. J. Creasey, C. Wüstefeld, A. P. Ehiasarian, P. Eh. Hovespian, Thin Solid Films, 503 (**2006**), 143

[4] H. A. Jehn, Surf. Coat. Technol., 125 (**2000**), 212
[5] J. Vetter, M. Stuber, S. Ulrich, Surf. Coat. Technol., 168 (**2003**), 169
[6] J. Ohser, K. Schladitz, 3D Images of Materials Structures – Processing and Analysis, Wiley, 2009
[7] S. H. Tsai, J. G. Duh, Journal of The Electrochemical Society, 157 (**2010**) 5, 89

UDK 539.374:620.186
Original scientific article/Izvirni znanstveni članek

ISSN 1580-2949
MTAEC9, 46(4)355(2012)

DIGITAL IMAGING ANALYSIS OF MICROSTRUCTURES AS A TOOL TO IDENTIFY LOCAL PLASTIC DEFORMATION

DIGITALNA ANALIZA POSNETKOV MIKROSTRUKTUR KOT ORODJE ZA UGOTAVLJANJE LOKALNE PLASTIČNE DEFORMACIJE

Marjan Suban, Robert Cvelbar, Borut Bundara

Institute of metal constructions, Mencingerjeva 7, 1001 Ljubljana, Slovenia
marjan.suban@imk.si

Prejem rokopisa – received: 2011-10-25; sprejem za objavo – accepted for publication: 2012-03-22

This paper presents a methodology to detect plastic deformation at the micro level. The analysis is based on the statistical data describing the morphological and crystallographic textures of a sample microstructure. This data was obtained from optical microscopy using a digital imaging analysis. The important parameters necessary to describe the microstructure were identified as the grain-size and grain-orientation distributions. A change in the weighted product of these two parameters, the grain size as the area of grains and the grain orientation as the moment of inertia of grains, can represent a measure to identify plastic deformation on a small area. A demonstration of its applicability was performed on a real object as part of a ruptured-pipe-failure analysis in a thermal-power-plant boiler. The presented analysis leads to a fast identification of the local plastic deformation and, in the case of periodical analysis of the same sample, it can even be used as a measure to identify creeping.

Keywords: digital imaging analysis, plastic deformation, grain orientation, local-deformation analysis

V prispevku je predstavljena metodologija za odkrivanje plastične deformacije na mikroravni. Metoda temelji na podlagi statističnih podatkov, ki opisujejo morfološke in kristalografske teksture mikrostrukture. Vir podatkov je digitalna analiza posnetkov, pridobljenih iz optične mikroskopije. Kot pomembna parametra, potrebna za opis mikrostrukture, sta opredeljena distribucija velikosti zrn in usmerjenosti zrn. Sprememba tehtanega zmnožka teh dveh parametrov: velikosti zrna kot površine zrna in usmerjenosti zrna kot vztrajnostni moment zrna, je lahko merilo za identifikacijo plastičnih deformacij na majhnem področju. Za prikaz uporabnosti metode je bila izvedena analiza na realnem objektu kot del analize poškodb počene cevi v kotlu termoelektrarne. Predstavljena analiza omogoča hitro identifikacijo lokalne plastične deformacije, pri časovno zaporedni analizi istega vzorca pa se lahko celo uporablja za identifikacijo lezenja.

Ključne besede: digitalna analiza posnetkov, plastična deformacija, orientacija kristalnega zrna, analiza lokalne deformacije

1 INTRODUCTION

The quantification of a material microstructure is important for an evaluation of a material and some of its properties. Many properties of the material are strongly influenced by the size and shape of the grains. Observations of the changes in the geometric features of the grains may be quantified by an image analysis. Microscopy is a powerful non-invasive tool for studying a material microstructure, especially if complemented with an image analysis.

The paper presents the possibilities of evaluating plastic deformation based on microstructural grain layouts. Contrary to the other researchers' work, our methodology of identifying the grain shape and evaluating their orientation is based on the moments of inertia of individual grains. When a load is applied to a material, it will cause the material to change its shape. The observed effects of the deformation process on the material's microstructure using optical microscopy[1] can be evidently seen on **Figure 1**. The changes in the microstructure can be easily described for the grain level by using three parameters: the change in the grain area, the shape (elongation) and the orientation. The new proposed methodology for evaluating these three parameters is presented in the following sections.

1.1 Digital imaging

There are many imaging techniques available for viewing a microstructure in 2D and thus useful for collecting images of each cross section. These imaging methods include the techniques like secondary electron (SE), back-scattered electron (BSE), ion-induced secondary electron (ISE) and electron back-scatter diffraction[2] (EBSD) (**Figure 2**). While each method generates an image in 2D, important issues are to be discussed with regard to some of the techniques[3].

Many laboratories are unfortunately limited to the use of the optical microscopy as an essential and the only available method for evaluating microstructures. If grain boundaries are very clearly defined, the computer programs can be written in such a way that they allow higher-dimensional measurements (the area and shape measurements) recorded on digital images, but often many grain boundaries are hard to distinguish. The

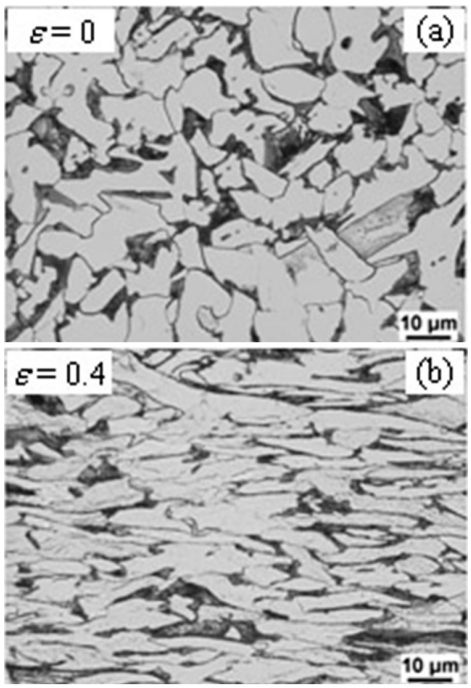

Figure 1: Microstructures of the C-Mn steel: a) the initial state; b) the microstructure after a deformation[1]
Slika 1: Mikrostruktura C-Mn-jekla: a) začetno stanje; b) mikrostruktura po deformaciji[1]

current state of the optical recognition software offers many tools to improve image resolutions, so that grain boundaries can be easily recognized.

1.2 Quantitative characterization

The quantitative characterization is an obvious tool for the researchers to use when attempting to establish a relationship between a microstructure and its properties. As a result of many studies numerous different methods and rules have been developed. In reality the application of the characterization greatly dictates the nature of the measurement technique chosen. Often the measurements are performed only in 2D using optical microscopy and digital imaging. In order to maximize the value of the data, microstructural quantification should be designed effectively. Almost an infinite number of parameters and correlations can be used to describe a microstructure, but just some of these parameters are actually important.

The measurement of the grain size is the most used method of all the techniques for quantifying the microstructural features. It is known that the grain size of a polycrystalline material is extremely important for determining its properties. Various properties exhibit a correlation with the grain size, such as: yield stress, ductility, and hardness[4]. Generally, the grain size is measured as an average scalar value, such as the intercept length, the grain area or the grain volume[5].

1.3 Grain shape and the principal-axis orientation

The shape of grains is likely to be of major significance in a number of applications, but irregular geometries of the grains in a polycrystalline microstructure make the grain shape a difficult parameter to quantify. The difficulty lies in the need for the data to express the true grain shape. Usually a number of simplifying assumptions are made.

Like the calculation of the grain size, the determination of the grain shape has been greatly aided by the EBSD maps. The boundaries of each grain can be clearly found and measured by identifying the local changes in the orientation. A problem may occur when two neighboring grains have the same orientation. The image analyzer can consider these two grains as one grain and that can lead to an error in determining the grain size and its shape. The difference between quantifying a grain shape and a grain size is related to the inability to clearly describe the shape. Determining a grain area is a relatively straightforward measurement yielding a scalar value, while a shape really needs to be described by the local curvatures, which is more complicated and requires higher-order mathematical descriptors. It is most common in everyday work to use simple objects to describe a shape, such as an ellipse. In this case, a

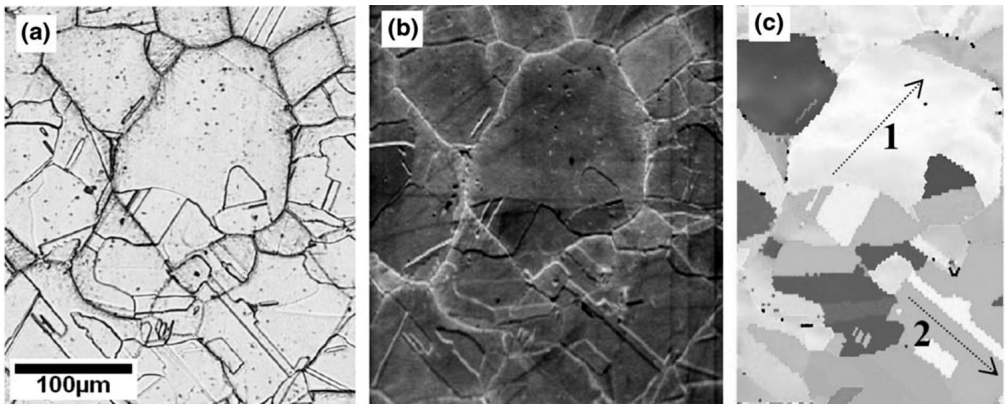

Figure 2: Analysis of the microstructure with: a) optical microscopy, b) secondary electron microscopy image, c) EBSD[3]
Slika 2: Analiza mikrostrukture: a) optična mikroskopija, b) SEM, c) EBSD[3]

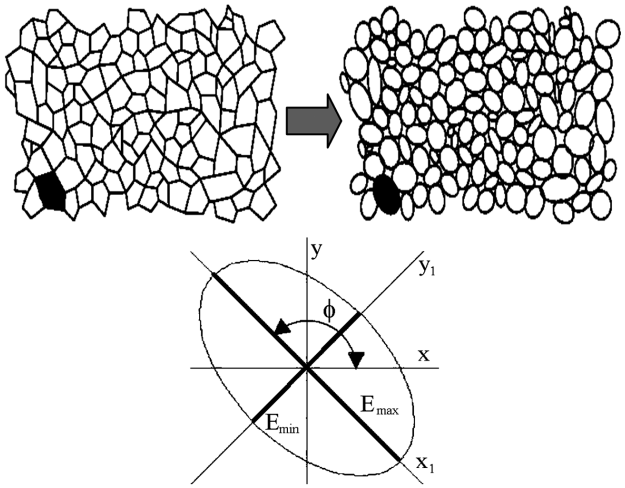

Figure 3: Schematic representation of the grains approximation with the equivalent ellipse

Slika 3: Shematski prikaz aproksimacije kristalnega zrna z njemu enakovredno elipso

quantification of the grain shape is done with the calculation of the length of an equivalent ellipse major E_{max} and minor axis E_{min}, where the area of a grain is equivalent to the area of the approximated ellipse. The ratio of the minor axis of the equivalent ellipse to its major axis represents the measure for grain roundness. The roundness is a measurement of the length – width relationship, with a value in the range from 0 to 1. A perfect round grain has a roundness of 1, while a very narrow, elongated grain has a roundness of about 0.

In addition, many shape descriptors involve combining groups of size parameters to generate dimensionless values like length/width (aspect ratio), area/convex area (solidity) and length/fiber length (curl)[6], which can sometimes be ambiguous. Some scalar parameters, such as the moments of inertia, can do an adequate, or a better, job of expressing the grain shape and orientation.

The principal-axes orientation quantifies the orientation of the grains' principal axes relative to the global coordinate system of the cross section. It is important to distinguish between the principal-axes orientation, which is the orientation referring to the principal axes and the crystal-lattice (crystallographic) orientation, which is usually determined with EBSD. In the case of an ellipse, the orientation is presented as angle ϕ measured counterclockwise from the horizontal axis x to the axis of lowest moment of inertia x_1, as shown on **Figure 3**.

2 METHODOLOGY

Generally, the microstructure images suffer from the defects of improper illumination, artifacts and noise that are developed at the time of the sample preparation. The first stage is important for attaining higher grain-segmentation accuracy. An RGB microstructure image was processed using the tools of digital imaging with the final goal to achieve an image without any noise, showing a set of individual grains and excluding the border grains. This is also the most important step for analyzing the differentiation between individual grains in the microstructure. If the grains are not clearly distinguished then the next steps of the methodology are purposeless. An application called the Particle Analysis, or the Blob Analysis, in the National Instruments IMAQ Vision software was used for digital imaging and calculating. The blob analysis is the process of detecting and analyzing distinct two-dimensional shapes within a region of the image. It can provide information about the number of grains, location, shape, area, perimeter, and the orientation of grains.

One of main results provided by the analyzing software is the moment of inertia, or the second moment of area, which is a property of a cross section and can be used to predict the resistance of the cross-section areas to the bending and deflection around an axis lying in the cross-sectional plane. The moments of inertia for any cross section defined as a simple polygon on the $x - y$ plane can be computed in a generic way by summing the contributions from each segment of the polygon. The equations marked as 1, 2 and 3 can be used to calculate the moments of inertia, where the parameters x_i and y_i represent the distance from the origin to the elementary triangle center point and a_i represents the area of this triangle.

$$I_x = \frac{1}{12}\sum_{i=1}^{n-1}\left(y_i^2 + y_i y_{i+1} + y_{i+1}^2\right)a_i \tag{1}$$

$$I_y = \frac{1}{12}\sum_{i=1}^{n-1}\left(x_i^2 + x_i x_{i+1} + x_{i+1}^2\right)a_i \tag{2}$$

$$I_{xy} = \frac{1}{24}\sum_{i=1}^{n-1}\left(x_i y_{i+1} + 2x_i y_i + 2x_{i+1} y_{i+1} + x_{i+1} y_i\right)a_i \tag{3}$$

From these values that represent the moment of inertia for the $x - y$ axis, the moments of inertia for the principal axis $x_1 - y_1$ can be calculated (for the axis presentation see **Figure 3**).

$$I_{x1,y1} = \frac{I_x + I_y}{2} \pm \sqrt{\left(\frac{I_x - I_y}{2}\right)^2 + I_{xy}^2} \tag{4}$$

In this case I_{x1} represents the minimum eigenvalue of the moment of inertia, while I_{y1} is the maximum value. The roundness of a grain can then be calculated using the ratio of these two values and it ranges from 0 (an extremely elongated grain) to 1 (a round grain).

$$R = \frac{I_{x1}}{I_{y1}} \tag{5}$$

The angle of the rotation of the coordinate system around the grain center of mass ϕ can be calculated using Eq. 6. It is used as a parameter to quantify the orientation of an individual grain. A correction of angle ϕ is needed to transform the angle range from 0–180° to

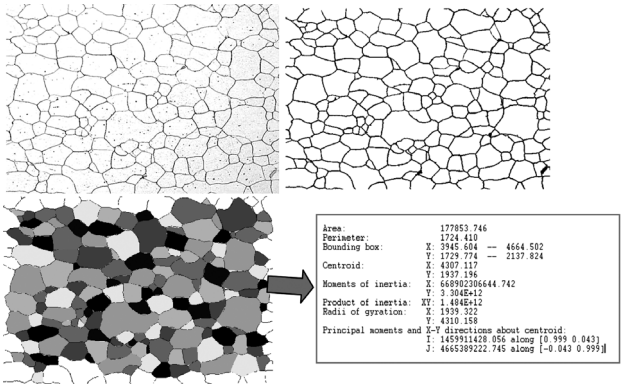

Figure 4: Schematic representation of the steps of digital imaging and the calculated result for one grain

Slika 4: Shematski prikaz faz digitalne obdelave posnetkov in rezultat izračuna za eno kristalno zrno

0–90° (e.g., the grain orientation for the angle of 1° is almost equal to the one for the angle of 179°).

$$\phi = \frac{1}{2}\operatorname{atan}\frac{2I_{xy}}{I_x - I_y} \tag{6}$$

3 EXPERIMENTAL RESULTS AND DISCUSSION

For the experimentation we have used many microstructure images of low-carbon and austenitic stainless steel at various resolutions (i.e., magnifications) and with different grain shapes. These images were obtained with optical microscopy. An example of a microstructure image (500-times) of the austenitic stainless steel and the steps of digital imaging are shown in **Figure 4**.

On the left-hand side of **Figure 5** the results for the examined sample from Figure 4 are shown. From the graph it can be concluded that the roundness of the grains in the microstructure is around 0.46 and that the median of the grain-orientation angle is approximately 15°, while the average value is 21°. In short, it can be said, that the grains are elongated in the direction close to the horizontal axis.

The results presented on the right-hand side of **Figure 5** show a comparison between the roundness calculated by using the ratio of the equivalent-ellipse axis and the roundness calculated by using the ratio of the moment of inertia for the principal axis. It is observed that the latter is much more sensitive to the grain shape then the former. The range of the calculated results is also much wider, which is a more authentic description of the real state.

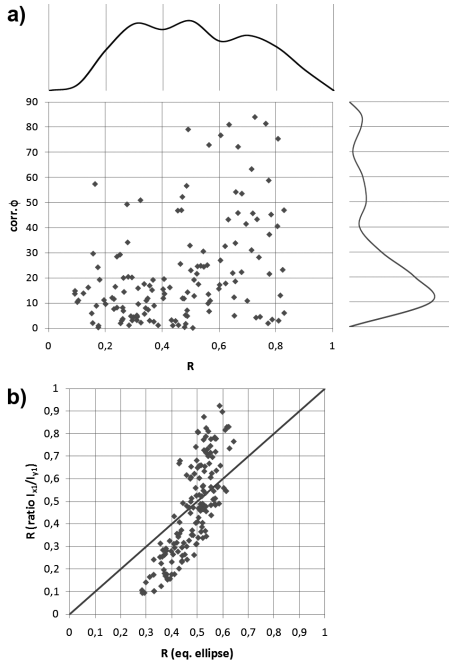

Figure 5: a) Correlation between the roundness and the orientation angle ϕ and b) the correlation between different calculations of the roundness

Slika 5: a) Korelacija med okroglostjo in kotom usmerjenosti ϕ in b) korelacija med različnima metodama izračuna okroglosti

4 CASE STUDY

For the practical demonstration, two samples taken from the ruptured steam pipe, marked as No. 2 and No. 4 (200-times), were analyzed using the above-described methodology. The average value of the roundness calculated by using Eq. 5 for sample No. 4 is 0.4, while it is 0.36 for sample No. 2. As it can be seen from **Figure 6**, the grains are more elongated in the case of sample No. 4 than in the other case. A similar difference can also be found when observing the grain-orientation angles. The grain-orientation angle distribution for sample No. 4 is

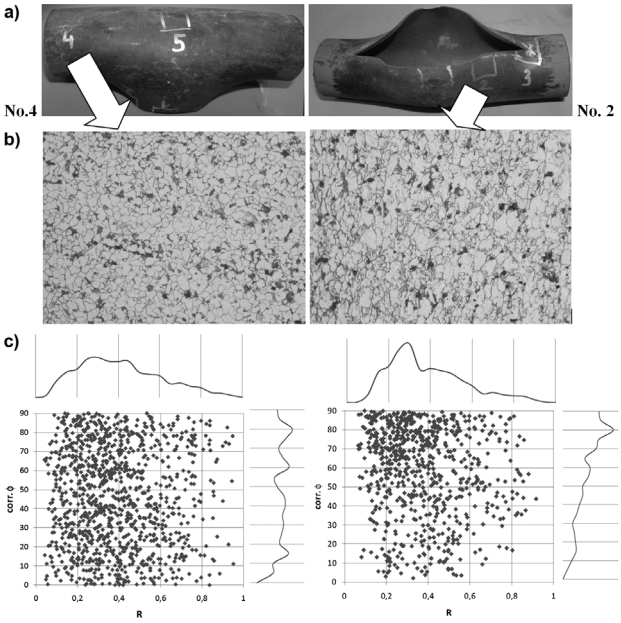

Figure 6: a) Positions of samples No. 4 (left) and 2 (right) of the ruptured steam pipe, b) the corresponding microstructures and c) the results of the analysis

Slika 6: a) Položaj vzorcev št. 4 (levo) in 2 (desno) na počeni cevi parnega kotla, b) pripadajoči mikrostrukturi ter c) rezultati analize

almost flat and its median is 45°, which means that these grains have no orientation tendency. In the second case the median of the grain-orientation angle is 64°, while the average value is 59°. This can also be observed from the grains in the microstructure on the right-hand side of **Figure 6**.

5 CONCLUSIONS

In this paper, a semi-automatic, digital, microstructure-image-analysis system for quantifying a microstructure is developed. As an input in the analysis process, the image obtained with optical microscopy was used. In the calculation part of the investigation, the moment of inertia was introduced as the major parameter to quantify the grain shape and the orientation. The results obtained with the above method are reproducible and repeatable, but can be misleading if the differentiation between individual grains in the microstructure is not clear. We can demonstrate the accuracy and usefulness of this method by comparing the computed values with the results of the other methods. The presented case study of the sample of a ruptured steam pipe demonstrates its usefulness for the laboratory and industrial applications in the field of material investigations.

6 REFERENCES

[1] R. Song, D. Ponge, D. Raabe, Texture evolution of an ultrafine grained C-Mn steel and its evolution during warm deformation and annealing, Acta Materialia, 53 (**2005**) 18, 4881–4892

[2] S. Xia, B. Zhou, W. Chen, Grain Cluster Microstructure and Grain Boundary Character Distribution in Alloy 690, Metallurgical and materials transactions A, 40 (**2007**) 12, 3016–3030

[3] M. Groeber, Development of an automated characterization-representation framework for the modeling of polycrystalline materials in 3D, Dissertation, Ohio State University, 2007

[4] R. W. Armstrong, I. Codd, R. M. Douthwaite, N. J. Petch, Plastic Deformation of Polycrystalline Aggregates, Philosophical Magazine, 7 (**1962**), 45–58

[5] L. Ciupinski, B. Ralph, K. J. Kurzydlowski, Methods for the characterization of grain size, Materials Characterization, 38 (**1997**) 3, 177–185

[6] S. Ghosh, D. Dimiduk (Eds.), Computational Methods for Microstructure-Property Relationships, 1st Edition, Springer New York, 2011

UDK 669.18
Original scientific article/Izvirni znanstveni članek

ISSN 1580-2949
MTAEC9, 46(4)361(2012)

THERMODYNAMIC ANALYSIS OF THE FORMATION OF NON-METALLIC INCLUSIONS DURING THE PRODUCTION OF C45 STEEL

TERMODINAMIČNA ANALIZA NASTANKA NEKOVINSKIH VKLJUČKOV PRI IZDELAVI JEKLA C45

Luka Krajnc[1], Grega Klančnik[2], Primož Mrvar[2], Jožef Medved[2]

[1]Štore Steel, d. o. o., Železarska 3, 3220 Štore, Slovenia
[2]University of Ljubljana, Faculty of Natural Science and Engineering, Department for Materials and Metallurgy, Aškerčeva 12, 1000 Ljubljana, Slovenia
luka.krajnc@store-steel.si

Prejem rokopisa – received: 2011-11-11; sprejem za objavo – accepted for publication: 2012-03-01

C45 steel belongs to the group of carbon steels and is used in the normalized and tempered states for heavily stressed parts in the automobile industry. Nowadays, a major problem in steelmaking is non-metallic inclusions, which can form during various steps of the steelmaking process and are detrimental to the mechanical properties of the steel.
In scope of this work we have tried to determine during which steps of the steelmaking process the non-metallic inclusions are formed. Samples were taken from three different steps of the steelmaking process, i.e., from the electric arc furnace, from the ladle furnace and from the tundish. The samples were then chemically analysed. The results were used for a thermodynamic simulation with Thermo-Calc. Other samples were prepared from another simultaneously taken probe and were partly subjected to differential scanning calorimetry (DSC) and partly metallographically prepared. Photographs were taken with a light microscope, from which the phase composition was calculated. The non-metallic inclusions in our samples were analysed with EDS – photographs were taken and point and mapping analyses were made on them.
We found that in our C45 steel sample, spinel ($MgO \cdot Al_2O_3$) and aluminate (Al_2O_3) inclusions can be found at the end of the ladle-furnace treatment. In the tundish sample only small aluminate and spinel inclusions and a lot of MnS inclusions were found.

Keywords: non-metallic inclusions, thermodynamics, C45 steel

Jeklo C45 je ogljikovo jeklo, ki se v normaliziranem in poboljšanem stanju uporablja za obremenjene dele v avtomobilski industriji. Slabše mehanske lastnosti in krajša uporabna doba pa so predvsem povezane z nekovinskimi vključki. Le-ti lahko nastanejo pri različnih stopnjah procesa izdelave jekla.
V okviru tega dela smo poskušali ugotoviti, pri katerih stopnjah procesa izdelave jekla nastanejo nekovinski vključki. V ta namen smo vzeli vzorce pri treh stopnjah izdelave jekla: na elektroobločni peči, na ponovčni peči in iz vmesne ponovce na napravi za kontinuirno litje jekla. Naredili smo kemično analizo vzorcev, ki smo jo uporabili za termodinamični ravnotežni izračun s programskim orodjem Thermo-Calc. Vzorce smo razrezali in naredili diferenčno vrstično kalorimetrijo (DSC), metalografsko pripravljene vzorce pa smo slikali s svetlobnim mikroskopom. Za kvalitativno metalografsko analizo smo uporabili program analySIS 5.0 in z njim ugotovili delež mikrostrukturnih sestavin. Vzorce smo pregledali in slikali še z vrstičnim elektronskim mikroskopom, naredili smo tudi točkovno analizo vključkov in določili porazdelitev elementov glede na površino.
Ugotovili smo, da so se v našem vzorcu jekla C45 pojavljali pri koncu obdelave na ponovčni peči špinelni ($MgO \cdot Al_2O_3$) in aluminatni (Al_2O_3) vključki, ki so neželeni, trdi in krhki vključki. Pri litju jekla na napravi za kontinuirno litje so se v našem vzorcu v jeklu pojavljali le majhni špinelni in aluminatni vključki, videli pa smo mnogo MnS-vključkov.

Ključne besede: nekovinski vključki, termodinamika, jeklo C45

1 INTRODUCTION

With the advances in technology, with the introduction of new secondary-steelmaking processes and with the increasingly higher quality demands from buyers, there has been, especially in recent years, a greater demand for better mechanical properties from steel. This can only be guaranteed, however, if we can control the quantity, size and distribution of the non-metallic inclusions in the steel.

The non-metallic inclusions in steel are formed from metal elements, such as iron, manganese, silicon, aluminium and calcium and non-metal elements such as oxygen, sulphur, nitrogen and phosphor. The non-metallic inclusions are divided in two groups, i.e., external and internal. The external inclusions are formed because the melt is in contact with slag and refractory and some parts of these two can be caught in the melt. These inclusions are large, with an irregular shape and they are detrimental to the mechanical properties of the steel. Internal inclusions, on the other hand, are formed with chemical reactions between the melt, slag and refractory. These are, in general, smaller. The biggest problem comes from hard and brittle oxide inclusions[1,2].

In the scope of this work we have focused our attention on the inclusions that are formed during the de-oxidation process with aluminium, on the modification of alumina inclusions and on the formation of spinel-type inclusions.

Steel can, after oxygen rafination, have as much as 0.1 % mass fractions of oxygen; therefore, it is essential

to have the steel deoxidized[3]. To achieve this we add different materials with a high affinity for oxygen, such as aluminium, silicon, etc. The process of de-oxidation is based on the following chemical reaction[4]:

$$x\,[\mathrm{Me}] + y\,[\mathrm{O}] = (\mathrm{Me}_x\mathrm{O}_y)^{\mathrm{slag}} \quad (1)$$

where [Me] is the dissolved metal in the liquid steel, [O] is the dissolved oxygen in the liquid steel and (Me_xO_y) is the product of the reaction, an inclusion which is reduced to slag.

Aluminium forms with oxygen alumina (Al_2O_3) inclusions, which are large, hard and brittle and are detrimental to the mechanical properties of the steel. Furthermore, they have a negative effect on the castability of the steel, because they clog the nozzles from the tundish in the continuous casting machine. With aluminium de-oxidized steel the addition of calcium modifies the alumina inclusions. The results of this reaction are calcium alumina inclusions ($CaO \cdot Al_2O_3$), which have a globular shape and their melting point is lower than the melting point of the steel[5]. They are normally larger than non-modified inclusions, however, and it is therefore essential that they are removed into the slag. Studies have shown that when we add too much calcium and the concentration of sulphur is high enough, inclusions of calcium sulphide (CaS) are formed, which also has a negative influence on the steel's castability. Thus it is important to add the correct amount of calcium to the steel, to be within the calcium concentration range, when most of the alumina inclusions are modified and the calcium content is not high enough for the CaS inclusions to form[6].

1.1 The formation of spinel phase

After de-oxidation and the formation of alumina inclusions, aluminium has a high activity as an element, because of the higher concentration in the steel and can reduce magnesium oxide from magnesite refractory and slag[7]. Magnesium forms with oxygen magnesite (MgO) inclusions. The increase in the concentration of MgO and Al_2O_3 increases the driving force for the formation of spinel-type inclusions in the calcium alumosilicate inclusion systems. Spinel-type crystals can grow almost as large as crystals of base calcium silicate.

This theory, which was suggested by Park *et al.*[8], shows the formation of spinel-type inclusions in large $CaO\text{-}SiO_2\text{-}MgO\text{-}Al_2O_3$-type inclusions with a low concentration of oxygen during the transportation of the melt from the ladle furnace to the continuous casting machine.

Another theory about the formation of spinel-type inclusions, which was suggested by Jiang *et al.*[9], shows us a different mechanism. As a result of de-oxidation alumina inclusions are formed. During the reaction between the melt, slag and refractory the magnesium is reduced from the slag or refractory:

$$2[\mathrm{Al}] + 3(\mathrm{MgO})^{\mathrm{slag\ or\ refractory}} = 3[\mathrm{Mg}] + (\mathrm{Al_2O_3}) \quad (2)$$

Before the addition of calcium for modifying the alumina inclusion, the activity of magnesium is higher than that of calcium, and therefore $MgO \cdot Al_2O_3$ and MgO inclusions are formed:

$$3[\mathrm{Mg}] + 4(\mathrm{Al_2O_3}) = 3(\mathrm{MgO} \cdot \mathrm{Al_2O_3})^{\mathrm{inclusion}} + 2[\mathrm{Al}] \quad (3)$$

$$[\mathrm{Mg}] + [\mathrm{O}] = (\mathrm{MgO})^{\mathrm{inclusion}} \quad (4)$$

After the treatment in the ladle furnace and after the addition of calcium, its activity is increased and the $CaO{\cdot}MgO \cdot Al_2O_3$ inclusions are formed:

$$4[\mathrm{Ca}] + 5(\mathrm{MgO} \cdot \mathrm{Al_2O_3})^{\mathrm{inclusion}} = 4(\mathrm{CaO} \cdot \mathrm{MgO} \cdot \mathrm{Al_2O_3})^{\mathrm{inclusion}} + [\mathrm{Mg}] \quad (5)$$

The purpose of this work was to find out which inclusions are formed in C45 steel and at what point in the steelmaking process they are formed. The study was made on C45 steel as a typical representative of the steel used for heavily stressed parts in the automobile industry.

2 EXPERIMENTAL

Samples of carbon C45 steel were taken at the company Štore Steel, d. o. o. Six samples were taken in all: the first one from the electric arc furnace, the next four from the ladle furnace and the final one from the tundish on the continuous casting machine. For the sampling we used the Sample-on-Line method or the Lollipop-Sampling method. The samples were taken at the same time as the samples for the company and they were marked from 1 to 6.

In Štore Steel, d. o. o., the chemical analysis was made on samples that were taken in parallel with our samples. Optical emission spectroscopy was used with the instrument, made by Spectro, LAVMC12A. The samples taken for further analysis were first cut, and then the smaller part was prepared for simultaneous thermal analysis (STA), while the larger part was used for the metallographic analysis, as shown in **Figure 1**. The chemical analysis of the slag was performed using a standard chemical analysis.

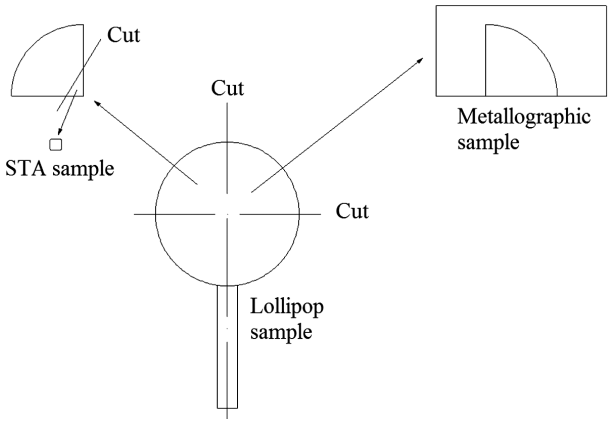

Figure 1: Cutting and preparing the samples
Slika 1: Razrez in priprava vzorcev

The characteristic temperatures were determined with a simultaneous thermal analysis (STA), which was made on a Jupiter 449c from NETSCH. For the reference an empty corundum crucible was used. The measurements were made using a dynamic argon flow.

The thermodynamic predictions were performed with Thermo-Calc TCW5 for the prediction of the solidification. The calculations were made using the TCFE3, SSUB3 and SLAG1 databases.

The metallographic analysis was made using a scanning electron microscope JEOL JSM – 5610, equipped with energy-dispersive spectroscopy (EDS). The light microscopy was made using OLYMPUS SZ61 and OLYMPUS BX61 microscopes. Finally, the micrographs were processed with the Analysis 5.0 computer program.

3 RESULTS AND DISCUSION

3.1 Chemical composition

The chemical composition of the C45 steel samples is given in **Table 1**. The chemical composition of the slag sample, which was taken at the end of ladle furnace treatment, is given in **Table 2**.

3.2 Thermodynamic calculations

The isopletic phase diagrams were predicted with Thermo-Calc. The chemical composition was taken for the calculations as shown in **Table 1**. The following elements, C, Si, Mn, Cr, Al, Mo, Ni and Fe, were taken into account; however, oxygen was not taken into account. In **Figure 2** an example of a calculated isopletic phase diagram for iron – carbon is shown, for sample 6, taken from the tundish on the continuous casting machine, with the correct carbon content marked.

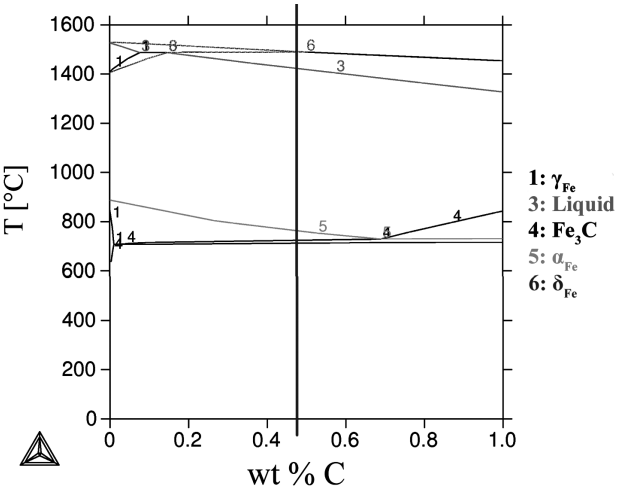

Figure 2: Isopletic phase diagram for iron–carbon for sample 6, with our carbon content marked
Slika 2: Navpični prerez faznega diagrama železo-ogljik za vzorec 6, z označeno vsebnostjo ogljika

In **Figure 3** the weight fraction of phases in dependence of the temperature is shown for sample 6, taken from the tundish on the continuous casting machine.

In **Figure 3**, in the sample taken from the tundish on the continuous casting machine, it is clear that initially a small fraction of δ-ferrite solidifies at 1490 °C, then the δ-ferrite begins its transformation into austenite at 1489 °C, and the rest of the melt begins to solidify at 1421 °C. At 761 °C the austenite begins its transformation into ferrite and later during the eutectoid phase transition into pearlite (α_{Fe} + Fe_3C). At lower temperatures the carbides precipitate from the austenitic matrix.

Table 1: Chemical composition of the C45 steel samples in mass fractions, *w*/%
Tabela 1: Kemijska sestava vzorcev jekla C45, *w*/%

Chemical element	C	Si	Mn	P	S	Cr	Mo	
Sample 1	0.13	0.03	0.13	0.011	0.036	0.11	0.04	
Sample 2	0.40	0.26	0.75	0.014	0.022	0.22	0.04	
Sample 3	0.47	0.28	0.75	0.014	0.017	0.24	0.04	
Sample 4	0.47	0.28	0.76	0.015	0.03	0.24	0.04	
Sample 5	0.47	0.27	0.75	0.014	0.027	0.24	0.04	
Sample 6	0.48	0.27	0.75	0.014	0.021	0.25	0.04	
Chemical element	Ni	Al	Cu	Sn	Ca	N	O	Fe
Sample 1	0.10	0.257	0.21	0.012	0.0004	0.007	0.0068	98.92
Sample 2	0.13	0.005	0.2	0.012	0.0004	0.008	0.0056	97.93
Sample 3	0.16	0.005	0.2	0.012	0.0005	0.008	0.0042	97.80
Sample 4	0.16	0.005	0.2	0.013	0.0003	0.007	0.0056	97.77
Sample 5	0.16	0.031	0.2	0.013	0.0003	0.008	0.0036	97.77
Sample 6	0.16	0.025	0.2	0.013	0.0001	0.008	0.0034	97.77

Table 2: Chemical composition of the slag sample
Tabela 2: Kemijska sestava vzorca žlindre

Chemical element	Si	Al	Fe	Mn	Ca	Mg	O
Content (*w*/%)	6.42	10.44	0.64	0.19	43.25	2.97	36.09

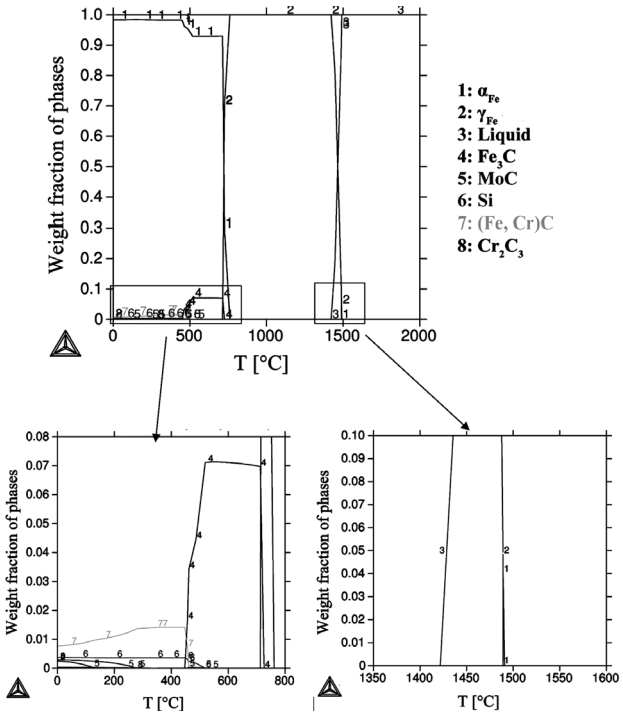

Figure 3: Weight fraction of phases in dependence of the temperature for sample 6
Slika 3: Masni delež faz v odvisnosti od temperature za vzorec 6

With Thermo-Calc it was calculated at which contents of magnesium and oxygen certain inclusions at 1550 °C are formed. Here, X represents the existence of inclusions inside the melt. The results are given in **Table 3**.

We can see that with small contents of oxygen, magnesite (MgO) inclusions are formed; with an increase of oxygen content, first the MgO inclusion and then also the spinel-type inclusions ($MgO \cdot Al_2O_3$) are formed. With the highest oxygen content the spinel-type inclusions and alumina inclusions are formed. The content of magnesium does not have an effect on the sequence of inclusion formation; it does, however, have an effect on when the inclusions are formed. At a magnesium content (in mass fractions, w) of $1 \cdot 10^{-3}$ % the first inclusions are formed at an oxygen content of $1 \cdot 10^{-5}$ %. At a magnesium content of $1 \cdot 10^{-4}$ % the first inclusions are already formed at an oxygen content of $1 \cdot 10^{-6}$ %.

With Thermo-Calc we have also analysed the slag, using the chemical composition presented in table 2. We found that at the temperatures at which the steel is in the molten state there are four different oxides in the molten or solidified state. $3CaO \cdot SiO_2$, MgO, $CaO \cdot Al_2O_3$ and $MgO \cdot Al_2O_3$ can be reduced to steel or they can first react with phases in the slag, steel, refractory or atmosphere and then be reduced to steel.

Table 3: Calculation of the possibility of inclusion formation at different contents of oxygen and magnesium
Tabela 3: Izračun možnosti nastanka vključka pri različnih vsebnostih kisika in magnezija

		Type of inclusion			Type of inclusion		
Sample 1	Content of oxygen (%)	Al(O,C)	Sample 2	Content of oxygen (%)	Spinel	MgO	Al_2O_3	mulite
Content of Mg is 0.001(%)	0.000001		Content of Mg is 0.001(%)	0.000001				
	0.00001	x		0.00001		x		
	0.0001	x		0.0001		x		
	0.001	x		0.001	x	x		
	0.0068	x		0.0056	x			x
Content of Mg is 0.0001(%)	0.000001		Content of Mg is 0.0001(%)	0.000001		x		
	0.00001	x		0.00001		x		
	0.0001	x		0.0001	x	x		
	0.001	x		0.001	x		x	
	0.0068	x		0.0056	x			x

		Type of inclusion					Type of inclusion		
Sample 5	Content of oxygen (%)	Spinel	MgO	Al_2O_3	Sample 6	Content of oxygen (%)	Spinel	MgO	Al_2O_3
Content of Mg is 0.001(%)	0.000001				Content of Mg is 0.001(%)	0.000001			
	0.00001		x			0.00001		x	
	0.0001		x			0.0001		x	
	0.001	x	x			0.001	x	x	
	0.0036	x		x		0.0036	x		x
Content of Mg is 0.0001(%)	0.000001		x		Content of Mg is 0.0001(%)	0.000001		x	
	0.00001		x			0.00001		x	
	0.0001	x	x			0.0001	x	x	
	0.001	x		x		0.001	x		x
	0.0036	x		x		0.0036	x		x

3.3 Differential scanning calorimetry

Differential scanning calorimetry was made for all the investigated samples. The rate of heating and cooling was 5 K/s. The results of the differential scanning calorimetry are DSC heating and cooling curves with determined characteristic points (solidus, liquidus) and enthalpies of fusion and solidification. We have taken a closer look at sample 6, and because it is the last sample taken from the melt it is the most representative as to which inclusions are still in the melt.

In **Figure 4** we can see a heating DSC curve for sample 6 and the process of melting. At 738.5 °C the ferrite and pearlite begin to transform to austenite. At 1401.8 °C the austenite begins to transform to δ-ferrite and to the melt, at 1509.7 °C δ-ferrite begins to melt, according to thermodynamic predictions.

In **Figure 5** we can see a cooling DSC curve for sample 6 and the process of solidifying. At 1392 °C the δ-ferrite begins to solidify and at 1383.3 °C the δ-ferrite and the melt begin to transform or solidify into austenite. At 861.8 °C the ferrite begins to segregate.

By comparing different DSC curves, we can see the difference in the characteristic temperatures and energies in more detail. In **Figure 6** is a comparison of the heating DSC curves in the temperature range from 670 °C to 850 °C, where the transformation of ferrite and pearlite to austenite occurs. The enthalpies necessary for the eutectoid phase transition are given in **Table 4**. We can see a

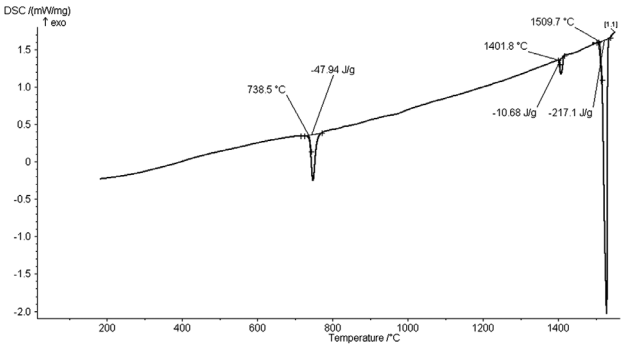

Figure 4: Heating DSC curve for sample 6
Slika 4: DSC krivulja pri segrevanju vzorca 6

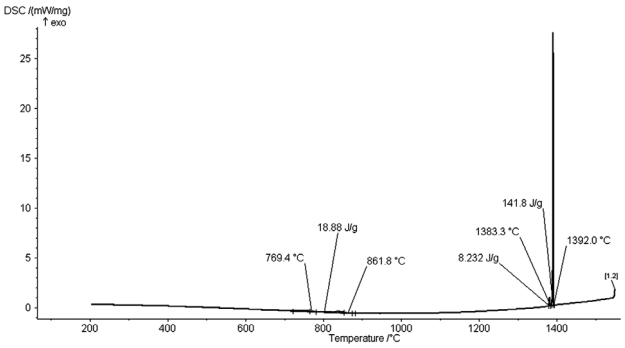

Figure 5: Cooling DSC curve for sample 6
Slika 5: DSC krivulja pri ohlajanju vzorca 6

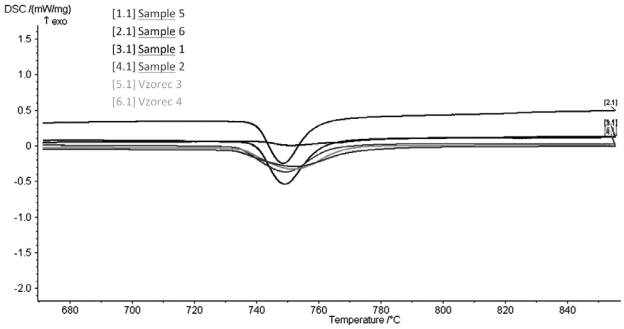

Figure 6: Enlarged comparison of the heating DSC curves for all 6 samples
Slika 6: Primerjava povečanih DSC krivulj segrevanja vseh 6 vzorcev

significant difference in sample 1; this is due to the fact that the eutectoid reaction is presented in a small manner. After the treatment on the ladle furnace the enthalpy is higher.

Table 4: The enthalpy necessary for eutectoid phase transition
Tabela 4: Entalpija, potrebna za eutektoidno fazno premeno

Sample	1	2	3	4	5	6
Energy (J/g)	3.18	35.29	38.61	38.16	47.38	47.94

In **Figure 7** we can see a comparison of the DSC curves in the temperature range from 530 °C to 1020 °C or during the eutectoid phase transition. In **Table 5** the enthalpies during the eutectoid phase transition are given. We can see a major difference between the samples 2 and 4 and the rest of the samples. This can be explained by the fact that with samples 2 and 4 the eutectoid phase transition occurs at a lower temperature than with the other samples and a certain part of the energy released is related to the magnetic phase transition, resulting in the determined enthalpy values.

Table 5: The enthalpy during the eutectoid phase transition
Tabela 5: Entalpija pri eutektoidni fazni premeni

Sample	1	2	3	4	5	6
Energy (J/g)	22.67	65.93	35.9	63.29	28.73	18.88

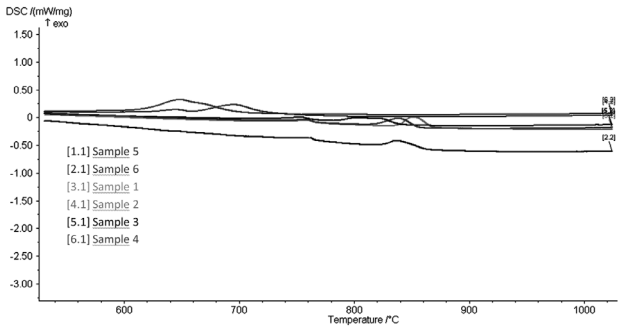

Figure 7: Enlarged comparison of the cooling DSC curves for all 6 samples
Slika 7: Primerjava povečanih DSC krivulj ohlajanja, za vseh 6 vzorcev

In general we can see that the heating DSC curves relate well to the microstructure of our samples. The calculated enthalpies necessary for the eutectoid phase transition and the calculated fraction of microstructural phases have a high correlation; this is a result of the fast cooling of the industrial samples. The cooling DSC curves, on the other hand, have a much better correlation with the phase diagrams calculated with Thermo-Calc because of a steady cooling rate.

3.4 Microstructure analysis

The microstructure of our samples can be seen in **Figure 8**. It has, with the exception of sample 1, a small fraction of ferrite (α_{Fe}) and a large fraction of pearlite (α_{Fe} + Fe_3C). Sample 1 has a small fraction of pearlite (α_{Fe} + Fe_3C) and a large fraction of ferrite (α_{Fe}). The precise fractions of the microstructural phases are shown in **Table 6**. These fractions were calculated at 200-times magnification.

Table 6: Fraction of microstructural phases for all samples.
Tabela 6: Delež faz v mikrostrukturi vseh vzorcev

Sample	1	2	3	4	5	6
Ferrite (%)	77.1	7.1	3.2	4.7	1.9	2.2
Pearlite (%)	22.9	92.9	96.8	95.3	98.1	97.8

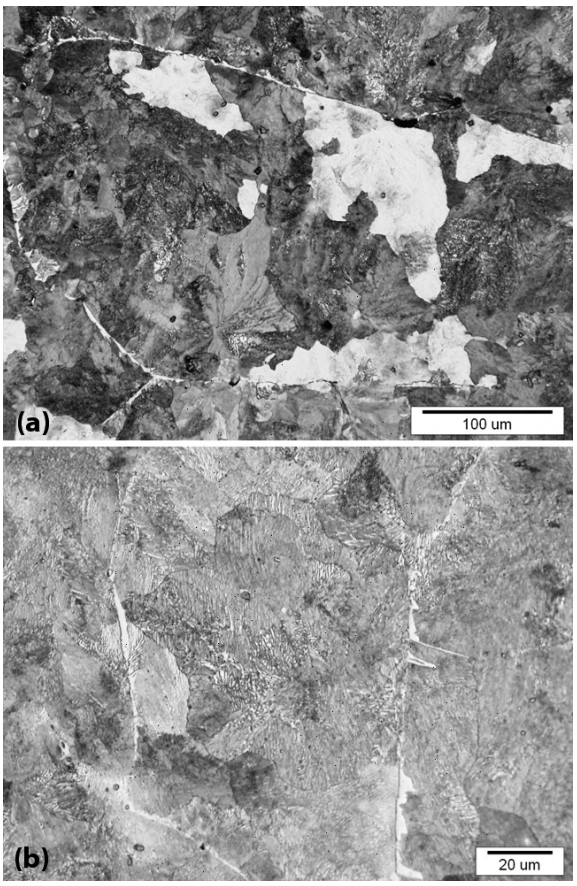

Figure 8: Microstructure: ferrite and pearlite; a) sample 5, b) sample 6
Slika 8: Mikrostruktura: ferit in perlit; a) vzorec 5, b) vzorec 6

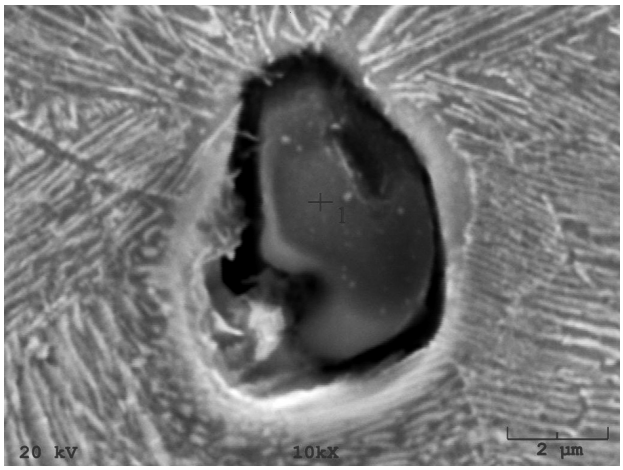

Figure 9: Alumina inclusion (Al_2O_3) and the place of the point analysis determined in sample 6
Slika 9: Vključki Al_2O_3 in mesto točkaste analize na vzorcu 6

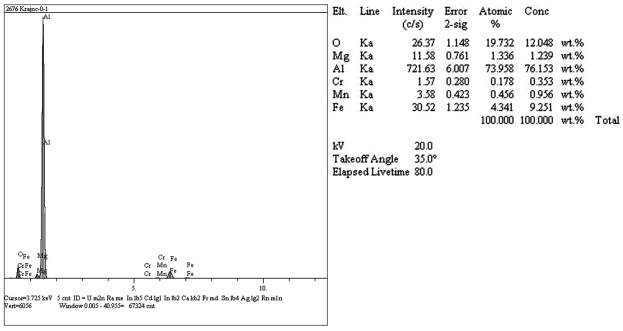

Figure 10: The result of the point analysis of an alumina inclusion
Slika 10: Rezultati točkaste analize vključka Al_2O_3

In **Figure 8** the microstructures of sample 5 and 6 can be seen. There is a large fraction of pearlite (α_{Fe} + Fe_3C) and small fraction of ferrite (α_{Fe}) on the austenite phase boundaries.

With the scanning electron microscope we found different types of inclusions in our samples: Al_2O_3, MnS and spinel-type ($MgO \cdot Al_2O_3$) modified with calcium. We made a point and mapping analysis. In **Figure 9** we can see an alumina inclusion in sample 6. The results of the EDS analysis of the alumina inclusion are presented in **Figure 10**.

In the sample 6 microstructure there are also MnS inclusions. Similar inclusions where found by Lamut *et al.*[10] in a sample taken from the tundish on a continuous casting machine. The EDS analysis of this inclusion is shown in **Figure 11**. In our sample taken from tundish some magnesite and alumina inclusions were also found, but they were small and usually not larger than 1 µm.

In **Figure 12** a spinel-type ($MgO \cdot Al_2O_3$) inclusion modified with calcium is shown. It was found in sample 5 and its chemical composition is determined with a mapping analysis, also shown in **Figure 12**.

The inclusion found in sample 5 is a product of the de-oxidation process with aluminium, during which

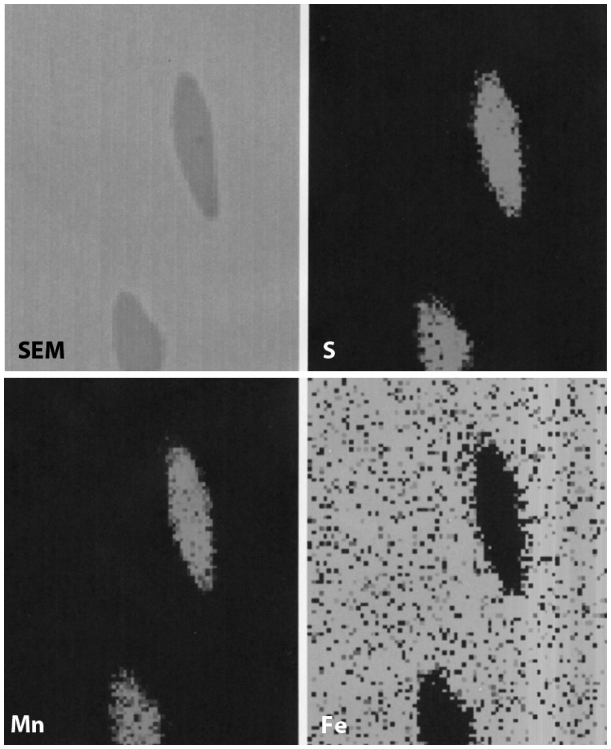

Figure 11: Microstructure and mapping analysis of MnS[10]
Slika 11: Mikrostruktura in razporeditev elementov v MnS[10]

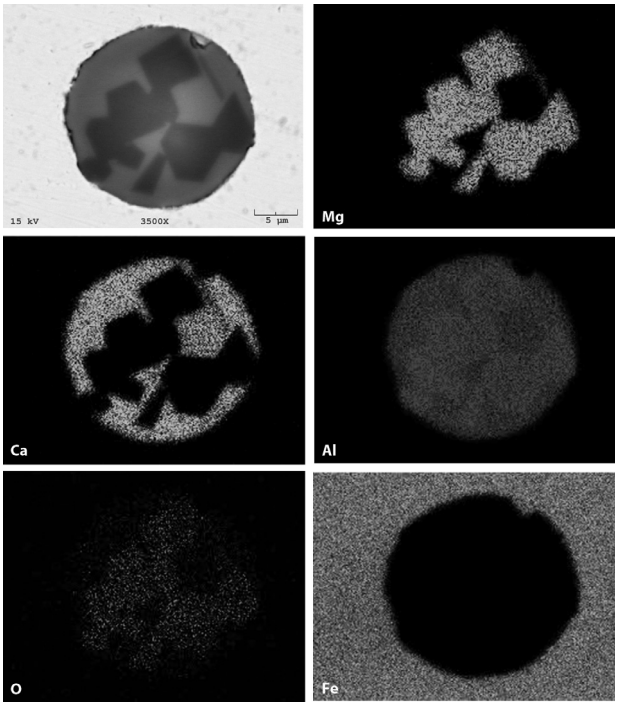

Figure 12: Mapping analysis of the spinel-type inclusion modified with calcium
Slika 12: Razporeditev elementov v vključku špinela, modificiranega s kalcijem

alumina inclusions were formed. We assume that because of the high content of aluminium in the melt, it has reduced the magnesium from the refractory and the slag. The magnesium then reacted with the oxygen and magnesite inclusions were formed. These have then, because of the high content, reacted with alumina and spinel-type inclusions were formed. With the addition of calcium for modifying the inclusions, there was a reaction between the spinel-type inclusions and pure alumina with calcium. The result of this was a large globural CaO-MgO-Al_2O_3 system inclusion.

In agreement with the literature[7] alumina inclusions are created during the de-oxidation process with aluminium. Furthermore, in accordance with Jiang *et al.*[9], the aluminium content in the melt is increased and it reduces the magnesium. Magnesium in turn, according to Park *et al.*[8], because of the high activity, reacts with the remaining oxygen, and forms magnesite inclusions, which then react with alumina and spinel-type inclusions are formed[7]. Because there are more alumina inclusions, some of them are trapped in the matrix of the spinel-type inclusion and these are, with the addition of calcium in accordance with Pires *et al.*[6], modified into large globular inclusions[5]. The EDS analysis verifies this theory, as we see in **Figure 11** that there is an angular phase formed from MgO and Al_2O_3 in the middle of the inclusion, while there is a CaO and Al_2O_3 phase surrounding the first one and making the inclusion globular.

4 CONCLUSIONS

Based on an analysis of the C45 steel sample, the following conclusions can be drawn:

The thermodynamic calculation has shown that for low contents of oxygen in the melt, initially magnesite inclusions are formed, and with an increase in the oxygen content magnesite and spinel-type inclusion are formed, whereas at high oxygen contents spinel-type and alumina inclusions are formed.

The thermodynamic calculation of the phase equilibrium revealed that the formation of $3{\cdot}CaO \cdot SiO_2$, MgO, $CaO \cdot Al_2O_3$ and $MgO \cdot Al_2O_3$ oxides in the slag is possible. These can react with phases in the slag, steel, refractory or atmosphere and can be reduced to steel.

With the calculation of the thermodynamic equilibrium we found that the magnesite, alumina and spinel-type inclusion are formed during the ladle furnace treatment. The EDS analysis confirmed that at the end of the ladle furnace treatment there are spinel-type inclusions in the melt and that they are modified with calcium. There is a possibility that the inclusions are removed during the manipulation from the ladle furnace to the continuous casting machine, because no large oxide inclusion was found in our tundish sample. Small alumina inclusions (1 µm) were found as were small MnS inclusions.

5 REFERENCES

[1] Y. Payandeh, M. Soltanieh, Oxide Inclusions at Different Steps of Steel Production, Journal of Iron and Steel Research, International, 14 (**2007**) 5, 39–46

[2] H. V. Atkinson, G. Shi, Characterization of Inclusions in Clean Steel: a Review Including the Statistics of Extreme Methods, Progress in Materials Science, 48 (**2003**), 457–520

[3] V. Gontarev, Teorija metalurških procesov. Univerza v Ljubljani, Naravoslovnotehniška fakulteta, Oddelek za materiale in metalurgijo. Ljubljana, 2005, 129

[4] A. Ghosh, Secondary Steelmaking: Principles and Aplication. Library of Congress Cataloging-in-Publication Data, 2000, 672

[5] F. Tehovnik, B. Koroušić, V. Prešeren, Optimizacija modifikacije nekovinskih vključkov v jeklih obdelanih s Ca, Kovine Zlitine Tehnol., 26 (**1992**) 1/2, 125–130

[6] J. C. S. Pires, A. Garcia, Modification of Oxide Inclusions Present in Aluminum-Killed Low Carbon Steel by Addition of Calcium. REM: R. Esc. Minas, Ouro Preto, 57 (**2004**) 3, 183–189

[7] D. Steiner Petrovič, B. Arh, F. Tehovnik, M. Pirnat, Magnesium Non-metallic Inclusions in Non-Oriented Electrical Steel Sheets, ISIJ International, 51 (**2010**) 12, 2069–2075

[8] J. H. Park, Formation Mechanism of Spinel-Type Inclusions in High-Alloyed Stainless Steel Melts, The Minerals, Metals & Materials Society and ASM International, 38B (**2007**), 657–663

[9] M. Jiang, X. Wang, B. Chen, W. Wang, Laboratory Study on Evolution Mechanisms of Non-metallic Inclusions in High Strength Alloyed Steel Refined by High Basicity Slag, ISIJ International, 50 (**2010**) 1, 95–104

[10] J. Lamut, M. Knap, H. Ploštajner, B. Senčič, Proces modifikacije vključkov s CaSi, 13. Seminar o procesni metalurgiji jekla, 2007, 134–137

UDK 621.318.1:544.171.6
Original scientific article/Izvirni znanstveni članek

ISSN 1580-2949
MTAEC9, 46(4)369(2012)

SMALL-ANGLE X-RAY SCATTERING SPECTRA OF IRON-BASED MAGNETIC FLUIDS

MALOKOTNO SIPANJE RENTGENSKEGA SPEKTRA MAGNETNIH TEKOČIN NA OSNOVI ŽELEZA

Supagorn Rugmai[1], Chitnarong Sirisathitkul[2], Komkrich Chokprasombat[2], Prawet Rangsanga[2], Phimphaka Harding[2], Toemsak Srikhirin[3], Pongsakorn Jantaratana[4]

[1]School of Physics, Institute of Science, Suranaree University of Technology and Synchrotron Light Research Institute (Public Organization), Nakhon Ratchasima, Thailand
[2]Molecular Technology Research Unit, School of Science, Walailak University, Nakhon Si Thammarat, Thailand
[3]Department of Physics, Faculty of Science, Mahidol University, Bangkok, Thailand
[4]Department of Physics, Faculty of Science, Kasetsart University, Bangkok, Thailand
schitnar@wu.ac.th

Prejem rokopisa – received: 2011-11-29; sprejem za objavo – accepted for publication: 2012-03-05

Two types of superparamagnetic nanoparticles, namely magnetite (Fe_3O_4) and iron-platinum (FePt), with their surface modified by oleic acid and oleyleamine were synthesized using the the polyol process and dispersed in *n*-hexane. Vibrating-sample magnetometry (VSM) was used to characterize the FePt and the magnetic susceptibility of the Fe_3O_4 was measured as a function of magnetic field and frequency at room temperature. Synchrotron, small-angle, X-ray scattering (SAXS) patterns revealed the polydispersity of the magnetic nanoparticles with average radii below 5 nm. As confirmed by transmission electron microscopy (TEM) images and dynamic light scattering (DLS), the Fe_3O_4 nanoparticles had a larger average size. The DLS measurement gave larger radii than those obtained from the SAXS because of the effect of aggregates and surfactants.

Keywords: magnetic fluid, magnetite, iron-platinum, synchrotron radiation, SAXS

Dve vrsti superparamagnetnih nanodelcev, magnetit (Fe_3O_4) in železo-platina (FePt), s površino, modificirano z oleinsko kislino in oleinaminom, sta bili sintetizirani s polyolnim postopkom in dispergirani v n-heksanu. Vibracijska magnetometrija vzorcev (VSM) je bila uporabljena za karakterizacijo FePt in magnetna občutljivost Fe_3O_4 je bila izmerjena pri sobni temperaturi kot funkcija magnetnega polja in frekvence. Sinhrotronsko malokotno sipanje rentgenskih žarkov (SAXS) je odkrilo polidisperznost magnetnih nanodelcev s povprečnim premerom, manjšim od 5 nm. Kot so potrdili posnetki s transmisijsko elektronsko mikroskopijo (TEM) in dinamičnim sipanjem svetlobe (DLS), imajo nanodelci Fe_3O_4 večjo povprečno velikost. Meritve DLS so pokazale večje premere delcev kot meritve SAXS zaradi učinka združevanja delcev in tenzidov.

Ključne besede: magnetna tekočina, magnetit, železo-platina, sinhrotronsko sevanje, SAXS

1 INTRODUCTION

Magnetic fluids are a special class of materials that possess the advantages of a liquid state of the carrier and a magnetic state of the nanoparticles.[1] Either ferromagnetic or superparamagnetic nanoparticles can be stabilized without agglomeration and sedimentation in a liquid by surfactant molecules, such as oleic acid and oleyleamine.[2] In addition to an increase in the magnetization in response to an applied magnetic field, the single-domain, superparamagnetic particles are able to generate heat in an alternating magnetic field. Moreover, some product properties, such as magnetoviscosity, are exclusively observed in a magnetic fluid.[1] As a result, magnetic fluids are increasingly implemented in engineering and biomedical applications. Magnetite (Fe_3O_4) nanoparticles in either water or oil are commercially available. In addition to the conventional uses, such magnetic fluids are the subjects of research and development as drug-delivery, hyperthermia and MRI-contrast agents.[3,4] On the other hand, iron-platinum (FePt) is investigated as a material for ultra-high-density recording.[5] The as-synthesized FePt nanoparticles in the superparamagnetic state are commonly stored in the form of a magnetic fluid.

The magnetic properties of Fe_3O_4 and FePt nanoparticles can be characterized in the forms of colloidal particles or dried particles on solid substrate using either a susceptometer or a magnetometer. Since their magnetic properties are highly dependent on the shape and size distribution, several techniques have been employed to characterize such nanoparticles. Transmission electron microscopy (TEM) provides images, but the qualitative analysis is based on sampling. Dynamic light scattering (DLS) gives an overall size distribution, but the size of the aggregate is usually measured instead of the individual particles.[6] Small-angle, X-ray scattering (SAXS) using a synchrotron source offers an alternative characterization of the shape and the size distribution. In addition to common uses in the case of organic nanostructures, the technique can also characterize magnetic nanoparticles, including ferrites[7,8], maghemite[9], Fe_3O_4 [6,10,11] and FePt.[12–14]

In this work, Fe_3O_4 and FePt nanoparticles synthesized using the polyol process and dispersed in hexane were characterized by synchrotron SAXS. The results

were used to complement those from DLS, TEM and magnetic measurements.

2 EXPERIMENTAL

The polyol processes adapted from Sun et al.[15] were carried out under standard airless Schlenk line techniques in a nitrogen (N_2) atmosphere. For the Fe_3O_4 nanoparticles, a mixture of 2.0 mmol of $Fe(acac)_3$ (99.99 %), 10 mmol of 1,2 hexadecandiol (90 %), 6 mmol of oleic acid (90 %) and 6 mmol of oleyleamine (70 %) was added to a 100-mL Schlenk flask containing 20 mL of benzyl ether (99 %). The solution was heated and dwelled at 200 °C for 2 h and then allowed to reflux at 300 °C for 30 min. In the synthesis of FePt, 1.0 mmol of $Fe(acac)_3$ and 0.5 mmol of $Pt(acac)_2$ (97 %) were poured into a flask, and then 20 mL of ethylene glycol was added. The mixture was moderately stirred, purged with N_2 for 15 min at room temperature before increasing the temperature to 120 °C. After the addition of 5 mmol of oleic acid and 5 mmol of oleyleamine, the solution was heated to 205 °C and then allowed to reflux for 2 h.

After the heating source was removed, the solution was allowed to cool down to room temperature under N_2. The product was precipitated by adding ethanol and separated by centrifugation. The precipitate was dispersed in *n*-hexane. Extra ethanol was added in this dispersion and the dispersion was centrifuged again for purification. After washing the particles in ethanol for three or more times, they were dispersed in *n*-hexane with the presence of a small amount (≈0.05 mL) of oleic acid and oleyleamine, followed by purging with N_2 to remove the oxygen and then stored in glass bottles at 0–4 °C.

The morphology of the nanoparticles was inspected by TEM. The samples were prepared by depositing a few drops of the final hexane dispersion on a carbon-coated grid, acting as a substrate. Magnetization as a function of the applied magnetic field for the FePt nanoparticles was measured by vibrating-sample magnetometry (VSM). To characterize the magnetic properties of the Fe_3O_4 nanoparticles, the mass susceptibility of the magnetic fluid in a capsule was measured as function of the static (dc) magnetic field, as well as alternating (ac) magnetic field and its frequency using a susceptometer at room temperature.

The SAXS measurements were performed at BL2.2 of the Synchrotron Light Research Institute, Thailand. The X-ray wavelength was set to 0.155 nm. A CCD detector (Mar SX165) was used to record the 2D scattering patterns. The sample-detector distance of 1587.46 mm, set for the experiments, was calibrated by measuring the scattering of silver behenate powder. For the measurements, each magnetic fluid was injected into a sample cell with aluminum foil windows. The background subtraction was carried out by subtracting the sample scattering patterns from that of *n*-hexane. The absorptions of X-rays by the sample and the *n*-hexane were taking into account in the background-subtraction process by measuring the transmitted beam intensity, with reference to that of an empty cell, using a photodiode located in front of the beamstop. The scattering profiles for the FePt and Fe_3O_4 nanoparticles were then obtained by circularly averaging the background-subtracted patterns.

3 RESULTS AND DISCUSSION

The variation of the complex magnetic susceptibility of the Fe_3O_4 fluid with the frequency follows the trend previously shown by Fannin et al.[16–18] The response of the superparamagnetic fluid to an alternating magnetic field can be modeled and experimentally fitted. In **Figure 1a**, the real part is decreased gradually from 1.6 × 10^{-6} m^3/kg at 100 Hz to 1.4 × 10^{-6} m^3/kg at 600 Hz. It has a linear decrease with the log of the frequency from 800 Hz to 4 000 Hz before dropping to the saturation around 4.0 × 10^{-7} m^3/kg at 6 000 Hz. The imaginary part is modest and remains constant over a wider frequency range from 100 to 1000 Hz. The peak in the literature[16–18] centered around 1500–2 000 Hz is not clearly observed. At a fixed frequency, the susceptibility does not have

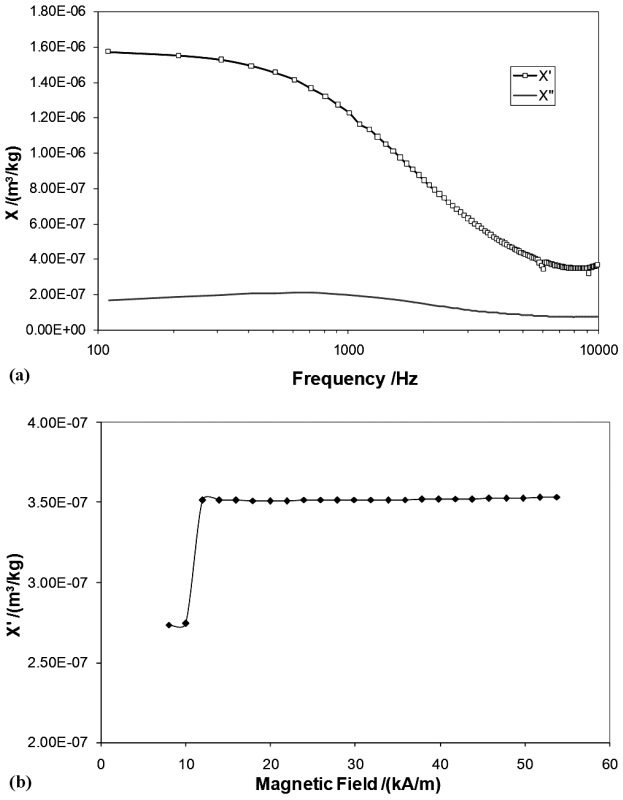

Figure 1: Susceptibility of Fe_3O_4 in hexane as a function of: a) frequency and b) ac magnetic field at 7 kHz

Slika 1: Občutljivost Fe_3O_4 v heksanu kot funkcija: a) frekvence in b) izmeničnega magnetnega polja pri 7 kHz

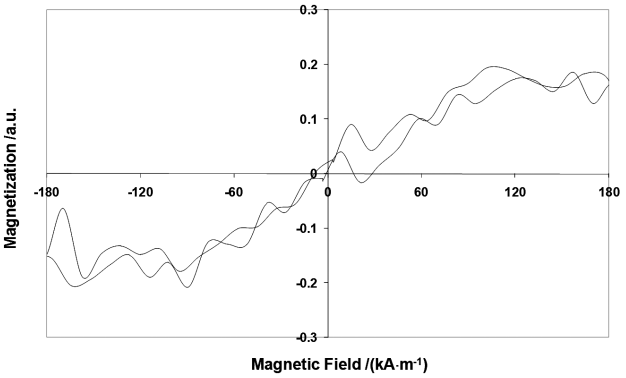

Figure 2: Magnetization of FePt as a function of applied magnetic field measured by VSM

Slika 2: Magnetizacija FePt kot funkcija uporabljenega magnetnega polja, izmerjena z VSM

significant variations in response to the changes in the dc magnetic field between –1 kA/m and 1 kA/m and the ac magnetic field up to 56 kA/m. There is an exception in **Figure 1b**: the sudden increase in the real susceptibility from 2.75×10^{-7} to 3.5×10^{-7} m^3/kg occurs by increasing the ac field from 12 kA/m to 16 kA/m. Similar behavior was previously observed in the case of maghemite.[17, 18] According to the magnetization curve in **Figure 2**, the FePt fluid also exhibits superparamagnetic behavior with saturation from 180 kA/m.

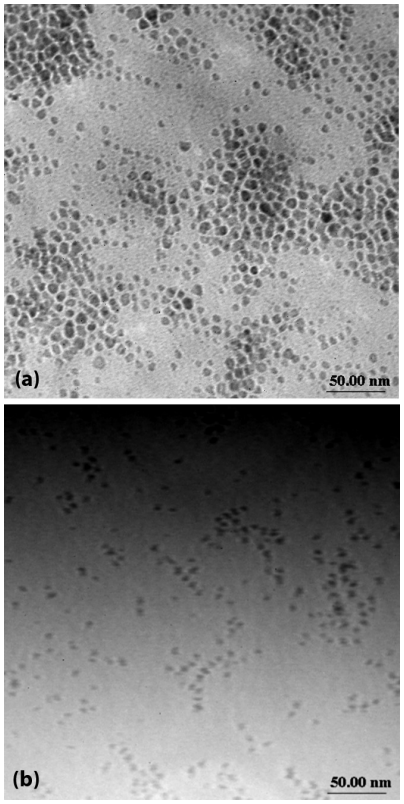

Figure 3: TEM images of: a) Fe_3O_4 and b) FePt nanoparticles on substrates

Slika 3: TEM-posnetek: a) Fe_3O_4- in b) FePt-nanodelcev na podlagi

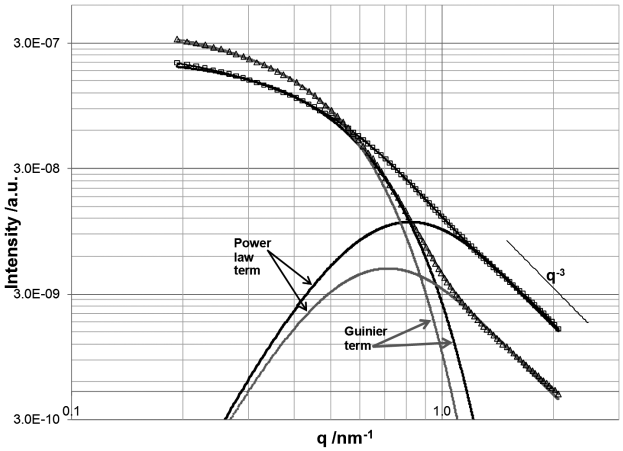

Figure 4: Measured SAXS profiles from FePt- (squares) and Fe_3O_4- (triangles) nanoparticles. The black and grey solid lines are the unified exponential power-law fits for FePt and Fe_3O_4, respectively, with the contributions from the Guinier and power-law terms. The q^{-3} line is shown to indicate –3 slope obtained from the fit.

Slika 4: Izmerjen SAXS-profil iz FePt- (kvadratki) in Fe_3O_4- (trikotniki) nanodelcev. Črna in siva linija sta prilagojeni eksponentnemu zakonu za FePt in Fe_3O_4, združeni s prispevkom zakonitosti Guinierja in izrazi zakona moči. Prikazana je linija q^{-3}, ki kaže naklon –3, dobljen iz prileganja.

TEM images of the as-synthesized particles are compared in **Figure 3**. The morphology of the Fe_3O_4 nanoparticles can be described as spheroid with a rough surface. The size distribution around 5 nm in radius and some aggregates are observed. The FePt nanoparticles in **Figure 3b** are less concentrated and generally smaller than the Fe_3O_4. The DLS size distribution curves of surfactant-coated Fe_3O_4 and FePt have their peaks centered at approximately 7.96 nm and 4.28 nm in radius, respectively.

The measured SAXS intensity profiles for FePt and Fe_3O_4 are shown in **Figure 4**. The intensity profiles are plotted as a function of the scattering vector q, given by

$$q = 4\pi \sin\left(\frac{\theta}{\lambda}\right) \tag{1}$$

where θ denotes half the scattering angle and λ is the X-ray wavelength. The measured SAXS intensity profiles from both the FePt and Fe_3O_4 nanoparticles appear to have a certain slope in the high q region and then a transition to an exponential-like profile at small q. Considering the characteristics of the SAXS intensity profile of homogeneous spheres, the appearance of the measured intensity indicates that the q-range of the measurement may contain parts of the Guinier and the fractal regimes, as well as the transition between the two regimes.[19]

In order to analyze the particle size and size distribution, the unified exponential-power law model of Beaucage[20] was used to fit the measured data, where the scattering intensity is given by:

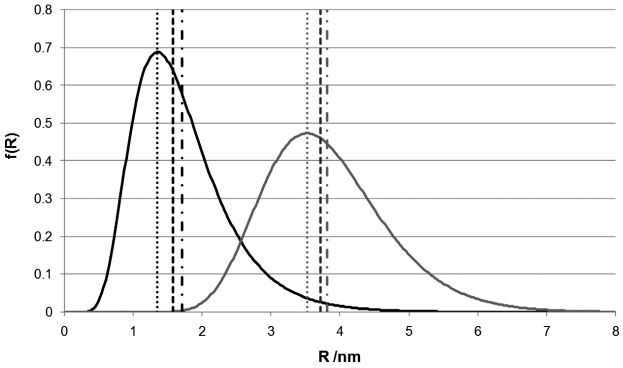

Figure 5: Lognormal size distributions for FePt (black solid line) and Fe_3O_4 (grey solid line) obtained from the unified exponential power-law fit. The positions of the mode, median and mean radii are also shown for each distribution by dotted, dashed and dot-dashed lines, respectively.

Slika 5: Normalna logaritemska razporeditev velikosti FePt (črna linija) in Fe_3O_4 (siva linija), dobljena iz poenotene eksponentne odvisnosti. Prikazane so tudi pozicije vrste srednje in največje velikosti delcev za vsako razvrstitev s pikčasto, črtkano in pikčasto-črtkano linijo.

$$I(q) = G\exp\left(-\frac{q^2R_g^2}{3}\right) + B\left(\left[\operatorname{erf}\left(\frac{qR_g}{\sqrt{6}}\right)\right]^3 / q\right)^P \qquad (2)$$

The prefactors G and B, the radius of gyration R_g and the exponent P are fit parameters. This model, including its more general form for multi-level structure,[20] has been successfully applied to describe systems with multiple structures.[21–23] The fitting was carried out with a least-squares minimization procedure using the software package SASfit.[24] The fitted scattering-intensity curves are shown in **Figure 4**, where contributions from the Guinier and the power law terms in Eq. (2) are also shown. The fitted exponent P = 3 was obtained for both samples. This value is at the limit of the mass and surface fractal and may indicate contributions from a uniformly dense aggregate with a very rough surface.[22] To investigate the particle size and size distribution, the lognormal distribution of the particle size is assumed, where the lognormal distribution function is given by:[25]

$$f(R) = \frac{1}{R\sigma\sqrt{2\pi}}\exp\left\{\frac{[\ln(R/m)]^2}{2\sigma^2}\right\} \qquad (3)$$

with m denoting the median and σ is the shape parameter of the distribution. The mode, the value of R at the maximum, for the lognormal distribution is $m\exp(-\sigma^2)$. The mean particle radius $\langle R\rangle$ can be found from the first moment of the distribution and is related to the two parameters of the distribution by:

$$\langle R\rangle = m\exp\left(\frac{\sigma^2}{2}\right) \qquad (4)$$

where $\langle R\rangle$ is the mean particle radius. The standard deviation (SD) of the distribution is also related to the two parameters, and is given by:

$$SD = m\sqrt{\omega(\omega-1)} \qquad (5)$$

where $\omega = \exp(\omega^2)$. Following Beaucage *et al.*,[26] the two parameters m and σ of the lognormal distribution can be explicitly given in terms of the ratio B/G and the radius of gyration R_g of the SAXS intensity profile. This enables one to extract the particle size and the distribution information from the fit of the unified model of Beaucage, Eq.(2), to the measured SAXS intensity profile. The parameters m and σ are given by:[26]

$$m = \sqrt{\frac{5R_g^2}{3\exp(14\sigma^2)}} \qquad (6)$$

$$\sigma = \sqrt{\frac{\ln(BR_g^4/1.62G)}{12}} \qquad (7)$$

The value $(BR_g^4/1.62G)$ in Eq.(7) also serves as an index of polydispersity, in which the value is 1 for a monodisperse sphere.[20] The lognormal distribution functions for both types of nanoparticles are shown in **Figure 5**. The relevant fitted parameters and calculated mean particle radii and standard deviations of the size distribution are shown in **Table 1**. The results give a smaller particle size for FePt than for Fe_3O_4, which agrees with the observation from the TEM images. The high standard deviation and index of polydispersity relative to the size of FePt can be described by the heterocoagulation model of FePt formation in the modified polyol process.[27] The obtained sizes of both types of particles are smaller than those obtained by DLS, which is a trend previously observed in the literature.[6] The reason is not only due to the exclusion of surfactants by the SAXS but also the effect of aggregation in the case of DLS.

Table 1: Fitted parameters for the SAXS intensity profile and calculated mean particle radius and standard deviation compared with the DLS results

Tabela 1: Prilagojeni parametri SAXS intenzitetnega profila in izračunan premer delca ter standardni odklon v primerjavi z DLS-rezultati

Sample	SAXS				DLS
	$BR_g^4/(1.62G)$	R_g/nm	$\langle R\rangle$/nm	SD	R_{peak}/nm
FePt	6.55	3.67	1.71	0.70	4.28
Fe_3O_4	1.92	4.21	3.82	0.90	7.96

4 CONCLUSION

Synchrotron SAXS spectra revealed the polydispersity of superparamagnetic Fe_3O_4 and FePt nanoparticles in *n*-hexane synthesized using the polyol process. FePt nanoparticles had a smaller average size, which is in a good agreement with DLS and TEM images. The radii obtained from the DLS measurement tended to be larger than those from SAXS because the aggregates and surfactants were also taken into account.

5 REFERENCES

[1] S. Odenbach, Recent progress in magnetic fluid research, Journal of Physics: Condensed Matter, 16 (**2004**) 32, R1135–R1150

[2] A. Drmota, A. Kosak, A. Znidatrzik, A mechanism for the adsorption of carboxylic acids onto the surface of magnetic nanoparticles, Mater. Tehnol., 42 (**2008**) 2, 79–83

[3] Q. A. Pankhurst, J. Connolly, S. K. Jones, J. Dobson, Applications of magnetic nanoparticles in biomedicine, Journal of Physics D: Applied Physics, 36 (**2003**) 13, R167–R181

[4] S. Campelj, D. Makovec, L. Skrlep, M. Drofenik, Preparation of nano-composites for biomedical applications, Mater. Tehnol., 42 (**2008**) 4, 179–182

[5] S. Sun, Recent advances in chemical synthesis, self-assembly, and applications of FePt nanoparticles, Advanced Materials, 18 (**2006**) 4, 393–403

[6] E. V. Shtykova, X. L. Huang, N. Remmes, D. Baxter, B. Stein, B. Dragnea, D. I. Svergun, L. M. Bronstein, Structure and properties of iron oxide nanoparticles encapsulated by phospholipids with poly(ethylene glycol) tails, Journal of Physical Chemistry C, 111 (**2007**) 49, 18078–18086

[7] R. Itri, J. Depeyrot, F. A. Tourinho, M. H. Sousa, Nanoparticle chain-like formation in electrical double-layered magnetic fluids evidenced by small-angle X-ray scattering, European Physical Journal E, 4 (**2001**) 2, 201–208

[8] F. L. O. Paula, G. J. da Silva, R. Aquino, J. Depeyrot, J. O. Fossum, K. D. Knudsen, G. Helgesen, F. A. Tourinho, Gravitational and magnetic separation in self-assembled clay-ferrofluid nanocomposites, Brazilian Journal of Physics, 39 (**2009**) 1A, 163–170

[9] M. J. Park, J. Park, T. Hyeon, K. Char, Effect of interacting nanoparticles on the ordered morphology of block copolymer/nanoparticle mixtures, Journal of Polymer Science Part B-Polymer Physics, 44 (**2006**) 24, 3571–3579

[10] N. Suzuki, P. Gupta, H. Sukegawa, K. Inomata, S. Inoue, Y. Yamauchi, Aerosol-assisted synthesis of thiol-functionalized mesoporous silica spheres with Fe_3O_4 nanoparticles, Journal of Nanoscience and Nanotechnology, 10 (**2010**) 10, 6612–6617

[11] G. Utkan, F. Sayar, P. Batat, S. Ide, M. Kriechbaum, E. Piskin, Synthesis and characterization of nanomagnetite particles and their polymer coated forms, Journal of Colloid and Interface Science, 353 (**2011**) 2, 372–379

[12] K. Shinoda, K. Sato, B. Jeyadevan, K. Tohji, S. Suzuki, Local structural studies of directly synthesized L10 FePt nanoparticles by using XRD, XAS and ASAXS, Journal of Magnetism and Magnetic Materials, 310 (**2007**) 2, 2387–2389

[13] C. Hendrich, L. Favre, D. N. Ievlev, A. N. Dobrynin, W. Bras, U. Hormann, E. Piscopiello, G. van Tendeloo, P. Lievens, K. Temst, Applied Physics A, 86 (**2007**) 4, 533–538

[14] C. C. H. Lo, S. C. Tsang, C. H. Yu, K. Tam, Magnetic properties of macroscopic colloid crystals of silica-coated FePt nanoparticles with controllable interstices for molecular separation, Journal of Applied Physics, 105 (**2009**) 7, 07C101

[15] S. Sun, H. Zeng, D. B. Robinson, S. Raoux, P. M. Rice, S. X. Wang, G. Li, Monodisperse MFe_2O_4 (M = Fe, Co, Mn) nanoparticles, Journal of the American Chemical Society, 126 (**2004**) 1, 273–279

[16] P. C. Fannin, Investigating magnetic fluids by means of complex susceptibility measurements, Journal of Magnetism and Magnetic Materials, 258–259 (**2003**), 446–451

[17] P. C. Fannin, C. Mac Oireachtaigh, L. Cohen-Tannoudji, E. Bertrand, J. Bibette, Complex susceptibility measurements of a suspension of magnetic beads, Journal of Magnetism and Magnetic Materials, 300 (**2006**) 1, e210–e212

[18] P. C. Fannin, L. Cohen-Tannoudji, E. Bertrand, A. T. Giannitsis, C. Mac Oireachtaigh, J. Bibette, Investigation of the complex susceptibility of magnetic beads containing maghemite nanoparticles, Journal of Magnetism and Magnetic Materials, 303 (**2006**) 1, 147–152

[19] G. C. Bushell, Y. D. Yan, D. Woodfield, J. Raper, R. Amal, On techniques for the measurement of the mass fractal dimension of aggregates, Advances in Colloid and Interface Science, 95 (**2002**) 1, 1–50

[20] G. Beaucage, Approximations leading to a unified exponential/power-law approach to small-angle scattering, Journal of Applied Crystallography, 28 (**1995**) 6, 717–728

[21] G. Beaucage, D. W. Schaefer, Structural studies of complex systems using small-angle scattering: a unified Guinier/power-law approach, Journal of Non-Crystalline Solids, 172–174 (**1994**) 2, 797–805

[22] D. W. Schaefer, R. S. Justice, How nano are nanocomposites?, Macromolecules, 40 (**2007**) 24, 8501–8517

[23] G. J. Schneider, V. Vollnhals, K. Brandt, S. V. Roth, D. Goeritz, Correlation of mass fractal dimension and cluster size of silica in styrene butadiene rubber composites, Journal of Chemical Physics, 133 (**2010**) 9, 094902

[24] J. Kohlbrecher: A program for fitting elementary structure models of small angle scattering data. Available from World Wide Web: http://kur.web.psi.ch/sans1/SANSSoft/sasfit.html

[25] C. Forbes, M. Evans, N. Hastings, B. Peacock, Statistical Distributions, 4th ed., John Wiley and Sons Inc., New York 2011, 131

[26] G. Beaucage, H. K. Kammler, S. E. Platsinis, Particle size distributions from small-angle scattering using global scattering functions, Journal of Applied Crystallography, 37 (**2004**) 4, 523–535

[27] W. Beck Jr., C. G. S. Souza, T. L. Silva, M. Jafelicci Jr., L. C. Varanda, Formation mechanism via a heterocoagulation approach of FePt nanoparticles using the modified polyol process, Journal of Physical Chemistry C, 115 (**2011**) 21, 10475–10482

UDK 66.017:666.3/.7
Original scientific article/Izvirni znanstveni članek

ISSN 1580-2949
MTAEC9, 46(4)375(2012)

MICROSTRUCTURE OF METAL-MATRIX COMPOSITES REINFORCED BY CERAMIC MICROBALLOONS

MIKROSTRUKTURA KOMPOZITOV S KOVINSKO OSNOVO, OJAČANO S KERAMIČNIMI MIKROKROGLICAMI

Imre Norbert Orbulov, Kornél Májlinger

Department of Materials Science and Engineering, Budapest University of Technology and Economics, Bertalan Lajos utca 7., 1111, Budapest, Hungary
orbulov@eik.bme.hu, orbulov@gmail.com

Prejem rokopisa – received: 2011-12-03; sprejem za objavo – accepted for publication: 2012-02-06

Metal-matrix composites reinforced by ceramic hollow microspheres were produced as special porous metals, called metal-matrix syntactic foams (MMSFs). In this paper the microstructure of the ceramic hollow microspheres as reinforcing elements is investigated in connection with the production of MMSFs with the pressure infiltration. SL150- and SL300-type ceramic microspheres from Envirospheres Ltd (Australia) were investigated. They contained various oxide ceramics, mainly Al_2O_3 and SiO_2. The chemical composition and the microstructure of the microspheres had a strong effect on their infiltration characteristics; therefore, in the view of the MMSF production it was very important to know microstructural details about the microspheres. Due to this energy-dispersive X-ray spectroscopy, maps were recorded from the cross-sections of the microspheres' walls. The results showed that the Al_2O_3 and SiO_2 distribution were not equal; the Al_2O_3 phase was embedded in the surrounding mullite, while the SiO_2 phase occurred in the form of needles. Line energy-dispersive X-ray spectroscopy measurements were performed in order to investigate the possible reaction between different aluminium alloy matrices and the ceramic microspheres. The results showed that, due to an uneven distribution of Al_2O_3, rich particles of the molten aluminium could reduce the SiO_2 rich parts of the microspheres and the walls of the hollow microspheres became damaged and degraded. This chemical reaction between the microspheres and the walls could make the infiltration easier, but the resulting mechanical properties will be reduced due to the damaged microsphere walls.

Keywords: microsphere, microballoon, energy dispersive X-ray spectroscopy, metal matrix syntactic foam, metal matrix composite

Kompoziti s kovinsko osnovo, ojačano s keramičnimi votlimi mikrokroglicami, so bili izdelani kot posebna porozna kovina z nazivom sintaktična pena s kovinsko osnovo (MMSF). V tem članku je opisana raziskava mikrostrukture keramičnih votlih mikrokroglic v povezavi z izdelavo MMSF z infiltracijo pod tlakom. Preiskovane so bile SL150- in SL300-keramične mikrokroglice proizvajalca Envirospheres Ltd (Avstralija). Vsebujejo različne keramične okside, večinoma Al_2O_3 in SiO_2. Kemijska sestava in mikrostruktura mikrokroglic imata velik vpliv na sposobnost njihove infiltracije, zato je z vidika izdelave MMSF pomembno poznati podrobnosti mikrostrukture teh mikrokroglic. Zaradi tega je bila na prerezu stene mikrostrukturnih kroglic posneta razporeditev elementov z energijsko disperzijsko spektroskopijo. Rezultati kažejo, da razporeditev Al_2O_3 in SiO_2 ni enaka: Al_2O_3-faza je vgrajena v obkrožajoči mulit, medtem ko se SiO_2-faza pojavlja v obliki igel. Da bi preiskali morebitne reakcije med osnovo iz različnih aluminijevih zlitin in keramičnimi mikrokroglicami, je bila izvršena linijska energijsko disperzijska rentgenska spektroskopija. Rezultati so pokazali, da zaradi neenakomerne razporeditve z Al_2O_3 bogati delci v staljenem aluminiju lahko reducirajo s SiO_2 bogata področja mikrokroglic, in stene votlih mikrokroglic postanejo poškodovane in degradirane. Kemijske reakcije med mikrokroglicami in stenami lahko olajšajo infiltracijo, vendar pa se mehanske lastnosti poslabšajo zaradi poškodovanih sten mikrokroglic.

Ključne besede: mikrokroglice, mikrobaloni, energijsko disperzijska rentgenska spektroskopija, pena, skladna s kovinsko osnovo, kompozit s kovinsko osnovo

1 INTRODUCTION

Nowadays metallic foams are more and more important and this is confirmed by the increasing number of papers published on this topic. The žconventional' metallic foams, which contain only metallic and gas phases, are widely covered by the literature. However, there are still unsolved problems, for example the foaming process of the foams[1,2]. The metallic foams belong to a special class that also satisfies the definition of the particle-reinforced metal-matrix composites. These are the metal-matrix syntactic foams (MMSFs). They were first produced in the 1990s. The MMSFs have numerous promising applications, such as covers, hulls, castings, or they can be used in the automotive and electromechanical industry sectors because of their high-energy absorbing and damping capabilities. In these porous materials the porosity is ensured by incorporating ceramic hollow microspheres[3]. The microspheres are commercially available and they mainly contain various oxide ceramics[4,5]. The quality of the microspheres has a strong effect on the mechanical and other properties of the foams. The behavior of the foams has been widely studied.

The most important properties of the foams are the compressive strength and the absorbed energy. Wu et al. examined the effects of the microballoon size on the compressive strength. They found that smaller microspheres ensure higher compressive strength because they contain fewer flaws in their microstructure than the larger ones. The damage propagation of the foams was also investigated. The fracture was initialized in the cor-

ners of the specimens by the shearing of the microspheres[6]. Rohatgi et al. also investigated the size effect of the microspheres, but not only in view of the compressive strength, but in view of infiltration, too. Their measurements showed that larger microspheres can be infiltrated easier[7]. Palmer et al. proved that larger microspheres contain more porosity in their walls and more flaws in their microstructure than the smaller ones[8]. The results of the performed upsetting tests were compared to the other research on this topic. The conclusions were the same[9,10]. Balch et al. performed a special upsetting test. The loading was applied in small steps and after each test, X-ray or neutron-diffraction measurements were carried out. The main aim of the work was to investigate the load transfer from the matrix to the microspheres. They found a chemical reaction between the microspheres and the matrix materials, which has a detrimental effect on the load transfer and, through that, on the mechanical properties of the foams[11]. In their previous work Balch et al. found that the microspheres have at least the same importance in the syntactic foams as the matrix material. The fracture strength and the yield strength of the matrix determine the failure stress of the syntactic foams. Therefore, the investigation of the microstructure and the quality of the microspheres is very important[9]. In addition to the compressive strength, other mechanical properties, such as the tensile strength, or the hardness of the syntactic foams were investigated[12,13]. The sliding behavior of the syntactic foams was also examined because the ceramic microspheres have high hardness and therefore the composites show a better wear behaviour than the pure matrix[14,15].

As it can be seen in the previous paragraph, the quality and chemical composition of the microspheres influence many properties of the syntactic foams. And they also have a strong influence on the production of the syntactic foams. The foams are usually produced by the mixing technique and gravitational casting or by the pressure infiltration. In all these cases the contact angle between the ceramic microspheres and the metal matrix has a detrimental effect on the infiltration characteristics and on the threshold pressure (in the case of pressure infiltration)[16–18]. The contact angle is influenced by many parameters like the chemical composition and the possible reaction between the reinforcement and the matrix material. Therefore, the microspheres should be precisely investigated on the microstructure's scale.

The ultimate method for this purpose is the scanning electron microscopy and the energy-dispersive X-ray spectroscopy (EDS). EDS is sensitive to the chemical composition and able to investigate a point, a line or even an area. These possibilities give extremely good opportunities for acquiring detailed information about the microstructure of the microspheres and about the distribution of their constituents. According to the published works mentioned above, the main aim of this work was to investigate the microstructure and the distribution of the constituents in the ceramic hollow microspheres and to investigate the interface between different aluminium-alloy matrices and the ceramic microspheres in order to provide information about the metal-matrix syntactic foam production and their expectable mechanical behaviour.

2 MATERIALS AND METHODS

The investigated materials were the SL150- and SL300-type microspheres provided by Enviro spheres Ltd (Australia)[4]. Their main parameters are listed in **Table 1**. The phase composition was determined by X-ray diffraction measurements. For this purpose a Phillips X-Pert-type diffractometer with 35-mA cathode heating current

Table 1: Morphological properties and the phase constitution of the applied hollow ceramic spheres
Tabela 1: Morfološke značilnosti fazne sestave uporabljenih votlih keramičnih kroglic

Type	Average diameter	Size range	Specific surface	Al_2O_3	Amorphous SiO_2	Mullite	Quartz	Other
	(μm)	(μm)	(μm^{-1})	*w*/%				
SL150	100	56–183	0.060	30–35	45–50	19	1	*bal.*
SL300	150	101–330	0.040					

Table 2: Calculated and measured density and porosity values of the MMSFs[3]
Tabela 2: Izračunane in izmerjene vrednosti za gostoto in poroznost MMSF[3]

Specimen	Density (g cm^{-3})		Porosity (%)		
	Theoretical	Measured	Particle	Matrix	Total
Al99.5-SL150	1.34	1.43	50.9	–6.2	44.7
Al99.5-SL300	1.42	1.52	48.2	–7.2	41.0
AlSi12-SL150	1.32	1.31	50.9	1.1	52.0
AlSi12-SL300	1.40	1.37	48.2	1.9	50.1
AlMgSi1-SL150	1.34	1.52	50.9	–13.4	37.5
AlMgSi1-SL300	1.42	1.57	48.2	–10.5	37.7
AlCu5-SL150	1.37	1.53	50.9	–11.6	39.3
AlCu5-SL300	1.44	1.62	48.2	–12.2	36.0

and a copper anode (Cu K_α, λ = 0.154186 nm) with a 40-kV voltage were used. The rotating speed of the goniometer was 0.04° s^{-1}. The Scanning Electron Microscope (SEM) tests were performed by a Phillips XL-30-type electron microscope equipped with an EDAX Genesis EDS analyzer. The ceramic microspheres were coated with carbon in order to put a conductive layer on them, but basically they were investigated in as-received condition. The excitation was 15 kV and EDS maps were recorded from the surface of the microspheres. Five typical microspheres from each SL-type microsphere group were investigated.

Later the microspheres were incorporated in pure aluminium (Al 99.5), aluminium-silicon (AlSi12), aluminium-magnesium-silicon (AlMgSi) or aluminium-copper (AlCu5) alloys to create MMSFs. The foams were designated according to their matrices and reinforcement. For example, Al99.5-SL150 denotes a pure aluminium-matrix syntactic foam with an SL15-microsphere reinforcement. The volume fraction of the microspheres was maintained at a relatively high volume fraction (≈60 %) level and the production method is described, in details, elsewhere[3]. The density and the porosity values of MMSFs are listed in **Table 2**, while the chemical compositions of MMSFs are shown in **Table 3**. In **Table 2** theoretical density and particle porosity were calculated from the geometrical parameters of the microspheres. The matrix porosities were calculated as the difference between the theoretical and the measured density divided by the theoretical density. The negative matrix porosity refers to the infiltrated microspheres (the particle porosity should be decreased). However, the values of the matrix porosity were always below 8 %, so the infiltration can be qualified as good enough. The values of **Table 3** were determined with the XRD measurements described above. EDS line measurements were carried out on the foams to characterize the elemental distribution at the interfaces, where the hollow microspheres are in contact with the matrix. All EDS-line analyses were performed on metallographically polished surfaces, and the preparation steps for the EDS analysis with an automatic grinding / polishing machine are listed in **Table 4**. The excitation voltage for the EDS analysis was 20 kV. The line EDS measurement started on the matrix material and crossed the wall of a hollow sphere. One hundred points were measured along each line; each point was excited for 20 s with a 35-µs detector acquisition rate.

3 RESULTS AND DISCUSSION

3.1 Investigation of the microspheres' walls (map EDS measurements)

In **Figure 1** a typical site from the outer surface of an SL150-type microsphere is shown, while in **Figure 2**, a SEM micrograph from the cross-section of a microsphere in an Al99.5-matrix foam sample is presented. In both images needle-like structures can be clearly observed. They are densely situated and they do not have any distinguished direction. The different gray scale of the needles on the back-scattered electron (BSE) images indicates a somewhat different chemical composition. The needles are very small, their length is between 5 µm and 10 µm, while their diameter is smaller than 0.5 µm. EDS maps provide information that is much more useful than the single EDS spot measurements, because single spots can be largely effected by the surrounding matrix. This effect can be decreased, or avoided, with the EDS maps, which can show the distribution of the elements.

Because of this reason the EDS-map analyses were performed on the cross-sections of the microspheres to

Table 3: Phase constitution of aluminum-matrix syntactic foams according to the XRD measurements (in mass fractions, *w*/%)
Tabela 3: Fazna sestava pen, skladnih s kovinsko osnovo, izvršena z XRD-meritvami (v masnih deležih, *w*/%)

Specimen	Al	Si	Mullite	α-Al_2O_3	γ-Al_2O_3	Amorph.	$CuAl_2$
Al99.5-SL150	67	8	11	3	11	0	-
Al99.5-SL300	78	0	11	0	0	11	-
AlSi12-SL150	72	7	13	0	0	8	-
AlSi12-SL300	72	7	12	0	0	8	-
AlMgSi1-SL150	60	7	8	0	25	0	-
AlMgSi1-SL300	60	6	6	0	28	0	-
AlCu5-SL150	60	6	8	8	12	0	6
AlCu5-SL300	60	5	10	7	12	0	6

Table 4: Sample-preparation steps for the EDS analysis with an automatic grinding / polishing machine
Tabela 4: Stopnje priprave vzorcev za EDS-analizo z avtomatskim brusilno-polirnim sistemom

Abrasive material	Duration of grinding/ polishing (min)	Grinding/polishing force (N)	Rotation speed (r/min)	Rotation direction
P 320 SiC	1	22	220	counter
6 µm diamond	15	27	150	counter
3 µm diamond	6	27	150	counter
0.05 µm SiO	3	27	125	compliance

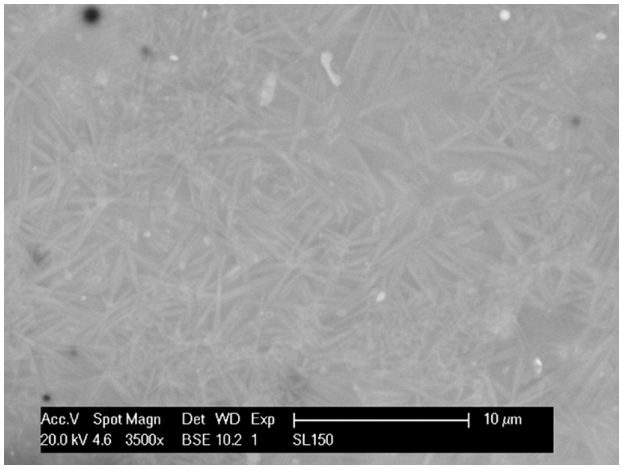

Figure 1: SEM image from the surface of an SL150-type ceramic hollow microsphere

Slika 1: SEM-posnetek površine SL150 votle keramične mikrokroglice

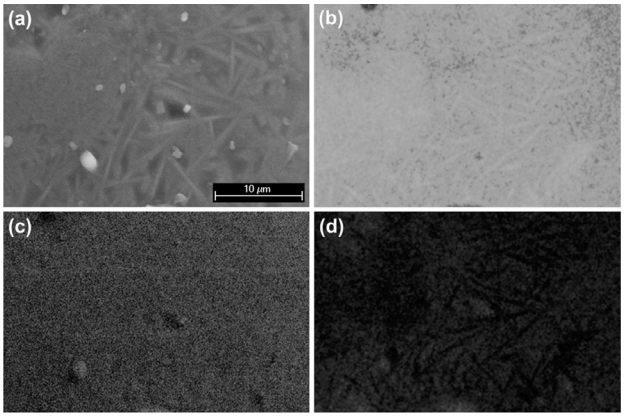

Figure 3: SEM image a) from the surface of an SL300-type microsphere and EDS maps of this area showing element distributions of: b) Al, c) O and d) Si

Slika 3: SEM-posnetek a) površine SL300 mikrokroglice in EDS posnetek razporeditve elementov: b) Al, c) O in d) Si

get additional information about the element distribution in a microsphere's wall. To illustrate this analysis, the EDS maps of an SL300-type microsphere are presented (**Figure 3**). It is important to emphasize that all of the other microsphere types (SL150 and SL300) showed the same features. **Figure 3a** shows a SEM image of the investigated surface. The needle-like structure is again very clear. **Figure 3b** shows the distribution of aluminium. It is evident that the needles contain more Al than the surrounding environment, but Al can be found everywhere, not only in the needles. From the XRD measurements it is also clear that Al_2O_3 and SiO_2 form mullite ($3Al_2O_3{\cdot}2SiO_2$), therefore – in accordance with the EDS map and **Table 1** – the wall of a microsphere is built up from the mixture of mullite and amorphous SiO_2. This means that the distribution of Al_2O_3 is uneven; it can be found as a part of mullite in the wall and as Al_2O_3 needles embedded in this wall matrix. **Figure 3d** definitely confirms this conclusion by showing the distribution of silicon. Si can be found everywhere on the surface (mainly amorphous SiO_2 mixed with mullite) except in the needles (the needles appear black in this picture). This indicates that the needles do not contain Si and, therefore, they are really Al_2O_3 needles. Finally, as it is expected, the oxygen distribution (in **Figure 3c**) is totally balanced; it is built in both Al_2O_3 and SiO_2.

The analysis above shows the formation of the Al_2O_3 rich zones and it also indicates the presence of the amorphous SiO_2 rich zones. The amorphous SiO_2 is undesir-

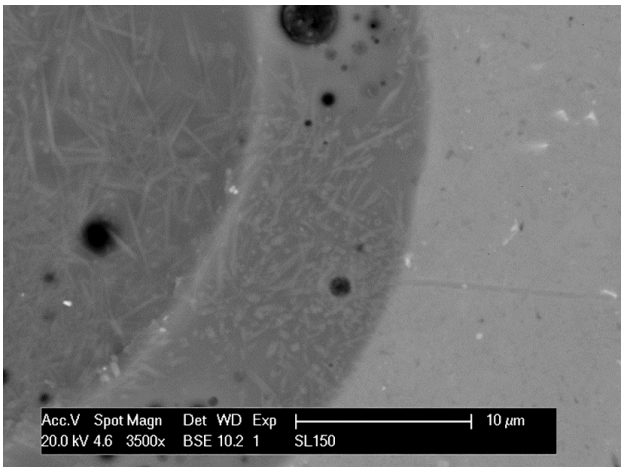

Figure 2: SEM image of the cross-section of an SL150-type ceramic hollow microsphere's wall

Slika 2: SEM-posnetek prečnega prereza stene SL150 votle keramične mikrokroglice

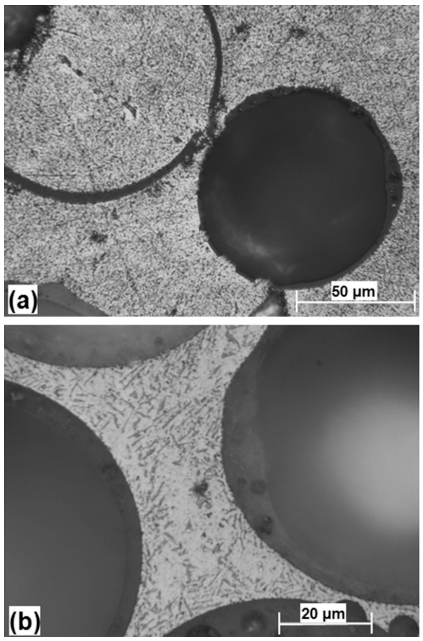

Figure 4: Micrographs of: a) damaged and b) undamaged microspheres in the a) Al99.5 and b) AlSi12 matrices

Slika 4: Mikroposnetek: a) poškodovane in b) nepoškodovanih mikrokroglic v a) Al99,5 in b) AlSi12 osnovi

able, because – opposite to Al_2O_3 and mullite – the chemical stability of SiO_2 at an elevated temperature is not good enough. During the production of MMSFs the molten aluminium can reduce SiO_2 according to the following chemical reaction:

$$4Al(liq) + 3SiO_2\ (sol) \rightarrow 2Al_2O_3\ (sol) + 3Si(sol)$$

At first sight this reaction is advantageous, because it forms Al_2O_3 (with better properties) from amorphous SiO_2. But this is a diffusion-controlled reaction leading to a degradation of the microspheres' walls as it is shown in **Figure 4a**. This indicates a drastic drop in the compressive strength and other mechanical properties as it was shown in the previous papers[3,19,20]. As indicated by the XRD results of **Table 3**, the reaction mainly produced γ-Al_2O_3 and it took place only in the case of a pure aluminium matrix reinforced with the SL150- and SL300-type microspheres. In the case of the SL300-type microspheres the reaction was suppressed with a lower infiltration temperature. The infiltration temperature had a strong influence on the kinetics of the change reaction. That is why there was no reaction in the case of the Al99.5-SL300-type syntactic foams infiltrated at a lower (690 °C) temperature[3]. This indicates that there is a limit relating to the temperature. Above this temperature the reaction is intensive, but below the temperature limit, the reaction will not occur (for details see[3]). The reaction did not take place in the case of the AlSi12-matrix material, because the driving force of the diffusion-controlled chemical reaction is the Si difference between the molten matrix and the solid microspheres. In the case of the AlSi12 metal, the large Si content decreased the driving force; the reaction became suppressed and did not take place. The walls of the microspheres remained unharmed as it can be observed in **Figure 4b**. Most of γ-Al_2O_3 was found in the MMSFs with the AlMgSi1 matrix and the above mentioned reaction also took place in the samples with the AlCu5 matrix. In the case of the MMSFs with the AlCu5 matrix, the thermodynamic conditions also enabled the formation of the $CuAl_2$ phase.

To summarize, the microspheres form the Al_2O_3 needles embedded in the mixture of the amorphous SiO_2 and mullite. The chemically reactive molten aluminium can damage the microspheres by reducing their amorphous SiO_2-rich parts. This is undesirable with respect to mechanical properties.

3.2 Investigation of the interface layer between microspheres and the matrix

After a detailed examination of the microspheres' surfaces, the investigations of MMSFs were carried out.

First, EDS overview-map measurements were performed in the microsphere-matrix region of the MMSFs with different matrices. For example, in the case of an Al99.5 matrix with SL300 microspheres, the EDS-map results are shown in **Figure 5**. The area of the SEM image (**Figure 5a**) was investigated for the distribution of the alloying elements (**Figures 5b** to **5d**). The microstructure of the matrix-grain boundaries formed after the solidification can be seen clearly in the concentration differences between aluminium (**Figure 5b**) and silicon (**Figure 5d**) in the EDS images covering all the samples. Oxygen in a higher concentration was only detected in the walls of the microspheres (**Figure 5c**), for all of the samples. In the case of the AlSi12 matrix larger areas of primer silicon were detected as expected. In the samples with the AlCu5 matrix copper-rich precipitations can be observed (with a dimension of approx. 1 μm × 20 μm in **Figure 6**); according to the XRD measurements they are $CuAl_2$ particles. In the samples with the AlMgSi1 matrix magnesium showed a uniform

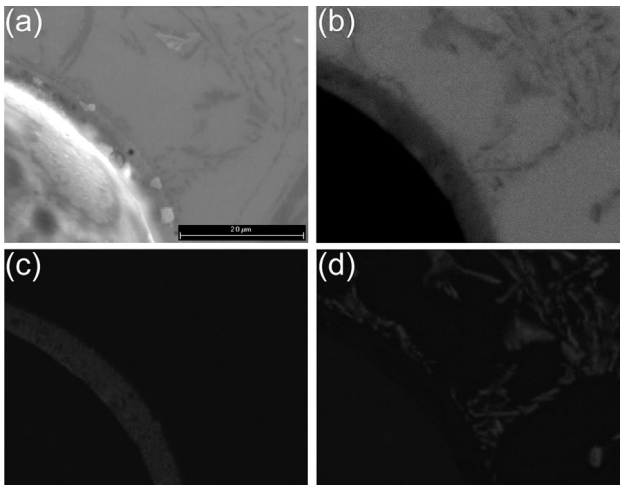

Figure 5: SEM image: a) from an Al99.5-matrix MMSF with an SL300-type microsphere and EDS maps of this area showing element distributions of: b) Al, c) O and d) Si

Slika 5: SEM-posnetek: a) Al99,5 MMSF osnove z SL300 mikrokroglico in EDS razporeditev elementov: b) Al, c) O in d) Si

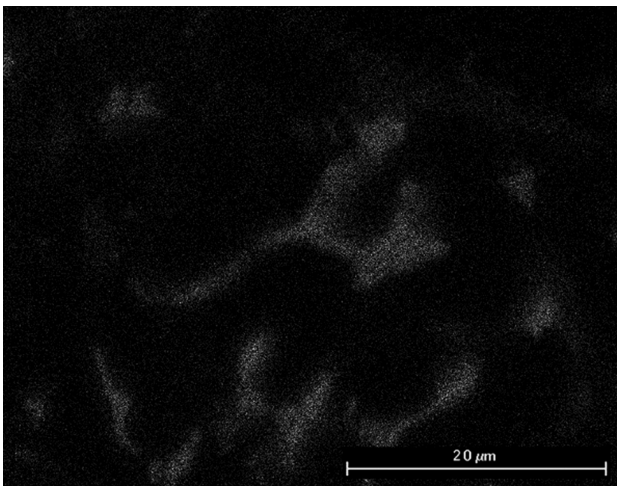

Figure 6: EDS map of an AlCu5-matrix MMSF with an SL150-type microsphere showing copper distribution and precipitations with the $CuAl_2$ phase

Slika 6: EDS-razporeditev bakra in izločki $CuAl_2$ faze v AlCu-osnovi MMSF z mikrokroglico SL150

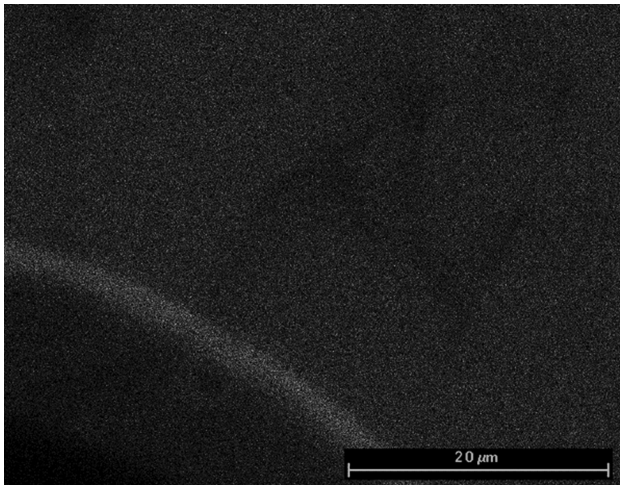

Figure 7: EDS map of an AlMgSi-matrix MMSF with an SL300-type microsphere showing Mg distribution and Mg enrichment in the microsphere's outer wall

Slika 7: EDS-razporeditev in obogatitev Mg v zunanji steni mikrokroglice v AlMgSi-osnovi MMSF z mikrokroglicami SL300

distribution in the aluminium areas, and no magnesium was detected in the primer silicon precipitations at all. Magnesium enrichment was detected alongside the microspheres' outer walls (**Figure 7**) indicating the solution of magnesium in the microspheres walls. For a more detailed investigation of the microsphere interface-matrix region, EDS line measurements were done at a higher resolution.

EDS line measurements were performed on polished specimens perpendicular to the interface layer between the microspheres and the matrix material. The interface layer is very important, because it is responsible for the load transfer from the matrix to the microspheres. The line-scan profiles showed the alternation of chemical elements along the line. The biggest advantage of the EDS line method is that it offers a very good opportunity to examine the interface layer and the changes in a hollow-microsphere wall in the matrix. Examples for the AlMgSi1 and the AlCu5 matrices are shown in **Figures 8** and **9**, respectively.

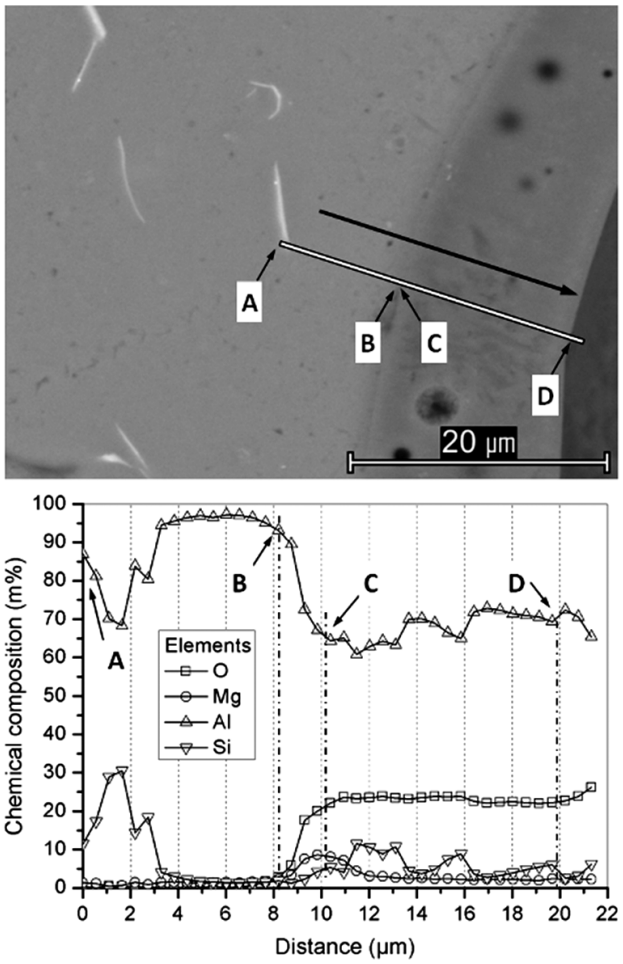

Figure 8: BSE image and EDS line-scan profiles of the AlMgSi-SL150 syntactic foam

Slika 8: BSE-posnetek in profil EDS-linijske analize pene, skladne z AlMgSi-SL50

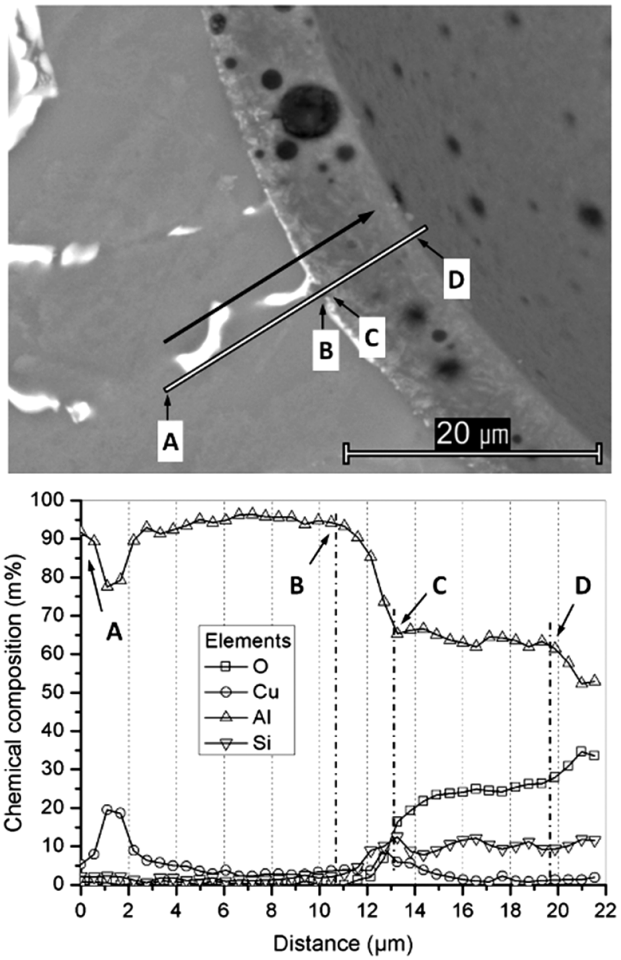

Figure 9: BSE image and EDS line-scan profiles of the AlCu5-SL300 syntactic foam

Slika 9: BSE-posnetek in profil EDS-linijske analize pene, skladne z AlCu5-SL300

In **Figure 8**, the wall of an SL150-type hollow microsphere can be observed in the high-magnification BSE image. It can be seen that the outer edge of the wall is not very well defined. This means that the surface of the microsphere is degraded. As mentioned above, the exchange reaction produces Al_2O_3, which is advantageous, but not at the price of degrading the hollow microsphere's wall. The diffusion process made a relatively wide interface layer on the outer surface of the hollow microspheres (i.e. from point B to point C). The width of the interface layer was relatively wide ≈2–4 μm (in previous research it was 6 μm [20]) and it was measured between the significant changes of the derivation of the fitted curves showing the changing of the Al. Along the interface the Si and Al contents increased and decreased, respectively, with a moderate slope. After point C the Al content was alternated according to the actual composition of the wall. From point D the measurement is not reliable because of the curvature of the inner surface of the hollow microsphere.

In all of the aluminium and Al-alloy matrices the alternation of the Al and Si contents was observed because of the presence of the primer-Si precipitations in the alloy. In the case of the AlMgSi1 matrix (**Figure 8**) such primer-Si precipitation can be seen between points A and B. Points B and C were close to each other. This indicates that there is a very narrow (i.e. less than 3 μm) observable interface layer. In the concentration-sensitive BSE image, the lighter needle-like phases can be observed again in the walls of the SL150 spheres. The increase of the Mg content after point B confirms the presence of the magnesium solution in the microsphere wall, less than 4 μm deep (this was also indicated by the EDS map measurements). In the case of the AlCu5 matrix (**Figure 9**) a precipitation (the $CuAl_2$ phase) can be observed between points A and B, while the interface layer was about 3 μm on both SL150 and SL300 microspheres. Parts of the microspheres' walls were covered with the Cu precipitations, which can be clearly seen on the BSE image, but according to the EDS line measurements (between point B and C) this is not a solution in the microspheres' walls, but just a precipitation on them. In the case of the AlSi12 matrix the outer surface of the microsphere was seemingly unharmed as the exchange reaction was suppressed by the large Si content of the matrix. The interface layer was less than 1.5 μm for both SL-type microspheres.

According to this, a well-defined Al and Si alternation occurred in the line of the EDS analysis diagram. In the lighter areas, the Si content decreased, while the Al content increased. There was no big fluctuation in the oxygen content within the matrix and within the microspheres' walls. This implies that, again, the lighter phases in the walls of the hollow microspheres are the Al_2O_3 particles embedded in the SiO_2 and mullite matrix. At point D, on the inner side of the hollow microsphere's wall, a very narrow Fe, Mg and K rich zone can be observed (originated from the various oxides of the hollow microspheres).

Considering the possibility of chemical reactions between the microspheres and the matrix materials, it is worth mentioning that the ceramic microspheres can be used as a source of alloying elements in the MMSF systems. The appropriate choice and concentration of an alloying element in the wall material, or in the surface coating[8] of the microspheres, can result in precipitation, grain refinement, and microstructure as per the designed scheme. These alloying elements can enhance the mechanical and/or other properties of the MMSFs. However, there is an effective range of the alloying elements due to the limited time after the infiltration and before the cooling. If the effective distance between the microspheres is small enough, it is possible to guarantee a homogenous microstructure. If the distance is larger, then the alloying effects are only in the vicinity of the microspheres.

To summarize, the EDS line measurements are applicable when investigating the interface layer between the microspheres and the matrix material. The investigations proved the presence of the Al_2O_3 needles in the walls and an exchange reaction between the SiO_2 content of the microsphere and the molten aluminium during the production. The suppressing effect of a high Si content was also confirmed. The alloying, or the coating, of the microspheres offers a great opportunity to influence the microstructure and the properties of MMSFs.

The authors assume that the microspheres also have an effect on the orientation and the size of the matrix-material grains. Therefore, the following paper will deal with the electron backscatter diffraction (EBSD) investigation of MMSFs.

4 CONCLUSIONS

From the results of the above mentioned and discussed EDS and XRD measurements, the following conclusions can be drawn:

The microstructures of the microspheres, their volume fraction and properties have a strong effect on the properties of MMSFs. The SEM and EDS investigations showed that Al_2O_3 needles can be found in the walls of the hollow ceramic microspheres. These needles are packed densely and they are embedded in the mixture of mullite and SiO_2.

Due to the uneven distribution of Al_2O_3, SiO_2 rich zones were formed on the surfaces of the microspheres. During the MMSF production the molten aluminium chemically attacked these zones and this reductive chemical reaction resulted in a severe damage of the microspheres' walls.

In the case of the Al99.5, AlCu5 and AlMgSi1 matrices the reaction was intensive. The driving force of the diffusion-controlled reaction was the Si concentration gradient between the microspheres and the matrix. In the

case of the AlSi12-matrix syntactic foams, the reaction was suppressed by a considerable amount of Si in the matrix alloy.

In the case of the AlCu5 matrix, local-copper precipitations were found on the microspheres' walls, while in the case of the AlMgSi1matrix, magnesium was solved into the outer regions of the microspheres' walls.

In addition to the concrete conclusions above, it is worth mentioning that the ceramic microspheres can be used as a source of alloying elements in the MMSF systems. The appropriate choice and concentration of an alloying element in the wall material, or in a surface coating, of the microspheres can enhance the properties of MMSFs.

Acknowledgements

Special thanks to Professor J. T. Blucher for his kind support and to I. Sajó for XRD measurements. The Metal Matrix Composites Laboratory is supported by Grant # GVOP 3.2.1-2004-04-0145/3.0. This paper was supported by the János Bolyai Research Scholarship of the Hungarian Academy of Sciences. The investigations were supported by the Hungarian Research Fund, NKTH-OTKA PD 83687. This work is connected to the scientific programme of the "Development of quality-oriented and harmonized R+D+I strategy and functional model at BME" project. This project is supported by the New Széchenyi Plan (Project ID: TÁMOP-4.2.1/B-09/1/KMR-2010-0002).

5 REFERENCES

[1] N. Babcsán, D. Leitlmeier, J. Banhart, Colloids and Surfaces A: Physicochemical Engineering Aspects, 261 (**2005**), 123–130
[2] N. Babcsán, F. García Moreno, J. Banhart, Colloids and Surfaces A: Physicochemical Engineering Aspects, 309 (**2007**), 254–263
[3] I. N. Orbulov, J. Dobránszky, Periodica Polytechnica Mechanical Engineering, 52 (**2008**), 35–42
[4] http://www.envirospheres.com/products.asp, 30. 11. 2011
[5] http://www.sphereservices.com/, 30. 11. 2011
[6] G. H. Wu, Z.Y. Dou, D. L. Sun, L. T. Jiang, B. S. Ding, B. F. He, Scripta Materialia, 56 (**2007**), 221–224
[7] P. K. Rohatgi, J. K. Kim, N. Gupta, S. Alaraj, A. Daoud, Composites Part A, 27 (**2006**), 430–437
[8] R. A. Palmer, K. Gao, T. M. Doan, L. Green, G. Cavallaro, Materials Science and Engineering A, 464 (**2007**), 85–92
[9] D. K. Balch, J. G. O'Dwyer, G. R. Davis, C. M. Cady, G. T. Gray III, D. C. Dunand, Materials Science and Engineering A, 391 (**2005**), 408–417
[10] W. J. Drury, S. A. Rickles, T. H. Sanders, J. K. Cochran: Light weight alloys for aerospace applications, The Minerals Metals and Materials Society, 1998, 311–322
[11] D. K. Balch, D. C. Dunand, Acta Materialia, 54 (**2006**), 1501–1511
[12] M. Ramachandra, K. Radhakrishna, Journal of Materials Science, 40 (**2005**), 5989–5997
[13] M. Ramachandra, K. Radhakrishna, Wear, 262 (**2007**), 1450–1462
[14] D. P. Mondal, J. Das, N. Jha, Materials Design, 30 (**2008**), 2563–2568
[15] P. K. Rohatgi, R. Q. Guo, Tribologycal Letters, 3 (**1997**), 339–347
[16] P. K. Rohatgi, R. Q. Guo, H. Iksan, E. J. Borchelt, R. Asthana, Materials Science and Technology A, 244 (**1998**), 22–30
[17] T. Bárczy, Gy. Kaptay, Materials Science Forum, 473–474 (**2005**), 297–302
[18] P. K. Trumble, Acta Materialia, 46 (**1998**), 2363–2367
[19] I. N. Orbulov, Á. Németh, J. Dobránszky: Hardness testing of metal matrix syntactic foams, Proceedings of 7th International Conference on Mechanical Engineering, Budapest, Hungary, 2010, 16–22
[20] I. N. Orbulov, J. Dobránszky, Á. Németh, Journal of Materials Science, 44 (**2009**), 4013–4019

UDK 621.9.025.7:669.715:620.179.11
Original scientific article/Izvirni znanstveni članek

ISSN 1580-2949
MTAEC9, 46(4)383(2012)

OPTIMIZATION OF MULTI-PROCESS PARAMETERS ACCORDING TO THE SURFACE QUALITY CRITERIA IN THE END MILLING OF THE AA6013 ALUMINUM ALLOY

OPTIMIZACIJA MULTIPROCESNIH PARAMETROV V ODVISNOSTI OD KAKOVOSTI POVRŠINE KOT MERILA PRI KONČNEM REZKANJU ALUMINIJEVE ZLITINE AA6013

Hülya Durmuş

Celal Bayar University, Engineering Faculty, Department of Materials Engineering, Muradiye, Manisa-Turkey
hulya.kacar@bayar.edu.tr

Prejem rokopisa – received: 2011-12-19; sprejem za objavo – accepted for publication: 2011-12-21

In the study the effects of multi-process parameters on the surface roughness during the machining of the AA6013 aluminum alloy with non-coated cemented carbide milling cutters were investigated by using Taguchi's experimental design method. Experiments were conducted on the basis of Taguchi's L16 orthogonal array (OA) at different levels of the factors relating to the aging process, the cutting speed, the feed rate, the axial depth of a cut and the radial depth of a cut; then they were evaluated through the signal/noise ratio (*S/N*), ANOVA and the main effects' graphic. Accordingly, the lowest surface roughness was estimated to be 0.436 μm and, finally, Taguchi's method allowed the optimization of the system for the verification of the tests.

Keywords: milling, surface roughness, Taguchi's method, aging, experimental design

Raziskan je vpliv multiprocesnih parametrov na hrapavost površine aluminijeve zlitine AA6013, obdelane s karbidnim rezkarjem in z načrtovanjem preizkusov po Taguchijevi metodi. Preizkusi so bili opravljeni na podlagi Taguchijeve ortogonalne porazdelitve L16 po različnem staranju zlitine, pri različnih hitrostih rezkanja, podajanja, aksialne in radialne globine rezov in ocenjeni na podlagi razmerja signal/hrup (*S/N*), ANOVE in grafičnih zapisov glavnih vplivov. Na podagi rezultatov je bila ocenjena kot najmanjša hrapavost površine 0,436 μm, s Taguchijevo metodo pa so bili verificirani preizkusi in optimiziran sistem.

Ključne besede: rezkanje, hrapavost površine, Taguchijeva metoda, staranje, načrtovanje preizkusov

1 INTRODUCTION

Aluminum alloys have been extensively used in aviation, automotive, plastic injection molding and defense industries due to their high resistance/weight ratios, good corrosion/fatigue resistance and high feed rates in recent years. Therefore, studies of the machining of these materials have become more important[1]. Most of the studies have been conducted on milling these materials, frequently focusing on the effects of cutting parameters and tool geometries on surface roughness. The studies conducted on the variation in surface roughness in end milling aluminum are evaluated below.

This is a method, in which effects of only quantitative parameters can be obtained in a small experiment number compared with full factorial experiment design and both the statistical model and the optimization can be obtained. Whang and Chang[2] modeled the effect of cutting parameters and cutter geometry on the surface roughness in milling Al2014-T6 under dry and wet conditions with RSM. It was determined that the factors of the cutting speed, the feed rate, the concavity and the axial gap angle were significant for the variation in the surface roughness under dry conditions, while the feed rate and the concavity angle were significant under wet conditions. Erzurumlu and Öktem[3] modeled the surface roughness of a mold made of AA7075 material with the help of the methods of RSM and artificial neural networks (ANN) and they found that the model based on ANN was higher in accuracy. Routara et al.[4] modeled the machining of the materials of AA6061-T4, AISI 1040 and UNS C34000 with a CVD-coated carbide end mill with RSM. They modeled it as the second-order regression equation for five surface roughness parameters of the depth of a cut, the spindle speed and the feed rate, which were reference parameters in this area, and they accomplished the optimization of the system.

Artificial neural networks, the neural fuzzy logic, fuzzy networks and genetic programming methods are also preferred in this area. Lou and Chen[5] investigated the variation in the surface roughness during the machining of the AA6061 aluminum alloy by considering the cutting parameters (the spindle speed, the feed rate and the depth of a cut) and the vibration criteria through the neural-fuzzy method. Their model predicted the surface roughness at the accuracy rate of 96 %. Chen and Savage[6] predicted the effects of the factors of the spindle speed, the feed rate, the type of the tool material, the tool diameter, and the vibration on the surface roughness in

the milling of AA6061 and AISI 1018 materials with the neural-fuzzy approach. The suggested method predicted surface roughness during cutting with a correlation of 90 %. Brezocnik et al.[7] modeled the effect of the process parameters of the spindle speed, the feed rate, the depth of a cut and the vibration on the surface roughness in the end milling of AA6061 alloy with a HSS plain-end mill by using genetic programming.

Taguchi's method can determine effects of the factors on the quality characteristic with the smallest experiment number without any need for complex calculations, accomplishing the optimization of the system at a certain confidence level. The method is very preferable in this area because it requires only a small experiment number and, as a result, a lower cost and shorter time. Yang and Chen[8] determined the effects of the factors of the spindle speed, the feed rate and the tool diameter on the surface roughness during the machining of AA6061 with a HSS plain-end mill and they accomplished the optimization of the system through Taguchi's method. Lo et al.[9] investigated the effects of the factors of the spindle speed, the feed rate, the depth of a cut and the tool material in the high-speed milling of AA6061 by using Taguchi's method. They evaluated the results of the experiments belonging to the L9 orthogonal array of Taguchi through the S/N ratio and the variance analysis, and presented the significance of the factors and their orders. Öktem et al.[10] evaluated the data obtained in a 3-numbered study by using Taguchi's method and the full factorial experiment-design methods for this time. They modeled the surface roughness at the correlation coefficient of 0.96 by using regression analysis. They found, in the analyses conducted with Taguchi, that the machining tolerance was the most significant factor influencing the roughness, followed by the radial depth of a cut, the axial depth of a cut, the feed rate and the cutting speed per thread. Pinar et al.[1,11,12] investigated the effects of the cutting speed, the feed rate, the depth of a cut and the machining pattern on the surface quality in the milling of the alloys of AA5083, 6013 and 7075 by using Taguchi's method. The experiments conducted on the basis of the standard L27 orthogonal array of Taguchi were assessed by using *S/N*, ANOVA and the main effects' graphics so that the system was optimized.

In this study, unlike other studies, the effect of the aging process, which was imposed on the material, was added to the effects of the other cutting factors (the cutting speed, the feed rate, the axial depth of a cut and the radial depth of a cut) influencing the surface roughness to be analyzed by Taguchi's method so that the system was optimized.

2 MATERIAL AND METHOD

The AA 6013 alloy, whose chemical composition is given in **Table 1**, was used as a test sample. The samples to which precipitation hardening had, or had not, been applied were used in the experiments. The pre-tests were conducted to find the situation, in which the mechanical properties were at their maximum. During the first step of the precipitation hardening, the samples were solution treated at 560 °C for 5 h. Then the quenching step was completed. Finally, the samples were aged processed at 190 °C and their hardness was measured for 42 h once every 2 h to find the optimum aging time. The hardness tests were conducted by using Brinell hardness device. The aging time achieving the maximum hardness was determined to be 32 h (**Figure 1**). The end-milling tests of the aged and non-aged samples were conducted in a vertical machining center of First MCV 300 CNC operating in line with Fanuc control unit. The single-insert non-cemented carbide end mill with a 90-degree incidence, a 14-mm diameter and a 0.8-mm insert diameter, recommend by Mitsubishi Company in end milling of aluminum, was used as the cutting tool

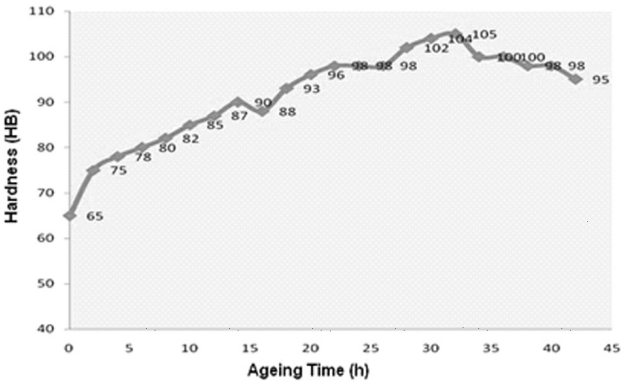

Figure 1: Hardness graph employed in the determination of aging time
Slika 1: Zapis trdote, uporabljen za določitev časa staranja

Figure 2: Cutting tool employed in the experiments
Slika 2: Rezno orodje, uporabljeno pri preizkusih

Table 1: Chemical composition of AA6013 experiment specimen
Tabela 1: Kemična sestava AA6013 raziskanega vzorca

Si	*Fe*	*Cu*	*Mn*	*Mg*	*Zn*	*Cr*	*Al*
1.2	0.339	0.16	0.799	1.01	0.21	0.059	Geri kalan

(**Figure 2**). Machining operations were conducted by up milling with liquid cooling using Ecocool 2030 MB with a 5 % oil emission.

The CNC part programs of the samples were obtained in MasterCAM V10 software as 2½-axial contour machining. The cutting parameters were specified on the basis of the manufacturer's catalog data and bench capacity. The surface-roughness measurements were repeated three times perpendicular to the machining traces through Mitutoyo Surftest SJ 311 profilometer operating on the basis of the insert principle. Their arithmetical means were used in the statistical analyses.

3 EXPERIMENTAL DESIGN AND STATISTICAL ANALYSIS

Taguchi, which has become prevalently preferable in recent years, only requiring experiments in a small number and allowing system optimization without the need for complex mathematical calculations, was used for the experimental design and the statistical-analysis method[13,14].

The system design is the part, in which the factors affecting the quality characteristic to be investigated and their degrees are determined and it requires technical data related to engineering knowledge in this area. The parameter design is the most comprehensive and important step of Taguchi's method. In this phase, the experiments conducted on the basis of the specified experiment plan are analyzed, the optimum levels for the factors are determined and the optimum dependent variable is predicted for these levels. The final step is the tolerance design, in which the average result of the verification experiments is checked to find out whether or not it is within the specified confidence interval[12].

4 APPLICATION OF THE OPTIMIZATION PROCESS

In the present study, the effects of the process parameters, which are the cutting speed, the feed rate, the radial/axial depth of a cut and the aging, as well as their dual interactions on an average surface roughness (R_a/μm) are evaluated and the system is optimized. **Table 2** shows the factors used in the experimental system and their levels.

Table 2: Choosen factors and their levels
Tabela 2: Izbrani faktorji in njihovi nivoji

Factors		Level	
		1	2
Cutting speed (A)	m/min	100	300
Feed (B)	mm/min	100	1200
Axial depth of cut (C)	mm	0.75	2
Radial depth of cut (D)	mm	5	10
Ageing treatment (E)	–	No	Yes

The OA establishing the experimental plan is selected on the basis of the degree of freedom. Accordingly, the freedom degree of the OA to be selected should be higher than, or equal to, the freedom degree of the system[1]. The freedom degree (FD) of the experimental system is obtained by summing up the freedom degrees of the factors and their interactions. The freedom degree of the experimental system is specified according to the number of the factor level interaction. The freedom degree of a factor is specified as the level number of that factor-1. Accordingly, because there are 5 factors, the freedom degree of the factors is 5 × 1 = 5. In case of interactions, individual freedom degrees of the factors establishing interactions are multiplied to calculate the overall freedom degree. Accordingly, because there are 10 interactions, their freedom degree is 10 × 1 = 10. The freedom degree of the system is 15 being the summation of 5 + 10. According to this data, L16 OR with the freedom degree of 15, having 15 columns and 16 rows was selected. If the same factors were investigated by using the full factorial experimental design method, 25 experimental studies would be required. Thus, the saving in terms of the number of experiments is 50 %. Consequently, savings were obtained in time, sample cutters and the power consumed by the bench. The factors and their interactions were transferred to the columns of OA by using the linear graphic method (**Figure 3**). In line with this, the first column was assigned to the cutting speed, while the second was assigned to the feed rate. The forth column was assigned to the axial depth of a cut, the eighth to the radial depth of a cut, the fifteenth to the aging and the remaining columns were assigned to the interactions.

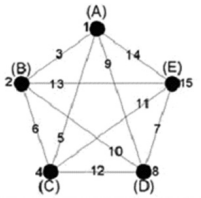

Exp. Number	Column Number														
	1	2	3	4	5	6	7	8	9	10	11	12	13	14	15
	A	B	AXB	C	AXC	BXC	-	D	AXD	BXD	-	CXD	-	-	-
1	1	1	1	1	1	1	1	1	1	1	1	1	1	1	1
2	1	1	1	1	1	1	1	2	2	2	2	2	2	2	2
3	1	1	1	2	2	2	2	1	1	1	1	2	2	2	2
4	1	1	1	2	2	2	2	2	2	2	2	1	1	1	1
5	1	2	2	1	1	2	2	1	1	2	2	1	1	2	2
6	1	2	2	1	1	2	2	2	2	1	1	2	2	1	1
7	1	2	2	2	2	1	1	1	1	2	2	2	2	1	1
8	1	2	2	2	2	1	1	2	2	1	1	1	1	2	2
9	2	1	2	1	2	1	2	1	2	1	2	1	2	1	2
10	2	1	2	1	2	1	2	2	1	2	1	2	1	2	1
11	2	1	2	2	1	2	1	1	2	1	2	2	1	2	1
12	2	1	2	2	1	2	1	2	1	2	1	1	2	1	2
13	2	2	1	1	2	2	1	1	2	2	1	1	2	2	1
14	2	2	1	1	2	2	1	2	1	1	2	2	1	1	2
15	2	2	1	2	1	1	2	1	2	2	1	2	1	1	2
16	2	2	1	2	1	1	2	2	1	1	2	1	2	2	1

Figure 3: Assignment of the factors and interactions to L27 OA by means of linear graph
Slika 3: Porazdelitev faktorjev in interakcij za L27 OA z linearno grafiko

4.1 Analyzing the data

The experimental results given in **Table 3** were evaluated by using the signal/noise ratio (*S/N*), the variance analysis and the main effects' graphic, with the help of Minitab software, at the confidence level of 95 %.

4.1.1 S/N ratio analysis

Taguchi's method uses the signal/noise ratio to measure the existing variation. Description of the *S/N* ratio varies according to the objective function or, in other words, quality characteristic to be investigated. Three different *S/N* ratios are used in the analyses as the nominal values are the best (NB), smaller is better (SB) and bigger is better. Since the average surface roughness was investigated in the study as the quality characteristic and the objective was a minimization of these parameters, the SB was selected as the NB. The following equation refers to it.

$$S/N = -10\lg\left[\frac{1}{n}\sum_{i=1}^{n} y_i^2\right] \quad (1)$$

Herein, n represents the number of measurements and y_i is the measured roughness value. The *S/N* ratio unit is a decibel. **Table 3** shows the results of the experiments conducted on the basis of the L16 orthogonal array, the means and the corresponding *S/N* ratios.

4.1.2 ANOVA

In the study, the influence of the process parameters on the quality characteristic and percentage distributions were established through ANOVA. **Tables 4 and 5** give ANOVA results corresponding to the means and *S/N* ratios. The significance of the process parameters and their interactions are determined in ANOVA by comparing the *F* values (the ratio of the relevant parameter's variance to the error variance) in the fifth column of the tables with the corresponding F_{table}. If a process or an

Table 3: Experimental results, means and corresponding S/N ratios
Tabela 3: Eksperimentalni rezultati, povprečja in ustrezna razmerja S/N

Exp. Number	Cutting speed (A)	Feed (B)	Axial depth of cut (C)	Radial depth of cut (D)	Ageing treatment (E)	R_{a1}	R_{a2}	R_{a3}	R_{aort}	*S/N*
1	100	100	0.75	5	No	0.58	0.58	0.58	0.580	4.731
2	100	100	0.75	10	Yes	0.76	0.76	0.8	0.773	2.230
3	100	100	2	5	Yes	0.8	0.8	0.8	0.800	1.938
4	100	100	2	10	No	0.84	0.81	0.81	0.820	1.722
5	100	1200	0.75	5	Yes	0.9	0.94	0.91	0.917	0.754
6	100	1200	0.75	10	No	0.92	0.95	0.94	0.937	0.568
7	100	1200	2	5	No	1.11	1.12	1.13	1.120	-0.985
8	100	1200	2	10	Yes	1.2	1.2	1.26	1.220	-1.730
9	300	100	0.75	5	Yes	0.38	0.38	0.38	0.38	8.404
10	300	100	0.75	10	No	0.4	0.4	0.4	0.4	7.959
11	300	100	2	5	No	0.62	0.64	0.65	0.637	3.920
12	300	100	2	10	Yes	0.7	0.66	0.67	0.677	3.390
13	300	1200	0.75	5	No	0.78	0.78	0.82	0.793	2.008
14	300	1200	0.75	10	Yes	0.8	0.8	0.84	0.813	1.792
15	300	1200	2	5	Yes	0.9	0.89	0.9	0.897	0.947
16	300	1200	2	10	No	0.9	0.9	0.92	0.907	0.851

Table 4: ANOVA results for means
Tabela 4: ANOVA rezultati za povprečja

Source	SD	SS	V	F	F_{table}	KT'	P
Cutting speed (A)	1	0.172917	0.172917	44.94	4.75	0.169069	22.28
Feed (B)	1	0.402167	0.402167	104.51	4.75	0.398319	52.49
Axial depth of cut (C)	1	0.137517	0.137517	35.74	4.75	0.133669	17.62
Radial depth of cut (D)	(1)	(0.011201)		Pooled	–	Pooled	–
Ageing treatment (E)	(1)	(0.005017)		Pooled	–	Pooled	–
AxB	(1)	(0.000584)		Pooled	–	Pooled	–
AxC	(1)	(0.000034)		Pooled	–	Pooled	–
AxD	(1)	(0.003701)		Pooled	–	Pooled	–
BxC	(1)	(0.000851)		Pooled	–	Pooled	–
BxD	(1)	(0.000951)		Pooled	–	Pooled	–
Error	12	0.046176	0.003848			0.05772	7.61
Total	15	0.758777				0.758777	100

SD: Degree of freedom, SS: Sum of squares, V: Variance, KT': Pure sum of squares, P: Percent of contribution

Table 5: ANOVA results for S/N ratios
Tabela 5: ANOVA rezultati za razmerje S/N

Source	SD	SS	V	F	F_{tablo}	SS'	P
Cutting speed (A)	1	25.104	25.1044	27.42	4.75	24.188	20.85
Feed (B)	1	56.584	56.5838	61.80	4.7	55.668	48.00
Axial depth of cut (C)	1	21.144	21.1439	23.09	4.75	20.228	17.44
Radial depth of cut (D)	(1)	1.524	-	Pooled	-		
Ageing treatment (E)	(1)	0.581	-	Pooled	-		
AXB	(1)	2.295	-	Pooled	-		
AXC	(1)	0.865	-	Pooled	-		
AXD	(1)	0.348	-	Pooled	-		
BXC	(1)	2.493	-	Pooled	-		
BXD	(1)	0.375	-	Pooled	-		
Error	12	10.988	0.9157			15.903	13.71
Total	15	115.987				115.987	100

SD: Degree of freedom, SS: Sum of squares, V: Variance, KT': Pure sum of squares, P: Percent of contribution

interaction parameter has a *F* value higher than this value, it is deemed significant. Thus, it was observed that the process parameters of the cutting speed, the feed rate and the axial depth of a cut were significant, while their interactions did not have a significant effect on surface roughness in the cases of the two ANOVAs. Percentage distributions are given in the last column of the ANOVA table indicating significance degree of each of the process parameters and dual interactions. On the basis of this data, it can be established that the most significant process parameter is the feed rate, followed by the cutting speed and the axial depth of a cut. In Taguchi's method the factor levels indicating the optimum surface roughness are determined by considering ANOVAs, the main effects' and interactions' graphics. Significant parameters are considered in both ANOVAs in the calculation of the optimum surface roughness. According to this, the means of the parameters of the feed rate, the cutting speed and the axial depth of a cut will be considered. The levels to be selected are determined by using the main effects' and interactions' graphics. As none of the interactions in the experimental system is significant, the main effects' graphic will be sufficient in this phase. **Figure 4** shows the main effects' graphic. According to this graphic, surface roughness varies depending on the cutting speed in inverse proportion and also on the feed rate, the axial depth of a cut and the radial depth of a cut in direct proportion. In the case of the aging-state parameter, it was seen that surface roughness increased a bit during the machining of the aged samples. According to this data, the optimum surface roughness was achieved at the cutting rate of 300 m/min, a feed rate of 100 mm/min, an axial depth of a cut of 0.75 mm and a radial depth of a cut of 5 mm in non-aged samples. The optimum surface roughness is obtained through the following equation:

$$P_r = O_{A2} + O_{B1} + O_{C1} - 2K \quad (2)$$

Herein, O_{A3} stands for the means from the experiments conducted at the second level of the cutting speed. O_{B1} stands for the means from the experiments conducted at the first level of the feed rate. O_{C1} stands for the means from the experiments conducted at the first level of the axial depth of a cut. *K* stands for the means from all experiments. **Table 6** shows the relevant means. According to Equation 2, the optimum surface roughness was predicted to be 0.436 μm.

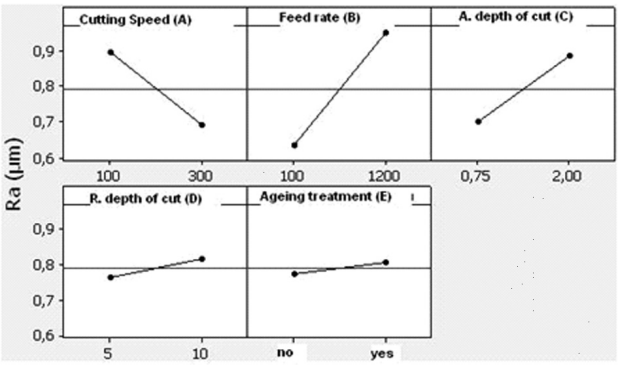

Figure 4: Main effects plot of the factors
Slika 4: Glavne povezave faktorjev

Table 6: Means of factor levels
Tabela 6: Nivoji povprečnih faktorjev

Level	Cutting speed (A)	Feed rate (B)	Axial depth of cut (C)	Radial depth of cut (D)	Ageing treatment (E)
1	0.8958	0.6333	0.6992	0.7654	0.7742
2	0.6879	0.9504	0.8846	0.8183	0.8096
Delta	0.2079	0.3171	0.1854	0.0529	0.0354
Rank	2	1	3	4	5

Overall average (K)=0.792μm

In the last step of Taguchi, called the tolerance design, the confidence interval is determined, in which the upper and the lower limits of the existing predicted surface roughness are determined. The means of the roughness results from the conducted verification tests should be within this interval. The following equation is used to calculate the confidence interval[12,14].

$$CI = \left(F_{\mathrm{CI}} \cdot V_{\mathrm{e}} \left[\frac{1}{n_{\mathrm{eff}}} + \frac{1}{R} \right] \right)^{1/2} \quad (3)$$

Herein, F_{CI} is obtained from the standard tables at the significance level of 0.05 according to the freedom degree of 1 including an error and it is 4.75. V_{e}, is the variance value of the error in the ANOVA table and calculated as 0.003848 (**Table 4**). R is how many times the verification tests are repeated under optimum conditions (3) and finally, n_{eff} is the effective repeat number. This was obtained by using the following equation.

$$n_{\mathrm{eff}} = \frac{N}{1+V_{\mathrm{t}}} \quad (4)$$

Herein, N is the total number of the experiments in the experimental plan (16), while V_{t} is the total freedom degree of the factors existing in the equation, through which the optimum surface roughness is predicted (3). Accordingly, CI was calculated to be 0.103 at the confidence level of 95 % or at the significance level of 0.05. The mean of the results of the verification tests repeated three times should be within the interval of $0.333 < R_{\mathrm{a}} < 0.539$. The average surface roughness was determined to be 0.343 μm (0.35, 0.34 and 0.34 μm respectively) in the verification tests conducted under the optimum conditions. According to this data, it is clearly seen that Taguchi's method optimized the system successfully.

5 CONCLUSION

In the present study, the effects of multi-process parameters (the cutting speed, the feed rate, the axial depth of a cut, the radial depth of a cut and the aging state) and their dual interactions on the surface roughness in the end-milling operations were evaluated and the following conclusions were achieved:

Surface roughness varies depending on the cutting speed in inverse proportion and on the feed rate, the axial depth of a cut and the radial depth of a cut in direct proportion. It was seen that surface roughness increased a bit during the machining of aged samples.

Only the cutting speed, the feed rate and the axial depth of a cut are significant for both ANOVAs. It is seen that the most significant process parameter is the feed rate followed by the cutting speed and the axial depth of a cut.

The optimum surface roughness was predicted to be 0.436 μm found in the case of the second cutting speed (A = 300 m/min), the first feed rate (B = 100 mm/min), the first axial depth of a cut (C = 0.75 mm), the first radial depth of a cut (D = 5) and under the non-aging conditions. The average surface roughness was found to be 0.343 μm in the verification tests that were repeated three times, and it existed within the specified confidence interval. Thus, the system was optimized successfully. Furthermore, the minimum surface roughness was found to be 0.38 μm in the nine-number experiment in the experimental plan (A = 300 m/min, B = 100 mm/min, C = 0.75 mm, D = 5 mm E: yes). With the result obtained during the verification tests an improvement of 9.74 % was obtained.

6 REFERENCES

[1] A. M. Pinar, E. Atik, U. Cavdar, A. F. Pinar: AA5083 Alaşımın Frezelenmesinde Yüzey Kalitesini Etkileyen Faktörlerin İstatistiksel Olarak Değerlendirilmesi, 14. Uluslararası Makina Tasarım ve İmalat Kongresi, Guzelyurt, KKTC, 789–804, 29 Haziran–02 Temmuz 2010

[2] M. Y. Wang, H. Y. Chang, Int. J. Mach. Tools Manufact., 44 (**2004**), 51–57

[3] T. Erzurumlu, H. Öktem, Mater. Des., 28 (**2007**), 459–465

[4] B. C. Routara, A. Bandyopadhyay, P. Sahoo, Int. J. Adv. Manuf. Tech., 40 (**2009**), 1166–1180

[5] S. J. Lou, J. C. Chen, Int. J. Adv. Manuf. Tech., 15 (**1999**), 200–209

[6] J. C. Chen, A. Savage, Int. J. Adv. Manuf. Tech., 17 (**2001**), 670–676

[7] M. Brezocnik, M. Kovacic, M. Ficko, Journal of Materials Processing Technology, 157/158 (**2004**), 28–36

[8] J. L. Yang, J. C. Chen, Journal of Industrial Technology, 17 (**2001**) 2, 1–8

[9] S. P. Lo, J. T. Chiu, H. Y. Lin, Int. J. Adv. Manuf. Tech., 26 (**2005**), 1071–1077

[10] H. Öktem, T. Erzurumlu, M. Çöl, Int. J. Adv. Manuf. Tech., 28 (**2006**), 694–700

[11] A. M. Pinar, E-Journal of New World Sciences Academy, 5 (**2010**) 1, 15–27

[12] A. M. Pinar, O. Uluer, V. Kirmaci, International Journal of Refrigeration, 32 (**2009**), 1487–1494

[13] A. M. Pinar, O. Uluer, V. Kirmaci, Experimental Heat Transfer, 22 (**2009**), 271–282

[14] P. J. Ross, Taguchi Techniques for Quality Engineering, McGraw Hill, New York 1988

UDK 669.131.6:536.421.4
Professional article/Strokovni članek

ISSN 1580-2949
MTAEC9, 46(4)389(2012)

NUMERICAL AND EXPERIMENTAL ANALYSES OF THE CHEMICAL HETEROGENEITY OF A SOLIDIFYING HEAVY DUCTILE-CAST-IRON ROLLER

NUMERIČNA IN EKSPERIMENTALNA ANALIZA KEMIJSKE HETEROGENOSTI STRJEVANJA LITEGA TEŽKO GNETLJIVEGA ŽELEZNEGA VALJA

Karel Stransky[1], Frantisek Kavicka[1], Bohumil Sekanina[1], Jana Dobrovska[2], Vasilij Gontarev[3]

[1]Brno University of Technology, Technická 2, 616 69 Brno, Czech Republic
[2]VSB TU Ostrava, 17.listopadu 15, 708 33 Ostrava, Czech Republic
[3]University of Ljubljana, Aškerčeva 12, 1000 Ljubljana, Slovenia
stransky@fme.vutbr.cz

Prejem rokopisa – received: 2011-10-17; sprejem za objavo – accepted for publication: 2012-02-24

The quality of the working rollers used for rolling rails is determined by the chemical and structural compositions of the material of the rollers and the production technology. It is necessary to cast rollers with significantly improved utility properties, i.e., mainly a high wear resistance and optimal mechanical and structural properties. It is, therefore, necessary to find and ensure the optimal relationships between the matrix structure and the resulting values of the mechanical properties of the rollers in order to maximize their life time. The requirements introduced here cannot be ensured without a knowledge of the kinetics of the solidification. Therefore, numerical and experimental investigations of the temperature field of the solidifying roller were conducted. The kinetics of the solidification has a measurable and non-negligible influence on the chemical and structural heterogeneity of the investigated type of ductile cast-iron. Linking to the results of the model of the temperature field of the cast rollers, an original methodology was developed for the measurement of chemical micro-heterogeneity. The structure of this cast-iron is created by a large amount of the transition form of graphite and a small amount of globular graphite, and also the lamellar graphite and cementite, whereas the structure of the metal matrix is perlitic. The volume amounts of the structural components were determined using a quantitative metallographic analysis, according to which the places for the analysis of the element composition using X-ray energy-dispersive spectral micro-analysis were selected. The chemical and structural heterogeneity of the cast roller is, therefore, a significant function of the method of melting, modification and inoculation and the successive procedures of risering, casting and crystallization after cooling.

Keywords: spheroidal graphite cast iron, roller, solidification, chemical and structural heterogeneity, methodology for measurement

Kakovost delovnih valjev za valjanje tirnic je določena s kemijsko in strukturno sestavo materiala za valje in s tehnologijo proizvodnje. Potrebno je ulivati valje z znatno povečanimi koristnimi lastnostmi, kot so obrabna odpornost in optimalne mehanske in strukturne lastnosti. Tako je treba ugotoviti in zagotoviti optimalne odnose med strukturo matrice in rezultirajočimi vrednostmi mehanskih lastnosti valjev za maksimiranje trajnostne dobe. Zahteve, ki so tu predstavljene, ne morejo biti zagotovljene brez znanja kinetike strjevanja. Zato je bila vpeljana numerična in eksperimentalna raziskava temperaturnega polja valja pri strjevanju. Kinetika strjevanja ima merljiv in ne brezpomemben vpliv na kemijsko in strukturno heterogenost raziskovanega gnetljivega litega železa. Glede na rezultate modela temperaturnega polja ulitih valjev je bila razvita originalna metodologija za merjenje kemijske mikroheterogenosti. Struktura tega ulitega železa je bila ustvarjena z veliko količino prehodnih oblik grafita in manjših količin kroglastega grafita in cementita, medtem ko je struktura kovinske osnove perlitna. Volumenska količina strukturnih komponent je bila določena s kvantitativno metalografsko analizo, po kateri so bila izbrana mesta za rentgensko analizo sestave ter spektrografsko mikroanalizo. Kemijska in strukturna heterogenost ulitih valjev je pomembna funkcija pri taljenju in modificiranju ter za uspešno ulivanje in kristalizacijo po ohlajevanju.

Ključne besede: siva litina s kroglastim grafitom, valj, strjevanje, kemijska in strukturna heterogenost, metodologija meritev

1 INTRODUCTION

The kinetics of solidification has a non-negligible influence on the chemical and structural heterogeneity of the cast-iron in question[1]. An original methodology for the measurement of the micro-heterogeneity was developed, based on the results of the model of the temperature field of the cast rollers. The chemical and structural heterogeneity of the cast roller has proven to be a significant function of the method of melting, modification and inoculation and the successive procedures of risering, casting and crystallization after cooling.

2 STRUCTURAL AND CHEMICAL HETEROGENEITY OF THE ROLLER

The final mechanical properties of the rollers – of the spheroidal graphite cast-iron – are determined, not primarily by the chemical composition, but mainly by their structural and chemical heterogeneity, which occurs during casting, crystallization and successive cooling of the material. Some defects occurring in this way can be corrected by heat treatment; however, the quality of the pouring structure is very important, especially with graphite cast-iron.

The chemical composition is given in **Table 1**.

The samples used for determining the structural and chemical heterogeneity were taken from the spheroidal graphite cast-iron roller with the chemical composition given in **Table 1** from the upper part (Section III) and from the bottom part (Section I). **Figure 1** shows how the four samples were taken, with the upper surfaces – marked "X" – being analyzed. In addition, they were specified as follows:

- The upper part of the roller on the outer surface ($R1$ = 540 mm) marked TR1, TR2
- The upper part of the roller on the inner surface ($R4$ = 400 mm) marked TR3, TR4
- The lower part of the roller on the outer surface marked BR1, BR2
- The lower part of the roller on the inner surface marked BR3, BR4

The actual analyses were conducted at a specialized workplace[2,3]. The structural analysis of the cast-iron samples was conducted using a Neophot 32 metallographic microscope and an Olympus digital camera. The measurements of the metallographic parameters of the graphite and the evaluation of the volume part of the structural components were conducted on the Olympus CUE4 image analyzer. The basic statistical parameters of the graphite particles and also the stereological estimate of certain other parameters[2] were calculated from the data files.

The JSM-840 (JEOL) electron scanning microscope was used for determining the chemical heterogeneity together with the LINK AN 10/85S X-ray energy-dispersive microanalyzer. Based on the results of the metallographic analysis[2], two pairs of graphite grains were selected on the ground surface of every sample in order for the line of measurement between the first pair to pass through the perlite (marked "a") and the cementite (marked "b"). The third line was selected through two boundaries created by particles of lamellar graphite, where the measurement passes through the basic perlite (marked "c"). The individual elements (Si, P, Mo, Cr, Mn, Fe, Ni, and Cu) were analyzed by means of a point

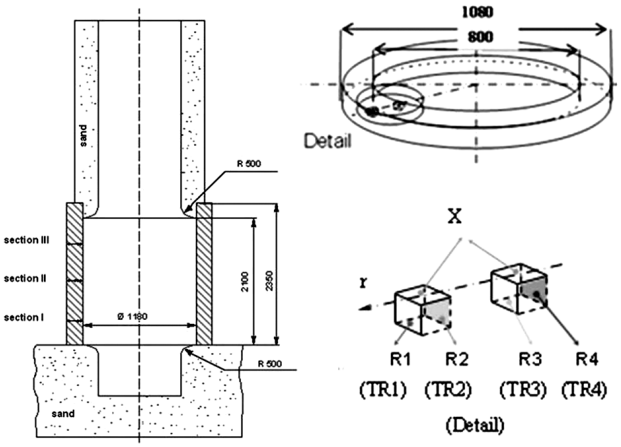

Figure 1: The set-up of a vertically cast roller and sampling
Slika 1: Pogled na navpično ulit valj in vzorčenje

X-ray microanalysis in a direct line with a step of 3 μm [3,4]. **Figure 2** illustrates the material around the selected line of the measurement on sample TR1 through the scanning electron microscope and the X-ray energy-dispersive microanalyzer. Following the chemical (elemental) analysis, the samples were etched using 2 % nital in order to make the contamination traces visible and display the line of measured points, including their connection to the sample microstructure.

2.1 Structural heterogeneity

Based on experience, it can be assumed that the structure of the material of the casting, spheroidized graphite cast iron (named "ductile cast-iron" for working purposes) will, besides the globular graphite that is characteristic of ductile cast-iron, also contain a mixture of a certain amount of transition forms of graphite and lamellar graphite found between the globular and lamellar graphite. **Table 2** shows the results from the quantitative metallographic analyses of the structures of the samples in **Figure 1**. The procedure of the quantitative structural measurements, including the results, is described in detail in a special report[2].

Table 1: The chemical composition of ductile cast-iron B10 (*w*/%)
Tabela 1: Kemijska sestava sive litine B10, z globularnim grafitom (*w*/%)

Cast-iron B10										
Element	C	Mn	Si	P	S	Cr	Ni	Mo	Mg	Cu
Content (%)	3.31	0.65	0.70	0.105	0.005	0.35	2.59	0.59	0.04	1.48

Table 2: The results from the quantitative measurements of the volume part of the components (in volume fractions, φ/%)
Tabela 2: Rezultati kvantitativnih meritev volumenskega dela komponent (volumenski deleži, φ/%)

Sample	All graphite, incl. micro-shrinkages	Globular graphite	Transition forms of graphite and lamellar graphite	Cementite	Perlite
BR1	10.5 ± 2.8	1.3	9.2	2.2 ± 1.7	87.3
BR3	13.0 ± 5.4	1.1	11.9	1.2 ± 1.2	85.8
TR1	13.4 ± 5.6	1.1	12.3	2.2 ± 1.8	84.4
TR3	12.6 ± 5.7	1.1	11.5	1.3 ± 1.4	86.1

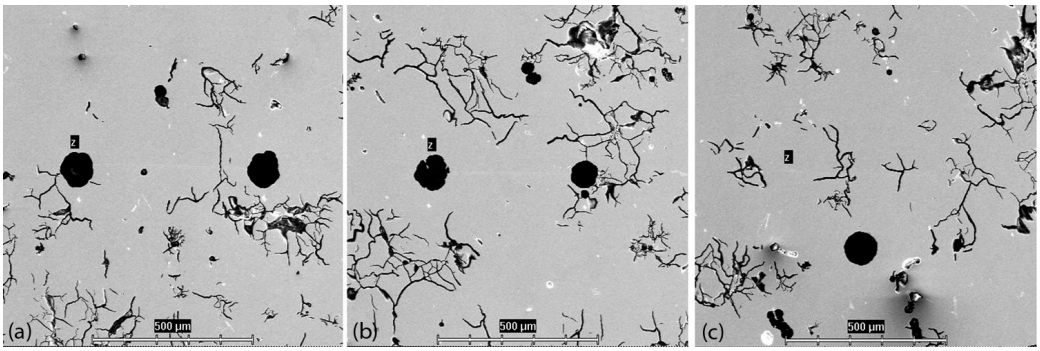

Figure 2: The structures in the area of sample TR1 selected for analysis: a) between two spheres of graphite through perlite, b) between the two spheres of graphite through cementite, c) through lamellar graphite

Slika 2: Strukture v območju vzorca TR1 za analizo: a) med dvema kroglama grafita v perlitu, b) med dvema kroglama grafita v cementitu, c) v lamelnem grafitu

2.2 Chemical heterogeneity

The distribution of the concentration of the eight elements, measured three times in one line for each of the samples (**Figures 2a–c**), was evaluated using statistics: the arithmetic mean of the concentration of the element in the selected interval c_{st}, the standard deviation σ_{n-1} of the measured concentration, the minimum concentration c_{min} and the maximum c_{max} – measured each time in the selected interval of the sample (in mass fractions, *w*/%). Besides these basic concentration parameters, the segregation index of each measured element was determined and defined as $I_S = c_{max}/c_{st}$, i.e., as the quotient of the maximum concentration of elements measured on the given interval and the arithmetic mean of its concentration in the same interval. The tendency of the element to segregate – based on experience – is expressed in the values of the segregation indexes. A detailed description of the measurement procedure and the corresponding results can be found in the reports[3,4].

Figure 3 illustrates the values of this parameter for individual elements and samples measured in one line across the lamellar graphite – c. Similarly, the segregation index values can be plotted for the area between the globular graphite in a line across perlite – a, and also in the area between the globular graphite in a line across cementite – b. **Figure 4** shows the segregation index values for the elements calculated as the average of the values for all three areas – a, b, c. Furthermore, the graphs in **Figures 3** and **4** also indicate that the segregation indexes of the highest values – from the set of measured elements – belong to phosphorus and molybdenum, and the lowest values refer to nickel and iron, which make up the matrix.

3 CONCLUSION

This article introduces an original methodology for the measurement of the chemical heterogeneity of cast-iron of the composition given in **Table 1**. The structure of this cast-iron is created by a large amount of the transition form of graphite and small amount of

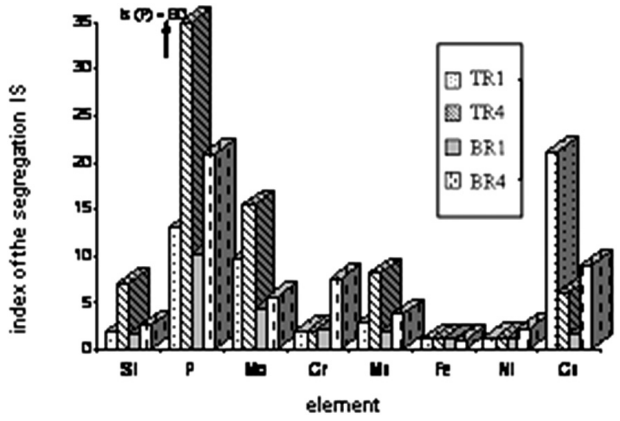

Figure 3: The index of the segregation of elements for individual samples in the area of the transition graphite in the measured area across lamellar graphite

Slika 3: Indeks izcejanja elementov posameznih vzorcev v območju prehoda grafita v merjeno področje lamelnega grafita

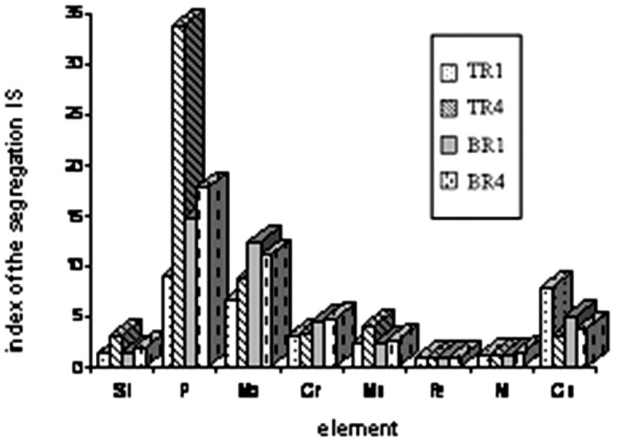

Figure 4: The average index of segregation of the analyzed elements in individual samples

Slika 4: Povprečni indeks izcejanja analiziranih elementov v posameznih vzorcih

globular graphite and also lamellar graphite and cementite, whereas the structure of the metal matrix is perlitic. The volume amounts of the structural components were determined using a quantitative metallographic analysis, which was simultaneously the basis for the selection of the places for the analysis of the element composition using an X-ray energy-dispersive spectral microanalysis. Inside the microstructure of four samples, taken from the outer and inner parts of the ring at the top and bottom of the roller (**Figure 1**), in a total of twelve areas, the linear concentration dispersion was measured on the eight elements which make up the basic constitution of the cast-iron: Si, P, Mo, Cr, Mn, Fe, Ni, and Cu. A statistical analysis was used to determine the distribution characteristics of the concentration of the individual elements, including the segregation indexes and the relationships among them. In this way it was possible to assess the influence of the changing kinetics of the temperature field on the resultant structural and chemical heterogeneity of the roller. The kinetics of the solidification of the cast-iron roller had a non-negligible influence on the chemical and structural heterogeneity of the investigated type of cast-iron. It is obvious that the chemical and structural heterogeneity of the cast roller is a significant function of the method of melting, modification and inoculation and the successive procedures of risering, casting and crystallization after cooling.

Acknowledgements

This analysis was conducted using a program devised within the framework of the GACR projects No. 106/08/0606, 106/09/0940, 106/09/0969 and P107/11/1566.

4 REFERENCES

[1] F. Kavicka et al.: Numerical optimization of the method of cooling of a massive casting of ductile cast-iron. In: Book of Abstracts and CD ROM of the 13th International Heat Transfer Conference, Sydney, Australia, August 2006, 27

[2] J. Belko, K. Stransky, Structural analysis of cast-iron samples (in Czech). Research report, VTUO Brno, 2005

[3] Z. Winkler, K. Stransky, Microheterogeneity of the composition ductile cast-iron samples alloyed with Mn, Cu, Ni and Mo (in Czech). Research report, VTUO Brno, 2005

[4] R. Kamensky, et al.: The influence of silicon on the thickness of the hardened surface layer of cast-iron castings (in Czech). Slevarenstvi, 16 (**1968**) 1, 35–39

UDK 621.785.797
Professional article/Strokovni članek

ISSN 1580-2949
MTAEC9, 46(4)393(2012)

INVESTIGATION ON THE AGING BEHAVIOUR OF THE FUNCTIONALLY GRADIENT MATERIAL CONSISTING OF BORON CARBIDE AND AN ALUMINUM ALLOY

RAZISKAVA PONAŠANJA PRI STARANJU FUNKCIONALNIH GRADIENTNIH MATERIALOV IZ BOROVEGA KARBIDA IN ALUMINIJEVE ZLITINE

Bertan Sarıkan[1], Erhan Balcı[1], Mustafa Übeyli[2], Necip Camuşcu[1]

[1]TOBB University of Economics and Technology, Mechanical Engineering, Söğütözü Cad. No:43 06560 Ankara, Turkey
[2]Osmaniye Korkut Ata University, Mechanical Engineering, Karacaoğlan Yerleşkesi, 80000 Osmanıye
mubeyli@gmail.com

Prejem rokopisa – received: 2011-10-18; sprejem za objavo – accepted for publication: 2012-03-05

In the current study the effect of different temperatures on the aging behaviour of a functionally gradient material was investigated to observe the variation of hardness with respect to the aging time. To do this, the functionally-gradient-material (FGM) specimens, containing boron carbide and aluminum alloy, were produced with hot pressing. Three different layers were used in the FGM samples. Then the macro and micro examinations were carried out to observe the interface between the layers, the porosity, the grain size and probable cracks in these samples. After that the specimens were solutionized at 470 °C for 1 h. Next, the artificial aging at 100 °C, 120 °C and 150 °C was applied to the FGM specimens for 96 h. During the aging treatment, the Brinell hardness measurements were made on the samples at certain intervals. Moreover, three-point bending tests were also carried out to clarify the influence of the aging treatment on the strength of the FGM. Experimental results indicated that the highest hardness values were obtained at 120 °C after the aging period of 48–65 h. The aged specimens exhibited higher bending strength than the solutionized specimens.

Keywords: metallic materials, inorganic materials, aging, three-point bending test

V tej študiji je prikazan vpliv različnih temperatur na staranje funkcionalnega gradientnega materiala in spreminjanje trdote v odvisnosti od časa staranja. Vzorci funkcionalno gradientnih materialov (FGM), ki vsebujejo borov karbid in aluminijevo zlitino, so bili izdelani s stiskanjem v vročem. Trije različni sloji so bili uporabljeni za FGM-vzorce. Na vzorcih so bile izvršene makro- in mikropreiskave stikov med sloji, določene so bile poroznost, velikost zrn in prisotnost morebitnih razpok. Potem so bili vzorci 1 h raztopno žarjeni na 470 °C, nato pa umetno starani 96 h na temperaturah 100 °C, 120 °C in 150 °C. Med postopkom staranja so bile v določenih intervalih izvršene meritve trdote po Brinellu. Dodatno je bil izvršen še tritočkovni upogibni preizkus, da bi opredelili vpliv staranja na trdnost FGM. Rezultati preizkusov kažejo, da je bila dosežena najvišja trdnost pri staranju med 48 h in 65 h na temperaturi 120 °C. Starani vzorci so pokazali večjo upogibno trdnost kot raztopno žarjeni vzorci.

Ključne besede: kovinski materiali, anorganski materiali, staranje, tritočkovni upogibni preizkus

1 INTRODUCTION

A new type of material called functionally gradient material (FGM) has been considered to be used for special purposes. In this type of material, at least two different types of layers are chemically used in a gradient form. In this way the properties change throughout the cross-section of the material. By definition, an FGM consists of one material being on one side and another material on the other side[1–21]. FGMs have been used in structural, electrical, chemical, optical, nuclear and biomedical applications[1]. The main methods for producing these materials are powder metallurgy, thermal spraying, coating, laser coating and other thermo-mechanical processes[1,2]. Among these methods, powder metallurgy techniques are very suitable for the FGM production[1,2]. The main advantages of chemically forming a gradient in a material are the creation of a metallurgical bond between the layers and different mechanical, nuclear, electrical and/or thermal properties of individual layers[1–20]. Producing a hard outer layer and a soft inner layer in the same material has been of key importance in the armour applications[1–3]. Therefore, the FGMs containing a hard front layer and a tough inner layer can be suitable for these applications. However, there is a large gap in the literature related to the production and mechanical properties of FGMs that need to be investigated extensively with respect to the objectives of materials science and manufacturing methods. In this paper an FGM with three layers, chemically changing from the top to the bottom, was produced using the powder metallurgy technique. In this material the bottom layer was chosen to be the aluminum alloy (AA) 7075, whereas the boron-carbide particles reinforcing the AA 7075 alloy were used, in different proportions, for the middle and the top layers. The influence of the artificial-aging treatments on the hardness of the layers was examined at different aging temperatures of 100 °C, 120 °C and 150 °C. In addition, the bending strength of the FGMs was determined for the solutionized and the aged samples.

2 EXPERIMENTAL PROCEDURE

The FGM samples with three layers were produced with the powder metallurgy technique. The powders used as starting materials were supplied from the market. The mean powder sizes of aluminum, boron carbide, chromium, copper, iron, silicon, zinc and magnesium were measured to be 10.22 μm, 4.04 μm, 33.42 μm, 19.17 μm, 6.66 μm, 3.53 μm, 6.7 μm and 45.08 μm, respectively. Furthermore, the powders had very high purities alternating between 99.5 % and 100 %. In the investigated aluminum alloy, the nominal chemical composition was taken as mass fractions 5.5 % Zn, 2.5 % Mg, 1.6 % Cu, 0.5 % Fe, 0.4 % Si, 0.23 % Cr. The powder size is very important when considering the sintering operation. A small powder size results in a higher surface area, which effectively enhances the sintering operation[22]. The FGM samples were based on the AA 7075 that can be hardened to a very high level by an artificial aging treatment[23–25].

In the investigated FGM samples, the bottom layer was considered to be a monolithic AA 7075 layer, while 20 % and 40 % B_4C (in volume) of the particle reinforcements in the AA 7075 matrix were used in the middle and top layers, respectively. Initially, the layers in the suitable chemical proportions were pre-shaped separately by cold pressing. Then they were transferred into the mould of a uni-axial hot press to be sintered at 590 °C for 20 min. After the sintering operation, the artificial aging treatments were performed to get the hardness-aging time curves for the produced FGM. Before the aging process, the samples were solutionized at 470 °C for 1 h and water quenched at 20 °C. The aging temperatures were 100 °C, 120 °C and 150 °C. Furthermore, the macro and the micro examinations on the samples were done to observe probable production defects such as cracks, pores and separations between the layers, as well as distribution of ceramic particles in the matrix. For the metallographic analysis, the samples were prepared with the standard methods and etched using the etchant, a modified Keller's reagent. The hardness tests and the three-point bending tests were made on the solutionized and peak-aged samples according to the standards of ASTM E 10-84 [26] and ASTM B 528-05 [27], respectively. For the hardness testing, the samples were taken out of the furnace and water quenched for the hardness measurement at certain intervals during the aging treatment (every half an hour during the first 6 hours and every hour during the period between the 7th and the 96th hour). Each time the mean values of five measurements were recorded.

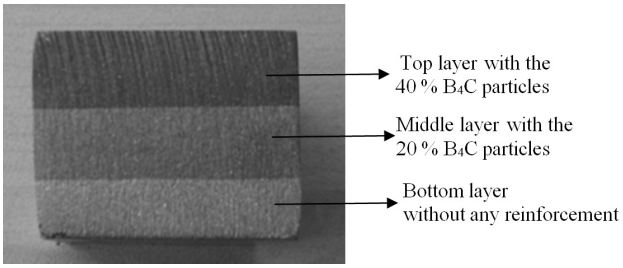

Figure 1: Typical cross sectional view of a produced FGM sample with the total thickness of 15 mm
Slika 1: Značilen prerez FGM-vzorca s skupno debelino 15 mm

3 RESULTS AND DISCUSSION

3.1 Macro- and microstructural observations

Figure 1 shows a typical macro view of the cross section for a produced sample with the total thickness of 15 mm. The three layers can be seen clearly in this figure. There are no macro-level cracks or separations observed between the layers of the produced sample. The adhesion of the layers with various compositions appears to be smooth. **Figures 2** and **3** illustrate the microstructure of the produced FGM taken by an optical microscope. A uniform distribution of ceramic particles can be observed on these figures. In addition, there is a good transition-and-interface formation between the layers.

Although the formation of interfaces and the distribution of ceramic particles throughout the samples are found to be uniform, some porosity is detected. The porosity level, detected by an image-analysis program, is estimated to be 5 %, 6 % and 8 % for the bottom, middle and top layers, respectively. Moreover, the average grain

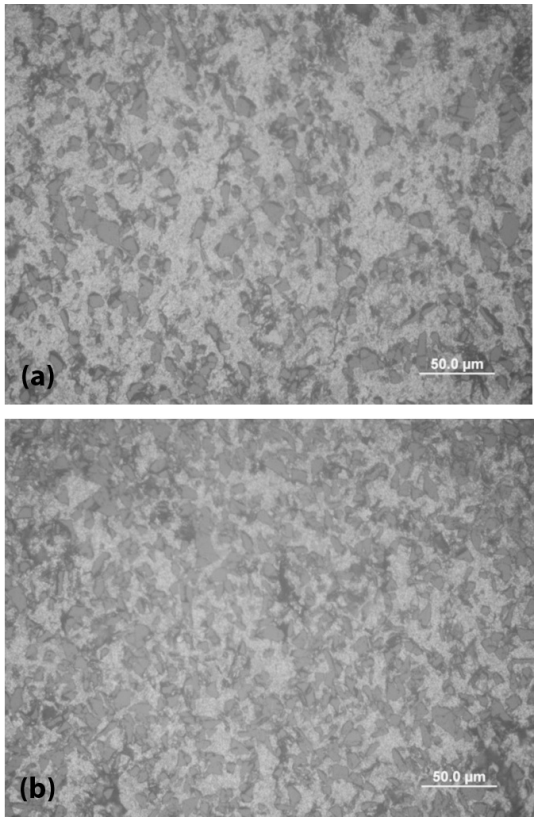

Figure 2: Micro view of: a) the middle and b) the top layers
Slika 2: Mikroposnetek: a) sredine in b) vrhnjih plasti

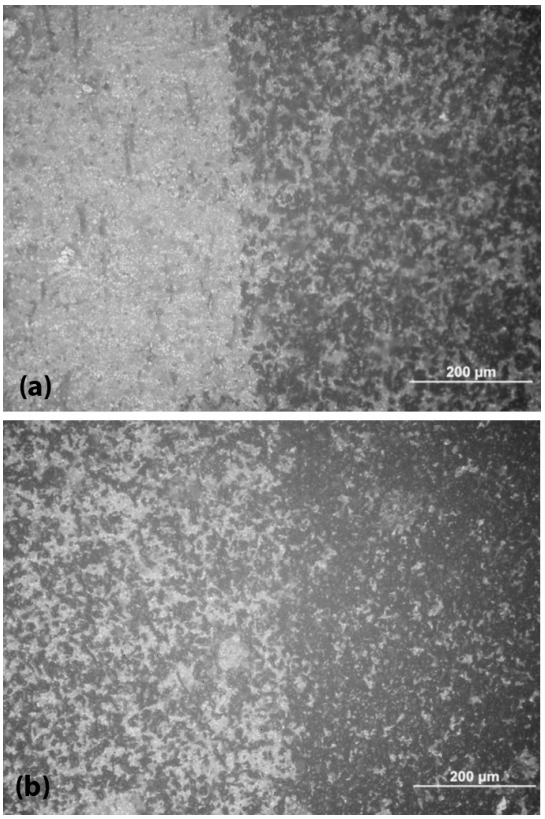

Figure 3: Interfaces between: a) the bottom and the middle, b) the middle and the top layers
Slika 3: Stik med: a) spodnjo in srednjo, b) srednjo in zgornjo plastjo

size was measured to be 24 µm according to the ASTM E 112 [28].

3.2 Aging effects on the hardness

Figure 4 gives the hardness/aging time curves for the sample aged at 100 °C. Initially, the hardness values for the bottom, middle and top layers are HB (104, 148 and 218), respectively. The hardness of all the layers increases after 30 min. Later there are some fluctuations in the curves in the aging period of the first 6 h. Finally, the hardness is stabilized for all three layers sometime between the 6th and the 96th hour. The highest hardness

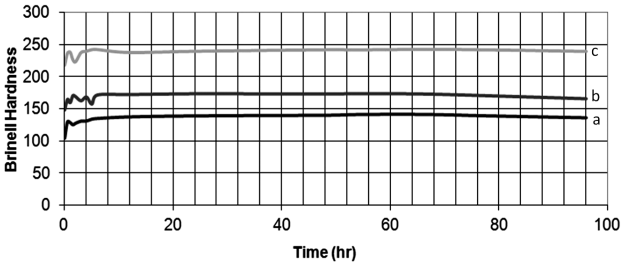

Figure 4: Hardness versus the aging time at 100 °C for: a) bottom, b) middle and c) top layers
Slika 4: Trdota v odvisnosti od časa staranja pri 100 °C za: a) spodnji, b) srednji in c) zgornji sloj

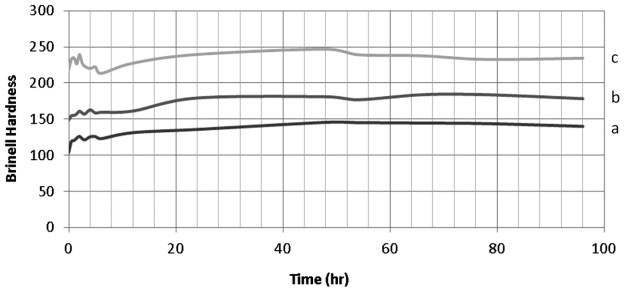

Figure 5: Hardness versus the aging time at 120 °C for: a) bottom, b) middle and c) top layers
Slika 5: Trdota v odvisnosti od časa staranja pri 120 °C za: a) spodnji, b) srednji in c) zgornji sloj

values recorded for the bottom, middle and top layers are HB (142, 172 and 242), respectively.

The aging curves for the sample aged at 120 °C are given in **Figure 5**. As expected, the highest hardness value belongs to the top layer. The general tendency in the shape of the curve is very similar for all three different layers. After the solutionizing treatment, the hardness is measured to be HB (104, 149 and 218) for the bottom, middle and top layers, respectively. During the aging period of the first 4–5 h, there are some fluctuations in the hardness profile. However, later the hardness starts to increase reaching the peak levels between the 48th and the 66th hour for all the layers. During the period between the 66th and the 96th hour, a gradual reduction in the hardness is observed due to over aging. The highest hardness values measured for the bottom, middle and top layers are HB (145, 181 and 247), respectively.

Figure 6 depicts the change in the hardness of the sample with respect to time at the aging temperature of 150 °C. As in the aging treatments at 100 °C and 120 °C, there is no change in the hardness profile of the alloy including the B_4C ceramic particles. After the aging period of 12 hours, the hardness is recorded to be HB (135, 171 and 239) for the bottom, middle and top layers, respectively. The hardness begins to decrease after the 12 h aging period. At the end of the 66th hour, the hardness becomes HB (116, 142 and 210) for the same layers, respectively. When aging the sample at 150

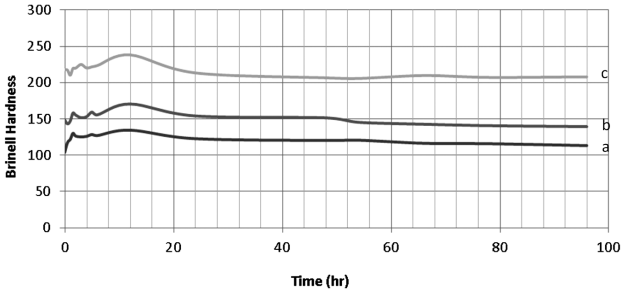

Figure 6: Hardness versus the aging time at 150 °C for: a) bottom, b) middle and c) top layers
Slika 6: Trdota v odvisnosti od časa staranja pri 150 °C za: a) spodnji, b) srednji in c) zgornji sloj

°C, the peak hardness values are obtained in shorter times, but they are lower than those obtained at the temperature of 120 °C.

The AA 7075 is a heat-treatable alloy[23] and its precipitation sequence can be given as follows[24]:

Super saturated solid solution $\longrightarrow$
$\longrightarrow$ GP zones $\longrightarrow \eta' \longrightarrow \eta$-$MgZn_2$

It is considered that the highest hardness is reached when the metastable phase of η' is formed during the aging[23,25]. The GP zones and η' form at the beginning of the aging treatment. The size and density of the precipitates very much affect the mechanical properties[23,25]. In the current work the higher hardness levels are obtained at the aging temperature of 120 °C. Therefore, it is thought that an extensive formation of the η' phase takes place at this temperature. Although the precipitation kinetics seem to be higher at 150 °C, the hardness values recorded at this temperature were lower than those obtained at 120 °C.

In a previous study[29] on the aging of AA 7075, the peak hardness value (≈HV 190) was reached at 121 °C and after 48 h. The general trend of the hardness profile and the hardness values found in this study are similar to those found in ref.[29]. Furthermore, in another study[30] the highest hardness value was recorded to be HV 170 at 120°C after 48 h for the AA 7075 produced with powder metallurgy. This result is also consistent with the current data given in this work.

3.3 Bending strength

During the bending test the force was applied through the layer with the 40 % B_4C particle reinforcement. The bending strength of the solutionized sample was found to be 456 MPa, whereas the bending strength of the aged sample was measured to be 527 MPa. A remarkable effect of the aging on the bending strength of the FGM was observed. During the testing a major crack was formed through the main axis that was exposed to the bending force and some particle fractures occurred on the bottom layer of the non-aged sample that has lower hardness (**Figure 7**). On the other hand, no big crack formation was observed on the aged sample, as only a fracture of some small particles were detected on its bottom layer. The rigidity of this sample increased with an increase in its hardness.

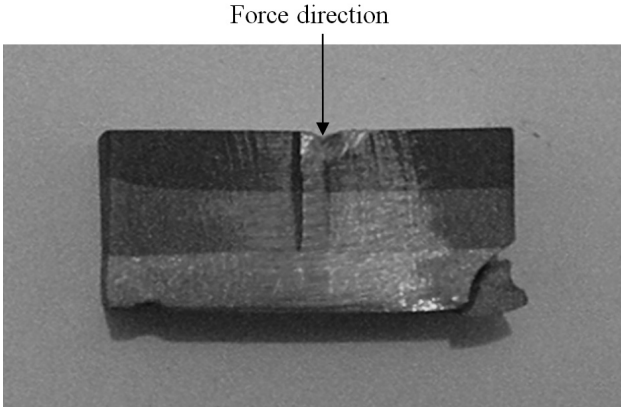

Figure 7: Macro view of the non-aged sample with the total thickness of 15 mm after the three-point bending test

Slika 7: Makrovidez nestaranega vzorca s skupno debelino 15 mm po tritočkovnem upogibnem preizkusu

4 CONCLUSIONS

The peak hardness values for all the layers of the investigated FGMs were found at the aging temperature of 120 °C. The artificial aging of the FGM at 120 °C allowed about 40 %, 21 % and 13 % increase in the hardness of the bottom, middle and top layers, respectively. The addition of the B_4C ceramic particles to the AA 7075 matrix had no significant effect on the aging behaviour of the alloy. The aged specimen exhibited a 15 % higher bending resistance than the non-aged one. In order to enhance the hardness and strength of the investigated FGMs, the porosity level should be reduced or eliminated using higher pressure and smaller powder sizes.

Acknowledgement

This work was supported by the Research Fund of Tübitak, Project # 110M034. The authors are thankful to Tübitak for its support.

5 REFERENCES

[1] A. Neubrand, J. Rödel, Gradient materials: An overview of a novel concept, Z. Metallkd., 88 (**1997**), 358–371

[2] A. Kawasaki, R. Watanabe, Concept and P/M fabrication of functionally gradient materials, Ceramics International, 23 (**1997**), 73–83

[3] Chin ESC. Army focused research team on functionally graded armor composites, Mat. Sci. Eng. A, 259 (**1999**), 155–161

[4] K. Tsuda, A. Ikegaya, K. Isobe, N. Kitagawa, T. Nomura, Development of functionally graded sintered hard materials, Powder Metall., 89 (**1996**), 296–300

[5] M. Jain, R. K. Sadangi, W. R. Cannon, B. H. Kear, Processing of functionally graded WC/Co/Diamond: Nanocomposites, Scripta Mater., 44 (**2001**), 2099–2103

[6] J. Zhu, Z. Lai, Z. Yin, J. Jeon, S. Lee, Fabrication of ZrO_2-NiCr functionally graded material by powder metallurgy, Mater. Chem. Phys., 68 (**2001**), 130–135

[7] L. M. Zhang, J. Liu, R. Z. Yuan, T. Hirai, Properties of TiC-Ni_3Al composites and structural optimization of TiC-Ni3Al functionally gradient materials, Mat. Sci. Eng. A, 203 (**1995**), 272–277

[8] C. Y. Lin, H. B. Bathias, H. B. Mcshane, R. D. Rawlings, Production of silicon carbide Al2124 alloy functionally graded materials by mechanical powder metallurgy technique, Powder Metall., 42 (**1999**), 29–34

[9] Y. Miyamoto, Z. Li, Y. S. Kang, K. Tanihata, Fabrication and properties of alumina-based hyperfunctional ceramics with symmetrically compositional gradient structures, Powder Metall., 42 (**1995**), 933–938

[10] Y. G. Jung, U. Paik, S. C. Choi, Influence of the particle size and phase type of zirconia on the fabrication and residual stress of zirconia/stainless steel 304 functionally gradient material, J. Mater. Sci., 34 (**1999**), 5407–5416

[11] G. Jin, M. Takeuchi, S. Honda, T. Nishikawa, H. Awaji, Properties of multilayered mullite/Mo functionally graded materials fabricated by powder metallurgy processing, Mater. Chem. Phys., 89 (**2005**), 238–243

[12] B. Kieback, A. Neubrand, H. Riedel, Processing techniques for functionally graded materials, Mat. Sci. Eng. A, 362 (**2003**), 81–105

[13] X. Jin, L. Wu, Y. Sun, L. Guo, Microstructure and mechanical properties of ZrO_2/NiCr functionally graded materials, Mat. Sci. Eng. A, 509 (**2009**), 63–68

[14] K. Tohgo, M. Iizuka, H. Araki, Y. Shimamura, Influence of microstructure on fracture toughness distribution in ceramic-metal functionally graded materials, Eng. Fract. Mech., 75 (**2008**), 4529–4541

[15] E. M. Ruiz-Navas, R. Garcia, E. Gordo, F. J. Velasco, Development and characterization of high-speed steel matrix composites gradient materials, J. Mater. Process. Tech., 143–144 (**2003**), 769–775

[16] Z. He, J. Ma, G. E. B. Tan, Fabrication and characteristics of alumina-iron functionally graded materials, J. Alloy Compd., 486 (**2009**), 815–818

[17] M. Bhattacharyya, A. N. Kumar, S. Kapuria, Synthesis and characterization of Al/SiC and Ni/Al_2O_3 functionally graded materials, Mat. Sci. Eng. A, 487 (**2008**), 524–535

[18] A. Kawasaki, R. Watanabe, Evaluation of thermomechanical performance for thermal barrier type of sintered functionally graded materials, Compos. Part B., 28B (**1997**), 29–35

[19] C. C. Ge, J. T. Li, Z. J. Zhou et al., Development of functionally graded plasma facing materials, J. Nucl. Mater., 283–287 (**2000**), 1116–1120

[20] A. H. Wu, W. B. Cao, C. C. Ge, J. F. Li, A. Kawasaki, Fabrication and characteristics of plasma facing SiC/C functionally graded composite material, Mater. Chem. Phys., 91 (**2005**), 545–550

[21] M. K. Öztaş, B. Sarıkan, M. Übeyli, N. Camuşçu, Ö. Keleş, Production of the functionally gradient material based on an aluminum alloy, The Eleventh International Scientifically-Practical Conference, 2 (**2011**), 283–285 (Saint-Petersburg, Russian Federation 26–29 April 2011)

[22] R. M. German, Powder Metallurgy & Particulate Materials Processing, Metal Powder Industry, 2005

[23] J. Chen, L. Zhen, S. Yang, W. D. S. Shao, Investigation of precipitation behavior and related hardening in AA 7075 aluminium alloy, Mat. Sci. Eng. A, 500 (**2009**), 34–42

[24] D. J. Lloyd, M. C. Chatuverdi, A calorimetric study of aluminum alloy AA-7075, Journal of Materials Science, 17 (**1982**), 1819–1824

[25] G. Sha, A. Cerezo, Early-stage precipitation in Al-Zn-Mg-Cu alloy (7050), Acta Materialia, 52 (**2004**), 4503–4516

[26] ASTM Standards, Designation E10-84, Standard Test Method for Brinell Hardness of Metallic Materials, 1984

[27] ASTM Standards, Designation B 528-05, Standard Test Method for Transverse Rupture Strength of Metal Powder Specimens, 2005

[28] ASTM Standards, Designation E 112-96e2, Standard Methods for Determining Average Grain Size, 2004

[29] S. V. Emani, J. Benedyk, P. Nash, D. Chen, Double aging and thermomechanical heat treatment of AA7075 aluminum alloy extrusions, Journal of Materials Science, 44 (**2009**), 6384–6391

[30] C. Y. Sheu, S. J. Lin, Ageing behavior of SiC_p-reinforced AA 7075 composites, Journal of Materials Science, 32 (**1997**), 1741–1747

UDK 621.74.043(437.3):519.872
Professional article/Strokovni članek

ISSN 1580-2949
MTAEC9, 46(4)399(2012)

SETTING A NUMERICAL SIMULATION OF FILLING AND SOLIDIFICATION OF HEAVY STEEL INGOTS BASED ON REAL CASTING CONDITIONS

POSTAVITEV NUMERIČNE SIMULACIJE POLNJENJA IN STRJEVANJA VELIKIH JEKLENIH INGOTOV NA PODLAGI REALNIH RAZMER PRI ULIVANJU

Marketa Tkadleckova[1], Pavel Machovcak[2], Karel Gryc[1], Petr Klus[1], Karel Michalek[1], Ladislav Socha[1], Marek Kovac[3]

[1]VŠB – Technical University of Ostrava, Faculty of Metallurgy and Materials Engineering, Department of Metallurgy and Regional Materials Science and Technology Centre, Ostrava-Poruba, Czech Republic
[2]VÍTKOVICE HEAVY MACHINERY, a. s., Ostrava-Vítkovice, Czech Republic
[3]MECAS ESI, s. r. o., Brno, Czech Republic
marketa.tkadleckova@vsb.cz

Prejem rokopisa – received: 2011-10-22; sprejem za objavo – accepted for publication: 2012-01-06

The paper is devoted to new experiences with the setting of a numerical simulation of filling and solidification of a 90-ton steel ingot in the ProCAST simulation programme. The aim of the numerical modelling realized under the conditions of the Department of Metallurgy and Regional Materials Science and Technology Centre (RMSTC) at VSB-TU Ostrava is the verification and optimization of the production technology for the heavy-steel ingots produced in VÍTKOVICE HEAVY MACHINERY a.s. The input parameters of the computation were determined with the real conditions of casting a 90-ton steel ingot. The ingot geometry was created in the CAD system SolidWorks. Before the computational grid generation of finite elements in the Visual-Mesh module, the geometry was subjected to an analysis of the topology. The material properties of the individual components of the ingot-casting system were defined with the Computherm calculating module selecting the materials from its own database of ProCast. In addition, the thermodynamic properties were determined by using the datasheets of the refractory materials of the manufacturer, and finally checked with the equations generally used to determine liquidus and solidus temperatures, density and enthalpy, etc. The boundary conditions and the heat transfer were also defined. In parallel with the numerical simulation, the operational experimental casting of a 90-ton ingot was carried out. To obtain more complete information about the temperature fields of the ingot-casting system and of the data about the values of the heat flow, the process of filling and solidification was monitored by using thermal imaging cameras. The conclusion summarizes the main knowledge obtained on the basis of the primary results of the computation and gives a guideline for further research.

Keywords: numerical simulation, heavy-steel ingot, heat flow, thermal measuring

Članek obravnava nove izkušnje z numerično simulacijo polnjenja in strjevanja 90-tonskega jeklenega ingota s ProCAST-programom za simulacijo. Namen izvršenega numeričnega modeliranja v Department of Metallurgy in Regional Materials Science and Technology Centre (RMSTC) na VSB-TU Ostrava je preverjanje in optimiranje proizvodne tehnologije težkih jeklenih ingotov, proizvedenih v Vítkovice Heavy Machinery, a. s. Vhodni parametri za izračun so bili določeni v realnih razmerah pri ulivanju 90-tonskega jeklenega ingota. Geometrija ingota je bila postavljena v CAD-sistemu SolidWorks. Pred postavitvijo mreže končnih elementov z Visual-Mesh-modulom je bila geometrija obdelana s topološko analizo. Lastnosti materiala posameznih komponent livnega sistema ingota so bile določene z računskim modulom Computherm in z izbiro materiala iz datoteke ProCast. Termodinamske lastnosti so bile določene z uporabo datotek proizvajalcev ognjevzdržnih materialov ter končno preverjene z izračunom po enačbah, ki se uporabljajo za določanje temperature likvidusa in solidusa, gostote, entalpije itd. Določeni so bili robni pogoji in prenos toplote. Vzporedno z numerično simulacijo je bilo izvršeno eksperimentalno ulivanje 90-tonskega ingota. Da bi dobili bolj popolno informacijo o temperaturnih poljih ulivnega sistema ingota in podatke o vrednostih toplotnega toka, je bil postopek polnjenja in strjevanja posnet tudi s termovizijsko kamero. Sklepi povzemajo glavne ugotovitve primarnih rezultatov izračunov in dajejo napotke za nadaljnje raziskave.

Ključne besede: numerična simulacija, težki jekleni ingot, toplotni tok, termografske meritve

1 INTRODUCTION

The numerical modelling of filling and solidification of a steel ingot was performed within the Department of Metallurgy and RMSTC using the ProCAST software. The software allows a 3D fully dimensional numerical simulation of filling and solidification of steel including a prediction of the ingot-volume defects such as porosity and shrinkage. Due to the Flow and Stress modules, it is possible to take into account the effects of natural convection and of the formation of the air gaps between the ingot body and the inner wall of the mould during the calculation, and to predict the emergence of the internal stress that can ultimately lead to cracks and rupture[1].

In general, the numerical solution of each task is divided into three stages:

1. *Pre-processing*: includes the geometric modelling, the computational mesh-generation process, and the definition of the calculation.
2. *Processing*: involves the computation in the solver.
3. *Post-processing*: focuses on the evaluation of the results.

The conditions for the numerical model setting were based on the real conditions of an experimentally cast,

90-ton steel ingot produced in VÍTKOVICE HEAVY MACHINERY, a. s.

2 GEOMETRY AND THE COMPUTATIONAL MESH

The computational-mesh geometry and the generation of the casting system for the 90-ton steel ingot were made in cooperation with MECAS ESI, s. r. o. The comparison between the real and the CAD geometry of the casting system is shown in **Figure 1**[2]. **Figure 2** shows the final computation mesh of the casting system. The volume ingot mesh consists of 348 794 nodes. The total volume of the tetra elements is 1 766 041. The mould has a rough mesh. For a more appropriate description of the geometry, the details, the insulation, and the ceramic parts have a better mesh.

The final mesh of geometry was saved in *. mesh format and subsequently loaded in the ProCAST module for a calculation entry, also called the PreCAST. It was necessary to define:

- the material properties of the individual parts of the casting system,
- the heat-transfer coefficients on the interface of the geometry elements,
- the boundary conditions, such as the casting temperature, the casting speed, the conditions of heat losses through the surface of the ingot,
- the operating conditions (such as gravity),
- the initial conditions for the calculation,
- the calculation parameters – the so-called RUN PARAMETERS.

Among the other things, the RUN PARAMETERS define the conditions for the calculation termination, the so-called STOP criteria. The stop criteria also include the attainment of a certain temperature in the ingot or the termination of the calculation at a particular time after the filling. The number of the steps of the calculation is also specified, as well as the length of the time step and the frequency of storing the results regarding the temperature field and/or the heat flux[2,3].

Figure 1: Comparison between the real and the CAD geometry of the casting system for a 90-ton ingot[2]

Slika 1: Primerjava realne in CAD-geometrije ulivnega sistema 90-tonskega ingota[2]

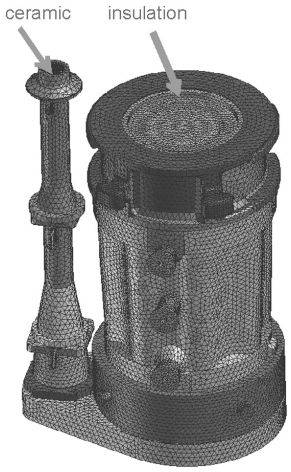

Figure 2: View of the final computational mesh of the casting system

Slika 2: Videz končne računske mreže ulivnega sistema

The computational time of one variant is around 96 h when two processor cores are used. However, the time needed for the preparation of the simulation and for the evaluation of the achieved results has to be added to the time taken by the computation.

3 MONITORING OF THE HEAT FLUX AND OF THE TEMPERATURE DURING THE EXPERIMENTAL CASTING

As mentioned above, the course of the changes in the temperature field on the surface of the casting system during the experimental casting of a 90-ton ingot was also monitored by using the thermal-imaging cameras. The thermography measurements were performed with AVIO TVS 700 cameras. According to the tables of the emission coefficients, the value of emissivity was set at 0.85. At the time of the measurement, an average ambient temperature was 26 °C corresponding to the conditions of the operation of a steel plant. The measurement was not affected by the increased dusting or drafts, and it was done with a tripod from a constant distance of 6.5 m. **Figure 3** shows the workers making the thermography measurements.

During the thermography measurements images were being taken in 10-minute intervals, from the moment when the casting system got preheated, during the casting itself and until after the stripping, therefore for 24 h. The temperatures were monitored on the surface of the head, the mould, the washers, and the casting stake. During the measurements, the temperature of the pit wall, in which the casting system was located, was scanned twice. After the completion of the filling, an image of the temperature-field distribution on the surface of steel, incurred after the addition of the insulation backfill, was recorded. A self-evaluation of images was

Figure 3: View of the workers making the thermography measurements
Slika 3: Delavci med izvajanjem termografskih meritev

performed in the SW GORATEC Thermography Studio v4.5. When evaluating the images, the temperature distribution, the temperature profile and the heat flux in the selected area were monitored. The values of the thermal flow and the temperature information were used to specify the parameters of the setting of the numerical simulation of filling and solidification of the steel ingot.

4 DISCUSSION OF THE ONGOING RESULTS

During the tuning of the setting of the numerical simulation of the filling and solidification of a 90-ton ingot, 9 configurations have been calculated up to now. The difference between the temperature profiles on the surface of the ingot obtained for the first variant and for 9th variant, 20 min after the initiation of the filling and at the end of the filling, when the thermography-measurement results were used, is captured in **Figure 4**.

The software for the image evaluation has different options for setting the displayed scale of temperatures; thus, the authors of the paper used the possibilities of the Visual Viewer of ProCAST and adjusted the scale of the numerical-simulation results to the scale of thermography. The selection and editing of the colours were dependent on the colour sense of the user. The advantage of the Visual-Viewer postprocessor is the display of the temperature in precise contours – changes to the minimum and maximum values can provide accurate information about the temperature in the chosen geometric location. In its first column **Figure 4** shows the temperature evolution on the mould surface for the original setting, where the values of the heat-transfer coefficients ranged from 100 W m^{-2} K^{-1} to 1000 W m^{-2} K^{-1} as is typical in these simulations. However, it is obvious that the temperature values on the mould surface are below the values measured during the thermography measurements (the second column). Therefore, it was necessary to adjust the coefficients according to the measured values depending on time. The third column already captures the evolution of the temperature on the mould surface after the adjustment of the heat-transfer coefficients. The

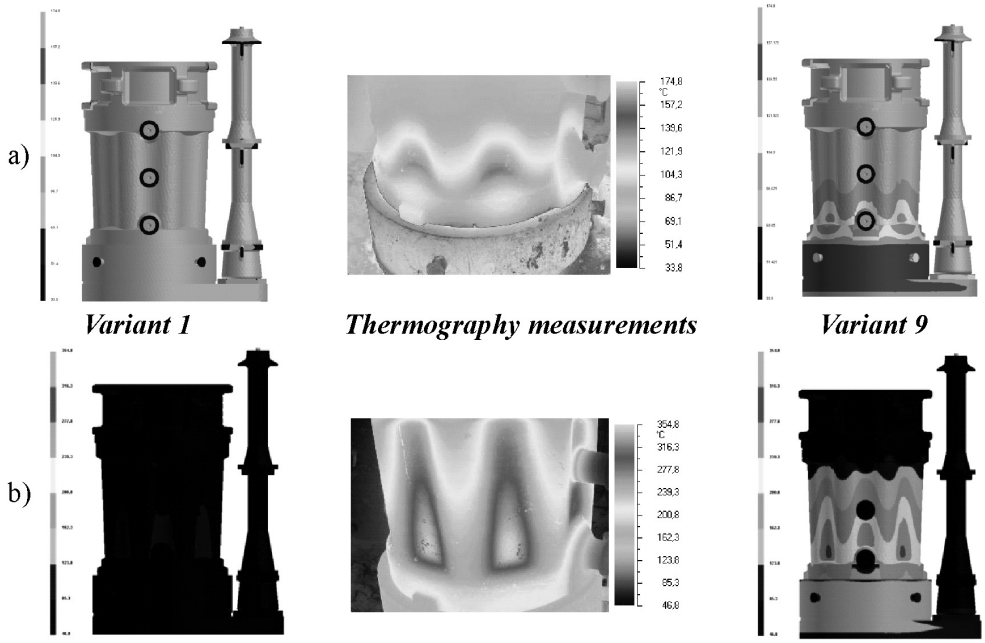

Figure 4: Comparison of the temperatures on the ingot mould surface: a) 20 min after the initiation of the filling, b) after the filling
Slika 4: Primerjava temperature površine kokile: a) 20 min po začetku ulivanja, b) po koncu ulivanja

results of the thermography measurements and the numerical simulation are already converging.

5 CONCLUSION

The setting of the numerical model for filling and solidification of a heavy 90-ton steel ingot was based on real experimental conditions of casting. The numerical modelling was carried out under the conditions of the Department of Metallurgy and RMSTC at VSB-TU Ostrava in ProCAST SW. During the solution, an import of the specific material properties was planned. For example, solidus or liquidus temperatures were determined for the material (steel) using the instrumentation for a thermal analysis (STA 449 Jupiter of NETZSCH Company) placed in the laboratory of RMSTC[4]. During the experimental ingot casting, the temperatures and the heat flows on the surface of the casting system were monitored with a thermal imaging camera. Once the process of the temperature profile on the mould surface of the numerical-simulation results corresponds to the results of the thermography measurements from the start of the filling to the actual stripping, the researchers will proceed to further stages of numerical simulations based on the distribution of the segregation of chemical elements through the cross section of the ingot. At the same time, the analysis of the segregation distribution will be evaluated on the experimental cut ingot. The aim of the numerical simulations will be to test the changes in the boundary conditions of casting that should help us not only to minimize the volume of defects, but also to minimize the occurrence of the segregation in the heavy forging of ingots produced by VÍTKOVICE HEAVY MACHINERY, a. s.

Acknowledgments

This paper was created within the project TIP No. FR-TI3/243, the Ministry of Industry and Trade of the Czech Republic, and within the project No. CZ.1.05/2.1.00/01.0040, "Regional Materials Science and Technology Centre" (ED0040/01/01), the operation programme "Research and Development for Innovations" financed by the Structural Funds and by the state budget of the Czech Republic.

6 REFERENCES

[1] M. Tkadlečková, K. Michalek, P. Klus, K. Gryc, V. Sikora, Testing of numerical model setting for simulation of steel ingot casting and solidification. In 20th Anniversary International Conference of Metallurgy and Materials Metal 2011. May 18th-20th, Brno, Czech Republic, EU. ©Tanger, s. r. o. Ostrava. pp. 6

[2] M. Tkadlečková, K. Gryc, K. Michalek, P. Klus, L. Socha, P. Machovčák, M. Kováč, Verifikace vlivu okrajových parametrů lití ocelových ingotů na velikost objemových vad. In XXI. International Scientific Conference Iron and Steelmaking. 19.–21. října 2011, Horní Bečva, Beskydy, Česká republika. s. 5

[3] ProCAST 2009, Release Notes & Installation Guide. 2009 ESI Group

[4] K. Gryc, B. Smetana, K. Michalek, V. Sikora, M. Tkadlečková, S. Zlá, M. Žaludová, Linking basic and apllied research in thermo physical study of the properties of steel, slag and ferro-alloys. In 20th Anniversary International Conference of Metallurgy and Materials Metal 2011. May 18th–20th, Brno, Czech Republic, EU. ©Tanger, s. r. o., Ostrava. pp. 6

UDK 669.1
Professional article/Strokovni članek

ISSN 1580-2949
MTAEC9, 46(4)403(2012)

A STUDY OF THE HIGH-TEMPERATURE INTERACTION BETWEEN SYNTHETIC SLAGS AND STEEL

ŠTUDIJ VISOKOTEMPERATURNE INTERAKCIJE MED SINTETIČNO ŽLINDRO IN JEKLOM

Karel Gryc[1], Karel Stránský[2], Karel Michalek[1], Zdeněk Winkler[3], Jan Morávka[4], Markéta Tkadlečková[1], Ladislav Socha[1], Jiří Bažan[1], Jana Dobrovská[5], Simona Zlá[5]

[1]VŠB – Technical University of Ostrava, Faculty of Metallurgy and Materials Engineering, Department of Metallurgy and Foundry, Czech Republic
[2]Brno University of Technology, Faculty of Mechanical Engineering, Institute of Materials Science and Engineering, Czech Republic
[3]Military Technical Institute of Protection in Brno, Czech Republic
[4]MATERIÁLOVÝ A METALURGICKÝ VÝZKUM s. r. o., Czech Republic
[5]VŠB – Technical University of Ostrava, Faculty of Metallurgy and Materials Engineering, Department of Physical Chemistry and Theory of Technological Processes, Czech Republic
karel.gryc@vsb.cz

Prejem rokopisa – received: 2011-10-27; sprejem za objavo – accepted for publication: 2012-02-15

The paper is devoted to selected aspects of the current issues of the high-temperature interaction of the synthetic multicomponent oxidic systems and selected grades of steel. Analysing the consequences of the interaction between slag and molten steel is an integral part of modern research that can be connected with subsequent, applied research in the field of producing and refining steel. The interactions between the synthetic slag and the molten metal is realized after the processing of the liquid steel in the primary metallurgical aggregates, i.e., at the beginning of refining processes of secondary metallurgy. The addition of these synthetic systems (slag) significantly affects many technological processes and indirectly affects the final quality of the cast steel. This influence can be seen on two levels: the metallurgical and the metallographic. Both of these levels of evaluation complement each other.

For the evaluation of the metallurgical aspects of refining processes a number of thermodynamic relations were used, supplemented by empirically established formulas and coefficients. Metallographic analyses utilize modern tools in the study of the structure and the chemical composition of materials, i.e., from light microscopy to sophisticated systems of microanalysis of elemental composition using a scanning electron microscope combined with an energy-dispersive X-ray micro-analyser. It is obvious that this area deserves more focused research and more attention, particularly in the context of the on-going needs for the identification and quantification of phenomena taking place in the following metallurgical innovations.

Keywords: synthetic slag, interaction with steel, saturation

Članek obravnava izbrane vidike aktualnih vprašanj o visokotemperaturni interakciji sintetičnih večkomponentnih oksidnih sistemov v izbranih vrstah jekel. Analiziranje posledic interakcije med žlindro in talino je sestavni del potekajočih raziskav in se lahko poveže z uporabnimi raziskavami na področju proizvodnje in rafinacije jekla. Do interakcije med sintetično žlindro in staljeno kovino pride po izdelavi taline jekla v primarni metalurški peči, na začetku postopka rafinacije v sekundarni metalurgiji. Dodatek sintetične žlindre močno vpliva na številne tehnološke procese in neposredno vpliva na končno kvaliteto ulitega jekla. Ta učinek se kaže na dveh nivojih: na metalurškem in metalografskem. Oba nivoja ocene sta med seboj komplementarna.

Za oceno metalurških vidikov postopka rafinacije je bilo uporabljeno več termodinamskih odvisnosti, dopolnjenih z empirično določenimi enačbami in koeficienti. Metalografska analiza uporablja sodobna orodja za študij strukture in kemijske sestave materiala – od svetlobne mikroskopije do zapletenih sistemov mikroanalize, elementne sestave z uporabo vrstičnega elektronskega mikroskopa v kombinaciji z energijsko disperzijsko rentgensko spektroskopijo. Očitno to področje zahteva bolj usmerjene raziskave in večjo pozornost, posebno v kontekstu zahtev, identifikacije in kvantifikacije pojavov, ki so posledica metalurških inovacij.

Ključne besede: sintetična žlindra, interakcija z jeklom, nasičenje

1 INTRODUCTION

It is necessary to continuously optimize the production of steel in steel mills. Such an optimization of the metallurgical processes is often connected with operational challenges that could be solved by changes in the slag regime. An integral part of the steel-making process is the use of different types of synthetic slag. These, together with other slag materials, facilitate the successful course of the metallurgical reactions that are necessary to achieve the desired chemical and metallurgical purity of the steels.

In addition to plant experiments, which are an essential and major part of the slag-optimization regimes and whose results are crucial for the innovations in the final steel production process, there is the possibility of studying the interaction of metal and oxidic systems, e.g., under laboratory conditions.[1–4]

This paper focuses on a discussion of the results of the oriented research that was realized within the grant project ID No. 106/09/0969 with the financial support of the (GACR) Czech Science Foundation. The presented results are not directly tied to any specific operating conditions in a steel plant.

The studied synthetic slags react in real conditions with steel, especially together with pre-existing slag and/or with currently added slag-forming materials. Al-

though this study of the high-temperature interactions between synthetic oxidic melts and steels lies outside the field of applied research, its results can extend current knowledge about the mechanisms associated with these systems of melts. The methods used could provide guidance to address the challenges associated with solving the practical aspects of steelmaking technology.

A series of interesting results was obtained in the course of this project. That is why the focus of this paper will be only on an analysis of the changes in the chemical composition of the studied synthetic oxidic mixtures, depending on the chemical composition of steel, with which these compounds reacted during the laboratory heats.

2 EXPERIMENTAL CONDITIONS AND CHARACTERISATION OF THE STUDIED MELTS

Heats designed for the study of the interaction between liquid metal and synthetic oxidic melts were carried out under laboratory conditions at the Department of Metallurgy in an induction furnace (**Figure 1**) connected to a GV 22 high-frequency generator.

Each 300 g sample of steel (**Table 1**) was melted in a corundum crucible under the continuous maintenance of a protective atmosphere (Ar, flow rate of 0.5 L min^{-1}). One of the following synthetic oxidic mixtures (**Table 2**) was added (30 g) after reaching the temperature of 1600 °C. The melting process of oxidic mixtures requires approximately 2.5 min. However, a stable temperature (1600 °C) was kept for an additional 10 min. Then, the generator was stopped. The solidified steel and slag were removed from the crucible after cooling down. Subsequently, samples were prepared to perform the appropriate analyses.

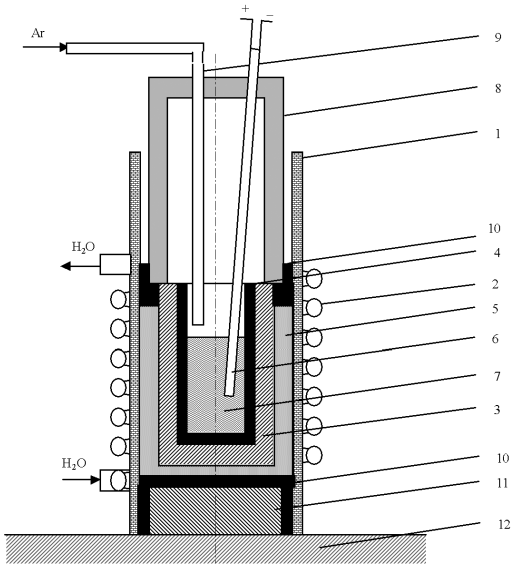

Figure 1: Diagram of the experimental equipment; 1 – protective cylinder of SiO_2, 2 – water-cooled inductor, 3 – graphite block, 4 – working crucible, 5 – protective Al_2O_3 powder, 6 – PtRh6 – PtRh30 thermocouple, 7 – molten metal, 8 – protective cover, 9 – supply of argon, 10 – TERMOVIT cotton, 11 – insulating brick, 12 – fireclay base

Slika 1: Shematski prikaz eksperimentalne opreme: 1 – zaščitna obloga iz SiO_2, 2 – vodno hlajen induktor, 3 – grafitni blok, 4 – talini lonec, 5 – zaščitni Al_2O_3 prašek, 6 – PtRh6 – PtRh30 termočlen, 7 – staljena kovina, 8 – zaščitni pokrov, 9 – dovod argona, 10 – TERMOVIT preja, 11 – izolacijska opeka, 12 – ognjevarna obloga

Table 1: The content of the monitored elements in the selected steels
Tabela 1: Vsebnost analiziranih elementov v izbranih jeklih

Identification of steel	Chemical composition in mass fractions, *w*/%					
	C	Mn	Si	P	S	Cr
1	0.19	1.16	0.14	0.015	0.033	1.100
2	0.21	1.04	0.13	0.033	0.170	0.054
3	0.12	1.20	<0.01	0.060	0.340	0.080
4	0.19	1.34	0.18	0.015	0.015	0.055

Table 2: Content of selected oxidic mixture components
Tabela 2: Vsebnost komponent v izbranih mešanicah oksidov

Identification of oxidic mixture	Chemical composition in mass fractions, *w*/%								
	Fe_{tot}	CaO	Al_2O_3	SiO_2	S	P_2O_5	MgO	MnO	Cr_2O_3
A	0.42	83	11	1	0.05	0.44	1.91	0.81	0.49
B	0.79	48	46	2	0.12	0.39	1.08	0.2	0.41
C	1.96	34	47	9	0.19	0.55	1.58	0.23	0.31
D	1.21	49	39	5	0.32	0.39	1.68	0.07	–
E	0.63	31	56	5	0.67	0.12	3.84	0.02	0.02

It is obvious (**Table 1**) that the steels were selected based on such a chemical composition in order to assess the impact of significant changes in the content of the significant elements on the result of the metallurgical refining process.

3 DISCUSSION

The contents of the elements in the steel and slag components listed in this paper in **Table 1** and **2** were determined using standard methods.

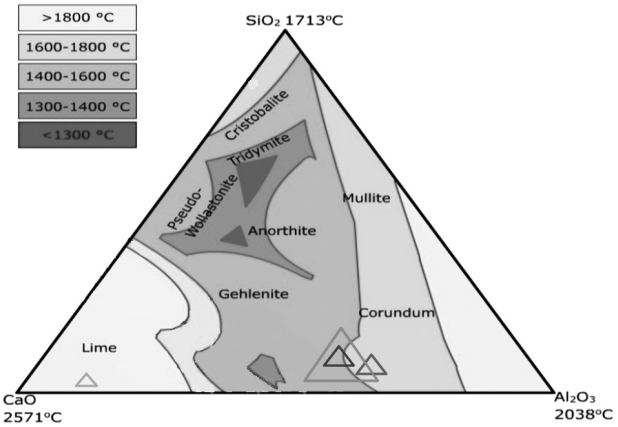

Figure 2: Ternary diagram for the starting oxidic mixture (A) and the slag obtained after the reaction with molten steels

Slika 2: Ternarni diagram začetne mešanice oksidov (A) in žlindra, ki je nastala po interakciji s staljenimi jekli

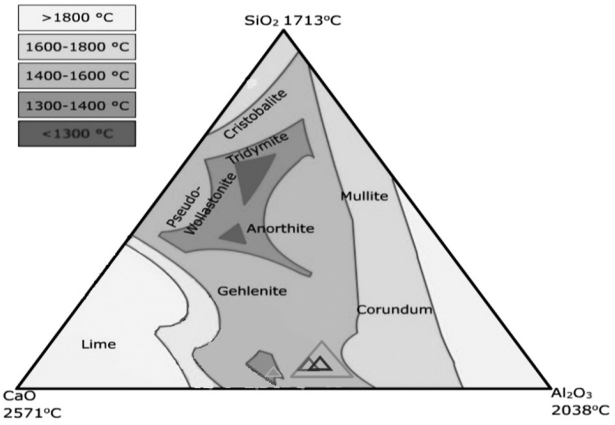

Figure 3: Ternary diagram for the starting oxidic mixture (B) and the slag obtained after the reaction with molten steels

Slika 3: Ternarni diagram začetne mešanice oksidov (B) in žlindra, ki je nastala po interakciji s staljenimi jekli

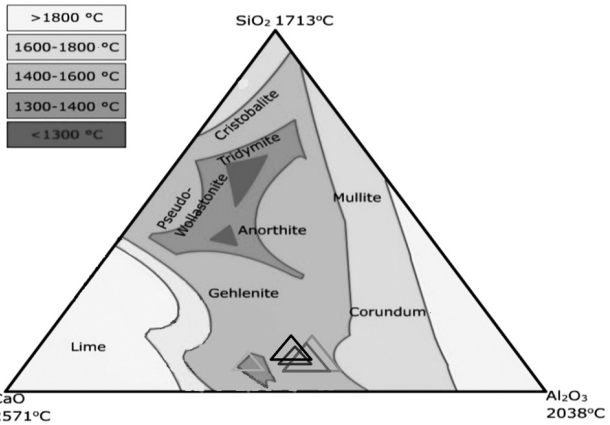

Figure 5: Ternary diagram for the starting oxidic mixture (D) and the slag obtained after the reaction with molten steels

Slika 5: Ternarni diagram začetne mešanice oksidov (D) in žlindra, ki je nastala po interakciji s staljenimi jekli

Analyses of the elements in the steel:

- C, S using a CS 230 LECO combustion analyser,
- Mn, Si, P, Cr using a PW 1400 Philips X-ray spectrometer.

The analysis of the content of the monitored slag components was implemented using the analytic complex formed by the EDAX PHILIPS energy-dispersive micro-analyser in conjunction with the PHILIPS scanning electron microscope. A detailed description of the apparatus and the applied methods can be, together with the results of the analysis, found in the report[5].

The results of the analyses are summarized in the simplified CaO-Al_2O_3-SiO_2 ternary diagrams (**Figures 2** to **6**). It is obvious that in terms of securing good kinetic conditions of the refining processes (low viscosity of the oxidic systems), it is advantageous to have a chemical composition of oxidic systems with a melting point below the working temperature of steel during its processing in a given technology node.

The ternary diagrams (**Figures 2** to **6**) show the chemical composition of the initial oxidic mixture (green) and the slag after laboratory heats with different steels (1 – dark blue, 2 – red, 3 – light blue, 4 – black).

Figure 2 shows a ternary diagram with plotted areas for the oxidic mixture A (83 % CaO-11 % Al_2O_3-1 % SiO_2) and the slag after the reaction with molten steels 1 to 3. It is obvious that there is a significant change in the chemical composition due to the interaction of an oxidic mixture with steels. The resulting oxidic melt contains mass fractions of Al_2O_3 from 51 % to 60 %. The chemical composition of the resulting slag, in the case of an interaction with the steels 1 and 3, ensures that the slag was liquid at temperatures above 1600 °C. In contrast, the resulting slag for the interaction with steel No. 2 occurs in an area that does not guarantee its liquid state.

The initial, synthetic slag B (48 % CaO-46 % Al_2O_3-2 % SiO_2) occurs in the ternary diagram area that is characterized by melting temperatures in the interval

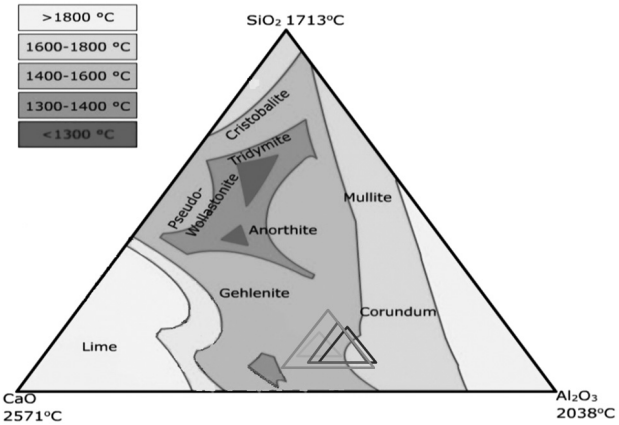

Figure 4: Ternary diagram for the starting oxidic mixture (C) and the slag obtained after the reaction with molten steels

Slika 4: Ternarni diagram začetne mešanice oksidov (C) in žlindra, ki je nastala po interakciji s staljenimi jekli

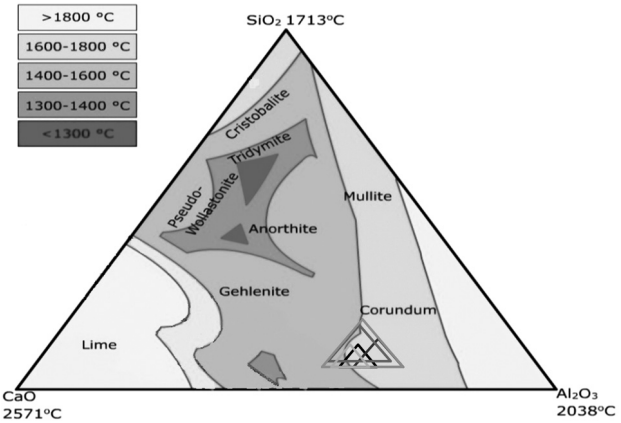

Figure 6: Ternary diagram for the starting oxidic mixture (E) and the slag obtained after the reaction with molten steels

Slika 6: Ternarni diagram začetne mešanice oksidov (E) in žlindra, ki je nastala po interakciji s staljenimi jekli

1300 °C to 1400 °C (**Figure 3**). The chemical composition of the reaction products, is after the interaction of the (B) oxidic mixture with steels No. 1 to 3, close to the original one. However, due to the increasing Al_2O_3 content, the steels have increased their melting temperature, to the 1400 °C to 1600 °C interval, which still guarantees their high reactivity in order to maintain their relatively low viscosity.

The initial oxidic mixture C (34 % CaO-47 % Al_2O_3-9 % SiO_2 – **Figure 4**) contains the most silica compared with the previous slag (**Figures 2** and **3**). The CaO-Al_2O_3-SiO_2 final slag remains in the ternary diagram, mostly in the same area, which is characterised by the melting-temperature interval from 1400 °C to 1600 °C after the reaction with steels 1 to 3. The melting temperature exceeds 1600 °C only partially.

The initial chemical composition of the oxidic mixture D (49 % CaO-39 % Al_2O_3-5 % SiO_2 – **Figure 5**) is very close to the chemical composition of the mixture B (**Figure 3**). Its position in the ternary diagram is also located in areas with a relatively low melting point (1300–1400 °C). The oxidic interaction products have, compared to the oxidic mixture B (w = 2–4 %) a higher content of silica (w = 5–7 %).

The oxidic mixture E (31 % CaO-56 % Al_2O_3-5 % SiO_2 – **Figure 6**) with its initial chemical composition, differs from the previous ones (B, C, D) in terms of a higher content of Al_2O_3 to the extent that it already appears in the area with a relatively high melting point (above 1600 °C) in the ternary diagram. The products of the mixture interaction with the metal melt no longer contain the higher content of Al_2O_3, and are located at the identical area in the ternary diagram.

4 CONCLUSION

The analysis of the interaction of synthetic oxidic mixtures with steels having different contents of the major metallurgical elements C, Mn, Si, P, S, Cr resulted in the following conclusions.

The interaction of the above-discussed oxidic systems and selected steels led to a final content of Al_2O_3 in the interval (w = 46–60 %). Although the content of Al_2O_3 in the initial oxidic mixture (A) was the lowest (11 wt.%), in comparison with the other mixtures the Al_2O_3 content was the highest of all (w = 60 %) after its interaction with the steel (2). These facts lead to the hypothesis that the settings of the experiments enabled the saturation of the resulting slag with Al_2O_3 content in the interval 46 % to 60 %. This saturation occurs within 10 min of the dissolution of the added oxidic mixtures. Furthermore, we can say that a clear dependence of the resulting chemical composition of the oxidic mixture on steels, with which they interacted, has not been proved. The content of SiO_2 did not increase above 9 % in all the studied cases and its influence on the change of the melting temperature of the oxidic mixtures was not significant.

Acknowledgement

The presented research focused on the high-temperature interactions between synthetic slag and steel was carried out with financial support from GACR (Czech Science Foundation) under project ID No. 106/09/0969.

5 REFERENCES

[1] B. Smetana, S. Zlá, M. Žaludová, J. Dobrovská, P. Kozelský, Application of High Temperature DTA to Micro-Alloyed Steels, Metalurgija, 51 (**2012**) 1, 121–124

[2] B. Smetana, S. Zlá, J. Dobrovská, P. Kozelský, Phase transformation temperatures of pure iron and low alloyed steels in the low temperature region using DTA, International Journal of Materials Research, 101 (**2010**) 3, 398–408

[3] R. Dudek, Ľ. Dobrovský, J. Dobrovská, Interpretation of Inorganic Melts Surface Properties on The Basis of Chemical Status and Structural Relations, International Journal of Materials Research, 99 (**2008**) 12, 1369–1374

[4] K. Gryc, B. Smetana, K. Michalek, V. Sikora, M. Tkadlečková, S. Zlá, M. Žaludová, J. Dobrovská, Connecting of Basic and Applied Research in the Field of Thermo-Physical Study of the Properties of Steels, Slag and Ferro-Alloys, In 20th Anniversary International Conference on Metallurgy and Materials – METAL 2011, 125–131

[5] K. Stránský, J. Janová, Chemical analysis of slags realized in laboratory of Brno University of Technology, FME in 2010. Technical report. BUT, FME, Brno 2010. [in Czech]

UDK 004.738.5:539.4
Professional article/Strokovni članek

ISSN 1580-2949
MTAEC9, 46(4)407(2012)

DEVELOPMENT OF A MODEL FOR THE INTERNET PORTAL "STRENGTH OF MATERIALS"

RAZVOJ MODELA ZA INTERNETNI PORTAL "TRDNOST MATERIALOV"

Larisa Globa[1], Rina Novogrudska[1], Ilija Mamuzić[2]

[1]National Technical University of Ukraine "Kyiv Polytechnic Institute", Institute of Telecommunication Systems, 37 Pobeda ave, 03056 Kyiv, Ukraine
[2]University of Zagreb, Faculty of Metallurgy, Berislavićeva 6, 10 000 Zagreb, Croatia
lgloba@its.kpi.ua

Prejem rokopisa – received: 2011-11-09; sprejem za objavo – accepted for publication: 2012-03-01

We present an approach to the development of a specialized-knowledge Internet portal for work with large quantities of information and computational resources in the field of strength of materials. The ontology-based portal provides an information basis for the design of alloys represented by the chosen fields of science, which may be difficult for formalizing, and it allows the use of web services for the realization of engineering tasks with the Internet and material-science knowledge that is accumulated in the databases.

Keywords: Internet portal, knowledge representation, model, ontology, strength of materials

Opisan je razvoj specializiranega znanja za internetni portal za uporabo velike količine informacijskih in podatkovnih virov s področja trdnosti materialov. Ontološka podlaga portala zagotavlja informacijsko osnovo za načrtovanje zlitin, ki obsegajo področja znanosti, ki jih je težko formalizirati, in omogoča uporabo web-storitev za realizacijo inženirskih nalog z uporabo interneta in znanosti o materialih, zbranih v bazah podatkov.

Ključne besede: internetni portal, predstavitev znanja, model, ontologija, trdnost materialov

1 INTRODUCTION

Nowadays, there is a wide variety of technical resources and software solutions that can be used to solve various engineering tasks. However, their use is sometimes restricted for two reasons: the software and technical resources of this type are either very expensive or kept hidden for commercial purposes. Also, the new theoretical and practical results obtained by researchers in numerous institutions may be concentrated in institutions, meaning their external use is limited. Thus, providing access to the information for as many users as possible is actually becoming a real challenge.

On the other hand, large quantities of information are already stored on the Internet, but it may be poorly structured and systematized and distributed across different sites, electronic libraries and archives. This may prevent the rapid and easy access to specific knowledge.

To solve these problems a specialized-knowledge Internet portal for work with a large quantity of information and computational resources in a defined technical sphere is proposed. Such a portal cannot only provide the possibility to search and systematize the information, but it can also help to realize specific computational tasks for the users.

2 KNOWLEDGE REPRESENTATION IN THE FIELD OF THE STRENGTH OF MATERIALS

When we introduce a formal description of the subject field in the form of object classes and their mutual relations, the portal's ontology gives the structures that present real data and their interconnections. The use of an ontology to construct the informational basis of the portal gives an integral presentation of the technical fields that are considered to be difficult to formalize, and also to allow the automation of the processes of acquiring information and its storage on any chosen field. Such a conceptual model makes it possible to uniformly present the knowledge data and the semantic coherence.

The knowledge-portal ontology in the field of the strength of materials was constructed on the basis of the above descriptions. Formally, the ontology may be specified as $O = \{C, A, R, T, F, D\}$. Here, C is the set of classes that describes the notions of a subject field; A is the set of attributes that describes the features of the notions and relations; R is the set of relations specified for the classes $R = \{R_{AS} R_{IA}, R_N, R_{CD}\}$, with R_{AS} – associative relation, R_{IA} – relation "is-are", R_N – relation of "heredity", R_{CD} – relation "class-data"; T – the set of standard types of attribute values; F – set of limitations for values of attribute notions and relations; and D is the set of class exemplar[1,2].

Such an ontology may serve to present the notions that are necessary for describing the knowledge in the field of the strength of materials as well as for the engineering activities performed in this context.

3 ONTOLOGY OF THE PORTAL "STRENGTH OF MATERIALS"

The ontology of the portal in the field of the strength of materials includes four ontologies: engineering-activity ontology, engineering-knowledge ontology, engineering-computations ontology and subject-field ontology (**Figure 1**).

The engineering-activity ontology (EAO) includes the general classes of notions related to the organization of scientific activities. The engineering-knowledge ontology (EKO) includes the meta-notions that specify the structures to describe the problem field, the engineering-computations ontology (ECO) groups classes that describe the portal's calculation abilities and the subject-field ontology (SFO) represents the general knowledge of the subject field, such as the hierarchy of notions classes and their semantic relations.

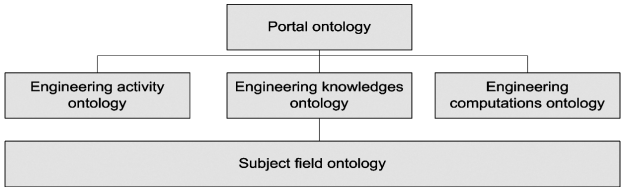

Figure 1: Portal ontology model
Slika 1: Portal ontologije modela

In **Figure 2** the EAO, EKO and ECO classes, as well as their specified relations, are shown. The classes are mapped as an oval line forms in the definite rectangle corresponding to the ontology the class belongs to. For example, the classes "Person", "Organization", "Activity" and etc. are elements of the EAO and are placed in the first rectangle. The classes "Research method", "Research object", "Research result" etc. belong to EKO and are located in the second rectangle, while the classes "Calculation", "Service", "Parameters" and "Result" are part of the ECO and are located in the third rectangle.

The classes enumerated are related to each other in single ontology and to classes of other ontologies by associative relations. For example, the classes of the EAO "Person" and "Organization" are related through the associative relations "Be a member of". It means that in real life a person may be a member of some organization. Associative relations may correlate the classes of a single ontology and the classes that belong to a different ontology, also. For example, the class "Literature" being a class of the EAO is associatively correlated by the relation "Describe" with the ECO class "Research result". The associative relations allow the understanding of the correlation of notions that are described in one class of ontology with another class notion in reality. In addition to the associative relations, in working up the portal ontologies the relations of the type "is-are" to relations of subclasses with their parent classes are used. For example, the class "Literature" is related to "is-are", to the classes "Documents", "Training materials", and "Published materials". It means that the class "Literature" is a parent class for its subclasses "Documents",

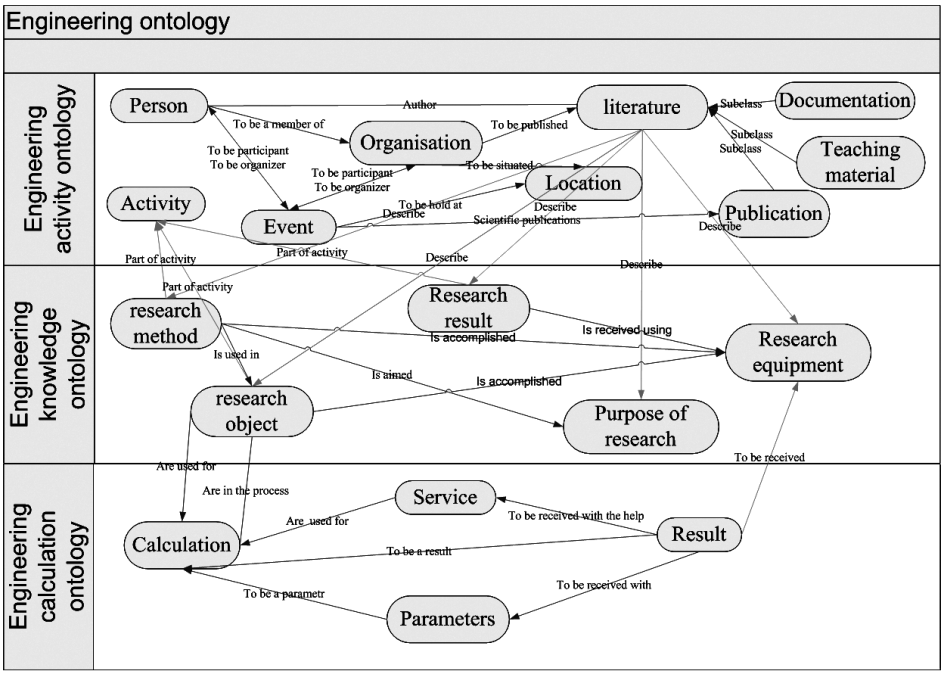

Figure 2: Elements of the portal ontology
Slika 2: Elementi ontologije portala

"Training materials" and "Published materials". Such types of relations play an important role in presenting the hierarchical structure of a model of engineering knowledge.

4 ONTOLOGY OF THE SUBJECT FIELD

The ontology of the subject field describes the strength of materials as a whole as science and its parts, notions and their connections. These notions are the realizations of meta-notions of the EKO and may be put in the order into the hierarchy "is-are". For example, "Research methods" (class of the EKO) correspond to such methods as the methods of strain, the discharge method, the stress distribution method, etc. in the strength of materials[3,4]. The "Research objects" are materials, material groups or specific material properties (**Figure 3**). The main class of the ECO "Calculation" corresponds to such notions from the field of strength of materials as the limit state design, deformation analysis, stress calculation, etc.

The classification of materials was carried out on the basis of the classification system (a hierarchy that was constructed according to the properties of materials and their features) and is shown below[5]:

Level 1 – *types of materials:*

Steel, aluminum alloys, titanium alloys, copper, etc.

Level 2 – *purpose:* (if above steel was chosen)

Structural steel, tool steel, cast steel.

Level 3 – *composition* (if above steel –> steel structural were selected)

carbon steel, carbon steel of high quality, low-alloy steel, alloy steel, etc.

Level 4 – description according to the:

Bars, plates and sheets, mass fraction of elements, etc.

Level 5 – *general properties:*

Mass content of elements, temperature of critical points, assignment, etc.

Level 6 – *mechanical properties.*

Level 7- *technological characteristics,*

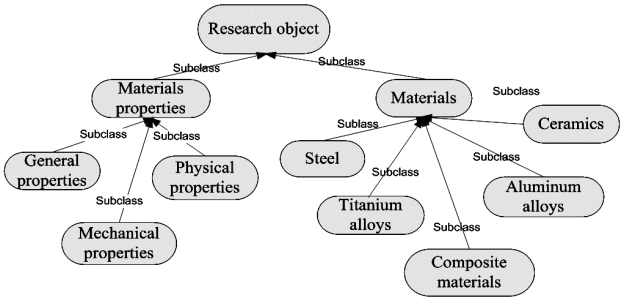

Figure 3: Ontology of the subject field

Slika 3: Ontologija polj subjektov

5 OPTIONS OF THE PORTAL

The portal information is systematized in the following areas:

- investigation of the mechanical properties of materials, the construction components and the structures:
  - types of research,
  - methodologies,
  - techniques and research tools,
  - processing of experiments results and their statistical analysis,
  - software,
  - certification of testing equipment and research laboratories,
  - regulation in the field,
  - etc.
- mechanical properties of materials:
  - static loading,
  - sustained static loading,
  - dynamic loading,
  - cyclic loading,
  - combined loading,
  - etc.
- strength calculation
  - calculation methods,
  - evaluation of stress-strain state of structures,
  - software resources,
  - specifications,
  - etc.

The proposed portal will provide access to databases, reference books, manuals, express information, network resources, etc. for the browsing of different types of theoretical information and practical results collected and stored for years in different institutions. By means of this portal it will be possible to solve different calculation and computational tasks according to the user's needs. For example, the portal will make it possible: to

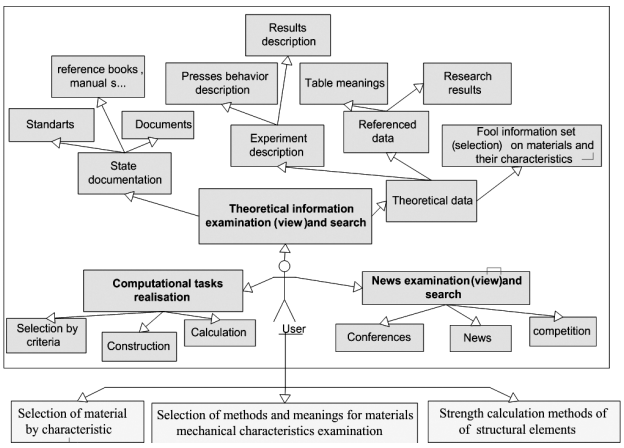

Figure 4: Portal options

Slika 4: Možnosti portala

find a material according to some criteria (characteristics), to plot different graphs, diagrams and dependences, to compute the data of various types according to the user's needs. The portal will make it possible to browse blocks of news, information about conferences (upcoming and past), competitions and grants, as well as other information about various events relevant to this area of knowledge (**Figure 4**). An important step in the portal's construction is the structuring and systematization of the information and knowledge in the field of strength of materials that will allow users to browse and search specific information in the area chosen. The placement of information on the portal is organized comfortably for end-user implementing problem-oriented navigation and search tools. Thus the search for information is organized to give the user the possibility to specify a search request, not only using keywords, but using well known terms of the portal subject field as well.

6 CONCLUSIONS

The possibility of a "strength of materials" portal design is described. The portal's informational model is presented by means of an ontology that allows us to systematize and structure the information and to organize an effective search and navigation through the information space of the engineering-knowledge portal.

7 REFERENCES

[1] O. A. Andreeva, O. I. Borovikova, Y. A. Zagogulko et al.: Archeological portal of knowledge: substantial access to knowledge and informational resources / 1st national conference of artificial intelligence KII 2006. – M.: PhithMathLit., 2006, 832–840

[2] Y. A. Zagogulko, O. I. Borovikova, The technology of ontologies constructing for the portals of scientific knowledge, Journal of NGU. Series: Informational technologies, 5 (**2007**) 2, 12–15

[3] Ya. B. Fridman, Mechanical properties of metals – M.: Mechanical engineering, 1974, 2p, 368

[4] Strength of materials and constructions / editorial board: V. T. Troshenko (editor-in-chief) and others. – K.: Akademperiodica, 2005, 1088p

[5] A. C. Zubchenko: Book of steels and alloys. – M. - Mechanical engineering, 2001, 663p

UDK 669.245:621.785
Professional article/Strokovni članek

ISSN 1580-2949
MTAEC9, 46(4)411(2012)

THE INFLUENCE OF THE HEAT-TREATMENT REGIME ON A FRACTURE SURFACE OF NICKEL-BASED SUPPERALLOYS

VPLIV TOPLOTNE OBDELAVE NA POVRŠINO PRELOMA SUPERZLITIN NA OSNOVI NIKLJA

Andjelka Milosavljevic[1], Sanja Petronic[2], Suzana Polic-Radovanovic[3], Jasmina Babic[4], Darko Bajic[5]

[1]Faculty of Mechanical Engineering, Belgrade, Serbia
[2]Innovation Center of the Faculty of Mechanical Engineering, Belgrade, Serbia
[3]Central Institute for Conservation, Belgrade, Serbia
[4]Military Technical Institute, Belgrade, Serbia
[5]Faculty of Mechanical Engineering, Podgorica, Montenegro
sanjapetronic@yahoo.com

Prejem rokopisa – received: 2012-01-11; sprejem za objavo – accepted for publication: 2012-02-23

Nickel-based superalloys are distinguished from other materials by their excellent mechanical and physical properties. As they are used at high temperatures and pressures, as well as in aggressive environments, their characteristics need constant improvement. An adequate choice of their chemical composition and the heat-treatment regime contributes to the improvement of the chemical, physical and mechanical properties of these nickel-based superalloy materials. During the heat treatments of the superalloys Nimonic 263 and Hastelloy S some changes in their microstructures were observed. In this paper the changes in the microstructures after various regimes of the heat treatment were analysed on the fractured surfaces. The fractured surfaces were observed using light microscopy, scanning electron microscopy (SEM), and energy-dispersive X-ray spectrometry (EDS).

Keywords: superalloy, heat treatment, microstructure, EDS, SEM

Superzlitine na osnovi niklja se razlikujejo od drugih materialov zaradi svojih odličnih mehanskih in fizikalnih lastnosti. Ker se jih uporablja pri visokih temperaturah in tlakih ter v agresivnem okolju, je potrebno stalno izboljševati njihove lastnosti. Primerna izbira kemijske sestave in načina toplotne obdelave prispevata k izboljšanju kemijskih, fizikalnih in mehanskih lastnosti superzlitine na osnovi niklja. Med toplotno obdelavo superzlitine Nimonic 263 in Hastelloy S se opazijo spremembe v mikrostrukturi. V tem članku so analizirane spremembe mikrostrukture na prelomnih površinah po različnih toplotnih obdelavah. Površina prelomov je bila opazovana s svetlobno mikroskopijo, vrstično elektronsko mikroskopijo (SEM) in rentgensko disperzijsko spektroskopijo (EDS).

Ključne besede: superzlitina, toplotna obdelava, mikrostruktura, EDS, SEM

1 INTRODUCTION

Modern industry has a high demand for superalloys due to their enhanced technological features, such as good mechanical strength and hardness, corrosion resistance, heat resistance, wear resistance and surface degradation[1–3].

The good tensile strength of superalloys is based on the principle of a stable face-centered cubic matrix combined with precipitation hardening and/or solid-solution strengthening[4].

Precipitation hardening produces a high strength with finely dispersed precipitates formed during the heat treatment and deposited in the elastic matrix. These particles can be obstacles to the movement of dislocations through the crystal structure, thus reinforcing the heat-treated alloy.

The effect of the superalloys' strengthening depends on the type of particles. The best results can be achieved when the coherent and partially coherent particles finely disperse within the matrix.

Precipitation hardening increases the mechanical properties, especially the strength of the materials, with the precipitation from supersaturated solid solutions. The principal strengtheners in the nickel-based superalloys are complex precipitates of γ'[Ni_3(Al, Ti)] and γ" [Ni_3(Nb, Al, Ti)] and the carbide particles. Other phases have a negligible effect on increasing the tensile strength, but a significant effect on increasing the creep and fracture strength, and the segregation[5].

Some unwanted phases can precipitate during the heat treatment, plastic deformation and/or long-time service. By selecting the optimal heat-treatment time and the optimal heat-treatment temperature, these phases could be avoided[5,6].

In addition, a proper selection of the chemical composition and the heat treatment contributes to an improvement of the chemical, physical and mechanical properties of the nickel-based superalloys[7].

During the heat treatment of the superalloys Nimonic 263 and Hastelloy S the phase transformations occurred[8].

The influence of the heat treatment on the microstructure of various metals and their alloys has been

investigated so far[5,9–12], but, bearing in mind the importance and applicability of these superalloys in industry, it is undoubtedly important to further investigate the influence of heat treatment on the microstructure of these superalloys.

In this paper, the influence of heat treatment on the microstructure of two nickel-based superalloys, which have been strengthened with different strengthening mechanisms, is investigated. Hastelloy S is a solid-solution strengthened alloy with a high content of molybdenum. Nimonic 263 is a precipitation-hardenable alloy with an addition of molybdenum for the solid-solution strengthening. These two superalloys are very often used in domestic industry.

2 EXPERIMENTAL

In this paper, the experimental investigations are carried out on the commercial, nickel-based superalloys Nimonic 263 and Hastelloy S. The samples are cut from the sheets, thickness of 1.2 mm. The chemical composition is determined by the gravimetric method and listed in **Table 1**.

The homogenization heat treatment of the superalloys Nimonic 263 and Hastelloy S is performed in a vacuum at a temperature of 1050 °C and for 16 h, with the aim to achieve a homogeneous structure.

The samples of Nimonic 263 superalloy are subjected to a two-stage heat treatment:

1) solid solution at 1150 °C and cooling in water,
2) aging at 800 °C/8 h and cooling the air.

The solid solution time at a temperature of 1150 °C for one group of Nimonic 263 samples is 10 min (regime – R1). As the results obtained after regime R1 suggest that the solid-solution time is short, the second group of samples is subjected to a solid solution treatment for 60 min (regime – R2), due to the assumption that longer periods of solid solution treatment could bring about the formation of coarse particles. The regime of precipitation hardening for both groups is the same – 800 °C/8 h cooled air.

The heat treatment of the superalloy Hastelloy S, described according to literature data and experience[5,13]:

- Solution treatment at 1080 °C/1 h and rapidly cooled in water to room temperature,
- Primary precipitation hardening at 840 °C/4 h and cooling to room temperature,
- Secondary precipitation hardening at 760 °C/3 h and cooling in air to room temperature.

After the heat treatment carried out according to the described regime, the superalloy samples were prepared for light microscopy. After the polishing of the samples the etching was performed for the superalloys Nimonic 263 and Hastelloy S in a solution with the following composition: 30 % H_2O, 20 % HNO_3, 10 % HF, 20 % H_3PO_4 and 10 % CH_3COOH.

The fractured surfaces were observed with a light microscope (model KEYENCE VH-Z100), a scanning electron microscope (model JOEL JSM-5800) and analysed using energy-dispersive X-ray spectrometry.

The tensile tests were performed with a mechanical universal testing machine (Schenck-Trebel, RM400) and the 0.2 % offset yield strength, tensile strength and elongation were determined. The tensile tests were carried out at room temperature according to the en 10002-1 standard. The hardness tests were made with a semi-automatic Hauser 249A and the HV_{30} was measured.

3 RESULTS AND DISCUSSION

The first step in the heat treatment of superalloys is usually a solid-solution treatment. The solid-solution temperature depends on the required characteristics.

Higher temperatures are used for optimum creep-fracture properties, and produce a higher yield and a more extensive carbide dissolution. Lower temperatures result in the optimal yield strength at elevated temperature and a resistance to fatigue[14].

By observing the microstructure of the Nimonic 263 samples, prepared for light microscopy by polishing and etching, at 225-times magnification, there is a difference in grain size, i.e., a finer grain size is achieved for the heat treatment regime R2 (**Figure 1b**) than for the heat-treatment regime R1 (**Figure 1a**). The average grain size is calculated using the method of the circle[15] and their values are as following: F_m = 314.78 μm^2 and F_m = 237.68 μm^2 for the regimes R1 and R2 applied, respectively.

The values measured by Vickers hardness with a load of 30 N are:

- HV_{30} = 283 regime R1,
- HV_{30} = 302 for regime R2.

The finer grain structure and the higher hardness values imply that the heat treatment carried out by regime R2 has a more favourable impact on the properties of the superalloy Nimonic 263, compared to the heat treatment by regime R1.

After the heat treatment, regime R2, which was preceded by homogenization, the microstructure of the

Table 1: Chemical composition of Nimonic 263 and Hastelloy S superalloys in mass fractions (*w*/%)
Tabela 1: Kemijska sestava superzlitin Nimonic 263 in Hastelloy S v masnih deležih (*w*/%)

Element	C	Si	Mn	Al	Co	Cr	Cu	Fe	Mo	Ti	Ni
Nimonic 263	0.06	0.3	0.5	0.5	20	20	0.1	0.5	5.9	2.2	49.94
Hastelloy S	0.3	0.5	0.5	0.3	–	15.3	–	1.34	14.4	–	67

Table 2: Results of EDS-analysis of the spectrums in **Figure 2a** (*w*/%)
Tabela 2: Rezultati EDS-analize spektrov s **slike 2a** (*w*/%)

Spectrum	Al	Si	Ti	Cr	Mn	Fe	Co	Ni	Mo
Spectrum 1	0.2	0.11	1.99	32.42	0.32	0.25	13.87	44.82	6.02
Spectrum 2	0.22	0.21	6.73	19.35	0.34	0.26	17.82	49.25	5.82
Spectrum 3	0.51	0.28	2.01	19.89	0.5	0.48	20	50.4	5.93
Spectrum 4	0.47	0.32	2.2	20.03	0.46	0.52	20.32	49.85	5.83
Spectrum 5	0.54	0.27	2.18	19.95	0.53	0.51	19.98	50.14	5.9

superalloy Nimonic 263 consists of the following: γ solid solution, γ' intermetallic compounds – γ'[Ni_3(Al, Ti)], carbides $M_{23}C_6$, MC carbide and a number of annealing twins. The volume fraction of γ' for the start of the thermal deposition is about 10 % [16], and its fraction increases with the deposition time, and is unevenly distributed in the γ solid solution. The $M_{23}C_6$ carbides are densely distributed at the grain boundaries, while the amount of MC carbide is small and mainly formed during solidification and precipitation. The MC carbides are mainly Ti carbides, and Ti is a γ' former as well. This explains the creation of γ'-free zones at the grain boundaries, as Ti forms carbides, and depletes Ti in the γ solid solution near the grain boundaries.

Figure 2a shows a micrograph of the microstructure of superalloy Nimonic 263, after heat treatment – the regime R2. The results of the EDS analysis are listed in **Table 2**. It is clear that the Cr and Ti carbides precipitate at the grain boundaries, which confirms the increased content of Cr in spectrum 1 and the increased content of Ti in spectrum 2. An analysis of the grain (spectrums 3, 4, 5) indicates that the chemical composition is generally close to the average one. For chromium carbides we could not exactly determine the type of carbide. According to the literature[3,5,17,18] they could be the $M_{23}C_6$ type carbide, which are densely distributed at the grain boundaries. The size of these carbides is up to 600 nm. Their shape is elliptical, and they are uniformly distributed at the grain boundaries. The size, morphology, distribution and location of these carbides are favourable for the straightening of superalloy. Comparing to[16] where time of the solid solution was shorter, these carbides are finer and more uniformly distributed at the grain boundaries.

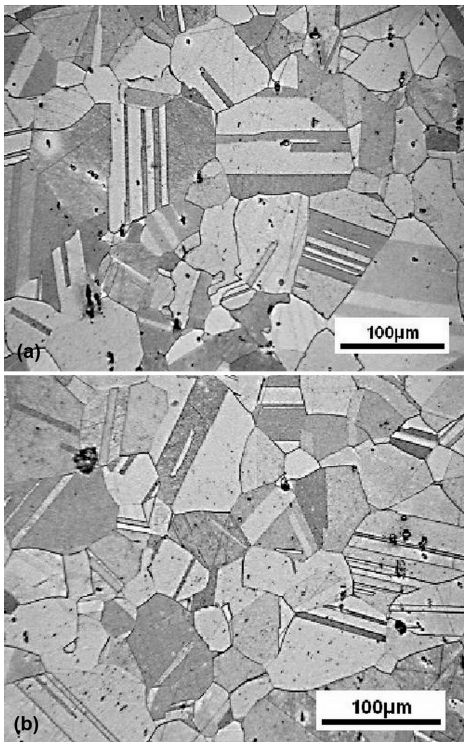

Figure 1: The microstructure of the superalloy Nimonic 263 after heat treatment by: a) regime R1, b) regime R2, taken with an optical microscope
Slika 1: Mikrostruktura superzlitine Nimonic 263 po toplotni obdelavi: a) način R1, b) način R2, optični mikroskop

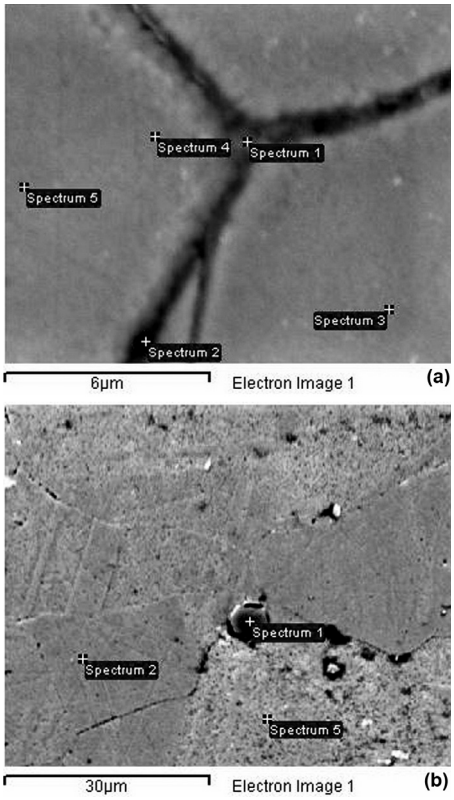

Figure 2: a) Carbides precipitated at the grain boundaries after the heat treatment regime R2, b) TiC carbide precipitated by solution treatment of regime R1 (SEM)
Slika 2: a) Karbidni izločki po mejah zrn po toplotni obdelavi z načinom R2, b) TiC karbidni izločki po raztopnem žarjenju po načinu R1 (SEM)

Table 3: Results of EDS analysis of the spectrums in **Figure 2b** (*w*/%)
Tabela 3: Rezultati EDS-analize spektrov s **slike 2b** (*w*/%)

Element	Al	Si	Ti	Cr	Mn	Fe	Co	Ni	Mo
Spectrum 1	–	–	80.99	3.83	–	–	0.35	14.83	–
Spectrum 2	0.34	0.35	2.32	18.9	0.29	0.47	19.95	51.28	6.1
Spectrum 3	0.44	0.38	18.58	16.15	0.29	0.52	15.15	48.49	–

Table 4: Results of EDS analysis of the spectrums in **Figure 3** (*w*/%)
Tabela 4: Rezultati EDS-analize spektrov s **slike 3** (*w*/%)

	Al	Si	Ti	Cr	Mn	Fe	Co	Ni	Mo
area in Fig. 3.a)	0.45	1.33	2.80	19.88	0.90	0.52	17.72	49.04	6.47
Spec1–Fig. 3.b)	0.47	0.48	8.79	19.13	0.39	0.80	16.40	46.17	6.37
Spec2–Fig. 3.b)	0.58	0.63	7.30	20.34	0.28	0.48	17.47	46.60	6.31

According to **Figure 2b** and **Table 3**, it can be concluded that in spectrum 1, at the grain boundaries, the carbide TiC precipitated. The grain boundaries are γ'-free, and the EDS analysis in spectrum 3 and **Figure 2b** indicates that Ti carbides are deposited at the grains. It is believed that this is the reason for the relatively small amount of γ' phase. The carbides at the grains are fine and considered as being favourable for the strengthening of the structure.

However, the Ti carbide in spectrum 1 is due to the short time of the solution treatment, and then the rapid cooling. It is considered to be too large to be beneficial to the microstructure. The carbide is hexagonal, up to 6.15 μm in size, and locally precipitated at the triple grain boundary. Due to its size, this carbide can be a convenient place for the deposition of a topologically close-packed (TCP) phase, and may be the initiator of the appearance of microcracks.

The characterization of the microstructural changes of the fracture surfaces occurring in the stated superalloys for the regimes R1 and R2 was made by scanning electron microscopy and energy-dispersive X–ray spectrometry analysis, as shown in **Figures 3** and **4**.

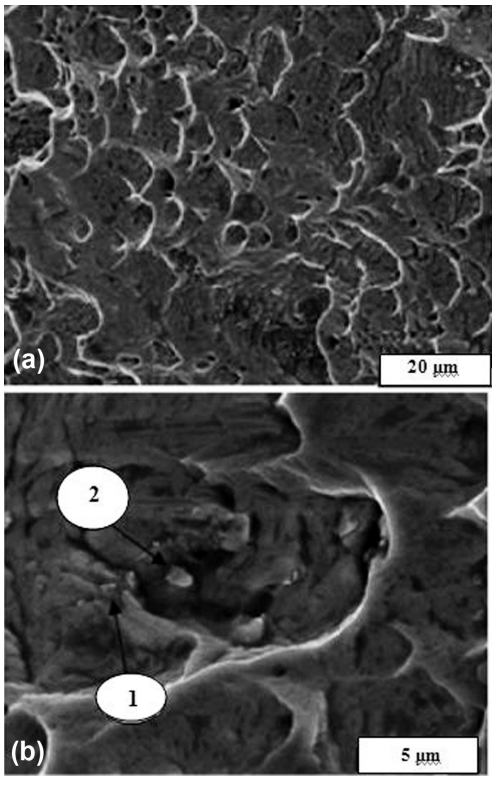

Figure 3: a) The appearance of a fracture surface after the heat treatment R2, b) carbides at the fracture surface
Slika 3: a) Videz površine preloma po toplotni obdelavi z načinom R2, b) karbidi na površini preloma

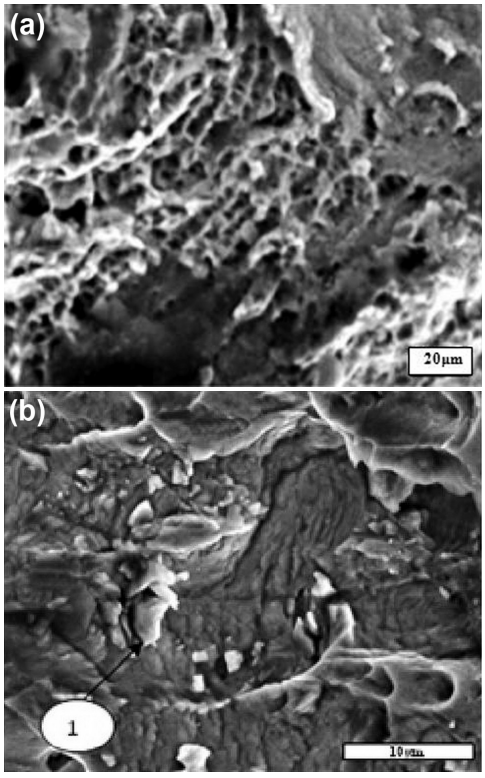

Figure 4: a) The appearance of a fracture surface of the Nimonic 263 superalloy after heat treatment R1, b) detail from **Figure 4a** – unfavourable Ti carbide
Slika 4: a) Videz površine preloma superzlitine Nimonic 263 po toplotni obdelavi z načinom R1, b) detajl s **slike 4a** – nezaželeni Ti-karbidi

Table 5: Results of EDS-analysis of the spectrums in **Figure 4** (*w*/%)
Tabela 5: Rezultati EDS-analize spektrov s **slike 4** (*w*/%)

	Al	Si	Ti	Cr	Mn	Fe	Co	Ni	Mo
The area in Fig. 4.a)	0.25	1.33	2.80	19.88	0.90	–	17.72	51.04	6.47
Spectrum 1 – Fig. 4.b)	–	–	46.55	12.01	0.51	0.21	10.20	28.47	2.16

Table 6: Results of EDS-analysis of the area in **Figure 6a** (*w*/%)
Tabela 6: Rezultati EDS-analize področja s **slike 6a** (*w*/%)

	Al	Si	Cr	Mn	Fe	Ni	Mo
Whole area in Fig. 6a	0.4	0.46	14.86	0.54	1.08	64.82	18.6
Whole area in Fig. 6b	0.38	0.48	15.04	0.56	1.33	65.41	17.8

Table 7: Mechanical properties of superalloys Nimonic 263 and Hastelloy S after applied heat treatments
Tabela 7: Mehanske lastnosti toplotno obdelanih zlitin Nimonic 263 in Hastelloy S

Mechanical properties	$R_{0.2}$ /(N/mm^2)			R_m /(N/mm^2)			A_5/(%)		
	I	II	III	I	II	III	I	II	III
Nimonic 263 R1	550	573	545	820	835	832	39	38	39
Nimonic 263 R2	582	587	593	972	975	979	39	40	39
Hastelloy S	464	450	466	845	839	837	49	48	50

The fractured surfaces were obtained from the tensile tests and the results of the tensile strength, yield strength (0.2 % offset) and elongation, together with the results obtained for the superalloy Hastelloy S, are given in **Table 7**.

Figures 3a and **3b** show the fracture surfaces of the superalloy Nimonic 263, after the heat treatment with regime R2. The fractured surface is relatively homogeneous and the dimples are relatively uniform. In **Figure 3b** the same fracture is presented at a higher magnification. The deposition of Ti carbides can be observed, as confirmed by the EDS analyses listed in **Table 4**. The size of carbides is up to 1.16 μm and it is believed that these carbides are not the cause of the fracture.

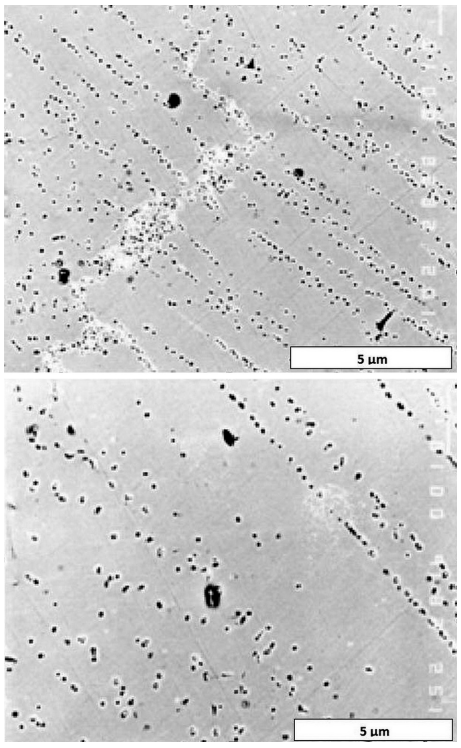

Figure 5: Molybdenum carbides precipitated in the superalloy Hastelloy S after heat treatment, taken with a light microscope
Slika 5: Karbidi molibdena, izločeni v toplotno obdelani superzlitini Hastelloy S; svetlobni mikroskop

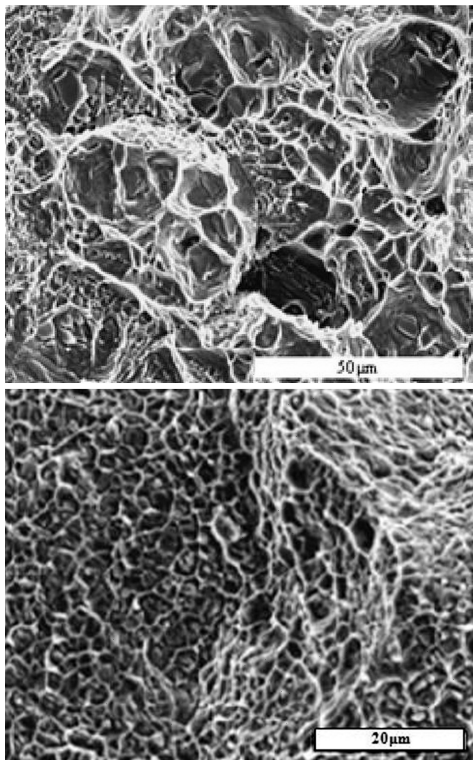

Figure 6: Fracture surfaces of the superalloy Hastelloy S taken with a SEM
Slika 6: Površina preloma superzlitine Hastelloy S (SEM)

Figures 4a and **4b** show the fractured surfaces of the Nimonic 263 superalloy after heat treatment – regime R1. In **Figure 4b** is a detail from **Figure 4a** – an unfavourable precipitated carbide. The EDS analysis results listed in **Table 5** confirm the assumption that it is a Ti carbide, and the place, morphology (irregular, hexagonal-like) and size (3.95 μm) suggest it has a negative influence on the mechanical characteristics of the material. It is believed that the large carbides contributed greatly to the breaking of the material.

Based on our observations of the samples of the superalloy Hastelloy S using a light microscope, the dark phases are visible, for which the energy-dispersive X-ray spectrometry analysis shows they are the molybdenum carbides. Their formation contributed the increased content of molybdenum in the alloy, as well, compared to the prescribed one.

The molybdenum carbides are segregated into arrays and nests – **Figures 5a** and **5b**. It is believed that these carbides, together with the Cr carbides that occur in these alloys, strengthened the alloy after the heat-treatment process.

Figures 6a and **6b** show the fractured surfaces of the superalloy Hastelloy S. In **Table 6** are the results of the EDS analysis of the whole areas presented in **Figure 6**. A higher content of molybdenum was observed, and this is consistent with light-micrograph analyses. The structure of the fractures is homogeneous and uniform, as confirmed by the EDS analysis conducted at the 150x and 5 000-times magnifications (**Table 6**). The chemical compositions of the two investigated surfaces differ very little, which implies the homogeneity of the structure.

The mechanical properties obtained with the tensile tests are listed in **Table 7**. Relatively high values of the tensile strength, the yield strength (0.2 % offset) and the elongation are in favour of a good heat treatment being applied. In this paper, the short-solid solution time (regime R1) results in lower values of the ultimate tensile strength and yield strength, while the elongation remains the same. The results listed in[16], where the authors applied different aging times for three groups of samples, show that the various heat treatments have a large effect on all the tensile properties of the material. Compared to the literature data[4,19] obtained for Nimonic 263 ($R_{0.2}$ = 580 MPa, R_m = 970 MPa and A_5 = 39 %) we observed slightly higher $R_{0.2}$ and R_m values. According to the literature[4,20] the tensile-test characteristics of the Hastelloy S alloy are: $R_{0.2}$ = 444 MPa, R_m= 844 MPa and A_5 = 49 %. In this paper, the higher value of $R_{0.2}$, the yield strength (0.2 % offset), is obtained – the important characteristic of the material used in design projects. Based on the results in **Table 7**, the fracture appearance and the EDS analysis, it can be assumed that during the heat treatment the creation of undesirable phases has not taken place, which would help in the breaking of the material.

4 CONCLUSIONS

The microstructure and mechanical characteristics of the superalloys Nimonic 263 and Hastelloy S, besides processing route and chemical composition, depend to a large extent on the applied heat treatment. The heat-treatment processes of the superalloys Nimonic 263 and Hastelloy S, carried out according to the regimes described in this paper, indicate their considerable influence on the microstructure transformations, and in this way on the material properties. During the applied heat-treatment regimes, the various micro-constituents formed with a major influence on the properties of the materials.

The heat treatment of the superalloy Nimonic 263, which included 60 min of solid solution time (R2), rather than the 10 min solid solution time (R1), resulted in a better microstructure and better mechanical properties of the stated superalloy. During both regimes of heat treatment, Ti carbides participated, but according to the size, the morphology and the distribution in regime R2 they are favourable, while in regime R1 they are not. The grains are finer and more uniformly distributed after the heat treatment of regime R2 than after regime R1, i.e., with a longer solid-solution time. Also, the values of mechanical properties: the hardness, the ultimate tensile strength and the yield strength (0.2 % offset), are higher when the time of the solid solution treatment is longer.

After the heat treatment of the nickel-based superalloy Hastelloy S, applied in this study, the molybdenum carbides segregated. As a result, a higher value of the yield strength is obtained. This characteristic is critical in design projects, which makes these results very useful for engineering practice.

Acknowledgements

This work was supported by the Ministry of Science of the Republic of Serbia under contract number TR-35040 and TR 34028.

5 REFERENCES

[1] R. C. Reed, The Superalloys, Fundamentals and Applications, 1th ed., Cambridge University Press, New York 2006, 163

[2] C. T. Sims, W. C. Hagel, The Superalloys, Wiley-Interscience, New York 1972, 576

[3] F. Tancret, H. K. D. H. Bhadeshia, D. J. C. MacKay, Key Engineering Materials, 171–174, (**2000**), 529–536

[4] Metal Handbook – Vol 1 & Vol 2, Properties and Selection: Iron, Steel, and High-Perf. Alloys, 10th ed., ASMI, Materials Park, Ohio 2005, 2301

[5] Metal Handbook, Vol 4, Heat treating, Cleaning, Finishing, 8th ed., ASMI, Metals Park, Ohio 1975, 1757

[6] www.specialmetalswiggin.co.uk

[7] V. Shankar, K. B. S. Rao, S. L. Mannan, Journal of Nuclear Materials, 288 (**2001**), 222–232

[8] J. C. Zhao, V. Ravikumar, A. M. Beltran, Metallurgical and Materials Transactions A, 32 (**2001**), 1271–1282

[9] J. X. Yang, Q. Zheng, X. F. Sun, H. R. Guan, Z. Q. Hu, Materials Science and Engineering A, 465 (**2007**), 100–108
[10] W. Österle, S. Krause, T. Moelders, A. Neidel, G. Oder, J. Völker, Materials Characterization, 59 (**2008**), 1564–1571
[11] P. N. Singh, V. Singh, Scripta Materialia, 34 (**2008**) 12, 1861–1865
[12] R. Cahn, P. Haasen, Physical Metallurgy, 4th ed., Elsevier Science B. V., 1996, 1817
[13] S. Petronic, A. Milosavljevic, FME Transactions, (**2007**) 35, 189–193
[14] S. Zhao, X. Xie, G. D. Smith, S. J. Patel, Materials Science and Engineering A, 355 (**2003**), 96–105
[15] H. Schumann, Metallographie, 9th ed., VEB Deutscher Verlag für Grundstoffindustrie – Leipzig, 1975, 41
[16] W. Z. Wang, H. U. Hong, I. S. Kim, B. G. Choi, H. W. Jeong, M. Y. Kim, C. Y. Jo, Materials Science and Engineering A, 523 (**2009**), 242–245
[17] X. Z. Qin, J. T. Guo, C. Yuan, C. L. Chen, J. S. Hou, H.Q. Ye, Materials Science and Engineering A, 485 (**2008**), 74 –79
[18] H. M. Wang, L. G. Yu, X. X. Li, P. Jiang, Science and Technology of Advanced Materials, (**2001**), 173–176
[19] http://www.matweb.com/
[20] http://www.haynesintl.com/pdf/ h3003.pdf

UDK 519.61/.64:666.3/.7
Strokovni članek/Professional article

ISSN 1580-2949
MTAEC9, 46(4)419(2012)

UPOGIBNA TRDNOST KORUNDNE KERAMIKE: PRIMERJAVA RAZLIČNIH TEORETIČNIH PORAZDELITEV NA OSNOVI EKSPERIMENTALNIH PODATKOV

BEND STRENGTH OF ALUMINA CERAMICS: A COMPARISON OF DIFFERENT THEORETICAL DISTRIBUTIONS ON THE BASIS OF EXPERIMENTAL DATA

Milan Ambrožič[1], Lovro Gorjan[2,3]

[1]Fakulteta za naravoslovje in matematiko, Univerza v Mariboru, 2000 Maribor, Slovenija
[2]Institut "Jožef Stefan", Jamova 39, 1000 Ljubljana, Slovenija
[3]Hidria AET d. o. o., Poljubinj 89A, 5220 Tolmin, Slovenija
lovro.gorjan@hidria.com

Prejem rokopisa – received: 2012-01-27; sprejem za objavo – accepted for publication: 2012-03-02

Statistično smo ovrednotili 5100 eksperimentalnih vrednosti upogibnih trdnosti testnih vzorcev iz redne proizvodnje korundnih keramičnih izdelkov. Primerjali smo teoretično izračunano Weibullovo porazdelitev z dvema drugima pogosto uporabljenima dvoparametričnima porazdelitvama, normalno in log-normalno, da bi ugotovili, katera se najbolj sklada z meritvami. Za izračun ustreznih prostih parametrov smo uporabili metodo največje verjetnosti (maximum-likelihood method). Potem smo za primerjavo rezultatov uporabili Q – Q-diagrame. Potrdili smo domnevo, da se z eksperimentalnimi vrednostmi trdnosti najbolj ujema Weibullova porazdelitev.

Ključne besede: Weibullova porazdelitev, metoda največje verjetnosti, Q – Q-diagram

We have performed a statistical evaluation of 5100 experimental values of the bend strength of test pieces from a serial production of alumina products. The Weibull distribution was compared with two other commonly used 2-parametric distributions, i.e., normal and log-normal, in order to reveal which of them best matches the experiments. The maximum-likelihood method was used to evaluate the corresponding parameters, and then a Q–Q plot was used for all the statistics. We confirmed that the Weibull distribution describes the experimental strengths most accurately.

Keywords: Weibull distribution, maximum-likelihood method, Q–Q diagram

1 UVOD

Neenakost množice merjenih vrednosti trdnosti keramičnih in drugih krhkih materialov v standardnih mehanskih preskusih je posledica naključne porazdelitve napak v vzorcih, največkrat pa te trdnosti opišemo z Weibullovo statistično porazdelitvijo[1–4]. Zanesljivost teoretičnih napovedi na osnovi Weibullove ali drugih pogosto uporabljenih porazdelitvenih funkcij, ki jih izračunamo za majhno število vzorcev, so veliko raziskovali teoretično in eksperimentalno (največkrat pa kombinirano) za različne pogoje merjenja[5–19]. Znano je na primer, da različni računski postopki sistematično dajejo prevelike ali pa premajhne vrednosti prostih parametrov raznih statističnih porazdelitev, če je število zlomljenih vzorcev relativno majhno, npr. 30 ali še manj[7,8]. Metoda največje verjetnosti (ML = maximum-likelihood method) se zaradi svoje učinkovitosti pogosto uporablja za izračun parametrov statističnih porazdelitev[20,21].

Veliko avtorjev se je že vprašalo o upravičenosti uporabe Weibullove porazdelitve, zato so zanesljivost njenih napovedi primerjali tudi z drugimi porazdelitvami: normalno (Gaussovo), log-normalno itd.[7,22]. Za majhno število testnih vzorcev namreč ne moremo zanesljivo izključiti veljavnosti vseh teh porazdelitev, posebno ne Gaussove[22]. Eden od zanimivih načinov vizualne primerjave eksperimentalnih trdnosti vzorcev s teoretičnimi vrednostmi iz ustrezne porazdelitvene funkcije so Q – Q-diagrami (Q = quantile)[23,24]. Ujemanje med teorijo in eksperimentom je dobro, če so točke v diagramu zelo blizu premici, ki oklepa z vodoravno osjo kot 45° (simetrala prvega kvadranta).

V članku opisujemo statistično obdelavo 5100 izmerjenih vrednosti upogibne trdnosti vzorcev iz redne proizvodnje korundnih keramičnih izdelkov. Za oceno parametrov treh različnih teoretičnih porazdelitev smo uporabili ML-metodo, potem pa med drugim primerjali ujemanje teoretično izračunanih in eksperimentalnih trdnosti s Q – Q-diagrami.

2 MERITVE TRDNOSTI

Keramične testne vzorce v obliki kvadrov dimenzij 4 mm × 3 mm × 45 mm smo izdelali v podjetju Hidria AET, d. o. o., s tehniko nizkotlačnega brizganja v kalupe. V enem letu se nam je nabralo 5100 meritev trdnosti vzorcev iz 425 proizvodnih serij, po 12 zlomljenih vzorcev iz vsake serije. Vzorci so bili iz korundne keramike

Al_2O_3 s 95-odstotno teoretično gostoto, pripravljeni s sintranjem tri ure pri temperaturi 1640 °C. Ta material se v glavnem uporablja za električno izolacijo in se zanj ne zahtevajo najvišje trdnosti, tako da ga v podjetju označujemo kot "Al_2O_3 keramiko srednjih trdnosti". Trdnosti smo izračunali z enačbo za 4-točkovni upogibni test[21]:

$$\sigma = \frac{3F(L_2 - L_1)}{2ah^2} \quad (1)$$

kjer je σ upogibna trdnost vzorca, F zlomna sila, L_2 = 40 mm in L_1 = 20 mm sta zunanji in notranji razmik podpor, a = 4 mm je širina vzorca, h = 3 mm pa njegova debelina.

3 STATISTIČNI MODEL IN GRAFIČNA PONAZORITEV

Naša naključna (statistična) spremenljivka je upogibna trdnost σ. V računih uporabljamo obe porazdelitveni funkciji: verjetnostno gostoto $p(\sigma)$ in kumulativno verjetnostno funkcijo $P(\sigma) = \int_o^\sigma p(x)\mathrm{d}x$. Primerjali bomo ujemanje med eksperimentalnimi podatki in tremi napovedanimi 2-parametričnimi porazdelitvami: Weibullovo, normalno (Gaussovo) in log-normalno.

3.1 Postopek za ocenitev stopnje ujemanja teorije in eksperimenta

Podroben postopek za oceno dveh prostih parametrov in vizualne ponazoritve ujemanja dane teoretične porazdelitvene funkcije z eksperimentalnimi podatki sestoji iz naslednjih korakov:

a) Za vsako od treh porazdelitev posebej dobimo najprimernejši vrednosti prostih parametrov z metodo največje verjetnosti (ML). N (= 5100) izmerjenih trdnosti, σ_i, i = 1 do N, vstavimo v verjetnostno gostoto $p(a, b; \sigma)$, kjer sta a in b ustrezna parametra, npr., $a \equiv m$ in $b \equiv \sigma_{0W}$ za Weibullovo porazdelitev (gl. spodaj). Z metodo ML poiščemo največjo mogočo vrednost naslednje funkcije glede na vse mogoče vrednosti a in b:

$$Y = \ln\left(\prod_{i=1}^{N} p(a, b; \sigma_i)\right) = \sum_{i=1}^{N} \ln p(a, b; \sigma_i) \quad (2)$$

V ustreznih (dveh) enačbah sta odvoda funkcije Y po parametrih a in b enaka nič.

b) Eksperimentalne vrednosti trdnosti σ_i uredimo po naraščajočih vrednostih, kjer gre indeks i od 1 do N = 5100. Vsaki številki i (in s tem ustrezni vrednosti trdnosti) priredimo verjetnost P_i za zlom, pri tem pa si pomagamo z enim od pogosto uporabljenih ocen iz literature: [22]

$$P_i = \frac{i - 0.5}{N} \quad (3)$$

Vrednost P_i ustreza kumulativni verjetnostni funkciji $P(\sigma)$ za izbrano teoretično porazdelitev. Namesto z oceno (3) smo poskusili s še drugimi ocenami za P_i iz literature in ugotovili, da ta izbira nič ne vpliva na končne rezultate, vsaj za tolikšno število merjenih vzorcev.

c) Za vsako vrednost P_i, dobljeno iz enačbe (3), smo z obratom teoretične funkcije $P(a, b; \sigma)$ z že prej izračunanima parametroma a in b (gl. točko a) izračunali ustrezno teoretično pričakovano trdnost $\sigma_{i,\mathrm{th}}$.

č) Uporabili smo poenostavljeno različico grafične ponazoritve $Q - Q$ za primerjavo teoretičnih trdnosti $\sigma_{i,\mathrm{th}}$ z eksperimentalnimi σ_i. Pare vrednosti ($\sigma_{i,\mathrm{th}}$, σ_i) v diagramu smo prikazali tako, da teoretična komponenta ustreza vodoravni osi, eksperimentalna pa navpični. Če se torej teoretična statistična napoved odlično ujema z eksperimentom, ležijo točke v diagramu vse blizu premice z naklonom 45° proti osema.

d) Kvantitativno lahko opredelimo ujemanje teoretičnih napovedi z eksperimentalnimi podatki s faktorjem R^2:

$$R^2 = 1 - \frac{\sum_{i=1}^{N} (\sigma_i - \sigma_{i,th})^2}{\sum_{i=1}^{N} (\sigma_i - <\sigma_i>)^2} \quad (4)$$

kjer je $<\sigma_i>$ izračunana povprečna vrednost eksperimentalnih trdnosti. Vrednost R^2 blizu 1 pomeni dobro ujemanje.

3.2 Primerjane teoretične porazdelitve

Drugi parameter bomo zaradi analogije pri vseh treh porazdelitvah označili s podobnim simbolom: σ_{0W}, σ_{0N} in σ_{0LN}. To je umeritveni parameter, ki ima enoto trdnosti. Prvi parameter pa ima pri treh porazdelitvah povsem drugačen pomen. Podali bomo le porazdelitveno funkcijo p za vse tri porazdelitve. Porazdelitvene funkcije za Weibullovo, normalno in log-normalno porazdelitev označimo po vrsti s p_W, p_N in p_{LN}:

$$p_W(\sigma) = \frac{m}{\sigma_{0W}} \left(\frac{\sigma}{\sigma_{0W}}\right)^{m-1} \cdot \exp\left(-\left(\frac{\sigma}{\sigma_{0W}}\right)^m\right) \quad (5a)$$

$$p_N(\sigma) = \frac{1}{\delta\sqrt{2\pi}} \left(\frac{\sigma}{\sigma_{0W}}\right)^{m-1} \cdot \exp\left(-\frac{1}{2}\left(\frac{\sigma - \sigma_{0N}}{\delta}\right)^2\right) \quad (5b)$$

$$p_{LN}(\sigma) = \frac{1}{\sigma} \frac{1}{w\sqrt{2\pi}} \cdot \exp\left(-\left(\frac{\ln\sigma - \ln\sigma_{0N}}{w}\right)^2\right) \quad (5c)$$

Pri Weibullovi porazdelitvi imenujemo brezdimenzijski parameter m Weibullov modul, σ_{0W} pa umeritveni parameter. Pri normalni porazdelitvi imata parametra enostaven pomen: σ_{0N} je povprečna trdnost, δ pa njena standardna deviacija. Pri log-normalni porazdelitvi so normalno porazdeljeni logaritmi trdnosti.

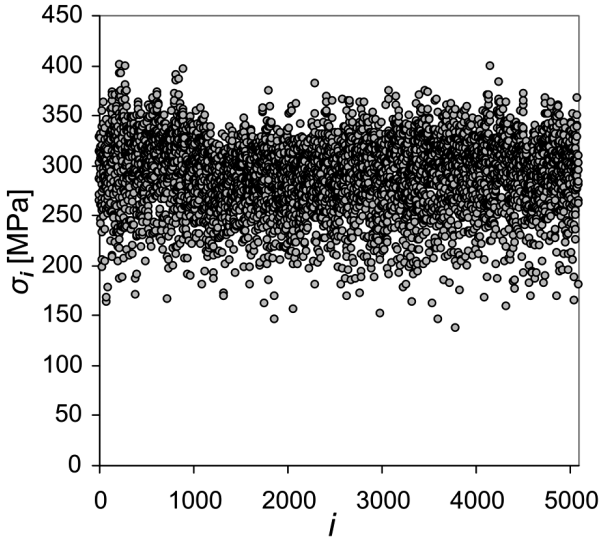

Slika 1: 5100 vrednosti upogibne trdnosti; številke na vodoravni osi ustrezajo časovnemu vrstnemu redu meritev
Figure 1: 5100 bending-strength values; the numbers on the horizontal axis correspond to the time sequence of the measurements

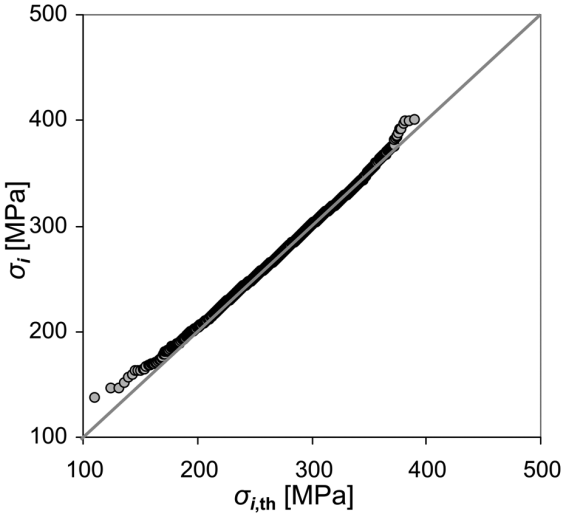

Slika 2: Q – Q-diagram za Weibullovo porazdelitev
Figure 2: Q – Q-diagram for the Weibull distribution

4 REZULTATI IN DISKUSIJA

Vseh 5100 eksperimentalnih trdnosti prikazuje **slika 1**, kjer je vsaka vrednost zapisana v kronološkem zaporedju (glede na čas meritve), njihova aritmetična povprečna vrednost pa je $<\sigma>$ = 289,557 MPa. V **tabeli 1** so podani z ML-metodo ocenjeni parametri treh porazdelitev, skupaj z R^2 faktorjem, ki je največji pri Weibullovi porazdelitvi. **Slika 2** prikazuje ustrezni Q – Q-diagram za to porazdelitev, druga dva pa sta temu kvalitativno podobna, le ujemanje točk s premico z nagibom 45° je nekoliko slabše.

Nazadnje smo naredili še primerjavo treh teoretičnih porazdelitev glede ujemanja teoretične pričakovane trdnosti $<\sigma>$, njene standardne deviacije $\delta\sigma$ in "kubične deviacije" $\delta_3\sigma$ z ustreznimi eksperimentalnimi vrednostmi. Kubično deviacijo smo definirali takole:

$$\delta_3\sigma = \sqrt[3]{<(\sigma - <\sigma>)^3>}$$

kjer trikotni oklepaji označujejo statistično povprečje. Rezultati so prikazani v **tabeli 2**. V prvi vrstici v vsakem od treh parov so eksperimentalne vrednosti teh parametrov, v drugi pa teoretične, in sicer v levem stolpcu (oznaka *) izračunane direktno iz prostih parametrov vsake porazdelitve, v desnem stolpcu (oznaka **) pa so izračunani s statističnim povprečjem "simuliranih teoretičnih" trdnosti $\sigma_{i,\mathrm{th}}$. Zaradi velikega števila podatkov lahko pričakujemo, da se bodo vrednosti, označene z **, zelo dobro ujemale s tistimi, označenimi z *, in to **tabela 2** tudi potrjuje. Medtem ko se pričakovana vrednost trdnosti in njena standardna deviacija pri vseh treh porazdelitvah dokaj dobro ujemata z ustreznimi eksperimentalnimi parametri, pa daje vsaj približno pravilen rezultat za kubično deviacijo samo Weibullova porazdelitev.

5 SKLEP

Primerjava treh teoretičnih porazdelitev s 5100 eksperimentalnimi trdnostmi keramike Al_2O_3 je pokazala, da je najustreznejši statistični opis z Weibullovo 2-para-

Tabela 1: ML-parametri in R^2 faktor za tri porazdelitve
Table 1: ML-parameters and the R^2 factor for the three distributions

Porazdelitev	1. parameter	2. parameter	R^2
Weibullova	m = 9,048	σ_{0W} = 305,54 MPa	0,9984
Normalna	δ = 37,49 MPa	σ_{0N} = 289,56 MPa	0,9855
Log-normalna	w = 0,1372	σ_{0LN} = 286,86 MPa	0,9468

Tabela 2: Eksperimentalni in teoretični statistični parametri porazdelitev
Table 2: Experimental and theoretical statistical parameters of the distributions

	$<\sigma>$		$\delta\sigma$		$\delta_3\sigma$	
Eksperiment	289,56		37,49		−29,58	
Weibullova	*289,41	** 289,41	*38,26	**38,26	*−32,15	*−32,12
Normalna	*289,56	** 289,56	*37,49	**37,48	*0	*1,19
Log-normalna	*289,57	** 289,56	*39,92	**39,91	*29,80	*29,75

metrično porazdelitveno funkcijo, kar med drugim potrjuje najvišji faktor R^2: 99,84 %, razlike v vizualni primerjavi statistik s Q – Q-diagrami pa so manj očitne. Omenimo lahko še, da daje ML-metoda za normalno porazdelitev natančne eksperimentalne vrednosti prvih dveh statističnih parametrov v **tabeli 2** (pričakovana vrednost trdnosti in standardna deviacija); v tem je torej normalna porazdelitev nekaj boljša od Weibullove, vendar pa daje popolnoma napačen rezultat za kubično deviacijo. Več podrobnosti lahko bralec najde drugje[25].

Zahvala

To raziskavo sta podprla Ministrstvo za šolstvo in šport ter Evropski socialni sklad. Zahvaljujemo se podjetju Hidria AET za eksperimentalne podatke.

6 LITERATURA

[1] W. Weibull, A statistical distribution function of wide applicability, J. Appl. Mech., 18 (**1951**), 293–297

[2] R. V. Curtis, A. S. Juszczyk, Analysis of strength data using two- and three-parameter Weibull models, J. Mater. Sci., 33 (**1998**), 1151–1157

[3] H. Peterlik, N. Orlovskaja, W. Steinkellner, K. Kromp, Prediction of strength of recrystallized siliconcarbide from pore size measurement – Part I – The bimodality of the distribution, J. Mater. Sci., 35 (**2000**), 699–707

[4] Q. S. Li, J. Q. Fang, D. K. Liu, J. Tang, Failure probability prediction of concrete components, Cem. Concr. Res., 33 (**2003**), 1631–1636

[5] D. Wu, J. Zhou, Y. Li, Methods for estimating Weibull parameters for brittle materials, J. Mater. Sci., 41 (**2006**), 5630–5638

[6] D. Wu, J. Zhou, Y. Li, Unbiased estimation of Weibull parameters with the linear regression method, J. Eur. Ceram. Soc., 26 (**2006**), 1099–1105

[7] R. Danzer, T. Lube, P. Supancic, Monte Carlo simulations of strength distributions of brittle materials – Type of distribution, specimen and sample size, Z. Metallkunde, 92 (**2001**), 773–783

[8] B. Bergman, On the estimation of the Weibull modulus, J. Mater. Sci. Lett., 3 (**1984**), 689–692

[9] A. Khalili, K. Kromp, Statistical properties of Weibull estimators, J. Mater. Sci., 26 (**1991**), 6741–6752

[10] J. Gong, A new probability index for estimation Weibull modulus for ceramics with the least-square method, J. Mater. Sci. Lett., 19 (**2000**), 827–829

[11] E. Barbero, J. Fernandez-Saez, C. Navarro, Statistical distribution of the estimator of Weibull modulus, J. Mater. Sci. Lett., 20 (**2001**), 847–849

[12] I. J. Davies, Empirical correction factor for the best estimate of Weibull modulus obtained using linear least squares analysis, J. Mater. Sci. Lett., 20 (**2001**), 997–999

[13] D. F. Wu, Y. D. Li, J. P. Zhang, L. Chang, D. H. Wu, Z. P. Fang, Y. H. Shi, Effects of the number of testing specimens and the estimation methods on the Weibull parameters of solid catalysts, Chem. Eng. Sci., 56 (**2001**), 7035–7044

[14] L. Song, D. Wu, Y. Li, Optimal probability estimators for determining Weibull parameters, J. Mater. Sci. Lett., 22 (**2003**), 1651–1653

[15] J. A. Griggs, Y. Zhang, Determining the confidence intervals of Weibull parameters estimated using a more precise probability estimators, J. Mater. Sci. Lett., 22 (**2003**), 1771–1773

[16] I. J. Davies, Best estimate of Weibull modulus obtained using linear least squares analysis: An improved empirical correction factor, J. Mater. Sci., 39 (**2004**), 1441–1444

[17] T. Tanaka, H. Nakayama, A. Sakaida, T. Imamichi, Evaluation of Weibull parameters for static strengths of ceramics by Monte Carlo simulation, Mater. Sci. Res. International, 1 (**1995**), 51– 8

[18] B. Faucher, W. R. Tyson, On the determination of Weibull parameters, J. Mater. Sci. Lett., 7 (**1988**), 1199–1203

[19] R. Langlois, Estimation of Weibull parameters, J. Mater. Sci. Lett., 10 (**1991**), 1049–1051

[20] M. Cacciari, G. Mazzanti, G. C. Montanari, Comparison of maximum likelihood unbiasing methods for the estimation of the Weibull parameters, IEEE Trans. On El. Ins., 3 (**1996**), 18–27

[21] ASTM C 1239 – 95: Standard practice for Reporting Uniaxial Strength Data and Estimating Weibull Distribution Parameters for Advanced Ceramics, American Society for Testing and Materials, Philadelphia, 1995

[22] C. Lu, R. Danzer, F. D. Fischer, Fracture statistics of brittle materials: Weibull or normal distribution, Phys. Rev. E, 65 (**2002**), 067102

[23] J. D. Gibbons, S. Chakraborti, Nonparametric statistical inference, CRC Press 2003

[24] R. Gnanadesikan, M. B. Wilk, Probability plotting methods for the analysis of data, Biometrika, 55 (**1968**), 1–17

[25] L. Gorjan, M. Ambrožič, Bend strength of alumina ceramics: A comparison of Weibull statistics with other statistics based on very large experimental data set, J. Eur. Ceram. Soc., 32 (**2012**) 6, 1221–1227

UDK 620.19
Professional article/Strokovni članek

ISSN 1580-2949
MTAEC9, 46(4)423(2012)

CREVICE CORROSION OF STAINLESS-STEEL FASTENING COMPONENTS IN AN INDOOR MARINE-WATER BASIN

ŠPRANJSKA KOROZIJA PRITRDILNIH KOMPONENT IZ NERJAVNEGA JEKLA V NOTRANJEM BAZENU Z MORSKO VODO

Matjaž Torkar, Franc Tehovnik, Matjaž Godec

Institute of Metals and Technology, Lepi pot 11, SI-1000 Ljubljana, Slovenia
matjaz.torkar@imt.si

Prejem rokopisa – received: 2012-02-07; sprejem za objavo – accepted for publication: 2012-02-16

Equipment made from austenitic stainless steel corroded already after six months of the operation of an indoor marine-water basin. Two super chlorinations were performed during this period. Corroded stainless-steel components and different fastening components were investigated to detect the corrosion causes and improve the bathers' safety. Pitting corrosion was observed on flat surfaces, while crevice corrosion prevailed on the nuts and spring washers of bolted joints. The main reasons for the corrosion damages were: a high concentration of chlorides, a deficient control of sacrificial anodes, a lower corrosion resistance of spring washers and an inaccurate montage of some fastening components. The corrosion processes due to chloride ions can be reduced with frequent washing of all stainless-steel components with clear water and timely replacements of the sacrificing anodes.

Keywords: stainless steel, SEM, cathodic protection, chlorination, pitting corrosion, crevice corrosion

V notranjem bazenu z morsko vodo je vsa oprema, izdelana iz avstenitnega nerjavnega jekla, po šestih mesecih obratovanja začela rjaveti. V tem obdobju sta bili izvršeni tudi dve superkloriranji. Površine komponent in različni pritrdilni elementi iz nerjavnega jekla, prizadeti s korozijo, so bili preiskani zaradi ugotavljanja vzroka korozije in tudi zaradi varnosti kopalcev. Na ravnih površinah je prevladovala jamičasta korozija, špranjska korozija pa je prevladovala pri maticah, vzmetnih podložkah in pri vijačenih spojih. Glavni razlogi za korozijske poškodbe so bili kombinacija velike koncentracije kloridov, pomanjkljiva kontrola žrtvenih elektrod, slabša korozijska obstojnost vzmetnih podložk in nenatančna montaža drugih pritrdilnih komponent. Korozijske procese zaradi kloridnih ionov zmanjšamo s pogostim čiščenjem in spiranjem komponent iz nerjavnega jekla s čisto vodo in s pravočasno menjavo žrtvenih elektrod.

Ključne besede: nerjavno jeklo, vrstična elektronska mikroskopija (SEM), katodna zaščita, klorinacija, jamičasta korozija, špranjska korozija

1 INTRODUCTION

The atmosphere of the indoor basins is one of the most aggressive in a building environment. Under specific temperature conditions chlorine containing chemical species in the vapours of the pool water can condense onto the stainless-steel components and dry out. After several repetitions of this process very aggressive concentrations of chlorine-containing mixtures may build up. As the presence of marine water accelerates the chloride attack[1], the use of austenitic stainless steel alloyed with molybdenum is recommended. The situation is aggravated when the austenitic stainless-steel components are not regularly cleaned.

Galvanic or sacrificial anodes are often used for the corrosion protection of the basin equipment. Stainless-steel components are connected with wires to the sacrificing anodes absorbing the corrosion currents to the anodes as they are designed to have a more negative electrochemical potential than the equipment to be protected. A sacrificing anode[2] (made of Zn or Mg alloys) continues to corrode (sacrifice), being consumed until a replacement becomes necessary. If the anode is not replaced in time, the system loses the protective role and the corrosion processes on the components become more intensive.

Bathers also introduce contaminants into the water. Being added to the water, the chlorine hydrolyzes rapidly and produces hypochlorous acid (HOCl) and hydrochloric acid (HCl) as described by equation (1):

$$Cl_2 + H_2O \approx HOCl + HCl \quad (1)$$

Depending on the variation of the water pH the concentration of hypochlorous acid versus the concentration of hypochlorite (OCl^-) varies as well. Hypochlorous acid is weak and it ionizes at pH 7.5 and at 25 °C [3] by equation (2).

$$HOCl \approx H^+ + OCl^- \quad (2)$$

When nitrogen and HOCI combine, chloramines like monochloramine, dichloramine and nitrogen trichloride are formed according to the equations (3 to 5):

$$NH_3 + HOCl \approx NH_2Cl + H_2O \quad (3)$$

$$NH_2Cl + HOCl \approx NHCl_2 + H_2O \quad (4)$$

$$NHCl_2 + HOCl \approx NCl_3 + H_2O \quad (5)$$

The reactions (1) to (5) are in equilibrium and occur in the forward and reverse directions.

The chloramine causes the characteristic chlorine pool smell[4]. The nitrogen trichloride is more problematic in the case of a heated indoor basin because more nitrogen trichloride is vaporised[5].

Two methods are used to eliminate chloramines[6,7]: break-point chlorination and super-chlorination. The later process is known as shocking because, with an addition of chlorine, the total chlorine in the basin water rises up to an amount ten times above the normal chlorine level. This operation is performed in a basin without any bathers. The basin can be used again when the level of chlorine is back down to around 5 μg/g. In general, the super-chlorination process is harmful to stainless-steel equipment and accelerates pitting- and crevice corrosions.

Chlorine is 100 % effective when the pH of water is 5.5. Such pH is too acidic for people to comfortably swim and it also accelerates the corrosion. At a higher pH, up to 7.0, algae will grow. The pH of 7.2 is the most comfortable for swimmers; however, having a pH of 7.2 chlorine is only 50-% effective and so a free-chlorine level should be increased to a minimum of 0.6 μg/g. The pH range of the pool water should be kept between 6.8 and 8 [8].

The latest research on super-chlorination revealed that the process is effective only for eliminating inorganic, ammonia-based chloramines. It was established that large doses of free chlorine react with organic contaminants and form a variety of disinfectants that are hazardous to the swimmers' health[9].

A new indoor basin with marine water was in operation for about six months. After that period traces of rust appeared around the screws and bolts, on all the surfaces of the equipment and on the stainless-steel decorative elements. The pillars holding the roof of the hall were decorated with vertical polished stainless-steel strips. The surface was covered with numerous speckles of rust, easily removable with a cloth. Corrosion pits were present on the steel surface under the rust. An in-situ control of all the basin components revealed rusted sites around the screws in the plastic inlets for fresh water (**Figure 1**), in the frames for the underwater lights and also on the joints connecting a step with a vertical holder tube (**Figure 2**). In fact, all stainless steel parts were more or less corroded.

The aim of this investigation was to reveal the reasons for general corrosion on all stainless-steel decorative and fastening components around and in the swimming pool. The safety of bathers was endangered also because of the rusted fastening joints of the vertical stairs.

2 EXPERIMENTAL PROCESS

After only six months of the operation corrosion products were observed on all the stainless-steel components. The rusted screws on the plastic frame of the fresh-water inlet, a nut, a spring washer and a bolt from the vertical stairs were removed and investigated.

An individual stair was fixed with a plastic inlet and a bolt on the vertical stair-holder tube. The rust was spread around the bolted connection (**Figure 2**), while no rust was observed around the direct contact of a longer bolt and the step holder. The removal of the step showed that the rust originated in the joint of the spring washer and the nut. The rust was concentrated around the spring washer, below the nut and spread around the bolted joints. The spring washer was heavily corroded.

A photograph of the rusted nut, the washer and the cross-head screw was taken (**Figure 3**) before further cleaning and the rust was removed from all the investigated samples in an ultrasound bath (**Figure 4**).

The surfaces damaged with the corrosion were examined with scanning electron microscopy (SEM) Jeol

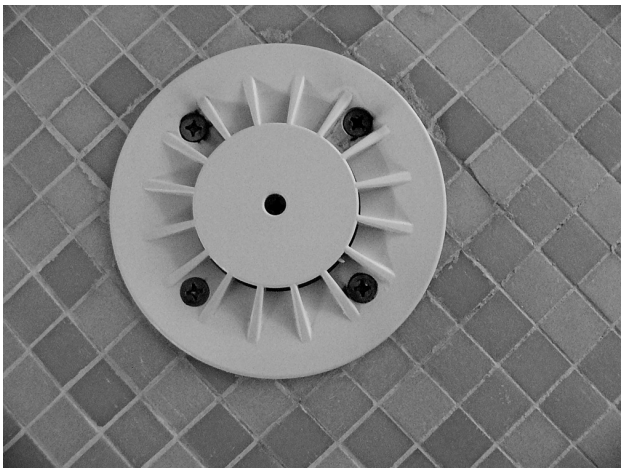

Figure 1: Rusted cross-head screws at the bottom of the pool
Slika 1: Rjasti vijaki s križno glavo z dna bazena

Figure 2: Rust on the vertical holder around the bolted-step connection
Slika 2: Rja na vertikalnem nosilcu okrog vijačenega spoja stopnice

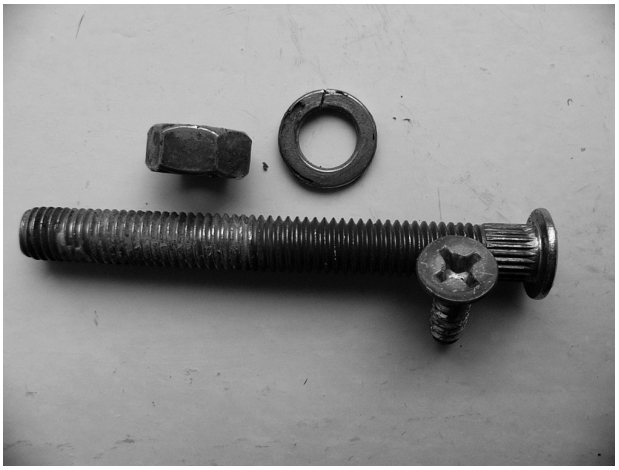

Figure 3: A nut, a spring washer, a structural bolt of the stairs and a cross-head screw, all cowered with rust
Slika 3: Matica, vzmetna podložka, vijak stopnice in vijak s križno glavo, vsi pokriti z rjo

Figure 4: Corrosion-damaged structural components after cleaning with ultrasound
Slika 4: S korozijo prizadeti konstrukcijski elementi po čiščenju z ultrazvokom

JSM-6500F having a field-emission gun and analysed with energy dispersive X-ray spectroscopy (EDS).

3 RESULTS AND DISCUSSION

Inside the screw head we observed dip caverns (**Figure 5** and **6**) resulting from crevice corrosion. The basic conditions for the start of crevice corrosion are a wet environment with chlorides and a narrow crevice where a renewal of a damaged protective oxide layer on stainless steel is not possible due to the restricted oxygen diffusion in the crevice. Chloride ions from the salt water migrate into the crevice and increase the solution acidity accelerating the corrosion attack on the protective layer on the stainless-steel surface. The results of crevice corrosion are either deep corrosion caverns, as observed in

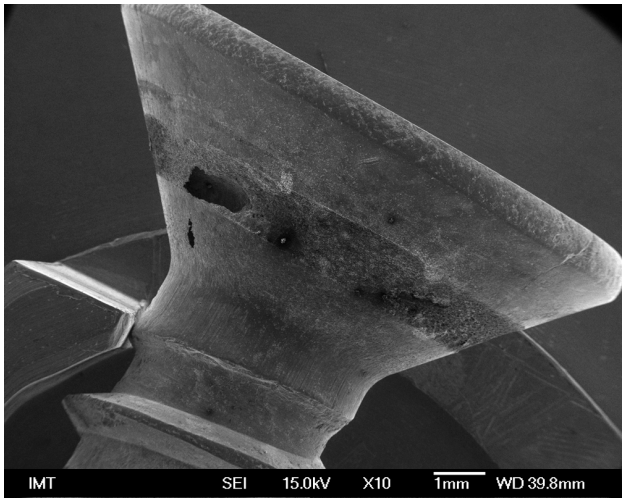

Figure 5: Screw damaged by crevice corrosion (SEM)
Slika 5: Vijak, poškodovan s špranjsko korozijo (SEM)

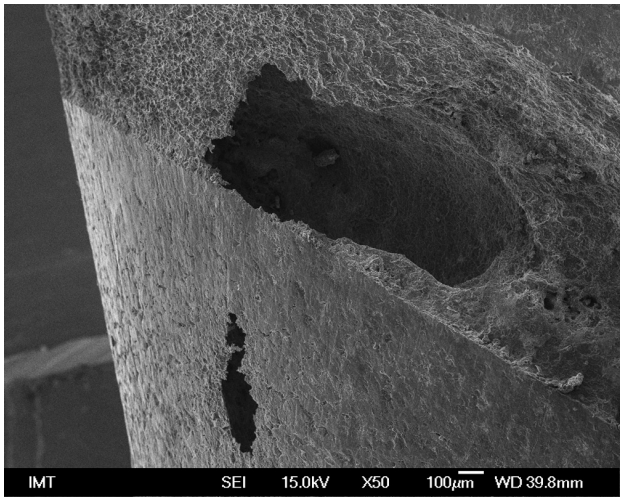

Figure 6: Detail from **Figure 5**: Crevice corrosion of a screw head (SEM)
Slika 6: Detajl s **slike 5**: špranjska korozija glave vijaka (SEM)

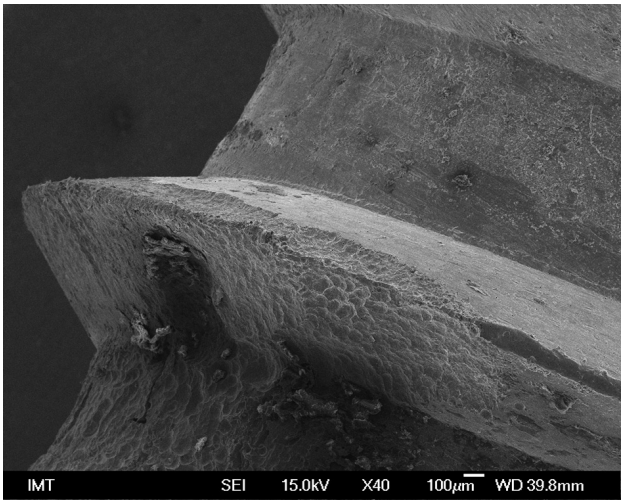

Figure 7: Corroded screw (SEM)
Slika 7: S korozijo poškodovan vijak (SEM)

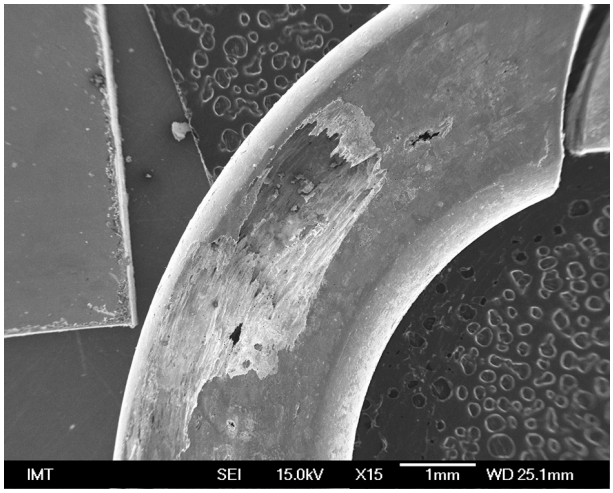

Figure 8: Crevice corrosion of a spring washer (SEM)
Slika 8: Špranjska korozija vzmetne podložke (SEM)

the screw head, or shallow pits, as observed on the screw body (**Figure 7**).

Corrosion caverns were also observed in the spring washer (**Figure 8, 9**), taken from the connection step of the vertical holder. A test of the spring washer with a magnet revealed slight magnetism in the cold-formed spring washer, probably due to the presence of deformation-induced martensite in the washer. This martensite in the austenitic stainless steel is magnetic and has a lower resistance to corrosion[9]. Deformation-induced martensite can be transformed back to austenite by heating at the temperature of 1 050 °C and by water rapid cooling. In the examined case, the spring washer was in the cold deformed state to keep the spring properties and for this reason the spring washer was the most sensitive component to corrosion. In general, there are two possible causes for the corrosion of a spring washer in a chloride environment: either crevice corrosion[10,11] due to geometrical reasons (the presence of a crevice) or stress corrosion[12] due to internal stresses in deformation-induced martensite of cold deformed steel. In the examined case it is supposed that the first cause prevailed because of the presence of corrosion caverns in the spring washer.

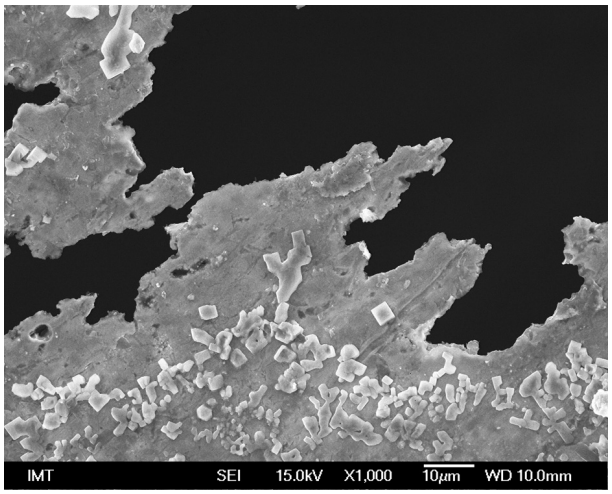

Figure 9: Remains of NaCl around a crevice-corrosion cavern (SEM)
Slika 9: Ostanki NaCl okrog izjede, povzročene s špranjsko korozijo (SEM)

The nut was from austenitic stainless steel, it was non-magnetic and after the removal of the rust the shallow pits were observed on the surface only. Comparing the corrosion damages on the nut and the spring washer, it looks that most of the rust originated from the spring washer.

The rust from the spring washer was spread also on the bolt and the bolt surface was coloured by the rust. No corrosion damages were observed on the bolt surface after being cleaned in the ultrasound bath.

An EDS analysis confirmed that the nut and the spring washer were made of austenitic stainless steel AISI 316 with 2 % to 3 % of molybdenum added to increase the corrosion resistance of stainless steel in a chloride environment.

The cross-head screw from the bottom of the basin did not contain molybdenum and was, thus, made of AISI 304 austenitic stainless steel that is less corrosion resistant in a chloride environment.

Stainless-steel components are usually corrosion protected with sacrificing electrodes made of Mg or Zn alloys. An in-situ control revealed that the sacrificing electrodes that were dissolved had neither been periodically checked nor replaced. For this reason, the austenitic stainless-steel stairs and fences were more serious attacked by corrosion.

4 CONCLUSIONS

Examinations revealed that after six months of the operation, severe corrosion damages appeared on all the stainless-steel components in the hall and in the basin with marine water.

Decorative bands, fences, the steps of vertical stairs and other austenitic stainless-steel components were damaged either by pitting or by crevice corrosion.

The spring washers and nuts were the most sensitive structural elements to corrode in the examined chloride environment.

The super-chlorination performed twice over a short period additionally increased the corrosion processes within the basin and the basin hall.

The corrosion processes due to chloride ions can be reduced with frequent cleaning of all stainless-steel components with clear water and timely replacements of the sacrificial anodes.

For the bathers' safety sake, all the vital joint connections in the vertical stairs need to be checked periodically and, if necessary, replaced in time.

5 REFERENCES

[1] D. R. Johns, K. Shemwell, The crevice corrosion and stress corrosion cracking resistance of austenitic and duplex stainless steel fasteners, Corrosion Science, 39 (**1997**) 3, 473–480

[2] C. R. Gagg, P. R. Lewis, Environmentally assisted product failure – Synopsis and case study compendium, Engineering Failure Analysis, 15 (**2008**) 5, 505–520

[3] L. F. Yee, Md. P. Abdullah, S. Ata, A. Abdullah, B. Ishak, K. Nidzham, Chlorination and Chloramines Formation, The Malaysian Journal of Analytical Sciences, 12 (**2008**) 3, 528–535

[4] W. Lee, P. Westerhoff, Formation of organic chloramines during water disinfection – chlorination versus chloramination, Water Research, 43 (**2009**) 8, 2233–2239

[5] C. Shang, W. Gong, E. R. Blatchley, Breakpoint Chemistry and Volatile Byproduct Formation Resulting from Chlorination of Model Organic-N Compounds, Environ. Sci. Technol., 34 (**2000**) 9, 1721–1728

[6] Applications of environmental aquatic chemisty: a practical guide, Eugene R. Weiner, CRC Press, Taylor@Francis Group, 2008

[7] D. Cassan, B. Mercier, F. Castex, A. Rambaud, Effects of medium-pressure UV lamps radiation on water quality in a chlorinated indoor swimming pool, Chemosphere, 62 (**2006**) 9, 1507–1513

[8] P. Sędek, J. Brózda, J. Gazdowicz, Pitting corrosion of the stainless steel ventilation duct in a roofed swimming pool, Engineering Failure Analysis, 15 (**2008**) 4, 281–286

[9] S. Weeb, Superchlorination — The Shocking Truth, May 10, 2011, http://aquamagazine.com

[10] M. Torkar, Corrosion of AISI 316 Ti in 50 % KOH due to deformation induced martensite, Engineering Failure Analysis, 13 (**2006**) 4, 624–628

[11] P. T. Jakobsen, E. Maahn, Temperature and potential dependence of crevice corrosion of AISI 316 stainless steel, Corrosion Science, 43 (**2001**) 9, 1693–1709

[12] B. Cai, Y. Liu, X. Tian, F. Wang, H. Li, R. Ji, An experimental study of crevice corrosion behaviour of 316L stainless steel in artificial seawater, Corrosion Science, 52 (**2010**) 10, 3235–3242